Modeling of microwave plasmas for carbon dioxide conversion

Proefschrift voorgelegd tot het behalen van de graad van doctor in de
wetenschappen aan de Universiteit Antwerpen te verdedigen door

Antonin Berthelot

PROMOTOR
prof. dr. Annemie Bogaerts

Faculteit Wetenschappen

Antwerpen 2018

Universiteit
Antwerpen

Universiteit Antwerpen

Modeling of microwave plasmas for carbon dioxide conversion

Proefschrift voorgelegd tot het behalen van de graad
van doctor in de Wetenschappen aan de Universiteit
Antwerpen te verdedigen door

Antonin Berthelot

Promotor: Prof. Dr. Annemie Bogaerts

Antwerp, 2018

Contents

List of Figures

List of Tables

Acknowledgments

First of all, I would like to thank my supervisor, Prof. Annemie Bogaerts, for giving me the opportunity to come to Antwerp for my PhD in the group PLASMANT. I have learned so much from you during these years. I could always count on your enthusiasm and your dedication to come up with a solution to the problems I've encountered. Even after all this time, I am still amazed by how cheerful you are. I am grateful for all the support you gave me and all the opportunities I got during my PhD. *Beste Annemie, hartelijk bedankt voor alles wat je voor mij hebt gedaan! Ik ben echt dankbaar dat je mijn promotor was.*

At the beginning of my PhD, and even later, I could always count on the advice and experience of Stanimir to build the 2D model. Thank you for all your help Stanimir! I am also indebted to Tomáš for always answering my questions about the CO_2 chemistry, even after you left the group.

I would also like to thank Luc. You've always answered the questions I had about Belgium and its ways during lunch, on top of providing me with technical help (and rebooting my computer!). Nelly, Ingrid were always kind and helpful with the administration.

I also had the opportunity to stay in DIFFER and TU/e to perform plasma experiments, and I would like to thank Prof. Gerard van Rooij and Dr. Richard Engeln for their hospitality. Thanks to Dirk, Claire and Niek for always having the patience to explain the experiments to me, I had a great time in the Netherlands thanks to you!

Thanks to the international group for making me feel at home in Antwerp and organizing all these events: Maryam (our energetic head organizer!), Monika, Fabiana, Stefano, Slavisa, Saeid, Amin, Natalia, Neda, Quan-Zhi, Weizong, Samira, Yu-Ru, Surong, Parisa, Mahdi, Mehdi, and all the others whom I've met in these parties. It was such a nice experience to meet friends from all around the world!

Georgi, Inne, Vincent and Yannick, thanks for the (non-?) scientific discussions during our coffee breaks, all the lunches, dinners and drinks we've had (and will have), (trying to?) motivating me to go to the gym, and all the office talks. It was always a pleasure coming to work thanks to you!

Thanks to all the others from Building B: Marleen, for the nice office talks, Damien, for the 'work' atmosphere during your stay, Erik, Chris, Sanne, Radu, Karen, Stijn (Hu & He), Kristof, Jonas, Violeta, Yannick E, Charlotte, Stefan, Maksud, Umid, Jamol, Robby, Ramses, Wouter, Koen, and many others! It was a pleasure working with you! Merci aussi à Alp pour toutes les discussions que l'on a eues à Anvers (et ailleurs!).

I also want to thank all the other members of the RAPID project: Igor, Natalia, Jean-Paul, Beata, Anna, Gert, Richard, Shaojun, Atta and Simon. Fiona and Patrick, it was always nice to have all these conversations in our awesome WhatsApp group! I'm really lucky that I've met all of you and I'm grateful for all the nice discussions and events we had (about plasma, obviously). I've learned a lot from this program.

Thanks to all my friends, in Belgium, in France and elsewhere for their support and for all the nice moments we shared: Niki and Caro, Bart, Matthieu, Laurent, Benoit, Anaïs, Florent, Thomas, Rachel, Jeremy, ... Thanks to Emma for all the moral support during these years.

Finally, thanks to my family: my parents, my sisters Laureline and Milène, my nephew Julien, and Marck and Quentin for their permanent support during all these years and for visiting me so often. *Merci pour tout ce que vous avez fait pour moi.*

CHAPTER I

Background

I.1 Introduction

A large part of the primary energy sources used on Earth is based on the combustion of fossil fuels. The burning of these fossil fuels emits greenhouse gases, and in particular CO_2. The concentration of CO_2 in the atmosphere has been steadily increasing over the last few decades due to the increasing energy demands of humanity. The strong correlation between the increase in atmospheric CO_2 concentration and the increase of the Earth's surface temperature is illustrated by figure I.1. There is now a common agreement among the scientific community that anthropogenic greenhouse gas emissions are responsible for the global warming observed over the past decades[1].

While the exact effects of global warming are difficult to predict, notably because of the uncertainty over the increase of the atmospheric CO_2 concentration, it is now well established that an increase of sea levels and of the frequency of extreme weather conditions are to be expected[2].

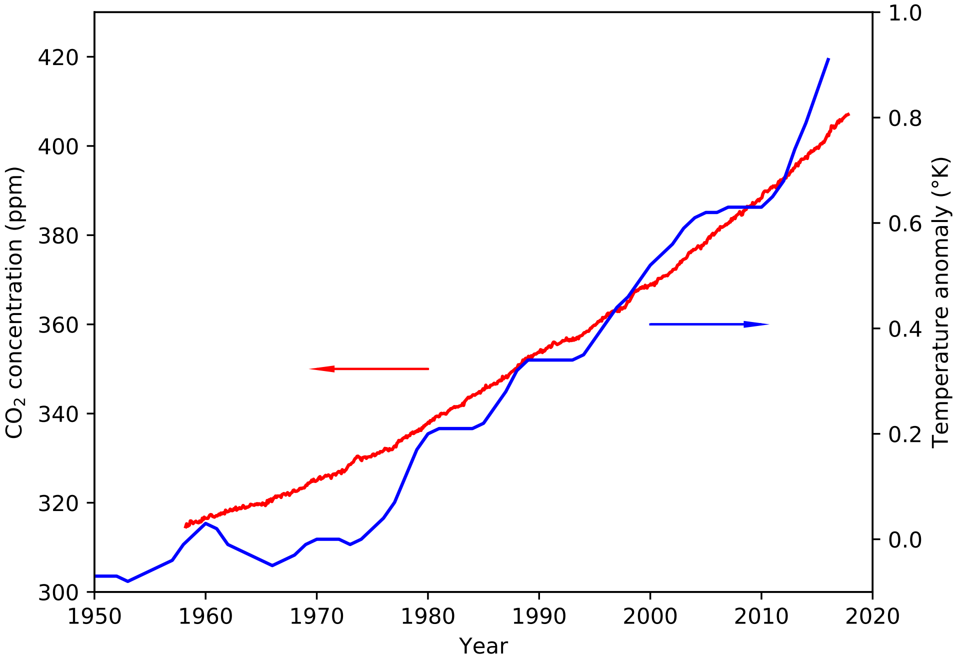

Figure I.1: Annual trend of atmospheric CO_2 concentration (left y-axis) and globally-averaged temperature anomaly since the 1950's with respect to the averaged temperature from 1951 to 1980 (right y-axis). Data obtained from NASA/NOAA[3].

I.1.1 The energy challenge of the 21st century

To reduce global warming, there has been a strong development of renewable energy production over the last decade. For instance, the share of energy produced by renewable energies (i.e. solar, wind, hydroelectric, ...) in the European Union has increased from 8.5 % in 2004 to 16.7 % in 2015 [4]. Moreover, following the Paris agreement, the European Union has agreed to cut its greenhouse gas emissions by 40 % compared to the 1990 level[5], by both reducing its energy consumption and increasing the share of renewable energy production up to 27 %, notably through an increase in wind and solar power generation.

These renewable energy sources, and in particular solar and wind power, suffer a major drawback: their intermittency. As an example of this intermittency, figure I.2 presents the electrical power by wind and solar production in France during the first 10 days of July 2015, as well as the electrical power consumption in the same period. Clearly, there is a temporal mismatch between both, as both solar and wind power production depend on the weather conditions. As the installed renewable power capacity increases, this mismatch will become a major problem for the power grid. Thus, there is a need for a solution to regulate the mismatch between supply and demand.

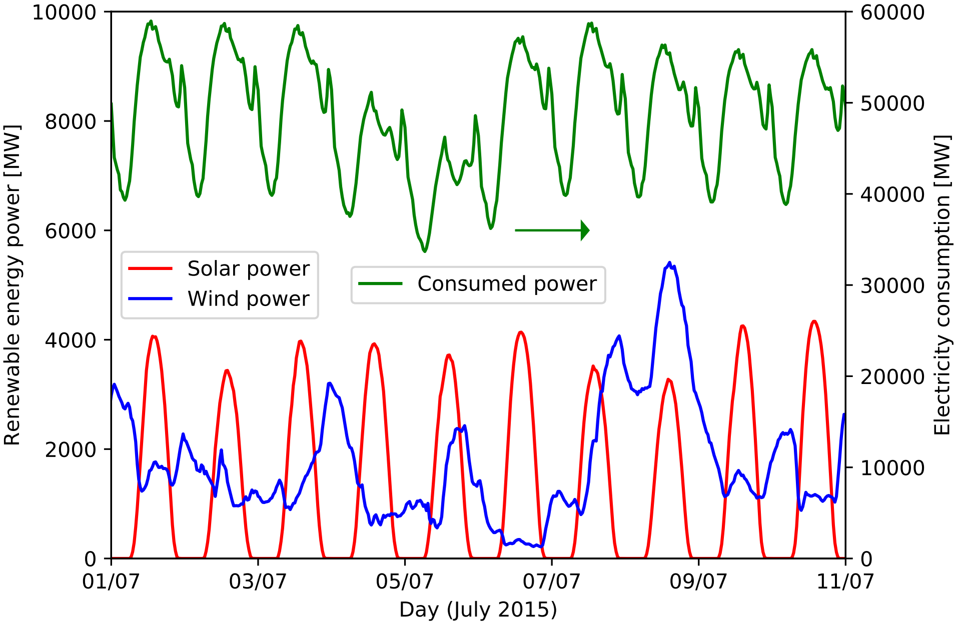

Figure I.2: Renewable power produced (left y-axis) and electric consumption (right y-axis) during the first 10 days of July 2015 in France. Data obtained from RTE[6]

Delucchi and Jacobson[7] give a list of potential solutions to this growing problem, with the idea of eventually reaching 100 % renewable energy production:

- Interconnecting geographically disperse renewable energy production plants can smooth out the production as well as the demand. As shown for example by Katzenstein *et al.*[8], increasing the distance between wind farms can decrease the correlation in their production, resulting in a smoother production. They have found, in Texas, that the correlation between the power outputs of wind farms situated 200km away from each other is half that of co-located wind plants.
- Using different types of renewable energy sources (i.e. wind, solar, water, geothermic, ...) would also smooth out the production, since it is unlikely that all of them produce energy at the same time. For instance, Lund[9] calculated the optimal mixture of renewable energy sources in Denmark to be 50 % onshore wind power, 20 % photo voltaic and 30 % wave power, assuming that renewable energy sources produce 80 % of the total energy consumption.
- Using a smart demand-response management so that the demand matches the production (and not the other way around)[10]. Indeed, while part of the energy consumption is an inflexible load (lighting, computers, ...), some of the demand is more flexible and can be shifted in time, for example charging electric vehicles or some kinds of heating and cooling. In order to match the demand better, forecasting the weather with a good accuracy is also required, so that grid operators have more time to plan ahead.
- Finally, storing the energy produced during the production peaks and releasing it when the production is minimum would allow to match time-dependent supply and demand, as detailed in the following section.

While the first three options of this list present the advantage of smoothing electricity production and demand in time and improve their matching, going to a 100 % renewable energy production, while ensuring that the electricity grid is reliable, would require efficient energy storage solutions.

I.1.2 Energy storage solutions

The various types of energy storage solutions can be classified in different categories depending on the physical/chemical or even biological properties they use. Among these categories, we can distinguish mechanical, electrochemical, thermal and chemical storage technologies.

Evidently, the energy efficiency of an energy-storage solution is its most important characteristic. This energy efficiency η is typically defined as:

$$\eta = \frac{E_{out}}{E_{in}} \tag{I.1}$$

where E_{out} and E_{in} are the output and input energy, respectively. Another important quantity to look at is the volumetric (or gravimetric) potential energy density, which is defined as the potential energy per unit volume (or per unit mass). It is of course more practical to have a high volumetric/gravimetric potential energy density.

Extensive reviews comparing the different energy storage techniques are available in literature[11–14]. The following gives a non-exhaustive list of various solutions for energy storage, with some of their positive and negative characteristics. Given the variety of energy storage technologies and the various characteristics that may be needed for different applications, there is of course not one ideal energy storage solution. Figure I.3 compares the cycle energy efficiency and volumetric energy density of the four types of energy storage technologies presented here, using data from Luo *et al.*[14].

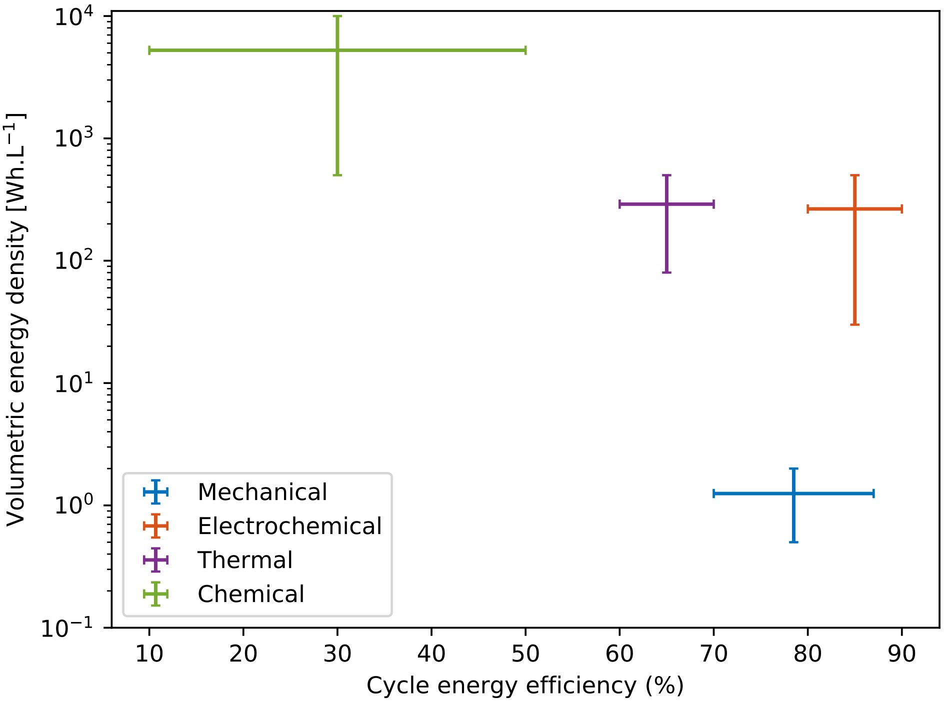

Figure I.3: Cycle energy efficiency and volumetric energy density of the four types of energy storage technologies presented here. Data obtained from Luo *et al.*[14]

I.1.2.1 Mechanical storage

Energy can be stored as potential mechanical energy. The most used form of mechanical storage is pumped hydroelectric energy storage [15]. It consists of two water reservoirs at two different altitudes. During production peaks, the water is pumped from the low reservoir to the higher level one. The potential mechanical energy can then be recuperated by releasing the water from the high reservoir to the low one, like in a conventional hydroelectric power plant. This technique can provide excellent energy efficiencies, typically ranging between 70 and 80 %. However, given the low energy density, between 0.5 and 2 $\mathrm{Wh.L^{-1}}$ (see figure I.3), it requires either a large body of water or a large variation of height.

I.1.2.2 Electrochemical storage

Batteries are one of the most common electrochemical energy storage solutions in our daily lives (phone, car batteries, ...). There exist many types of different batteries using various components, such as Li-ion, Pb-acid, Ni-Cd, Na-S, etc. [16]. While electrochemical storage technologies typically offer high energy efficiencies, often around 90 % (see figure I.3), their low volumetric and gravimetric energy density (between 30 and 500 $\mathrm{Wh.L^{-1}}$) is one of their main drawback, as well as the material they require.

I.1.2.3 Thermal storage

It is also possible to store energy as thermal energy, and in particular by changing its phase (e.g. solid to liquid)[17]. The volumetric and gravimetric energy densities thus depend on the specific heat capacity of the material and on its latent phase change heat, as well as on the temperature elevation. Using these technologies, solar power can be stored directly into thermal energy (i.e. no need to produce electrical energy first). However, their volumetric and gravimetric energy densities are again rather low, between 80 and 500 $\mathrm{Wh.L^{-1}}$ (see figure I.3).

I.1.2.4 Chemical storage

Electrical or thermal energy can be stored in bond energy. For example, water can be converted into hydrogen and oxygen. The reverse reaction $2H_2 + O_2 \rightarrow 2H_2O$ is strongly exothermic and can thus be used to release the energy stored in hydrogen. Chemical energy storage has several advantages compared to the other technologies that have potential large-scale applications[14]. (*i*) It shows the highest gravimetric and volumetric energy density, between 500 and 10000 $\mathrm{Wh.L^{-1}}$ (see figure I.3), which eases its transport. (*ii*) Chemical energy can be stored with no time limitations, provided that the chemicals produced are stable at the conditions of storage. (*iii*) Various molecules widely available on Earth can be used as reactants for the storage (H_2O, CO_2, ...). The main drawback of these techniques is the relatively low energy efficiency of the storage, typically ranging between 10 and 50 %(see figure I.3), although there is room for improvement, because these techniques are nowadays extensively investigated.

I.1.3 CO_2 conversion

The present work focuses on chemical energy storage by plasma-based CO_2 dissociation. Indeed, as explained by Martens *et al.*[18], storing hydrogen in gas phase can be technically challenging, since it is a small molecule and most materials are porous to H_2. On the other hand, hydrocarbons are nowadays widely used in the energy sector for their high volumetric energy density and the infrastructure for their storage, transport and use already exists. It is thus appealing to use hydrogen to form hydrocarbons using a carbon source, by using the Fischer-Tropsch process[19]:

$$(2n+1)\mathrm{H}_2 + n\mathrm{CO} \longrightarrow \mathrm{C}_n\mathrm{H}_{2n+2} + n\mathrm{H}_2\mathrm{O} \tag{I.2}$$

Using CO_2 as a carbon source, and thus obtaining CO from the dissociation of CO_2 appears to be a viable option. Indeed, given the raising awareness on global warming, there are increasing economic and political incentives towards the conversion of CO_2 into fuels and other value-added chemicals[20]. Moreover, CO_2 is nontoxic and abundant. The proposed scheme for CO_2 conversion is shown in figure I.4.

There exist a large number of other techniques to convert CO_2 into fuels or other value-added chemicals. While this thesis focuses on the conversion of pure CO_2, it is also possible to combine CO_2 with other chemicals, for instance dry-reforming of methane, i.e. combining CO_2 with methane to produce H_2 and CO directly.

Like any other chemical energy storage technology, the CO_2 conversion needs to satisfy certain specifications, for environmental, economical and technological reasons:

1. The process should be switched on and off rapidly, in order to adapt to the fluctuation of renewable energy production.
2. The materials required for building the device should be abundant.
3. The process should have a high energy efficiency.
4. The costs per dissociated CO_2 molecule should remain as low as possible.

There exist various different technologies for the conversion of pure CO_2 to CO, such as: thermal, electrochemical, solar thermochemical, photochemical, biochemical, catalytic and plasma technologies[21] .

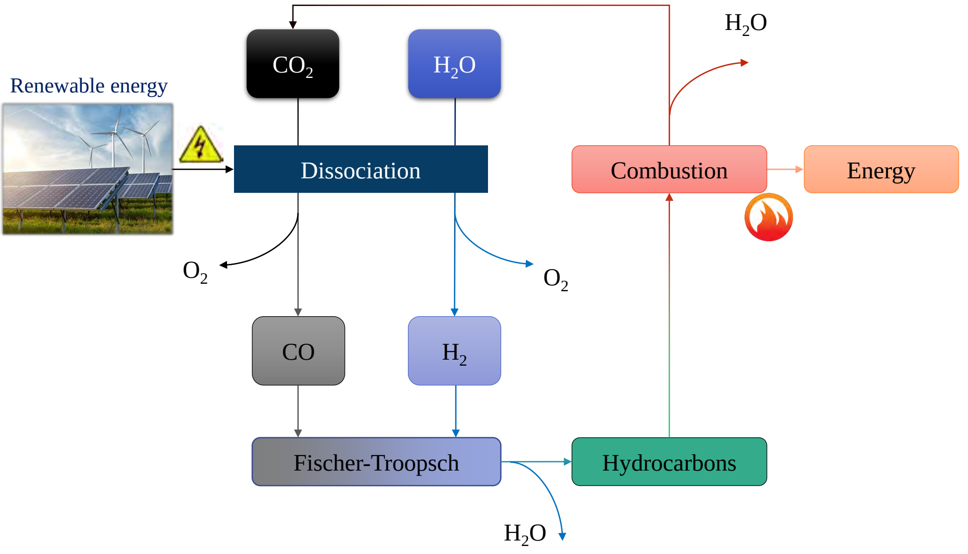

Figure I.4: Schematic representation of the carbon neutral CO_2 conversion process.

The endothermic dissociation of pure CO_2 can be summarized by the following formula [22;23]:

$$CO_2 \rightarrow CO + \frac{1}{2}O_2 \qquad \Delta H^{\circ} = +2.93\,\text{eV/molec} \tag{I.3}$$

This reaction is most efficient when it follows the two steps:

$$\begin{aligned} CO_2 \rightarrow CO + O \qquad & \Delta H^{\circ} = +5.51\,\text{eV/molec} \\ CO_2 + O \rightarrow CO + O_2 \qquad & \Delta H^{\circ} = +0.35\,\text{eV/molec} \end{aligned} \tag{I.4}$$

The standard enthalpy ΔH° of this reaction is high since CO_2 is a highly stable molecule. This means not only that a substantial amount of energy is required to dissociate CO_2, but also that the reaction equilibrium lies towards the left side of the reaction. Therefore, purely thermal conversion without removing the products (cf Le Chatelier principle) can only be favorable at high temperature, as can be seen in figure I.5. The data presented in this figure was obtained using the gas phase thermochemistry data of the NIST database[23]. It shows that while the conversion can reach a value close to 100 % at temperature of 5000 K and above, the energy efficiency is at best around 52 %. Moreover, the higher the gas temperature, the more energy is required to heat the gas, which becomes detrimental for the energy efficiency. Note that these values are to be seen as a theoretical maximum for thermal conversion, based on the data of reaction I.3. This work studies the CO_2 conversion by non-equilibrium plasmas, where it is possible to overcome this theoretical maximum of thermal conversion, as will be explained in next section.

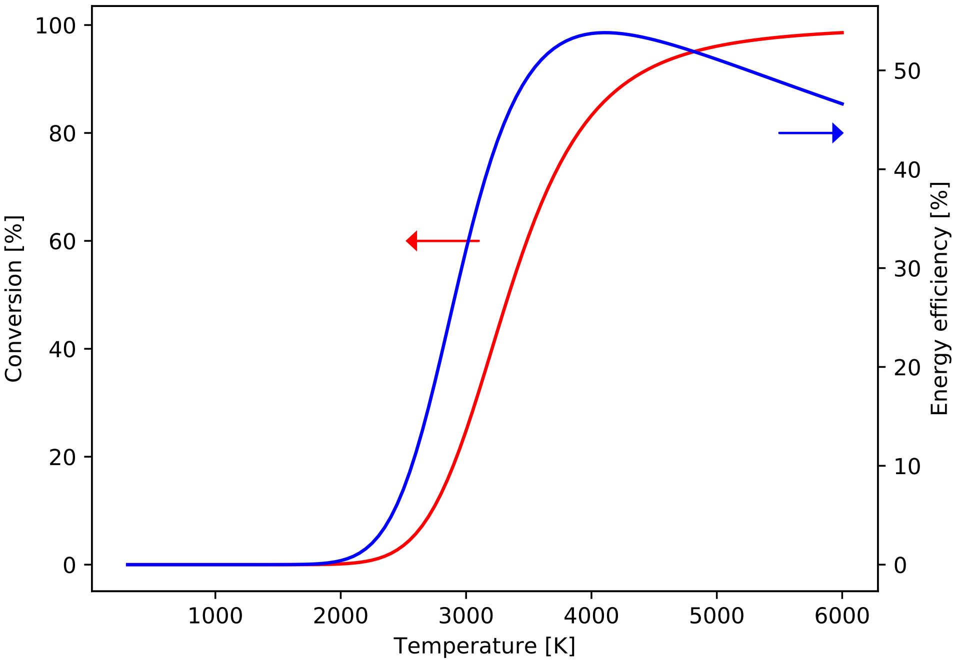

Figure I.5: Calculated theoretical thermal conversion of pure CO_2 (left y-axis) and corresponding energy efficiency (right y-axis) as a function of temperature.

I.2 Non-equilibrium plasmas

Plasmas are ionized gases. They are called plasmas, in analogy with blood plasma, since they are composed of various compounds interacting with each other. Namely, a plasma is composed of negative charges (electrons, negative ions), positive ions, radicals, atoms and molecules in their ground and excited states. Plasmas are sometimes referred to as the fourth state of matter, although there is no clear transition from the first three states to plasma. The plasma bulk can be considered neutral, since the positive and negative charges mostly compensate for each other.

Plasmas can be created by giving a sufficient amount of energy to a gas, a liquid or a solid in order to ionize its atoms or molecules. This energy can be given to the plasma by high-frequency electromagnetic fields (radio-frequency, microwave), heating, electric fields between two electrodes, magnetic fields, lasers, etc. The temperature of the heavy particles in a plasma ranges from room temperature for biomedical plasmas to 10^8 K for fusion plasmas. The ionization degree, defined as the ratio between the electron density and the neutral particle density can be almost equal to 1 in fusion plasmas, while it is typically lower ($10^{-7} - 10^{-4}$) in the plasmas used for gas conversion[24].

Typically, a distinction is made between equilibrium (or thermal) and non-equilibrium plasmas (sometimes referred to as cold plasmas). In equilibrium plasmas, the electrons and the heavy particles have similar temperatures. On the other hand, in non-equilibrium plasmas the electrons reach a temperature much higher than that of the heavy particles. The means electron energy is typically closely connected (linear dependence) to the reduced electric field E/N, which is simply the ratio between the absolute value of electric field and the neutral number density. It is often expressed in Townsend (Td), with 1 Td = 10^{-21} V.m^{-2}.

The non-equilibrium characteristic is particularly interesting in the framework of energy-efficient gas conversion. Indeed, because the electrons can acquire high energies, they can overcome the energy barrier of highly endothermic reactions. These reactions can then occur without the need to heat the gas as a whole, which can significantly improve the energy efficiency of a process.

I.2.1 Plasma chemistry

The collisions occurring in a plasma are either elastic or inelastic collisions. Elastic collisions conserve the internal energy of each of the particles colliding and only transfer kinetic energy from one particle to the other. During an inelastic collision, on the other hand, the internal energy of the particles changes. For instance, electron-impact electronic excitation is an inelastic collision. Tables I.1 and I.2 list the main inelastic reactions occurring in non-equilibrium plasmas.

All of the species present in a plasma can interact with each other and react together over various timescales. The collision frequency of the particles increases with their temperatures and their densities, and thus also with pressure. Therefore, the chemistry of a plasma also depends on macroscopic variables, and in particular on pressure and various temperatures (translational, rotational, vibrational, electronic).

Table I.1: Main plasma electronic and radiative inelastic processes[22]. A and B represent atoms or molecules and M is a temporary collision partner. X* denotes an excited state of X.

Electron-impact reactions	
Excitation	
Rotational	$AB + e^- \longrightarrow AB[r] + e^-$
Vibrational	$AB + e^- \longrightarrow AB[v] + e^-$
Electronic	$A + e^- \longrightarrow A[e] + e^-$
Ionization	
Direct ionization	$A + e^- \longrightarrow A^+ + 2e^-$
Step-wise ionization	$A^* + e^- \longrightarrow A^+ + 2e^-$
Dissociative ionization	$AB + e^- \longrightarrow A + B^+ + 2e^-$
Attachment	
Attachment	$A + e^- \longrightarrow A^-$
Dissociative attachment	$AB + e^- \longrightarrow A + B^-$
Recombination	
Three-body recombination	$A^+ + 2e^- \longrightarrow A + e^-$
Dissociative recombination	$AB^+ + e^- \longrightarrow A + B$
Dissociation	
Direct dissociation	$AB + e^- \longrightarrow A + B + e^-$
Polar dissociation	$AB + e^- \longrightarrow A^- + B^+ + e^-$
Detachment	$A^- + e^- \longrightarrow A + 2e^-$
Radiative reactions	
Photo-ionization	$A + \hbar\omega \longrightarrow A^+ + e^-$
Radiative transition	$A^* \longrightarrow A + \hbar\omega$

I.3 State of the art in CO_2 conversion by non-equilibrium plasmas

Historically, non-equilibrium CO_2 plasmas and their chemistry have been first studied in the field of CO_2 lasers[25–29]. These lasers emit photons in the infra-red range, centered either around 9.4 μm or 10.6 μm. The active laser medium is a mixture of CO_2, N_2, H_2 (and/or Xe) and He.

CO_2 discharges have also been studied in the framework of space research, for the Mars mission in order to produce oxygen from Mars atmosphere[30–32].

The use of plasma technologies for CO_2 conversion was first studied in the 1970's in the former Soviet Union[22]. More recently, the scientific and decision-making communities have regained interest in this technique with the increasing demand for clean energy

Table I.2: Main plasma atomic and molecular inelastic processes[22]. A and B represent atoms or molecules and M is a temporary collision partner.

Charged particle reaction	
Penning ionization	$AB + M \longrightarrow AB^+ + e^- + M$
Charge transfer	
Positive charge transfer	$A + B^+ \longrightarrow A^+ + B$
Negative charge transfer	$A + B^- \longrightarrow A^- + B$
Ion-Ion recombination	
Two-body ion-ion recombination	$A^- + B^+ \longrightarrow AB$
Three-body ion-ion recombination	$A^- + B^+ + M \longrightarrow AB + M$
Detachment	
Detachment	$A^- + B \longrightarrow A + B + e^-$
Associative detachment	$A^- + B^+ \longrightarrow AB + e^-$
Neutral particle reactions	
Penning dissociation	$AB + M \longrightarrow A + B + M$
Neutral recombination	$A + B + M \longrightarrow AB + M$
Heavy particle vibrational energy transfers	
Vibrational-Translation (VT)	$A[v_i] + M \longrightarrow A[v_{i-i}] + M$
Vibrational-Vibrational (VV)	$A[v_i] + A[v_j] \longrightarrow A[v_{i+1}] + A[v_{j-1}]$
Vibrational-Vibrational' (VV')	$A[v_i] + B[v_j] \longrightarrow A[v_{i+1}] + B[v_{j-1}]$

storage technologies. Non-equilibrium plasma technologies offer several advantages for CO_2 conversion. First, plasmas can be turned on and off almost instantly, so they can easily adapt to the energy demand-production mismatch. In addition, as explained in the following sections, plasma reactor devices are rather simple and typically only contain widely used electrical components made of abundant materials, which leads to rather low costs of operation and little environmental impact. Finally, energy efficiencies up to 90 % have been reported in the literature from the former USSR[22;33], although more recent experiments exhibit energy efficiencies up to about 50 %[21;34].

A very large number of publications have been written over the last few years, based on both experimental[34–48] and modeling work[49–64]. This section aims at pointing some of the main scientific and technological advances in CO_2 dissociation by non-thermal plasmas, which is the topic of this doctoral work.

I.3.1 The importance of vibrational excitation

CO_2 is a linear triatomic molecule and therefore has four vibrational modes. In practice, CO_2 is usually considered to have three vibrational modes, one of which is doubly degenerate. The vibrational configuration of CO_2 is often designated by (k,m,n), where k, m and n are the three quantum numbers corresponding to the three modes. The three basic modes are: the symmetric stretch mode (1,0,0), the symmetric bending mode $(0,1^l,0)$, which is degenerate, and the asymmetric stretch mode (0,0,1). The energy of the first level of these three modes is 0.165 eV, 0.083 eV and 0.291 eV, respectively. l is the quantum number for the angular momentum of the quasi-rotation around the principal axis of CO_2. Note that there is also an 'accidental' degeneracy between the symmetric stretch and bending modes, since the energy of the levels $(0,2^l,0)$ is almost equal to the energy of (1,0,0).

Figure I.6 presents the fraction of energy transferred through different inelastic processes as a function of the reduced electric field in pure CO_2, and as a function the mean electron energy. This figure was obtained using Bolsig+[65], a two-term approximation Boltzmann equation solver (see section II.2), and the cross section data considered in this work (see appendices A.1 and A.2).

The importance of vibrational excitation is very obvious in figure I.6. Indeed, for reduced electric fields of 60 Td and below, almost 100 % of the electron energy transfers to CO_2 vibrational excitation. At higher E/N, other processes with higher energy threshold, such as electron impact dissociation and ionization, become more and more likely to occur. Of course, the presence of other gases, molecular or not, would have an influence on these channels[66].

The asymmetric vibrational mode of CO_2 is particularly important since it tends to be more excited in a CO_2 plasma[22]. First, as seen in figure I.6, most of the electron energy goes to this mode with typical reduced electric field values (E/N > 50 Td). In addition, its vibration-translation (VT) relaxation rate is slower than the one of the two symmetric modes, which leads to an accumulation of vibrational energy in this mode. Finally, vibration-vibration (VV) exchanges among this mode are faster than for the symmetric modes, which helps the highly excited asymmetric mode levels to become populated. More information about these mechanisms is given in chapter III.

It is possible to vary the E/N to favor one electron energy loss pathway or an other. Andreev*et al.*[67] have shown that a lower E/N, and thus an enhanced vibrational excitation, lowers the energy cost per CO_2 molecule dissociated. In their conditions, the energy cost per CO_2 molecule dissociated was minimal (about 10 eV/molec) with an E/N of 20 Td.

From these observations, Fridman proposed a model[22] to explain the enhancement of CO_2 dissociation in vibrationally-excited plasmas, as summarized in figure I.7. There are two main ways to dissociate a CO_2 molecule in a non-equilibrium plasma:

(*i*) An energetic electron can collide with a $CO_2(^1\Sigma^+)$ molecule in ground electronic state and excite it to an electronic excited state $CO_2(^1B_2)$, which dissociates

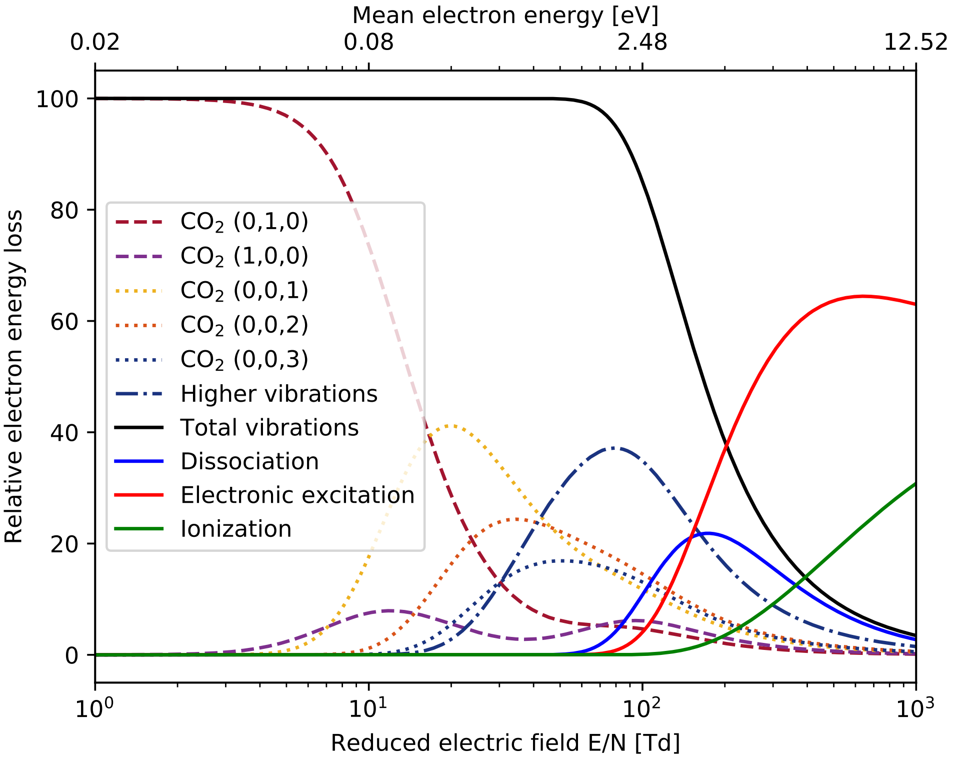

Figure I.6: Fraction of electron energy transferred through different inelastic processes as a function of the reduced electric field (bottom x-axis) and mean electron energy (top x-axis).

into CO($^1\Sigma^+$) electronic ground state and O(^{1}D) electronic excited state. This process has a large energy threshold of more than 7 eV.

(*ii*) An electron with somewhat lower energy can also vibrationally excite $CO_2(^1\Sigma^+)$ until the molecule reaches a high enough vibrational energy to transfer to another electronically excited state $CO_2(^3B_2)$. The dissociation of this state forms a CO molecule and an O atom in their ground electronic state. This process, also called ladder-climbing dissociation or vibration-induced dissociation, is thus more efficient as it requires a total energy of only 5.5 eV, which is equal to the OC=O bond energy.

I.3.2 Different types of plasma sources for CO_2 conversion

Various types of plasma reactors have been considered to convert CO_2 into value-added compounds. Each of them has its advantages and disadvantages. This section gives a short review of the different plasma reactor types used to convert CO_2 and highlights

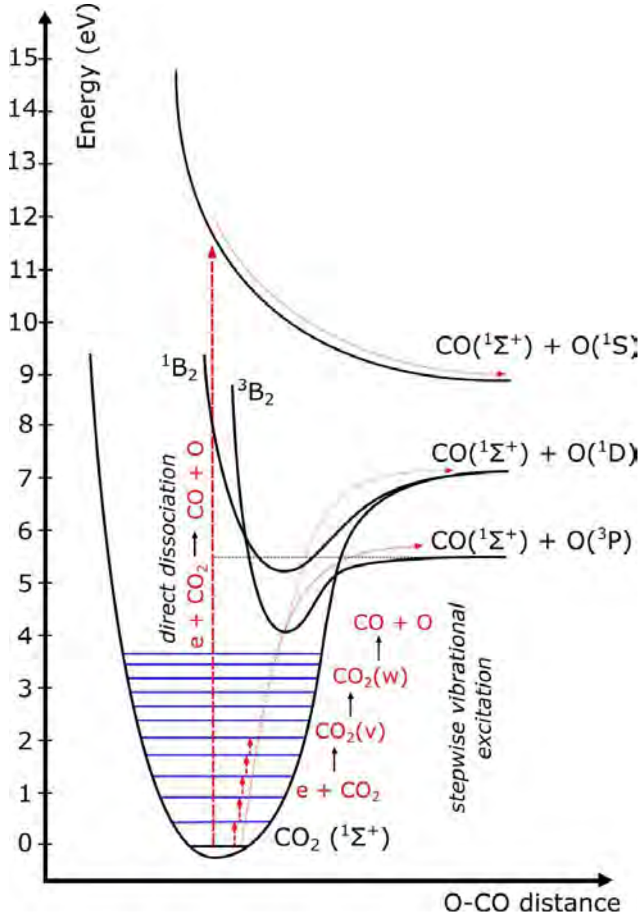

Figure I.7: Schematic diagram of the first CO_2 electronic and vibrational levels, illustrating direct electron impact dissociation and step-wise vibrational excitation, the so-called ladder climbing process. Taken from Bogaerts *et al.*[62]

the relevant differences between them.

I.3.2.1 Dielectric barrier discharges

Dielectric barrier discharges (DBD), also previously called silent discharges, are one of the oldest and simplest plasma devices. They simply consist of two electrodes separated by at least one dielectric barrier. The purpose of this dielectric barrier is to avoid the formation of sparks and/or arcs[68]. It can be made of various dielectric materials, such as quartz, glass, ceramic, etc. The process usually uses AC voltage, with a frequency ranging from a few kHz to the radio-frequency range[69]. A DBD system can be considered as a capacitor[70]. It is often electrically modeled as such.

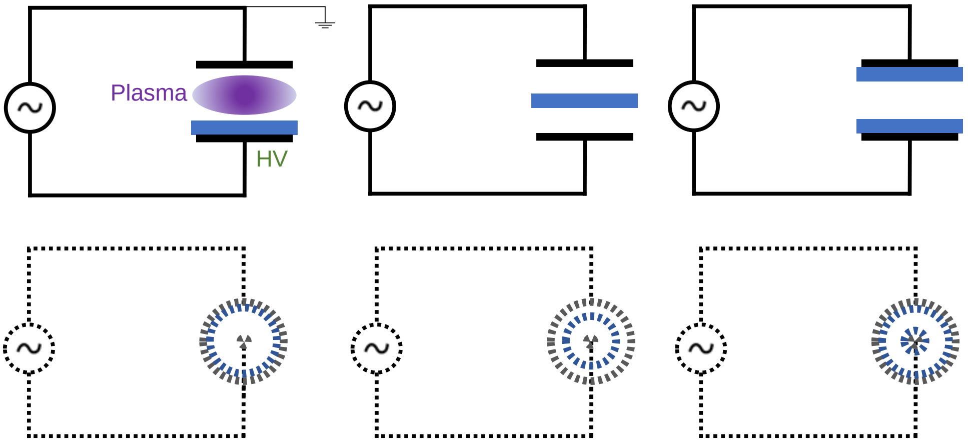

Figure I.8: Basic planar (top) and cylindrical (bottom) dielectric barrier discharge configurations. Adapted from Snoeckx and Bogaerts[21]

The ignition of a discharge in a DBD requires a certain voltage between the electrode, called the breakdown voltage V_b. It can be determined by Paschen's law[71]:

$$V_b = \frac{Bpd}{C + \ln(pd)} \tag{I.5}$$

where B and C and experimentally measured constants that depend on the gas composition, p is the pressure and d is the distance between the electrodes.

Figure I.8 shows the most common types of DBD configurations, with both planar and cylindrical electrodes.

More information on DBDs can be found in several review papers and books[69;71;72]. DBD systems are used in a variety of industrial application[73;74], notably thanks to their scalability and their simplicity. The most notorious application (and the oldest) is probably ozone production[75].

DBDs have recently been widely used for CO_2 splitting research[41–44;76;77]. To my knowledge, the best energy efficiency reported with a DBD setup is 23 %[77] using a pulsed power DBD with a duty cycle of 40 %. The corresponding CO_2 conversion is 26 %. However, most experimental values of energy efficiency stay below 15%[21].

A trade-off is usually found between energy efficiency and conversion[42], since an increase in conversion typically leads to a decrease in energy efficiency (and vice-versa).

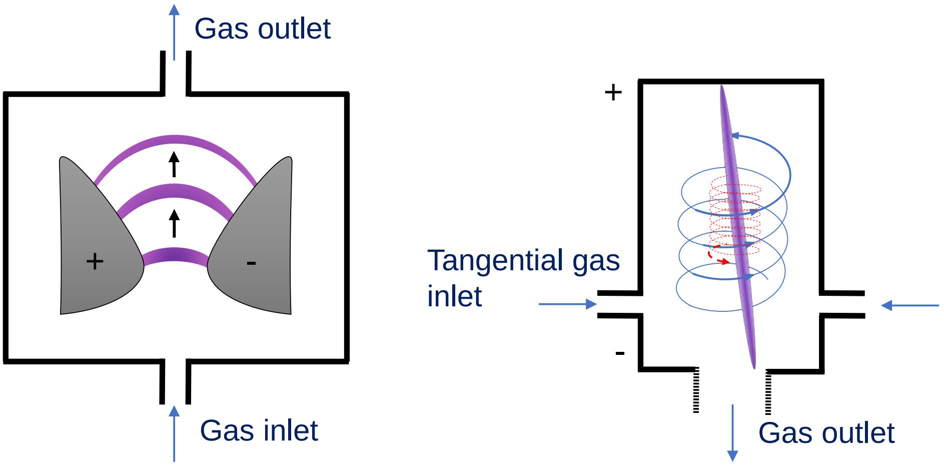

Figure I.9: Schematic representations of a classical gliding arc (left) and of a gliding arc plasmatron (right), with the arc presented in purple, and the forward and reverse vortex gas flows in blue and red spirals, respectively) . Adapted from Snoeckx and Bogaerts[21].

I.3.2.2 Gliding arc discharges

There exist different types of gliding arc discharges, including classical gliding arcs (GA) with 2D electrodes, and cylindrical GA discharges, such as rotating GA and (reverse) vortex flow GA, also called GA plasmatron (GAP).

In its simplest form, GA discharges are formed using two diverging flat electrodes in between which a gas flows, as illustrated by figure I.9 (left). When a potential difference is applied between the electrodes, an arc form at the shortest inter-electrode gap. The arc is then dragged upwards by convection, due to the heating it generates and by the gas flow. It goes upwards until the arc is too long to be sustained anymore. A new arc then forms again at the shortest inter-electrode gap and the cycle repeats itself. Although GA plasmas can reach rather high gas temperature, they are still in non-equilibrium, because of convectional cooling. The electron temperature is around 1 eV for an atmospheric pressure GA plasma. This is typically considered to be the most favorable electron temperature for CO_2 conversion, since it favors vibration-induced dissociation, as shown by figures I.6 and I.7.

There are only a few studies of CO_2 conversion in a gliding arc plasma. Indarto *et al.*[38] reported a CO_2 conversion up to 18 % and an energy efficiency of about 20 %. As shown by Sun *et al.*[78], only a limited fraction of about 20 % of the gas passes through the arc in a classical GA, with variations depending on the geometry, and the conversion thus cannot exceed this value of about 20 %. This is quite a strong limitation for classical GAs, which has lead to the development of cylindrical GA reactors, like the GAP.

A GAP is formed in a cylindrical plasma reactor and make use a vortex flow stabilization[39], as schematized in figure I.9 (right). The gas inlet is tangential, which creates the vortex flow. When a potential difference is applied between the reactor body and gas outlet (functioning as positive and negative electrode, respectively), the arc forms again at the shortest inter-electrode gap and then elongates from the top of the reactor (positive electrode) to the bottom of the reactor (gas outlet, negative electrode)[79]. It stays elongated in the middle of the reactor but keeps on moving under the effect of the flow.

Nunally *et al.*[39] reported energy efficiencies up to about 43 % for a conversion of less than 10 % using a GAP. Ramakers *et al.*[79] obtained an energy efficiency up to 46 % with a conversion of about 3 % (in the low current regime), or an energy efficiency around 30 % with a conversion up to 10 % (in the high current regime). They observed a slight decrease in energy efficiency with increasing specific energy input (SEI). Their GAP can operate both at low current (around 50 mA) and at high current (260-380 mA) regimes. As mentioned above, the former regime was found to give the highest energy efficiency but low conversion, while the high current regime yields a higher SEI, and thus a higher conversion, but somewhat lower energy efficiency. Kim *et al.*[80] showed an energy efficiency up to 52 % and demonstrated that the addition of CH_4 to the discharge in a GAP can further improve the energy efficiency. This was also demonstrated by Cleiren*et al.*[81] for a mixture of CO_2 and CH_4, where an energy efficiency of 66 %, with a total conversion of almost 30 %, was reported for 25 % CH_4 addition.

Gliding arc plasmas have the advantage to offer high energy efficiencies, even at atmospheric pressure. In contrast to DBD reactors, their scaling-up in view of industrial applications, however, has not yet been demonstrated[21].

I.3.2.3 Microwave discharges

Microwave (MW) discharges are very flexible systems and operate over a wide pressure range, going from a few mPa to atmospheric pressure. Microwaves are a form of electromagnetic radiation with frequencies ranging from 300 MHz to 300 GHz[82], although most plasma applications use frequencies of 915 MHz or 2.45 GHz, due to the regulations related to the use of radio-frequency (RF) and MW frequencies. Many different types of MW discharge setups exist. The three most common ones are presented in figure I.10.

The surfaguide consists of a waveguide, in which the MWs travel, pierced by a

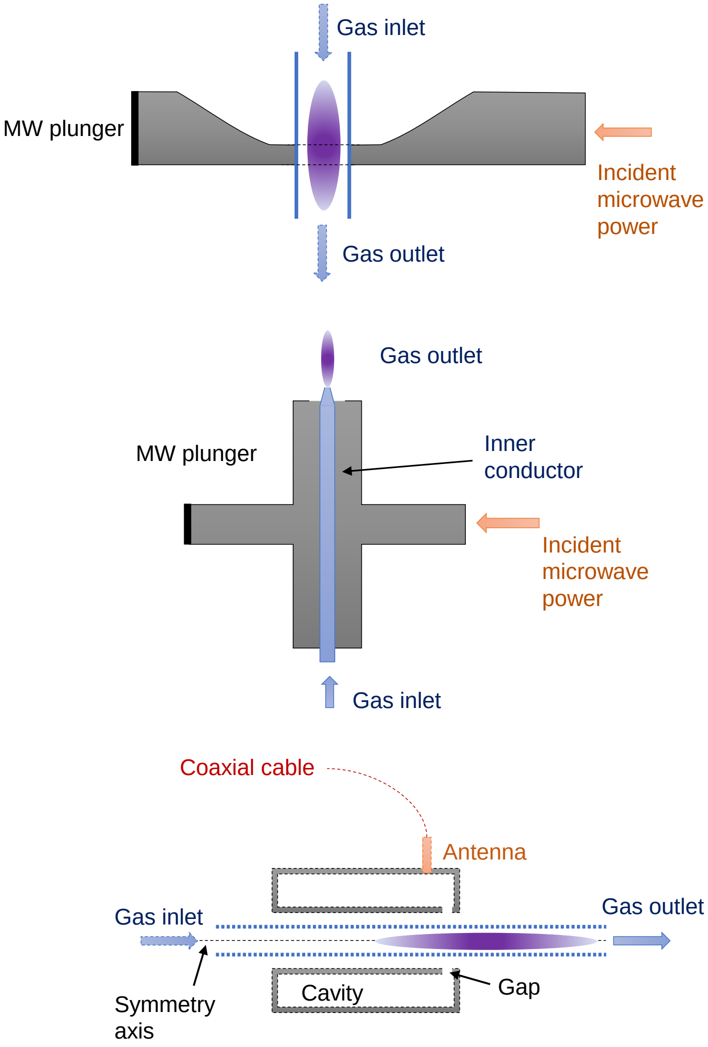

Figure I.10: Schematic representation of the three main microwave setups: the surfaguide (top), the plasma torch (middle) and the surfatron (bottom).

quartz tube in which a gas flows[83]. The energy from the MWs is transferred to the free electrons in the gas, thus creating ionization and forming a plasma. It was designed to work with high electromagnetic powers, from about 100 W to a few kW, thanks to its waveguide feeding system. This is an interesting property, keeping in mind the ultimate need to scale up these technologies for industrial use.

The development of plasma torches started in the 1950's[84]. It typically works at atmospheric pressure and has features close to that of a surfatron plasma, with the main exception that the plasma is not necessarily enclosed in a quartz tube. This type of setup can be interesting when using an atmospheric pressure plasma with large powers[85;86], since the plasma can damage the discharge tubes used in other configurations.

The surfatron consists of a microwave cavity with an antenna inside and pierced by a small gap allowing the microwave power to escape the cavity[87;88]. The cavity has a cylindrical symmetry and an annular shape. The antenna is fed by a coaxial cable and a quartz tube in which a gas flows is placed inside the annular cavity. The coaxial cable can usually not withstand powers above approximately 400 W at 2.45 GHz[83]. However, this configuration is very flexible, making it particularly useful for optical diagnostics.

De la Fuente *et al.* used a surfatron[89;90] setup with a CO_2/H_2O mixture. They obtained a CO_2 conversion of up to 50 %, although the energy efficiency was rather low, at about 8 %.

The surfaguide configuration is probably the most used in the frame of CO_2 dissociation.[22;33–37;91–94] This configuration was extensively studied in the 1970's-1980's for CO_2 conversion[22] in the former USSR. It was found that microwave plasmas are quite optimal for obtaining high energy efficiencies, since they exhibit low electron temperatures (around 1 eV), which is needed for efficient vibrational excitation, as will be further discussed in this work.

The best energy efficiencies reported with a microwave setup were up to 80 % with a subsonic flow and up to 90 % with a supersonic flow[33]. However, several attempts have been made recently to obtain these high energy efficiencies. So far, the best value reported without catalyst is in the vicinity of 50 %, with a corresponding CO_2 conversion around 10 %, obtained by Bongers *et al.*[34] using a vortex flow configuration to stabilize the plasma at higher pressure.

Spencer *et al.*[35] reported an energy efficiency of 20 % with a CO_2 conversion of 10 % at atmospheric pressure and found that the presence of a Rh catalyst is actually detrimental for the energy efficiency. Particularly high values of gas temperature were reported, up to 7000 K.

Silva *et al.*[36] performed optical emission spectroscopy to characterize their MW discharge by adding a small fraction of N_2 to the CO_2 feed gas. They have measured gas temperatures up to 1100 K with N_2 vibrational temperatures up to 8000 K, proving the strong non-equilibrium character of microwave discharges at these low/intermediate pressures (133-1333 Pa). CO_2 is assumed to have a similar asymmetric mode vibrational temperature, given that the first asymmetric vibrational level of CO_2 and the first level of N_2 are almost equal in energy (0.291 eV and 0.289 eV, respectively), thus enhancing the N_2-CO_2 vibrational energy transfers.

Chen *et al.*[91–94] studied in more detail the effect of the presence of a catalyst in the post discharge area, as well as the effect of the addition of water to the gas mixture. In pure CO_2, they have reported a maximum energy efficiency of 56 % with a conversion of 45 % at 70 Torr using an Ar-treated TiO_2 supported NiO catalyst[93].

I.3.2.3.1 Comparison of the different plasma sources for CO_2 conversion

It is clear that MW discharges show a great potential for energy-efficient CO_2 conversion. This is also shown by figure I.11, taken from the review paper of Snoeckx and Bogaerts[21].

This figure also shows that DBDs, although widely studied, appear to be not competitive for this process. This might change, however, for CO_2 conversion in the presence of a H-source and a suitable catalyst, when value-added compounds can be selectively formed, but more research is needed for this, to demonstrate its potential. On the other hand, GA plasmas also appear to be a suitable candidate for CO_2 conversion, especially because the results reported in literature (and presented in figure I.11) are obtained at atmospheric pressure.

Besides the plasma sources presented here, there exist some more non-thermal plasmas that have been used for CO_2 conversion, such as ns-pulsed discharges[45;46], spark discharges[95] and atmospheric pressure glow discharges[47]. The conversion and energy efficiency of these sources, and others, is labeled under the name 'other' in figure I.11. The thermal equilibrium limit shown in this figure is calculated in Snoeckx and Bogaerts[21], using the same procedure as the one to obtain figure I.5. An energy efficiency target is also defined (at 60 %), corresponding to the energy efficiency above which the CO_2 conversion process would be economically feasible.

I.3.3 Aim of this work and outline of the thesis

The aim of this work is to obtain a better understanding of the processes that result in energy-efficient CO_2 dissociation in a microwave plasma. Indeed, despite the large research efforts on the subject, it is still unclear whether CO_2 conversion by non-equilibrium plasma, and in particular MW plasmas, can be an efficient energy storage solution. The research strategy of this doctoral thesis is summarized in figure I.12.

In chapter II, the different models created in this work are described and explanations are given concerning the derivation of the most important equations controlling these models. The CO_2 chemistry set and the different scaling laws used in this work are presented in chapter III.

The results of a 2D argon model are shown in chapter IV. This forms the first step toward the later development of a 2D model for CO_2. The latter has not been realized in this thesis, among others because of computation time, but the 2D argon model gives

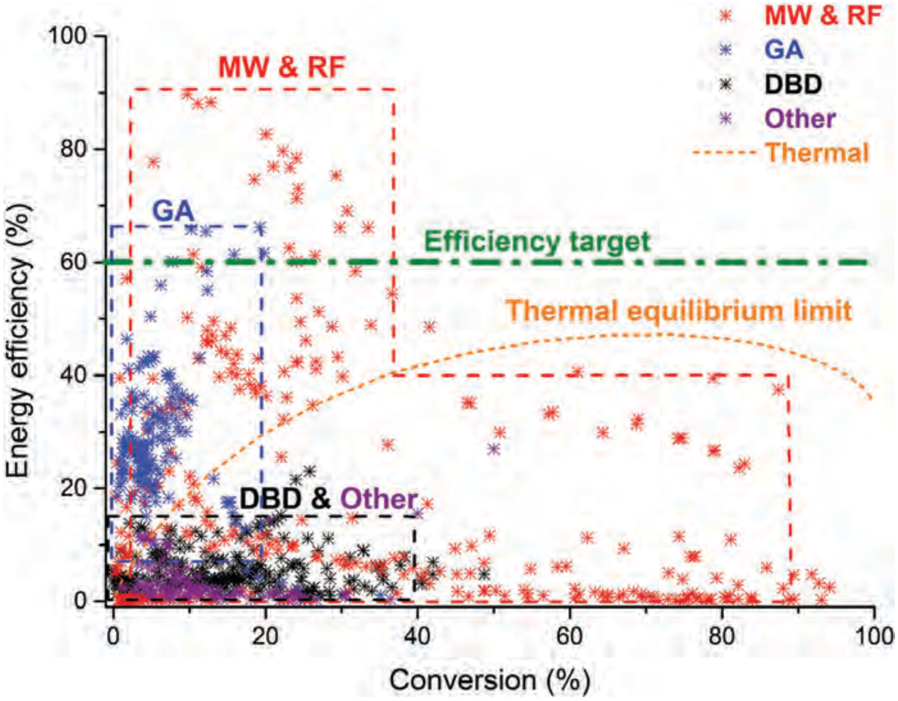

Figure I.11: Comparison of experimental energy efficiency vs CO_2 conversion values for various types of plasma reactors, as well as the thermal equilibrium limit and the specified efficiency target. Taken from Snoeckx and Bogaerts[21].

useful insights for the CO_2 chemistry models, described in the next chapters.

Chapter V presents the results of the level-lumping technique developed for the CO_2 kinetics in order to eventually use the CO_2 chemistry set in a multi-dimensional model. In chapter VI, the CO_2 dissociation kinetics is investigated in detail, using a 0D model. An extensive literature verification of the model input data and the effect of the uncertainty in the various rate coefficients on the model results are shown in chapter VII. Chapter VIII provides a detailed description of the energy transfers taking place in a non-equilibrium CO_2 plasma as well as the effect of scaling parameters on the results. Finally, general conclusions to this work are given in chapter IX.

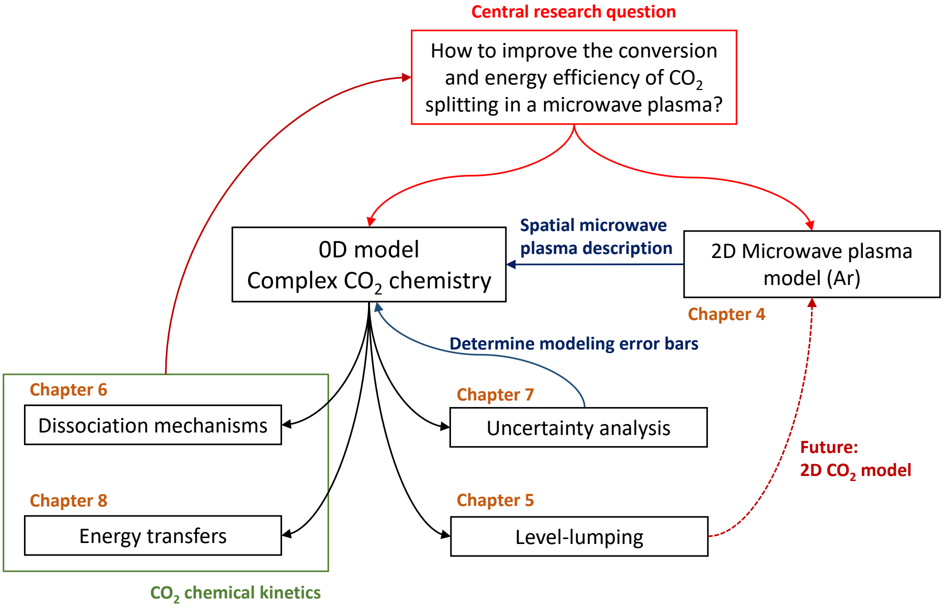

Figure I.12: Research strategy of this doctoral work.

CHAPTER II

Physical description and modeling strategy

II.1 Introduction

Plasma physics is inherently at the frontier between different fields of physics and chemistry[22;71]. Its description requires the description of the dynamics of the particles which compose the plasma. Understanding their behavior thus requires knowledge of electromagnetism, thermodynamics, statistical physics, fluid mechanics, but also chemical kinetics.

Indeed, a plasma is composed of many different types of particles interacting with each other. These particles can be subject to external electromagnetic fields and to gravity, and they also collide with each other and interact with the EM fields. When considering N particles in a plasma, a fully detailed representation of the plasma would require knowledge of their position and their velocity. In a 3D-representation, this leads to a 6N-dimension space, making it quite complicated.

Two main categories of plasma modeling are usually distinguished. The first one, the kinetic description, describes the behavior of the particles individually, or in a group of particles (i.e. macro-particles).

The second description, fluid modeling, which is used in this work, describes the plasma as a fluid and thus in terms of macroscopic quantities instead of individual particles. Indeed, given the very large number of particles and the various effects that can occur in a plasma, kinetic modeling, although more accurate, is in practice not feasible in many cases. This description requires that the density of a particle is sufficiently high, so that macroscopic effects can be derived from a large ensemble of particles.

This chapter gives an overview of the physics necessary to build the model and the equations that are solved within the models.

II.2 Boltzmann equation and its moments

II.2.1 Boltzmann equation

Most of the equations solved in plasma physics using a fluid description are derived from the Boltzmann equation. This equation describes the non-equilibrium behavior of the distribution functions $f(t, \boldsymbol{r}, \boldsymbol{v})$ of the particles in a gas, where t is the time, $\boldsymbol{r}$ the position vector and $\boldsymbol{v}$ the velocity vector. Its general form is given for a particle α by[96]:

$$\frac{\partial f_\alpha}{\partial t} + \boldsymbol{v} \cdot \frac{\partial f_\alpha}{\partial \boldsymbol{r}} + \boldsymbol{\gamma} \cdot \frac{\partial f_\alpha}{\partial \boldsymbol{v}} = (\frac{\delta f_\alpha}{\delta t})_c \tag{II.1}$$

where $\boldsymbol{\gamma}$ is the acceleration vector of the particle and $(\frac{\delta f_\alpha}{\delta t})_c$ is the rate of change of f due to collisions. Solving the Boltzmann equation is a complex task and requires approximations to be made.

II.2.2 Moments of the Boltzmann equation

As indicated in the introduction of this chapter (II.1), fluid descriptions of a plasma focus on macroscopic variables. Macroscopic variables, such as the density, the mean velocity, the temperature, etc., are only a function of time and position, and not of velocity. The conservation equations of these quantities can typically be derived from the Boltzmann equation.

For simplicity, let's define here the following normalization to f_α:

$$n_\alpha(t, \boldsymbol{r}) = \int f_\alpha(t, \boldsymbol{r}, \boldsymbol{v}) d\boldsymbol{v} \tag{II.2}$$

where n_α is the density of the particles α.

Moreover, from the definition of the distribution function we can write:

$$< a(t, \boldsymbol{r}) >= \frac{1}{n_\alpha(t, \boldsymbol{r})} \int a(t, \boldsymbol{r}, \boldsymbol{v}) f_\alpha(t, \boldsymbol{r}, \boldsymbol{v}) d\boldsymbol{v} \tag{II.3}$$

where $< a(t, \boldsymbol{r}) >$ is the mean value of a quantity a.

Some macroscopic quantities can be obtained by multiplying f_α by its mass m_α and by $\boldsymbol{v}^n$ ($n \in$) and integrating over the velocity space $\subset {}^3$, such that

$$X_\alpha(t, \boldsymbol{r}) = \int m_\alpha \boldsymbol{v}^n . f_\alpha(t, \boldsymbol{r}, \boldsymbol{v}) d\boldsymbol{v} \tag{II.4}$$

These quantities X_α are called moments of the distribution function.

The zeroth moment is simply given by n=0, which yields the mass density $\rho_\alpha = n_\alpha m_\alpha$.

The first moment is given by $n = 1$. It is equal to $\rho_\alpha \boldsymbol{u_\alpha}$, where $\boldsymbol{u_\alpha}$ is the mean velocity of particles α. This is the definition of the species mass density flux.

The second moment is given by $n = 2$. It is equal to $\boldsymbol{P}_\alpha = m_\alpha n_\alpha \boldsymbol{w_\alpha} \otimes \boldsymbol{w_\alpha}$ and is homogeneous to a pressure. $\boldsymbol{w_\alpha}$ is here the thermal velocity. Note that we have $< \boldsymbol{w_\alpha} >= 0$ and $\boldsymbol{v_\alpha} = \boldsymbol{w_\alpha} + \boldsymbol{u_\alpha}$. $\boldsymbol{P_\alpha}$ is called the partial pressure tensor. The plasmas considered in this work do not use a static magnetic field and thus exhibit isotropic pressures, which can be simply rewritten as $\boldsymbol{P}_\alpha = p_\alpha \boldsymbol{I}$, $\boldsymbol{I}$ being the 3x3 identity matrix and p_α the scalar partial pressure. Note that $\boldsymbol{P}$ is also a measure of the thermal motion of the particles.

II.2.3 Conservation equations of the moments of the Boltzmann equation

If we perform the same operations of multiplication by $m_\alpha \boldsymbol{v}^n$ over the whole Boltzmann equation (II.1), we obtain the conservation equations of these quantities. Most plasma models limit their description to up to the first three moments, but it is of course possible to use more of them[97], at the cost of complexity and numerical resources. Indeed, note that the higher the order of the moment, the more complex the derivation of the conservation equation. Therefore, we refer to the book of Bittencourt[96] for more information concerning the derivation of these equations. Under certain approximations, these conservation equations are equivalent to the Navier-Stokes equations.

II.2.3.1 Zero$^{\text{th}}$ order moment: mass conservation equation

The 0$^{\text{th}}$ moment is the mass density ρ_α. Integrating equation (II.1) over the velocity space after multiplying it by the mass m_α gives the well-known mass conservation equation for species α:

$$\frac{\partial \rho_\alpha}{\partial t} + \boldsymbol{\nabla}.\boldsymbol{\Gamma}_\alpha + (\boldsymbol{u}_\alpha.\boldsymbol{\nabla})\rho_\alpha = S_\alpha^m \tag{II.5}$$

where S_α^m is the mass density source term due to collisions.

S_α^m is the production rate of the mass density, summed over the various reactions j included in the model. We express it as:

$$S_\alpha^m = m_\alpha \sum_j (k_j \prod_l n_{l,j})[a_{\alpha j}^R - a_{\alpha j}^L] \tag{II.6}$$

with k_j the rate coefficient of reaction j, $n_{l,j}$ the density of the reactant in reaction j and $a_{\alpha j}^R$ and $a_{\alpha j}^L$ the right- and left-hand side stochiometric coefficients of species α in reaction j, respectively.

$\boldsymbol{\Gamma}_\alpha$ is expressed using the drift-diffusion approximation:

$$\boldsymbol{\Gamma}_\alpha = -D_\alpha \boldsymbol{\nabla}\rho_\alpha + Z_\alpha \mu_\alpha \rho_\alpha \boldsymbol{E}_{DC} \tag{II.7}$$

where D_α and μ_α are the diffusion and mobility coefficients of species α. $\boldsymbol{E}_{DC}$ is the DC electric field (see part II.3.2). Z_α is equal to -1, 0 and 1 for negative ions (and electrons), neutral species and positive ions, respectively (considering only first ionization degrees).

Note that instead of solving a mass conservation equation for each species, we could solve equivalently the species density equation of each species by simply dividing equation (II.6) by m_α.

Moreover, since the mass is conserved, the following relation holds:

$$\sum_{\alpha} S_{\alpha}^{m} = 0 \tag{II.8}$$

Equation (II.6) is solved for every particle in the model in the plasma kinetic module, i.e., electrons, various types of (positive and negative) ions, radicals, molecules, excited species. Moreover, the fluid is also treated as a whole, yielding a similar conservation equation for the sum of all the mass densities:

$$\frac{\partial \rho}{\partial t} + \rho \boldsymbol{\nabla}.\boldsymbol{u} + \boldsymbol{u}.\boldsymbol{\nabla} \rho = 0 \tag{II.9}$$

where ρ and $\boldsymbol{u}$ are the mass density and the velocity vector of the gas as a whole. This equation is solved in the flow module.

II.2.3.2 First order moment: momentum conservation equation

The first order moment is homogeneous to a mass density flux $\boldsymbol{\Gamma}_{\alpha} = \rho_{\alpha} \boldsymbol{u}_{\boldsymbol{\alpha}}$. The following conservation equation can be derived from the Boltzmann equation (II.1):

$$\frac{\partial \rho_{\alpha} \boldsymbol{u}_{\alpha}}{\partial t} + \boldsymbol{\nabla}(\rho_{\alpha} \boldsymbol{u}_{\alpha}.\boldsymbol{u}_{\alpha}) = -\boldsymbol{\nabla} p_{\alpha} + \boldsymbol{\nabla} \pi_{\alpha} + \boldsymbol{u}_{\alpha} S_{\alpha}^{m} + \boldsymbol{F}_{\alpha} \tag{II.10}$$

where π_{α} is the viscosity tensor and $\boldsymbol{F}_{\alpha}$ represents the different forces acting on species α, including among others gravitational, electromagnetic and friction forces.

This equation is only solved for the fluid as a whole, under the form:

$$\rho \frac{\partial \boldsymbol{u}}{\partial t} + \rho(\boldsymbol{u}.\boldsymbol{\nabla})\boldsymbol{u} = \boldsymbol{\nabla}.\Big[- p\boldsymbol{I} + \boldsymbol{\tau} \Big] + \boldsymbol{F} \tag{II.11}$$

$\boldsymbol{\tau}$ is the viscous stress tensor. In the cases under consideration, the fluid can be considered to be a Newtonian fluid, which leads to:

$$\boldsymbol{\tau} = \mu \Big(\boldsymbol{\nabla} \boldsymbol{u} + (\boldsymbol{\nabla} \boldsymbol{u})^{T} \Big) - \frac{2}{3} \mu (\boldsymbol{\nabla} \boldsymbol{u}) \boldsymbol{I} \tag{II.12}$$

where μ is the dynamic viscosity. Equation (II.11) is the Navier–Stokes momentum equation.

II.2.3.3 Second order moment: energy conservation equation

The second order moment is homogeneous to a pressure and can be used as a measure of the thermal excitation of a system, i.e. the temperature. The derivation of the conservation equation is rather complex.

The plasmas under consideration are considered in non-LTE (local thermal equilibrium), which means that the electron temperature T_e is not equal to the heavy particle temperature T_g. In theory, each type of heavy particle should be described with its own temperature. However, we can reasonably assume that all the heavy particles have the same temperature T_g. This type of modeling is called 'two-temperature' modeling. Therefore, we solve for two energy conservation equations (or temperature equations). For the electrons, we solve the averaged electron energy balance:

$$\frac{\partial n_e \epsilon_e}{\partial t} + \boldsymbol{\nabla}.\boldsymbol{\Gamma}_{\epsilon,e} + \boldsymbol{E}_{DC}.\boldsymbol{\Gamma}_e + (\boldsymbol{u}.\boldsymbol{\nabla}) n_e \epsilon_e = Q_{MW} - Q_{el} - Q_{inel} + Q_{bg} \tag{II.13}$$

where ϵ_e is the mean electron energy. Q_{MW} is the power received by the electrons from the microwave field (see part II.3.1). Q_{el} and Q_{inel} are the power received (or lost) by the electrons from elastic and inelastic collisions, respectively. Q_{bg} is a background stabilization power term, to ensure that the electron energy does not reach values too close to zero, which would lead to numerical problems. Its value is chosen so that it is several orders of magnitude lower than the microwave power density Q_{MW} in the plasma.

The elastic and inelastic power gain/loss terms are calculated as follows:

$$Q_{el} = \frac{3}{2} \sum_{\alpha \neq e} n_e \nu_{e\alpha} \Big(\frac{2m_e}{m_\alpha}\Big) k_B (T_e - T_g) \tag{II.14}$$

$$Q_{inel} = \sum_j R_j \Delta\epsilon_j \tag{II.15}$$

with $R_j = k_j \prod_l n_{l,j}$ the reaction rate of reaction j and $\Delta\epsilon_j$ the energy exchanged with the electrons per event of reaction j. ϵ_j is positive if the electron(s) involved in reaction j lose(s) energy. $\nu_{e\alpha}$ is the momentum transfer collision frequency between the electrons e and particles α. k_B is the Boltzmann constant.

$\boldsymbol{\Gamma}_{\epsilon,e}$, the electron energy flux,is also expressed with the drift-diffusion approximation:

$$\boldsymbol{\Gamma}_{\epsilon,e} = -D_{\epsilon,e} \boldsymbol{\nabla}(n_e \epsilon_e) - \mu_{\epsilon,e} n_e \epsilon_e \boldsymbol{E}_{DC} \tag{II.16}$$

$D_{\epsilon,e}$ and $\mu_{\epsilon,e}$ are now the electron energy diffusion and mobility coefficients. $n_e = \frac{\rho_e}{m_e}$ is the electron density.

For the heavy particles, we solve:

$$\rho C_p \frac{\partial T_g}{\partial t} + \rho C_p \boldsymbol{u}.\boldsymbol{\nabla} T_g = \boldsymbol{\nabla}.(\lambda \boldsymbol{\nabla} T_g) + Q_{el} - Q_{\Delta H} \tag{II.17}$$

C_p is the specific heat capacity at constant pressure and λ is the thermal conductivity. This equation includes convection and conduction effects but neglects radiative transfers. $Q_{\Delta H}$ is the heat source term due to the heat absorbed or released by endothermic and exothermic reactions. It can be expressed as:

$$Q_{\Delta H} = \sum_j \Delta H_j R_j \tag{II.18}$$

where ΔH_j is the change in the enthalpy H during reaction j. By convention, ΔH_j is positive when j is an endothermic reaction.

II.3 Electromagnetic and electrostatic equations

Additionally, plasmas are composed of charged particles, which interact with electromagnetic and electrostatic fields. These fields can provide energy to the elec- trons within the plasma and since a plasma is a conductive medium, their distribution is also affected by the plasma[98].

II.3.1 Maxwell equation and wave propagation equation

The well-known Maxwell equations are given by[82]:

$$\boldsymbol{\nabla}.(\epsilon\boldsymbol{\mathcal{E}}) = \rho_c \tag{II.19a}$$

$$\boldsymbol{\nabla}.\boldsymbol{\mathcal{B}} = 0 \tag{II.19b}$$

$$\boldsymbol{\nabla} \times \boldsymbol{\mathcal{E}} = -\frac{\partial \boldsymbol{\mathcal{B}}}{\partial t} \tag{II.19c}$$

$$\boldsymbol{\nabla} \times \frac{\boldsymbol{\mathcal{B}}}{\mu} = \boldsymbol{\mathcal{J}} + \frac{\partial \epsilon \boldsymbol{\mathcal{E}}}{\partial t} \tag{II.19d}$$

where $\mathcal{E}$ and $\mathcal{B}$ are the electric and magnetic field vectors, respectively. ϵ and μ are the electric permittivity and magnetic permeability, respectively. $\mathcal{J}$ is the free current density and ρ_c is the electric charge density. Since the media under consideration in this work are non-magnetic, $\mu = \mu_0$, where μ_0 is the vacuum permeability. ϵ can be rewritten as $\epsilon = \epsilon_0\epsilon_r$, ϵ_0 is the electric permittivity in vacuum and ϵ_r is the relative permittivity of the medium (also called dielectric constant). Note that the permittivity of a medium typically varies with the frequency of the wave.

II.3.1.0.1 Phasors Time-harmonic fields $\boldsymbol{\mathcal{F}}$ are typically written as $\boldsymbol{\mathcal{F}}(\boldsymbol{r}, t) = \boldsymbol{F}(\boldsymbol{r}) \cos(\omega t + \phi)$. ω is the wave angular frequency and ϕ is the phase. Thus, we can express the field $\boldsymbol{\mathcal{F}}$ using a complex exponential:

$$\boldsymbol{\mathcal{F}}(\boldsymbol{r},t) = Re(\boldsymbol{F}(\boldsymbol{r}).e^{i\omega t}) \tag{II.20}$$

$\boldsymbol{F}$ is called the phasor form of the field $\mathcal{F}$. Since the frequency of microwave fields considered in this work is in the order of 1 GHz, the field is considered to oscillate much faster than the other processes of interest here. It is therefore particularly useful to eliminate the time-dependency from the expression of $\mathcal{F}$ by solving the Maxwell equations in the frequency domain (or in phasor form).

It is quite straightforward to obtain the phasor form of Maxwell equations (II.19), using $\frac{\partial \boldsymbol{F}.e^{i\omega t}}{\partial t} = i\omega \boldsymbol{F}.e^{i\omega t}$:

$$\boldsymbol{\nabla}.(\epsilon \boldsymbol{E}) = \rho_c \tag{II.21a}$$

$$\boldsymbol{\nabla}.\boldsymbol{B} = 0 \tag{II.21b}$$

$$\boldsymbol{\nabla} \times \boldsymbol{E} = -i\omega \boldsymbol{B} \tag{II.21c}$$

$$\boldsymbol{\nabla} \times \boldsymbol{B} = \mu_0 \boldsymbol{J} + i\mu_0\omega\epsilon_0\epsilon_r \boldsymbol{E} \tag{II.21d}$$

II.3.1.0.2 Wave equation By inserting equation (II.21c) into equation (II.21d), we get:

$$-\boldsymbol{\nabla} \times \frac{\boldsymbol{\nabla} \times \boldsymbol{E}}{i\omega} = \mu_0 \boldsymbol{J} + i\mu_0\omega\epsilon_0\epsilon_r \boldsymbol{E} \tag{II.22}$$

Re-arranging the terms and using Ohm's law $\boldsymbol{J} = \sigma \boldsymbol{E}$, where σ is the conductivity, gives:

$$\boldsymbol{\nabla} \times (\boldsymbol{\nabla} \times \boldsymbol{E}) + i\sigma \boldsymbol{E}\omega\mu_0 - \omega^2\epsilon_0\epsilon_r\mu_0 \boldsymbol{E} = 0 \tag{II.23}$$

It is convenient to introduce the wave vector in vacuum $k_0 = \frac{\omega}{c} = \omega\sqrt{\epsilon_0\mu_0}$ to simplify this expression, with c the speed of light in vacuum.

$$\boldsymbol{\nabla} \times (\boldsymbol{\nabla} \times \boldsymbol{E}) - k_0^2\Big(\epsilon_r - \frac{i\sigma}{\omega\epsilon_0}\Big)\boldsymbol{E} = 0 \tag{II.24}$$

Note that $\epsilon_r - \frac{i\sigma}{\omega\epsilon_0} = \widehat{\epsilon_r}$ is called the complex relative permittivity. It can be shown that the plasma conductivity is expressed by[99]:

$$\sigma = \frac{e^2}{m_e}\frac{n_e}{\nu_m + i\omega} \tag{II.25}$$

v_m is the total momentum transfer frequency between electrons and heavy particles and e is the elementary charge.

Moreover, Ohm's law also yields $Q_{MW} = \frac{1}{2}\mathbf{Re}(\boldsymbol{J}^{*}.\boldsymbol{E}) = \frac{1}{2}\mathbf{Re}(\sigma)|\boldsymbol{E}|^{2}$. Given that the conductivity also depends on the electron density and the collision frequency, there is a direct coupling between the electron transport equation and the microwave equations.

II.3.2 Poisson equation

Although plasmas are mostly quasi-neutral, a small zone of non-neutrality can be created at the interface between the plasma and a solid inserted in the plasma. This zone is called the sheath. Extensive research has been made to understand its behavior[24]. Therefore, it can be useful in some situations to consider the DC electric field $\boldsymbol{E}_{\mathrm{DC}}$ formed by the plasma.

Let's associate to the electric field $\boldsymbol{E}_{\mathrm{DC}}$ an electric potential V. V is simply defined by:

$$\boldsymbol{E}_{\mathrm{DC}} = -\boldsymbol{\nabla}.V \tag{II.26}$$

Inserting equation (II.26) into the Gauss equation (II.19a) immediately gives Poisson equation:

$$\boldsymbol{\nabla}.(\epsilon_r \boldsymbol{\nabla} V) = -\frac{\rho_c}{\epsilon_0} \tag{II.27}$$

II.4 Models developed in this work

During this doctoral work, two types of models have been developed. First, a microwave 2D-axisymmetric model in argon was created using Comsol Multiphysics®. This model gives information on the shape of the discharge and the gradients of its different quantities. The results of this model are presented in chapter IV. Subsequently, to get more details on the chemistry set, a number of 0D chemical kinetics model were developed using ZDPlasKin[100]. The results of these 0D models are shown in chapters V, VI, VII and VIII.

This part aims at reviewing the main aspects of these two models, based on the equations presented above. More specific details are given in the different chapters presenting the results.

II.4.1 0D modeling

A 0D model assumes that the plasma is spatially homogeneous, i.e. that $\frac{\partial}{\partial r_i} \equiv 0$. This model calculates the evolution of the different variables as a function of time only and thus neglects all spatial effects (diffusion, heat conduction, ...), although it is possible to partially include these effects under certain approximations, as is done for heat conduction with the plasma walls (see equation II.29).

The model solves a density equation for each species α:

$$\frac{\mathrm{d}n_\alpha}{\mathrm{d}t} = \sum_j (k_j \prod_l n_{l,j})[a^R_{\alpha j} - a^L_{\alpha j}] \tag{II.28}$$

The gas temperature T_g can either be fixed or calculated using:

$$N\frac{\gamma k_B}{\gamma - 1}\frac{\mathrm{d}T_g}{\mathrm{d}t} = Q_{el} - Q_{\Delta H} - \frac{8\lambda}{R^2}(T_g - T_w) \tag{II.29}$$

$\gamma = \frac{C_p}{C_v}$ is the specific heat ratio. The last term of the right-hand side of equation II.29 represents the cooling due heat conduction and exchanges with the plasma walls, which are at a temperature $T_w = 300$ K. The plasma is assumed to be confined in a cylindrical tube of radius R, which is the case in most microwave plasma setups, as seen in figure I.10 above. This expression is derived by assuming that the gas temperature has a parabolic radial profile[101].

Because a 0D model does not consider geometrical aspects of the discharge, it is also quite fast computationally-speaking. This allows us to partially include a kinetic description by solving the Boltzmann equation to obtain the electron energy distribution function. ZDPlasKin[100] is coupled to Bolsig+, a two-term approximation Boltzmann solver freeware developed by Hagelaar and Pitchford[65]. Indeed, as pointed out by Pietanza *et al.*[50;51], the shape of the electron energy distribution function (EEDF) can have a large influence on the rate coefficients of electron impact reactions. The electron energy distribution function can be easily obtained from the velocity distribution function with $\epsilon = \frac{m_e}{2e}v^2$, where ϵ is the electron energy in electron-volts (eV). For simplicity, the EEDF F_0 (now in eV$^{-3/2}$) obeys the following normalization:

$$\int_0^\infty \epsilon^{1/2} F_0 \mathrm{d}\epsilon = 1 \tag{II.30}$$

The mean electron energy ϵ_e is then obtained from the EEDF and not by solving a continuity equation, following:

$$\epsilon_e = \int_0^\infty \epsilon^{3/2} F_0 \mathrm{d}\epsilon \tag{II.31}$$

The electron impact rate coefficients k_k of reactions k are also derived from the EEDF $F_0(\epsilon)$ and the process cross section σ_k, using:

$$k_k = \sqrt{\frac{2e}{m_e}}^{1/2} \int_0^{\infty} \epsilon \sigma_k F_0(\epsilon) d\epsilon \tag{II.32}$$

Detailed information concerning the CO_2 chemistry sets, and thus the rate coefficients and cross sections, in the 0D model are given in chapter III.

II.4.1.1 Plug-flow approximation

In order to account for the axial variation of the various plasma quantities, the 0D model can also follow a volume moving through a cylindrical discharge tube and passing through the plasma region. The 0D model then only allows following the axial variation of the plasma quantities and considers a radially homogeneous plasma. It could be considered as a quasi-1D static model.

The considered volume moves at an axial velocity u_z calculated from the conservation of the mass flow rate:

$$u_z = \frac{\phi_m}{\rho A} \tag{II.33}$$

where ϕ_m is the mass flow rate and $A = \pi R^2$ is the tube cross section area.

By means of this velocity, the time-dependence of the 0D chemical kinetics model can be converted into an axial-dependence throughout the discharge tube, described by a coordinate z at each time T: $z = \int_{t=0}^{t=T} u_z \mathrm{d}t$.

The plug-flow approximation is considered in chapter V and in the first part of chapter VI.

II.4.2 2D-axisymmetric modeling

Although the 0D approach can give great insights in the chemistry, it is based on approximations and it is therefore interesting to also have a description of the plasma in higher dimensions. However, accounting for more dimensions is numerically more challenging and increases the calculation time. It is therefore not always possible to include a complex chemistry set in a higher dimension model. Chapter V presents a method to include the complex CO_2 chemistry in a multi-dimensional model without increasing the computational costs too much. In this work, we did not yet manage to develop a 2D model for a CO_2 microwave plasma, but as a first step we developed a 2D model for a microwave plasma in argon, and the results are shown in chapter IV. The 2D model is built in Comsol Multiphysics. The different coupled modules and the equations solved are listed in table II.1. The equations were explained in more detail in sections II.2 and II.3 above. Comsol Multiphysics is a finite element analysis solver and multiphysics simulation software that offers the possibility to discretize and solve numerically a set of equations using a complex mesh. The meshing process is made within the Comsol framework using a combination of a triangular and rectangular mesh in 2D.

Table II.1: Equations solved in the 2D model. ^{a} indicates that the model solves the logarithm of the quantity instead of the quantity itself.

Plasma module	
Particle mass densities ^{a}	$\frac{\partial \rho_\alpha}{\partial t} + \boldsymbol{\nabla}.\boldsymbol{\Gamma}_\alpha + (\boldsymbol{u}_\alpha.\boldsymbol{\nabla})\rho_\alpha = S_\alpha^m$
Potential	$\boldsymbol{\nabla}.(\epsilon_r \boldsymbol{\nabla} V) = -\frac{\rho_c}{\epsilon_0}$
Electron energy ^{a}	$\frac{\partial n_e \epsilon_e}{\partial t} + \boldsymbol{\nabla}.\boldsymbol{\Gamma}_{\epsilon,e} + \boldsymbol{E}_{DC}.\boldsymbol{\Gamma}_e + (\boldsymbol{u}.\boldsymbol{\nabla}) n_e \epsilon_e = Q_{MW} - Q_{el} - Q_{inel} + Q_{bg}$
Microwave module	
MW electric field	$\boldsymbol{\nabla} \times (\boldsymbol{\nabla} \times \boldsymbol{E}) - k_0^2 \Big(\epsilon_r - \frac{i\sigma}{\omega \epsilon_0}\Big) \boldsymbol{E} = 0$
Flow module	
Mass density	$\frac{\partial \rho}{\partial t} + \rho \boldsymbol{\nabla}.\boldsymbol{u} + \boldsymbol{u}.\boldsymbol{\nabla}\rho = 0$
Flow velocity	$\rho \frac{\partial \boldsymbol{u}}{\partial t} + \rho(\boldsymbol{u}.\boldsymbol{\nabla})\boldsymbol{u} = \boldsymbol{\nabla}.\Big[-p\boldsymbol{I} + \boldsymbol{\tau}\Big] + \boldsymbol{F}$
Heat transfer module	
Gas temperature	$\rho C_p \frac{\partial T_g}{\partial t} + \rho C_p \boldsymbol{u}.\boldsymbol{\nabla} T_g = \boldsymbol{\nabla}.(\lambda \boldsymbol{\nabla} T_g) + Q_{el} - Q_{\Delta H}$

II.4.2.1 Numerical methods

Most of the equations considered in this work are non-linear. Therefore, an iterative procedure is required. Comsol makes use of the Newton-Raphson method, explained briefly below for a 1D case. This method is often used to find the zeros of a function when its derivative is known.

Let's consider a function $f(x)$ which is known for $x = x_0$. We want to find $x = x_z$ such that $f(x_z) = 0$. The first order Taylor expansion of $f(x)$ around x_0 is:

$$f(x) \simeq f(x_0) + f'(x).(x - x_0) \tag{II.34}$$

Therefore, we have:

$$0 \simeq f(x_0) + f'(x_0).(x_z - x_0) \tag{II.35}$$

An iterative procedure looping over an index i can then be used:

$$x_{k+1} = x_k - \frac{f(x_k)}{f'(x_k)} \tag{II.36}$$

Figure II.1 illustrates the Newton-Raphson method to determine the zero of $f(x) = \exp(x) - \exp(1)$. Clearly, the zero of $f(x)$ is easy to determine analytically here: $x_z = 1$. This is of course usually not the case. In the example shown in figure II.1, this method already gives a good estimate of the solution in the fourth iteration: $x_4 = 1.0002$ and $f(x_4) = 0.0005$.

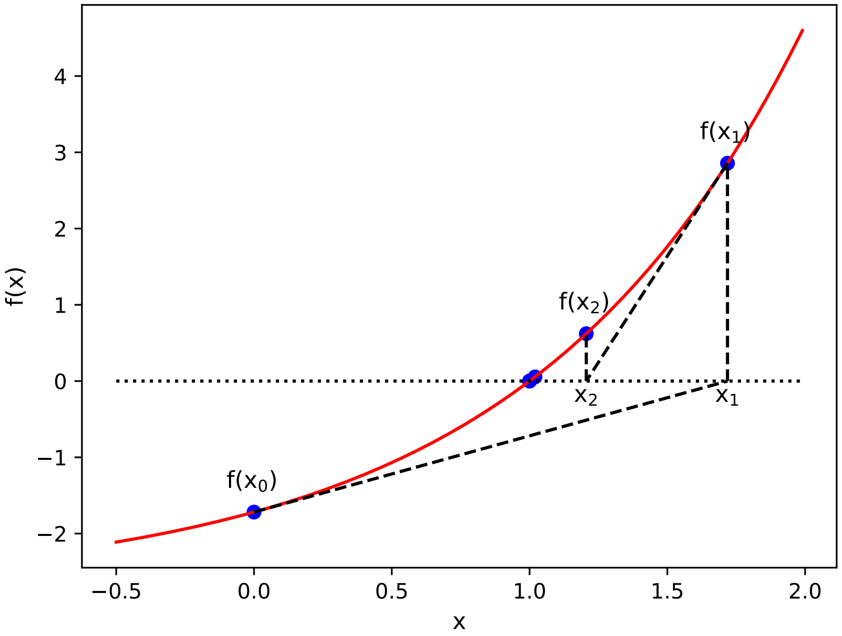

Figure II.1: Illustration of the Newton-Raphson method.

This method thus transforms a non-linear equation into a series of (approximative) linear equations. Next, to solve the set of linear equations, we use in this work the direct solver PARDISO[102;103] implemented within Comsol.

This chapter described the mathematical framework for the fluid modeling of plasmas used in this work. These models require also various input data, and in particular the rate coefficients for the chemical kinetics part. In a CO_2 plasma, various scaling laws are required to obtain the rate coefficient of reactions involving vibrationally excited levels. The following chapter focuses on the description of the chemistry set of CO_2.

CHAPTER III

CO_2 chemistry set and scaling laws

III.1 Species considered

The highly energetic electrons in a plasma have the ability to destroy molecular bonds and to excite the molecules and atoms. Therefore, a wide variety of different species are present in a plasma and the description of the chemistry should account for the most important species and reactions. This work considers either an extensive list of species ('full set' in chapter V and chapter VI) or a reduced list of species (in chapters VII and VIII), which is based on the 'reduced set' developed in chapter V.

The reduced list of species considered in the CO$_2$ model is shown in table III.1. The extra species included in the full set are listed in table III.2.

A first list of reactions for the CO$_2$ chemistry set is considered in chapters V and VI. This set of reactions was based on the work of Aerts *et al.*[49] and Kozák *et al.*[56;57].

In chapter VII, which is the result of later research, the set of reaction is thoroughly verified from literature by checking the original sources of the data. Some reactions were modified based on this study and the updated chemistry set is also considered in chapter VIII. The list of reactions considered is shown in appendix A.1 for chapters V and VI and in appendix A.2 for chapters VII and VIII.

III.1.1 Vibrational and electronically excited levels

As explained in part I.3.1, CO$_2$ has four vibrational degrees of freedom, which leads to three modes of vibrations, one of which is doubly degenerate. These vibrational modes are easily excited by the electrons in a non-equilibrium plasma. Suzuki[106] suggested a formula to express the energy of the vibrational levels of CO$_2$:

$$E_{CO_2} = \sum_i \omega_i(v_i + \frac{d_i}{2}) + \sum_{j\geq i} \omega_i x_{ij}(v_i + \frac{d_i}{2})(v_j + \frac{d_j}{2}) + x_{l_2l_2} l_2^2 \tag{III.1}$$

where ω_i, x_{ij} and $x_{l_2l_2}$ are spectroscopic constants determined by experiment and $d_i = (d_1\ d_2\ d_3) = (1\ 2\ 1)$ are the degeneracies of the three modes of vibration. We use the following values[106]: ω_1 = 1354.31 cm^{-1}, ω_2 = 672.85 cm^{-1}, ω_3 = 2396.32 cm^{-1}, $\omega_1 x_{11}$ = -2.93 cm^{-1}, $\omega_1 x_{12}$ = -4.61 cm^{-1}, $\omega_1 x_{13}$ = -19.82 cm^{-1}, $\omega_2 x_{22}$ = 1.35 cm^{-1}, $\omega_2 x_{23}$ = -12.31 cm^{-1}, $\omega_3 x_{33}$ = -12.47 cm^{-1}, $x_{l_2l_2}$ = -0.97 cm^{-1}.

Based on this formula, and taking into account the various possible combinations of different modes, we find that there are more than 10,000 vibrational levels with an energy below the dissociation limit of CO$_2$ (i.e. 5.51 eV). The vibrational energy diagram of CO$_2$ thus calculated is shown in figure III.1.

Obviously, it is not possible to describe the evolution of this many levels. Therefore, only the first four symmetric mode vibrational levels are considered ([v$_a$, v$_b$, v$_c$, v$_d$]),

Table III.1: Species described in the model.

Neutral ground states	CO_2	CO	O_2	O	$C_{(g)}$
Standard formation enthalpy[23] [eV]	-4.08	-1.15	0	2.58	7.43

Charged species
CO_2^+, CO^+, CO_4^+, O^-, O_2^-, CO_3^-, CO_4^-, e^-

Excited states	Associated energy [eV]	State[a]
$O_2[v_{1-4}]$	Anharmonic oscillator	
$CO[v_{1-10}]$	Anharmonic oscillator	
$CO_2[v_{1-21}]$	Anharmonic oscillator	(00n)
$CO_2[v_a]$	0.083	(010)
$CO_2[v_b]$	0.167	(020) + (100)
$CO_2[v_c]$	0.252	(030) + (110)
$CO_2[v_d]$	0.339	(040) + (120) + (200)
$CO_2[e_1]$	10.5	$(^1\Sigma_u^+) + (^3\Pi_u) + (^1\Pi_u)$
$O_2[e_1]$	0.98	$(a^1\Delta_g) + (b^1\Sigma_g^+)$
$O_2[e_2]$	8.4	$(B^3\Sigma_u^-)$ + higher triplet states
$CO[e_1]$	6.22	$(a^3\Pi_r)$
$CO[e_2]$	7.9	$(A^1\Pi)$
$CO[e_3]$	13.5	$(a'^3\Sigma^+) + (d^3\Delta_i) + (e^3\Sigma^-) + (b^3\Sigma^+)$
$CO[e_4]$	10.01	$(C^1\Sigma^+) + (E^1\Pi) + (B^1\Sigma^+) + (I^1\Sigma^-) + (D^1\Delta)$

[a] CO_2 electronic states designation from Grofulović et al.[104], O_2 and CO electronic states notation from Huber & Herzberg[105].

Table III.2: Additional species described in the extensive chemistry model.

Neutral species
C_2O, O_3, C_2

Charged species
CO_4^+, $C_2O_2^+$, $C_2O_3^+$, $C_2O_4^+$, C^+, C_2^+, O_2^+, O_4^+, O^+, O_4^-, O_3^-

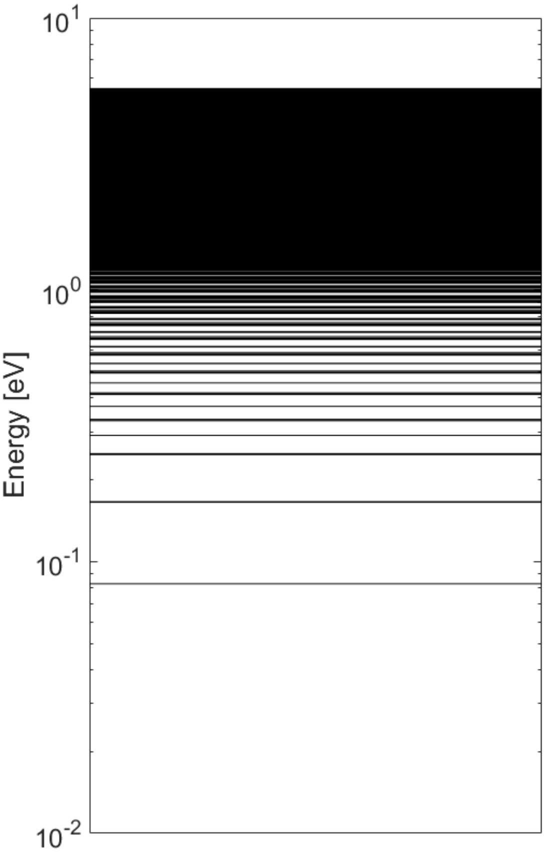

Figure III.1: Vibrational levels of CO_2, based on the formula of Suzuki[106].

which are a combination of the symmetric stretch and bending mode; see table III.1. The asymmetric mode is particularly important (see I.3.1). Thus, the first 21 asymmetric mode vibrational levels (i.e. until the dissociation limit) are considered. Each of these asymmetric mode vibrational levels v_n can be seen as a lumped level containing the asymmetric mode level v_n and the levels combining the asymmetric mode v_n with a symmetric mode v_a, v_b or v_c. In other words, the level v_n, in the model, actually contains (00n)+(01n)+(10n)+(02n)+(03n)+(11n).

The vibrational energy diagram of the CO_2 vibrational levels considered in the model is shown in figure III.2. Only one CO_2[e] level has been included, due to the lack of information concerning the kinetics of the higher electronic levels of CO_2.

The energies of the CO vibrational levels are calculated using an anharmonic oscil-

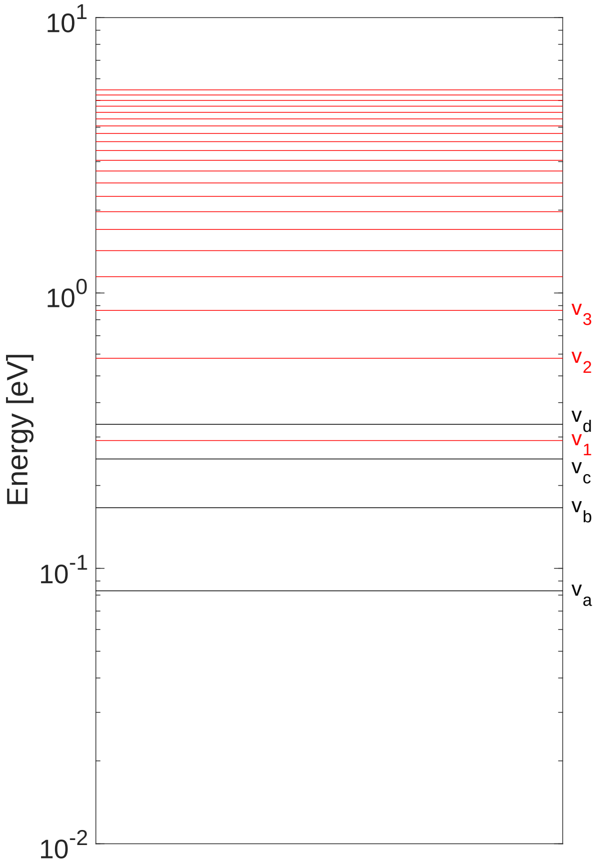

Figure III.2: Vibrational levels of CO$_2$ included in the model. The symmetric mode levels explicitly considered in the model are shown in black and the asymmetric mode levels are shown in red. The designation of the first few levels is shown on the right of the figure.

lator formula[107]:

$$E = \omega_e(v + 0.5) - \omega_e x_e(v + 0.5)^2 \tag{III.2}$$

v is the vibrational quantum number, $\omega_e = 2169.81$ cm^{-1} and $x_e = 6.12 \times 10^{-3}$ is the anharmonicity coefficient[108]. The energies of the O$_2$ vibrational levels are taken from the Phelps database[109]. 10 CO[v] and 4 O$_2$[v] levels have been included, as it was found during this study that including more levels had a negligible influence on the results, while increasing the calculation time. Similarly, 4 CO[e] and 2 O$_2$[e] electronic levels have been included, as their presence can have an effect on the discharge.

III.2 Scaling laws for the reactions from the vibrational levels

Most of the time, reaction rate data is only available for reactions taking place from the ground state of the molecule or its first vibrationally excited states. Therefore, scaling laws are required to estimate the value of the reaction rate constants occurring from higher excited states.

The procedure developed by Kozák and Bogaerts[56] is followed in this work. The reactions involving vibrational levels can be grouped in three categories: electron impact reactions (tables A.1 and A.6 in appendix A), vibrational energy exchanges (vibrational-vibrational (VV) and vibrational-translational (VT), tables A.4 and A.9 in appendix A) and neutral reactions (tables A.5 and A.10 in appendix A). For the electron impact cross sections, Fridman's approximation[22]. For VV and VT reactions, the SSH theory[110;111] is used. Finally, vibrational excitation can also lower the activation energy of a reaction between two neutral molecules and the so-called theoretical-informational approach is considered here[22;112].

III.2.1 Cross section data

The cross sections for vibrational excitation are typically only known for the transitions from the ground state or the first or second vibrationally excited states. We make use of Fridman's approximation[22;56] to determine the cross section σ_{nm} of a reaction $CO_2[v_n] + e^- \longrightarrow CO_2[v_m] + e^-$ from the known cross section σ_{01}:

$$\sigma_{nm}(\epsilon) = \exp\left(\frac{-a(m-n-1)}{1+bn}\right)\sigma_{01}(\epsilon + E_{01} - E_{nm}) \tag{III.3}$$

where $E_{nm} = E_m - E_n$ and $E_{01} = E_1 - E_0$ are the corresponding energy thresholds for the excitation. Fridman's semi-empirical formula shifts the cross section to account for the change in energy threshold. In addition, the magnitude of the cross section scales according to two parameters, a and b. For CO_2, $a = 0.5$ is used, according to the recommendations of Fridman[22], as this value gives good agreement with the experimental data available for σ_{02} and σ_{03}[56;113]. The parameters b is taken to be 0 for simplicity, due to the lack of experimental data for excitation of $CO_2[v_{i\geq 1}]$. This means that the cross sections σ_{nm} and $\sigma_{n+1,m+1}$ have the same magnitude.

The cross sections for the reverse de-excitation processes (i.e. superelastic collisions) are determined from the detailed balance principle.

III.2.2 Neutral dissociation reactions

Vibrational excitation has the ability to lower the activation energy of a reaction between two neutral molecules. To scale the neutral reactions with vibrational energy, we use the following formula, expressed in the framework of the so-called theoretical-informational approach[22;112]:

$$k(T_g, E_v) = A.\min[\exp(-\frac{E_a - \alpha E_v}{T_g}), 1] \tag{III.4}$$

where E_a is the activation energy, E_v is the vibrational energy of the molecule, α is a parameter determining the efficiency of the vibrational energy to help overcoming the activation energy barrier, varying between 0 and 1 depending on the reaction, and T_g is the gas temperature. Equation III.4 implies that a vibrationally excited molecule reacting in a dissociation reaction 'sees' an activation energy of $E_a - \alpha E_v$, instead of simply E_a. Thus, in order to overcome the activation energy barrier of a reaction, at conditions of negligible thermal energy (i.e. low gas temperature T_g), a molecule needs to have an energy $E_v \gtrsim E_a/\alpha$. In this case, the reaction can be considered barrierless and its rate coefficient becomes equal to the pre-exponential factor A in equation III.4.

The values of α considered here are given in tables A.5 and A.10 (in appendix A.1 and A.2).These values are calculated based on the Fridman-Macheret approximative α model[22] :

$$\alpha = \frac{E_a}{2E_a - \Delta H^\circ} \tag{III.5}$$

Equation III.5 shows that α, i.e. the efficiency of vibrational energy to overcome the activation energy barrier, depends only on the activation energy and the enthalpy of a reaction. It is close to 1, i.e. maximum efficiency, for endothermic reactions with activation energy close to their enthalpy. An endothermic reaction with a high activation energy $E_a \gg \Delta H^\circ$ will have α close to 0.5. Only exothermic reactions can have α below 0.5 and α is 0 for barrierless exothermic reactions.

The role of the α parameters of the two main dissociation reactions ($CO_2 + M \longrightarrow CO + O + M$ and $CO_2 + O \longrightarrow CO_2 + O_2$) is investigated in detail in chapter VIII. Likewise, in chapter VIII, we also discuss the effect of the activation energy of reaction $CO_2 + O \longrightarrow CO_2 + O_2$ linked with the α parameter of this reaction.

III.2.3 Vibrational energy transfers

Several theories have been developed to scale the rate coefficients of vibrational energy transfers (VV, VV' and VT)[56;114]. The most popular first-order theories are the Schwartz-Slawsky-Herzfeld (SSH) theory[110] for VT relaxation, the Rapp-Englander-

Golden (REG) theory[115] for VV relaxation and the Sharma-Brau theory[116] for VV' relaxation induced by long-range forces. These theories are popular for their simplicity.

More complex and more accurate theories have been developed, such as the scaling theory of De Pristo *et al.*[117], the forced harmonic oscillator theory[118;119] or the so-called semiclassical theory[120;121]. The latter is the most accurate theory, but was only used for diatomic molecules. Most of these theories have been developed in the framework of CO$_2$ laser research and are valid at low temperatures only[122]. Therefore, most theoretical models available at moderate temperatures are based on the SSH theory. The fact that it is valid at moderate temperature, and its simplicity, make the SSH theory widely used in vibrational kinetics modeling. In this work, we also use the SSH theory.

Several sources present the SSH theory for VT, VV and VV' relaxation[22;56;111;114] and the description summarized in Kozák and Bogaerts[56] is used in this work. For VT relaxation reactions, it reads:

$$k_{n,n-1}^{VT} = k_{1,0}^{VT} Z_n \frac{F(\gamma_n)}{\gamma_1} \tag{III.6}$$

where $k_{n,n-1}^{VT}$ is the rate constant for VT relaxation $X[n] \longrightarrow X[n-1]$. The scaling factor Z_n is expressed as:

$$Z_n = n_e \frac{1 - x_e}{1 - n x_e} \tag{III.7}$$

where x_e is the anharmonicity of the energy levels. The function F is given by:

$$F(\gamma_n) = \frac{1}{2}\left[3 - \exp(-\frac{2}{3}\gamma_n)\right] \exp(-\frac{2}{3}\gamma_n) \tag{III.8}$$

Finally, γ_n is a parameter measuring the adiabaticity of the reaction and is calculated as:

$$\gamma_n = \left(\frac{\pi^2 \omega_n^2 \mu}{2\delta_r^2 k_B T_g}\right)^{1/2} \tag{III.9}$$

with $\omega_n = \Delta E/\hbar = |(E_n - E_{n-1})|/\hbar$ the energy over the reduced Plank constant, μ is the reduced mass and δ_r is a parameter of the exponential repulsive potential. The value of δ_r is determined by using[110] $\delta_r = 17.5/r_0$, with r_0 the radius parameter of the Lennard-Jones potential. The values of r_0 considered are taken from Kozák and Bogaerts[56]: 3.94 Å, 3.69 Å and 3.47 Å for CO$_2$, CO and O$_2$, respectively.

For VV and VV' relaxations, the following scaling law is considered to obtain the rate coefficient of a reaction $X[v_n] + X[v_{m-1}] \longrightarrow X[v_{n-1}] + X[v_m]$. Note that we call VV relaxation those reactions that transfer vibrational energy from a molecule X to another molecule X in the same vibrational mode, while VV' relaxation refer to the vibrational energy transfers between different molecules or different modes.

$$k_{n,n-1}^{m-1,m} = k_{1,0}^{0,1} Z_n Z_m \frac{\gamma_{nm}}{\gamma_{11}} \tag{III.10}$$

γ_{nm} is simply calculated from equation (III.9), replacing $\omega_n = |(E_n - E_{n-1})|/\hbar$ by $\omega_{nm} = |(E_n + E_{m-1} - E_{n-1} - E_m)|/\hbar$ and Z_m and Z_n are defined by equation (III.7)

III.3 Analytic distributions for the vibrational energy

A large part of this work focuses on vibrational energy and on vibrational energy distributions (VDFs). While the VDFs predicted by the model usually cannot be analytically derived, it is useful to know the two main two analytical expressions for the VDF: the Boltzmann and Treanor distributions.

The well-known Boltzmann energy distribution is given by:

$$f_B(\epsilon) = \frac{g_i \exp(\frac{-\epsilon_i}{k_B T_g})}{Z_B(T_g)} \tag{III.11}$$

where g_i is the degeneracy of the state of energy E_i and Z is the partition function:

$$Z(T_g) = \sum_i g_i \exp(\frac{-\epsilon_i}{k_B T_g}) \tag{III.12}$$

The Boltzmann energy distribution function gives the population of vibrational levels once an equilibrium is reached. It is particularly useful to compare a distribution to the Boltzmann distribution in order to assess the degree of non-equilibrium of that distribution.

In addition, Treanor *et al.*[123] derived an analytic formula, based on the SSH theory[110], for the VDF when the latter is controlled by vibrational-vibrational (VV) processes, neglecting the effect of dissociation and VT relaxation on the distribution. This Treanor distribution is given by[22;123]:

$$f_T(v) = \frac{\exp(-\frac{\hbar\omega_e n}{T_v} + \frac{x_e \hbar\omega_e n^2}{T_g})}{Z_T(T_g, T_v)} \tag{III.13}$$

where T_v is an additional parameter, called the vibrational temperature, n is the vibrational quantum number, x_e and ω_e refer to the anharmonic oscillator parameters used in equation (III.2) and $Z_T(T_g, T_v)$ is a new partition function:

$$Z(T_g) = \sum_i \exp(-\frac{\hbar\omega_e n}{T_v} + \frac{x_e \hbar\omega_e n^2}{T_g}) \tag{III.14}$$

Note that for an anharmonic vibrational oscillator, in the limit $T_v = T_g$, the Treanor and Boltzmann distributions are identical.

Figure III.3 illustrates the Boltzmann and Treanor analytical distributions for two different gas temperatures (300 K and 1000 K) and two different vibrational temperatures (1000 K and 2000 K). It shows that while the equilibrium (i.e. Boltzmann) population of the vibrational levels decreases fast with energy, the Treanor distribution shows a larger population of the highly excited levels, especially in the case where the ratio T_g/T_v is minimum. Indeed, the Treanor distribution shows a minimum for a level $v_{n_{min}}$:

$$n_{min} = \frac{T_g}{2x_e T_v} \tag{III.15}$$

In the case of the asymmetric vibrational mode of CO$_2$, we have $x_{33} = 5.2.10^{-3}$. Therefore, the minimum is below the dissociation limit (i.e. $n \leq 21$), if and only if $\frac{T_g}{T_v} \leq 0.22$, or $4.5T_g \leq T_v$. In figure III.3, this is only the case for T_g = 300 K and T_v = 2000 K, where n_{min} = 14.4. Therefore, there is a minimum between levels v$_{14}$ and v$_{15}$, with vibrational energies of 3.8 and 4.1 eV, respectively. More generally, the lower the $\frac{T_g}{T_v}$, the more the VDF is in non-equilibrium.

This property is of course very relevant in this work, since it shows that it is in theory possible to obtain very large vibrational populations even at low gas temperature. However, it must be realized that the Treanor distribution neglects the effects of dissociation and VT relaxation, which reduce the population of the higher vibrational levels; see more details in Chapter VI.

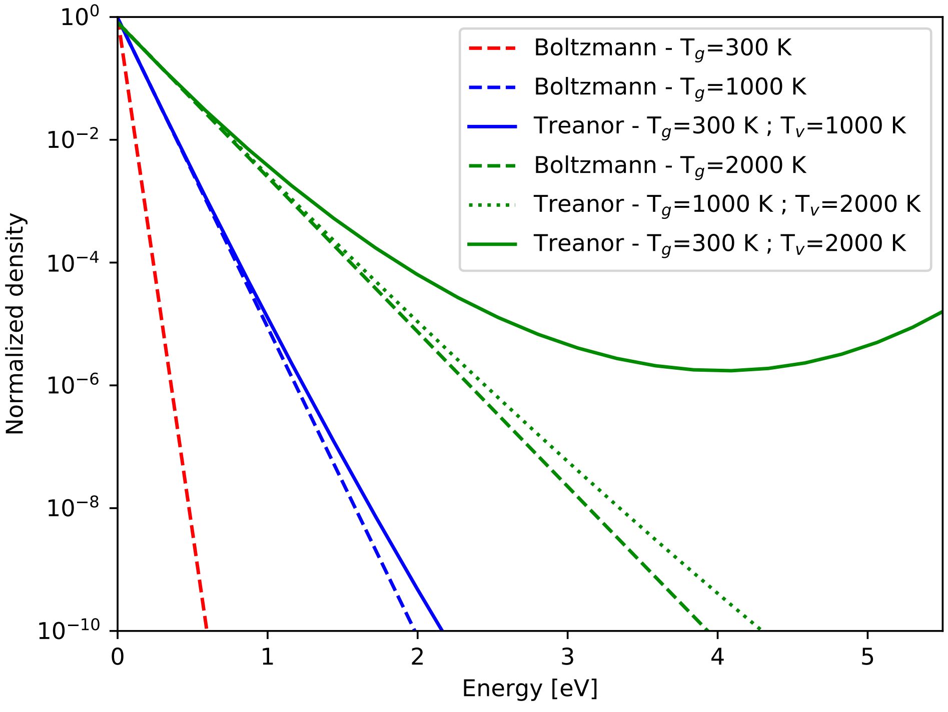

Figure III.3: Boltzmann and Treanor vibrational distribution functions (VDFs) for different gas temperatures T_g and vibrational temperatures T_v.

CHAPTER IV

Surfaguide simulations

The results presented in this chapter were published in:

- A. Berthelot, S. Kolev, and A. Bogaerts. *Different pressure regimes of a surface-wave discharge in argon: a modeling investigation.* Proceedings of IX International Workshop on Microwave discharges: Fundamentals and Applications, September 7-11, 2015, Cordoba, Spain, 2015
- V. Georgieva, A. Berthelot, T. Silva,S. Kolev, W. Graef, N. Britun, G. Chen, J. van der Mullen, T. Godfroid, D. Mihailova, J. van Dijk, R. Snyders, A. Bogaerts, and M. Delplancke-Ogletree. Understanding Microwave Surface-Wave Sustained Plasmas at Intermediate Pressure by 2D Modeling and Experiments. *Plasma Processes and Polymers*, 14 (4-5):1600185, 2017. DOI: 10.1002/ppap.201600185

IV.1 Introduction

The chemistry of CO_2 is too complex to be solved in a multi-dimensional model (see chapter V). Therefore, as a first step, we have built a 2D-axisymmetric model in argon. Argon has indeed a much simpler chemistry and there is an extensive literature on this type of plasma. As seen in figure I.12, the CO_2 chemistry will be incorporated in this model using the level-lumping method (see chapter V) in further work. Moreover, the information obtained from the 2D argon model can be useful in order to have a spatial description of the microwave plasma, to be used when making the 0D model.

Indeed, over the last decades, many studies focused on the description of surface-wave plasmas produced by microwave discharges in rare gases[125] both from a theoretical and an experimental point of view. These discharges have a wide range of applications, such as gas conversion, plasma medicine, material processing and surface treatment[99] as they offer relative simplicity and low running costs (see section I.3.2). They can be operated over a wide range of pressure (from few mtorr to several atmospheres), using different frequencies and various geometries, as shown in section I.3.2. Among these different geometries, the so-called surfaguide discharges offer the possibility to create low-temperature plasmas using a broad range of operating frequencies, determined by the geometry of the waveguide and they are able to handle high power coupling between the plasma and the microwave source.

A theoretical model for these discharges was presented by Ferreira and Moisan[126] at low pressure. More recently, a self-consistent 2D argon model was proposed by Castaños-Martinez *et al.*[127] and Kabouzi *et al.*[128] at atmospheric pressure. Baeva *et al.* modeled a microwave plasma setup, both using a stationary model at atmospheric pressure[129] and a time-dependent model between 20 and 40 mbar[130]. Jimenez-Diaz *et al.* first focused on the description of the electromagnetic field in a plasma torch and the influence of the boundary conditions[86] using the Plasimo platform[131]. Later, they developed a 2D quasi-neutral model to study a surfatron plasma at intermediate pressure (660 to 8800 Pa)[132]. In the same group, Rahimi *et al.*[133] presented a model to describe a similar microwave source, i.e. a coaxial plasma waveguide, at pressures ranging from 2 to 8 mbar.

The goal of the present chapter is to get a better understanding of the effect of the pressure on microwave discharges. The presented model is a self-consistent 2D fluid argon plasma model operated over a wide range of pressure conditions: from an intermediate pressure of 10 mbar to atmospheric pressure. In Georgieva *et al.*[134], we compared our results of this model with a similar model developed using Plasimo[131] at the Université Libre de Bruxelles (ULB, Belgium) and experimental results obtained at the University of Mons, Belgium.

IV.2 Model description

The model is a time-dependent model implemented in the commercial software COMSOL Multiphysics, as described in chapter II.

The model considers the following heavy species: Ar atoms, Ar^+ ions, Ar_2^+ molecular ions, Ar(4s), i.e., all 4s levels considered as a single lumped excitation level, Ar(4p), i.e., all 4p levels, as well as Ar_2^* which includes $Ar_2(^3\Sigma_u^+)$ and $Ar_2(^1\Sigma_u^+)$ excited molecules. The set of reactions between the different species, as well as the transport parameters used, are taken from Kolev and Bogaerts[135]. The reactions involving electrons are listed in table IV.1 and the reactions between heavy particles are presented in table IV.2. The EEDF is pre-calculated using Bolsig+[65] and it is used to calculate the rate coefficients of electron impact collisions and the electron transport parameters for each pressure regime as a function of the mean electron energy. The mobility coefficient of Ar^+ is expressed by[136]:

$$\mu_{Ar^+} = 1.52 \times 10^{-4} \times \frac{1.01 \times 10^5}{p} \frac{T_g}{273.16} \tag{IV.1}$$

The mobility coefficient of Ar_2^+ is correlated to μ_{Ar^+} by[136] $\mu_{Ar_2^+} = 1.2 \times \mu_{Ar^+}$. The diffusion coefficients of these two ions are obtained from the Einstein relation. The diffusion coefficient of Ar(4s) is given by[137]:

$$D_{Ar(4s)} = \frac{1.16 \times 10^{20}}{n_{Ar}} (\frac{T_g}{300})^{1/2} \tag{IV.2}$$

where n_{Ar} is the argon ground state density, calculated from the ideal gas law $\sum_i n_i = \frac{p}{k_B T_g}$. The same diffusion coefficient is used for Ar(4p) and Ar_2^* due to the lack of information. As noted by Kolev and Bogaerts[135], this may seem like a very rough approximation for Ar_2^*, but the diffusive term is typically much lower than the reaction term and therefore it does not significantly affect the results. There is no need for transport coefficients of ground state argon.

A photograph of the setup considered, located at the University of Mons in Belgium, is shown in figure IV.1 (left) with a schematic of this setup (right). A sketch of the 2D-axisymmetric computational domain is shown in figure IV.2.

Symmetric surface waves are launched by a surfaguide operating at 2.45 GHz in continuous regime. The discharge is generated in a quartz tube with 7 mm inner radius R_0 (light blue in figure IV.2), surrounded by a polycarbonate tube with 16 mm inner radius (dark blue in figure IV.2). The quartz and polycarbonate tubes have each 3 mm thickness. The inner tube is cooled down during the experiments by an oil flow at 10 °C (yellow area in figure IV.2). The metallic grid, which surrounds the plasma tubes

Table IV.1: Electron-heavy particle collisions included in the model. E_{thr} is the energy threshold, T_g is expressed in K and T_e in eV. The rate coefficients are in $[m^3.s^{-1}]$ or $[m^6.s^{-1}]$ for two-body and threebody reactions, respectively.

Reaction	E_{thr} [eV]	Rate coefficient	Reference
e + Ar → e + Ar	-	BOLSIG+[a]	138
e + Ar → e + Ar(4s)	11.55	BOLSIG+	138
e + Ar(4s) → e + Ar	-	BOLSIG+, DB[b]	138
e + Ar → 2e + Ar^+	15.7	BOLSIG+	138
e + Ar(4s) → 2e + Ar^+	4.15	BOLSIG+	139
e + Ar → e + Ar(4p)	13	BOLSIG+	138
e + Ar(4p) → e + Ar	-	BOLSIG+, DB	138
e + Ar(4p) → 2e + Ar^+	2.8	BOLSIG+	139
e + Ar(4s) → e + Ar(4p)	1.08	BOLSIG+	140
e + Ar(4p) → e + Ar(4s)	-	BOLSIG+, DB	140
2e + Ar^+ → Ar + e	-	$8.75 \times 10^{-39} T_e^{-4.5}$	71
e + Ar + Ar^+ → Ar + Ar	-	$1.5 \times 10^{-40} (\frac{300}{T_g})^{2.5}$	141
e + Ar_2^+ → Ar^+ + Ar + e	-	$1.11 \times 10^{-12} \exp(-\frac{2.94-3(T_g/11604-0.026)}{T_e})$	142
e + Ar_2^+ → Ar + Ar(4s)	-	$1.04 \times 10^{-12} (\frac{0.026}{T_e}) \frac{1-\exp(-418/T_g)}{1-0.31\exp -418/T_g}$	127;143

[a] Boltzmann solver: the rate coefficients are calculated from the corresponding cross sections, based on solution of the Boltzmann equation with BOLSIG+[65].

[b] Detailed balance (DB): the rate coefficients for the superelastic processes are calculated using the detailed balance principle[98] incorporated in BOLSIG+[65].

Table IV.2: Heavy particle-heavy particle collisions and radiative transitions included in the model. T_g is expressed in K and T_e in eV. The rate coefficients are in s^{-1} or $[m^3.s^{-1}]$ or $[m^6.s^{-1}]$ for spontaneous emission, two-body and three-body reactions, respectively.

Reaction	Rate coefficient	Reference
Ar(4s) + Ar(4s) → Ar_2^+ + e	$\frac{1}{2} 6.3 \times 10^{-16} [\frac{300}{T_g}]$	144
Ar(4s) + Ar(4s) → Ar^+ + Ar + e	6.2×10^{-16}	145
Ar^+ + 2Ar → Ar_2^+ + Ar	$2.5 \times 10^{-43} (\frac{300}{T_g})^{3/2}$	146
Ar_2^+ + Ar → Ar+ + 2Ar	$\frac{6.02 \times 10^{-12}}{T_g} \exp(-\frac{-1.51 \times 10^4}{T_g})$	142
Ar(4p) + Ar → Ar(4s) + Ar	5×10^{-18}	146
Ar(4s) + Ar(4p) → Ar^+ + Ar + e	6.2×10^{-16}	145
Ar(4p) + Ar(4p) → Ar^+ + Ar + e	6.2×10^{-16}	145
Ar(4s) → Ar + hν	$g_{eff} \times 3.145 \times 10^8$	147
Ar(4p) → Ar(4s) + hν 4.4×10^8	147	

[a] g_{eff} is the escape factor, which denotes the fraction of the radiation that can effectively escape from the plasma. It depends on the characteristic dimension of the reactor and is calculated to be 6×10^{-4} for the present reactor[148].

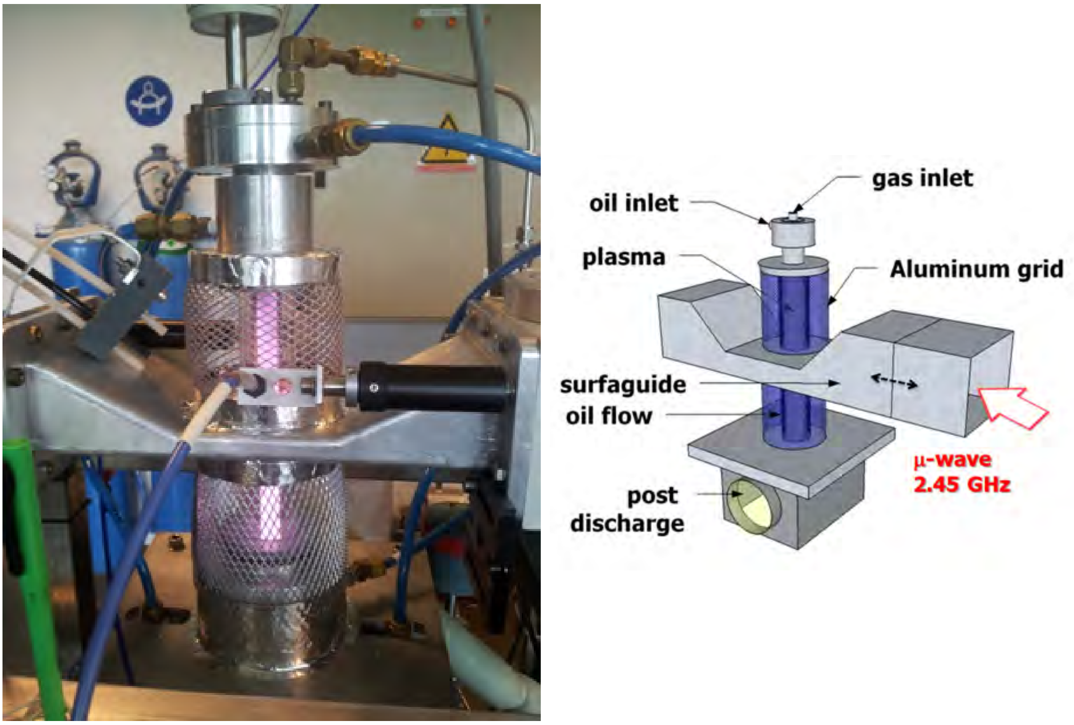

Figure IV.1: Photograph of the microwave plasma setup with an argon plasma on (left) and schematic of this setup (right), taken from Silva *et al.*[36].

and forms a Faraday cage, has a radius of 50 mm. There are two metal rings which confine the electromagnetic field in a region of 31 cm along the discharge tube (PL and QC in figure IV.2). The center of the quartz tube is positioned in the waveguide gap. Further details of the experimental surfaguide system used in the present research can be found in Silva *et al.*[36]. The coordinate in the direction along the axis of symmetry is referred to as z and the radial coordinate is noted r. The point O in figure IV.2 is taken as the origin of the 2D coordinate system (r,z).

The boundary conditions considered in the model are presented in table IV.3, using the points defined in figure IV.2. The boundary OA is a symmetry axis and a Neumann condition is considered for all variables ϕ (i.e. $\frac{\partial \phi}{\partial r} = 0$). γ_α is the sticking coefficient of species α, equal to 1 for all species in this study, i.e. each excited state or molecule returns to ground state argon after colliding with the wall. $v_{th,\alpha} = \sqrt{\frac{8k_BT_\alpha}{\pi m\alpha}}$ is the thermal velocity of species α, with $T_\alpha = T_e$ for the electrons and $T_\alpha = T_g$ for the heavy particles and $H(E_r)$ is the heaviside function (0 if E_r is negative, 1 otherwise).

ϕ_{slm} is the mass flow rate and the integral over $d\Omega$ refers to the inner cross section of the quartz tube, where the gas flows. The flow rate is typically expressed in units of slm (standard liter per minute) or sccm (standard cubic centimeter per minute), which gives the flow rate (in L.min^{-1} or $\text{cm}^3.\text{s}^{-1}$) that would be at standard conditions of pressure and temperature (1 atm and 0°C).

The microwaves travel in a TE_{10} mode in the waveguide, which leads to a microwave electric field in the direction of z at the excitation boundary GH: $\boldsymbol{E} = E_z\boldsymbol{u}_z$. α_E is calculated so that the power absorbed in the model matches the input power P_{in}, computing the volume integral of the power density:

$$P_{in} = \int_{Vol} \frac{1}{2}\text{Re}(\sigma)|\boldsymbol{E}|^2\text{d}V \tag{IV.3}$$

This configuration is not perfectly axisymmetric, as shown in figure IV.1. However, Moisan and Zakrzewski[83] have shown that the azimuthally symmetric mode m = 0 of a surface-wave can propagate if and only if $fR_0 < 2$ GHz.cm, which is the case here ($f = 2.45$ GHz and $R_0 = 0.7$ cm). Therefore, the MW field propagating at the inferface between the plasma and the quartz tube is azimuthally symmetric and, consequently, the setup can be approximated as axisymmetric.

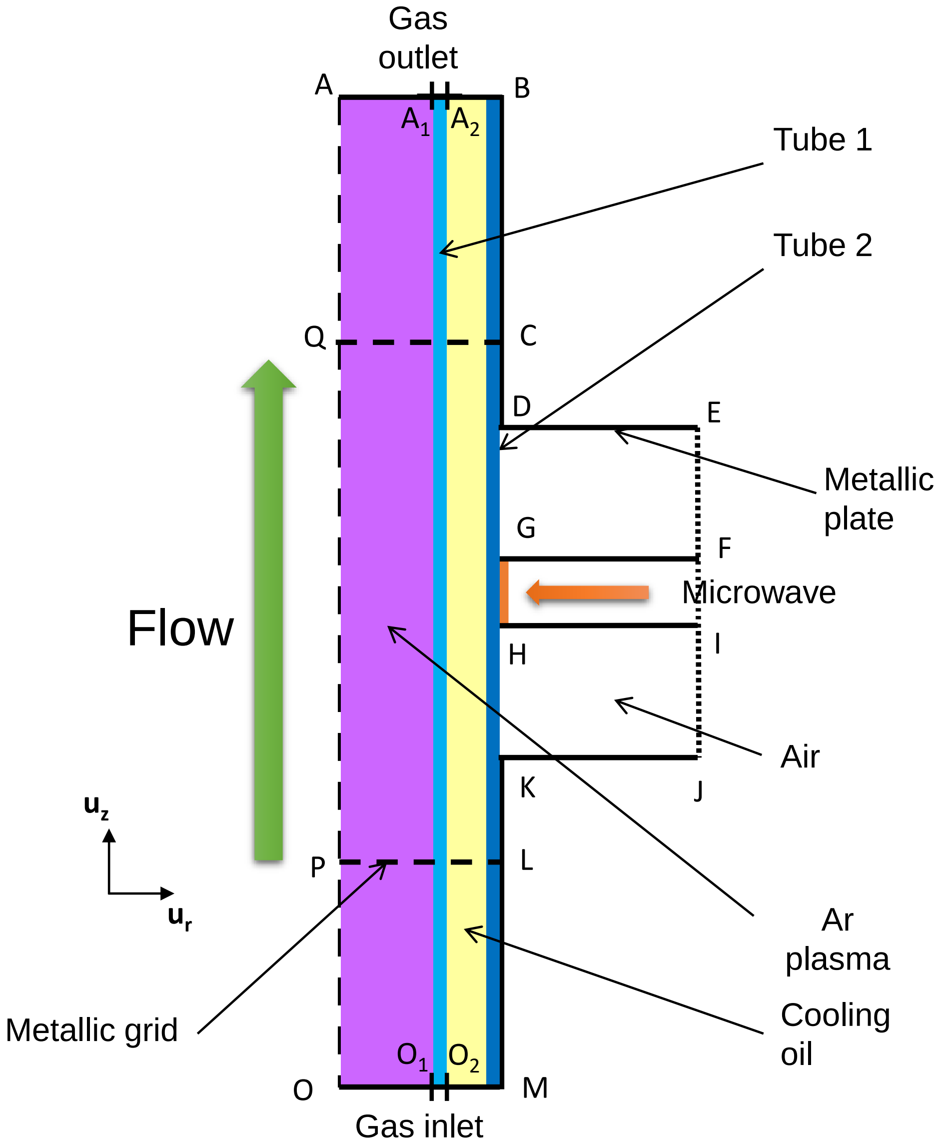

Figure IV.2: 2D axisymmetric computational domain.

Table IV.3: Boundary conditions in the model. The points are presented in figure IV.2. $\boldsymbol{n}$ is the unit vector normal to the boundary.

	Heavy particle density equations(II.5)
A_1A & O_1O	$\boldsymbol{n}.\boldsymbol{\nabla} n_\alpha = 0$
A_1O_1	$\Gamma_\alpha = \frac{\gamma_\alpha}{1-\gamma_\alpha/2} n_\alpha v_{th,\alpha} + Z_\alpha n_\alpha E_r H(E_r)$
	Electron density equation(II.5)
A_1A & O_1O	$\boldsymbol{n}.\boldsymbol{\nabla} n_e = 0$
A_1O_1	$\Gamma_e = \frac{1}{2} n_e v_{th,e}$
	Electron energy equation(II.13)
A_1A & O_1O	$\boldsymbol{n}.\boldsymbol{\nabla}(n_e \epsilon_e) = 0$
A_1O_1	$\Gamma_\epsilon = \frac{1}{2} n_e \epsilon_e v_{th,e}$
	Gas temperature equation(II.17)
A_2O_2O	$T_g = 300$ K
A_2A	$\boldsymbol{n}.(\lambda \boldsymbol{\nabla} T_g) = 0$
	Flow equation(II.11)
O_1A_1	$\boldsymbol{u} \times \boldsymbol{n} = 0$
OO_1	$\phi_{slm} = -\int_{d\Omega} \frac{\rho}{\rho st} \boldsymbol{u}.\boldsymbol{n} \mathrm{d}S$
AA_1	$p = p_0$
	Wave equation (II.24)
QCDEFG & HIJKLP	$\boldsymbol{n} \times \boldsymbol{E} = \boldsymbol{0}$
GH	$E_z = \alpha_E$
	Poisson equation (II.3.2)
AB & OM	$\boldsymbol{n}.\boldsymbol{E} = 0$
A_1O_1	$V = 0$

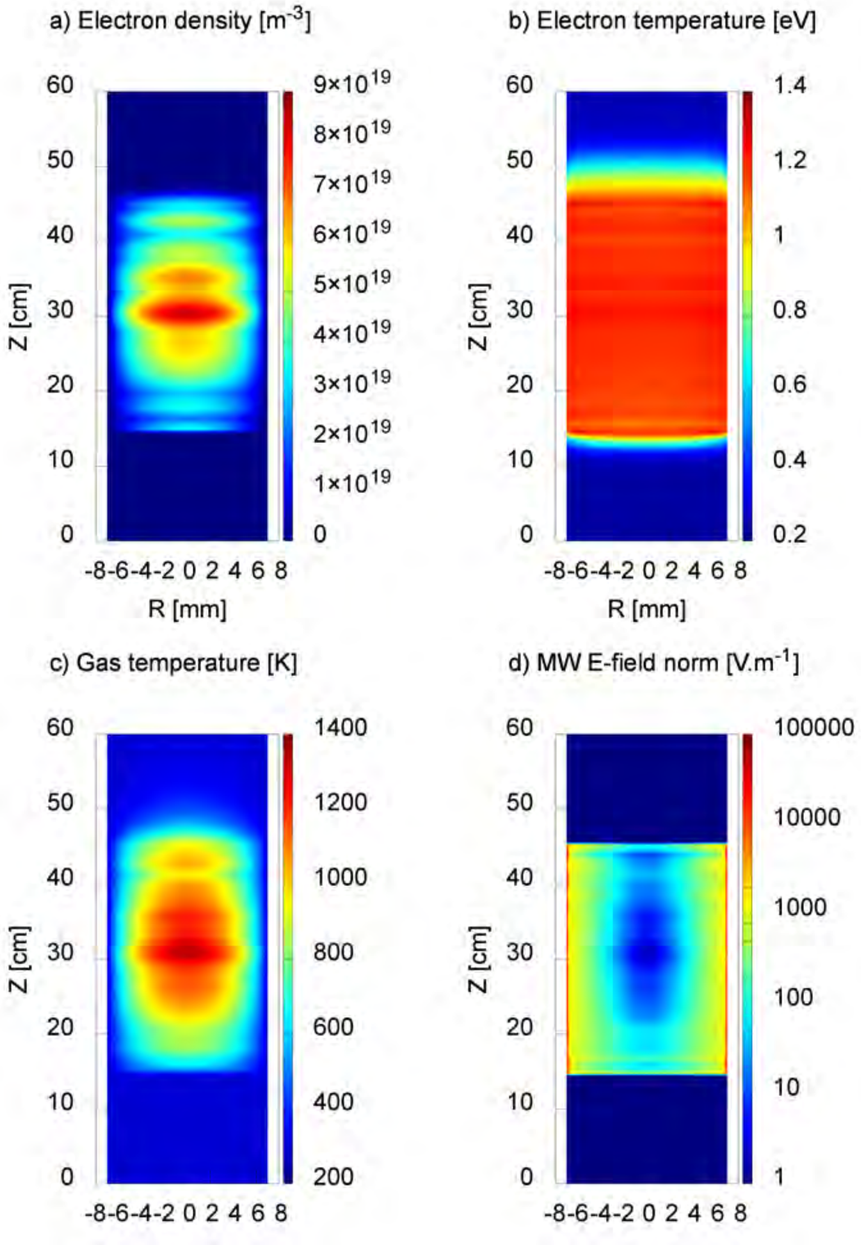

Figure IV.3: Electron density (a), electron temperature (b), gas temperature (c) and norm of the microwave electric field (d) Pressure: 1000 Pa, Power: 100W, Gas flow rate: 500 sccm

IV.3 Results

IV.3.1 Intermediate pressure

First, the model was developed for a pressure of 1000 Pa. Figure IV.3 shows the distribution of the electron density (a), the electron temperature (b), the gas temperature (c) and the norm of the microwave electric field (d) at a pressure of 1000 Pa, a flow rate of 500 sccm and with an absorbed microwave power of 100W.

The electron density reaches a maximum value in front of the waveguide. Moreover, the electron density profile exhibits secondary maxima that are located approximately 6 cm, i.e. half a wavelength, from each other. The maximum electron density is found to be 8.2×10^{19} m^{-3} with a 34 cm long plasma. The electron temperature profile is almost flat in the plasma with values between 1 and 1.2 eV. The gas temperature T_g profile resembles the electron density profile. The maximum value of T_g is 1400 K. Note that T_g drops to almost 300 K close to the quartz tube since the outer surface of the quartz tube is assumed to be cooled at 300 K. The norm of the microwave electric field is maximal at the boundary between the plasma and the quartz tube, in the sheath region. It decays exponentially in the radial direction, indicating a skin effect. The electron density is indeed too high in the plasma to allow the field to propagate there, since the plasma conductivity is high (see equation II.23). Therefore, the microwaves propagate axially at the boundary between the dielectric tube and the plasma. This type of discharge is called a surface-wave plasma and has been described experimentally and theoretically[83;88;99;149–151], in order to better understand the complex relation between the plasma characteristics and the wave propagation.

Axially, omitting the secondary maxima, the electron density decreases linearly from the maximum value in the centre of the tube to the end of the plasma, which is consistent with literature[152]. Note that these two secondary maxima are due to an additional resonance of the EM field caused by the two horizontal metallic grids shown in figures IV.1 and IV.2. The two metallic grids also confine the plasma in between them.

IV.3.2 Atmospheric pressure

Figure IV.4 shows the results obtained at atmospheric pressure in the same configuration and with the same conditions of flow rate and power. The maximum electron density is 4.5×10^{19} m^{-3}. It is located on the axis of symmetry but it is shifted axially by 3 cm compared to the intermediate pressure case. An off-axis secondary maximum is also present in front of the waveguide. The electron temperature shows values between 1.2 and 1.4 eV in the plasma. The electron temperature is maximal around the plasma.

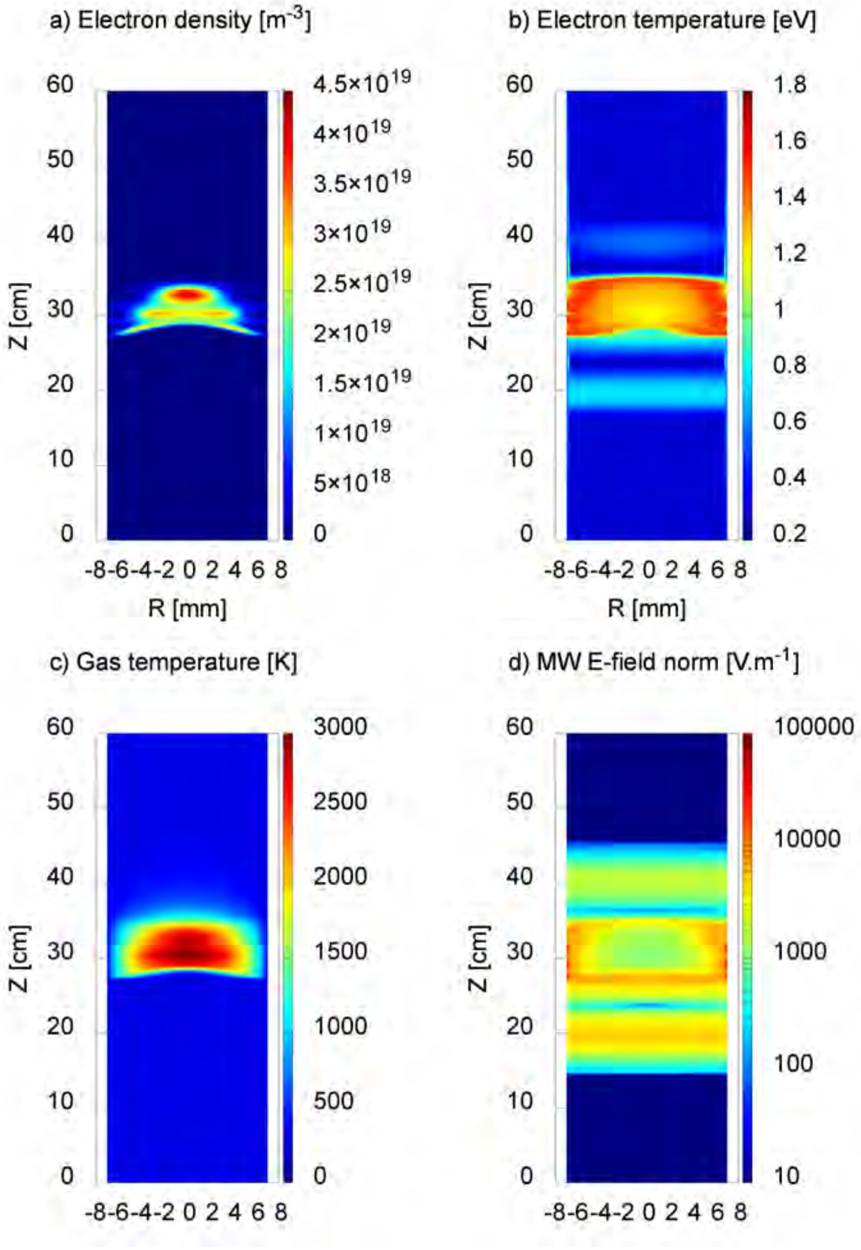

Figure IV.4: Electron density (a), electron temperature (b), gas temperature (c) and norm of the microwave electric field (d) Pressure: 10^5 Pa, Power: 100W, Gas flow rate: 500 sccm

The plasma is about 6 cm long in this case. The gas temperature reaches higher values at atmospheric pressure: between 1500 K and 3000 K in the plasma. The norm of the microwave electric field is still maximal at the interface between the quartz tube and the plasma, also showing a skin effect. However, it exhibits two weak secondary maxima outside the plasma. The presence of a microwave electric field outside the plasma is also visible in the electron temperature profile: a small number of electrons receive a small power deposition which results in a local increase of the electron temperature. The shape of the microwave field is explained by the presence of the two metallic grids which act together as a resonator. It is more visible than at intermediate pressure since the plasma does not occupy the whole space.

By comparing the results of the model at intermediate and at atmospheric pressure, it is clear that the discharge is more contracted axially at atmospheric pressure (6 cm vs 34 cm) but also radially as the plasma does not occupy the whole radial space. This effect has been observed experimentally and can be quite challenging to reproduce in a model[128]. Note that the filamentary structure that can be observed in some pressure regimes is not reproducible in a 2D axisymmetric model.

Benchmarking In Georgieva *et al.*[134], the results of the model were compared to experimental results from literature at similar conditions. A good agreement was found between experimental values and the model results, especially for electron density and electron temperature, which are particularly important outputs of the model.

IV.4 Conclusion

Microwave argon discharges are modelled using Comsol Multiphysics at different pressures, in order to better understand the propagation of microwaves and how pressure affects the shape of a microwave discharge. The findings of this chapter were used to estimate the power deposition profile to use in our 0D model in chapters V and VI. The shape of the plasma and its characteristic are largely affected by the pressure. A comparison of the model results at different pressures shows an axial and a radial contraction of the plasma upon higher pressure. The electron density decreases linearly with axial position, especially at intermediate pressure (1000 Pa), and the gas temperature follows a similar profile. The electron temperature appears to stay rather constant in the plasma. The skin effect of the microwaves is shown, as the microwaves cannot propagate in the plasma, due to its high conductivity.

Results at intermediate pressure is in good agreement with previous research conducted on similar setups.

CHAPTER V

Towards a 2D CO_2 model: the level lumping method

The results presented in this chapter were published in[153]:

- A. Berthelot and A. Bogaerts. Modeling of plasma-based CO_2 conversion: lumping of the vibrational levels. *Plasma Sources Science and Technology*, 25(4):045022, 2016. DOI: 10.1088/0963-0252/25/4/045022

V.1 Introduction

In order to describe the chemical processes taking place in a CO_2 plasma, a large chemistry set for CO_2 dissociation had been developed in our group[56;57], as detailed in chapter III. The number of species that needs to be taken into account in a state-to-state non-equilibrium CO_2 plasma model is very large and this makes such a model computationally expensive. Indeed, as discussed in chapter I, the vibrational excitation plays an important role in the efficient dissociation of CO_2[22] and an accurate description of the Vibrational Distribution Function (VDF) is needed. That is why most of the numerical studies done so far on the subject have been limited to 0D-models[49;50;56–58;76]. However, some processes cannot be accurately included in a 0D-model and strong approximations on the geometry and the diffusion processes need to be made. In order to model a discharge in more dimensions, it is necessary to considerably reduce the chemistry set with as little losses of accuracy as possible in the model predictions.

The Principal Component Analysis (PCA) method has been used by Peerenboom *et al.*[154] to reveal the underlying manifolds present in the plasma chemistry of CO_2. It was shown that using only two principal components, this method allows to accurately reproduce the entire chemistry of the CO_2 plasma. However, this method has not been implemented yet in a self-consistent plasma code and its use in an existing code can be complex due to the use of large-dimensional lookup-tables for the source terms, as well as the instabilities that can arise.

Therefore, we have decided to apply a different strategy to reduce the number of equations to be solved in the model, i.e., the lumping of the vibrationally excited levels. Le *et al.*[155] introduced a method to reduce the complexity of a collisional-radiative model in the case of atomic hydrogen, comparing two grouping strategies: uniform and Boltzmann groups. It was shown that the Boltzmann approach using different internal temperatures gives better results. Guy *et al.*[156;157] presented a multi-internal temperature model for the vibrational levels of N_2 and electronic levels of N in hypersonic nitrogen flows. A good agreement was observed between the multi-internal temperature model and the detailed model considering individual-levels. However, to our knowledge, such a level lumping method has not yet been applied for CO_2.

In this chapter, before applying the level-lumping, we first reduce the complexity and the number of species included in the chemistry set from the work of Kozák and Bogaerts[56;57]. Subsequently, a lumped-model is proposed to describe the VDF using fewer variables, thus making this chemistry set compatible with 2D or 3D models. In section V.2, we describe the self-consistent 0D model that was used to reduce the chemistry set and to test the accuracy of the level lumping strategy. We also present the reduced chemistry set and we introduce the equations used to describe the different groups in the lumped model. In section V.3, first, a comparison between the predictions given by the two chemistry sets is shown, followed by a comparison of the models considering the individual vibrational levels and the grouped-levels (with a different number of groups), for different conditions of pressure and power, and for fixed or self-consistently calculated gas temperature. The effect of the description of the VDF on the other plasma parameters is also shown, stressing the importance of an accurate description of the VDF in a self-consistent CO_2 plasma model. Finally, the limitations of the level-lumping strategy proposed here are discussed.

V.2 Model description

V.2.1 Discharge geometry and conditions

A 0D model only allows us to model simple reactors, such as the surfaguide[83] setup presented in Silva *et al.*[36] and presented in chapter IV. It consists of a quartz discharge tube and a waveguide bringing the microwaves perpendicular to the tube, forming a plasma. As discussed in chapters II and IV, the plasma also has an effect on the propagation of the electromagnetic waves and a self-consistent model including the description of the microwave fields requires going to higher dimensions, as shown in chapter IV with an argon plasma.

In this model, we use the plug-flow approximation described in section II.4.1. The direction of the flow is shown in Figure V.1. The shape of the microwave power deposition Q_{MW} can then be presented as a function of the axial position, according to theoretical calculations[125] and the results of chapter IV. This profile is also shown in Figure V.1. The absolute value of Q_{MW} is determined by solving:

$$P_{in} = \mathcal{A} \int_{z_p}^{z_p+L} Q_{MW}(z)\,\mathrm{d}z = \frac{\mathcal{A}L}{2} Q_{MW,max} \qquad \text{(V.1)}$$

$Q_{MW,max}$ is the maximum value of the local microwave power deposition, z_p is the axial position where the plasma starts and L is the plasma length, as shown in figure V.1.

Note that the use of this configuration, shown in figure V.1, is not motivated by the description of a particular experiment. Instead, the parameters are chosen as typical conditions studied for CO_2 dissociation by microwave plasma, as the set needs to be tested for realistic conditions.

The specific energy input (SEI) is an important quantity to describe a discharge used for CO_2 conversion and is defined by:

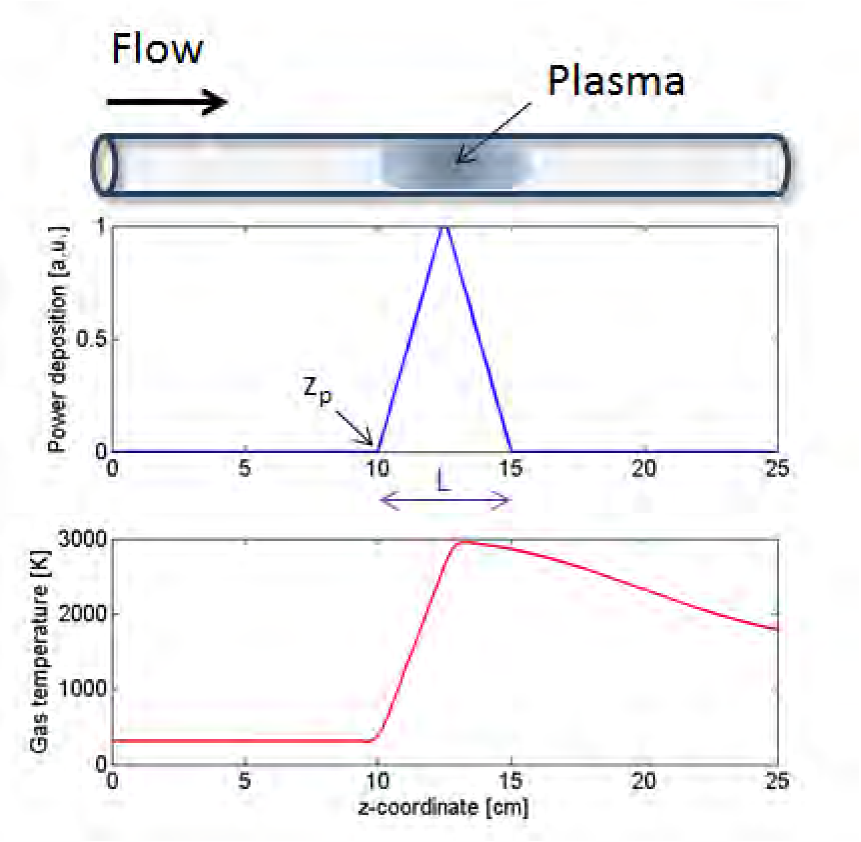

Figure V.1: Schematic description of the geometry (upper panel), shape of the power deposition profile (middle panel) and typical gas temperature profile (lower panel).

$$\mathrm{SEI(eV/molec)} = \frac{P_{in}}{\phi(sccm)} \frac{T_{ref}}{p_{ref}} \frac{k_B}{e} \frac{60(\mathrm{s/min})}{10^{-6}} \tag{V.2}$$

Where e, the elementary charge, is used to convert J into eV, $T_{ref} = 273.15$ K is the reference temperature and $p_{ref} = 10^5$ Pa is the reference pressure (see section IV.2). The factor 10^{-6} comes from the conversion of the flow rate, typically expressed in standard $\mathrm{cm^3.s^{-1}}$, into standard $\mathrm{m^3.s^{-1}}$.

V.2.2 Gas temperature

A self-consistently calculated gas temperature is used in section V.3.3, using equation (II.29). Note that in this chapter, we also neglect the heat losses by conduction (last term of the right-hand side of equation (II.29)). While this is an approximation in

Table V.1: Coefficients in [$J.kg^{-1}.K^{-1}$] for calculating the specific heat capacity C_p of CO_2 in equation V.4

Temperature	300-1200K	1200-3000K
A	369.4	1327
B	1845	-53.85
C	-1429	31.52
D	401.2	-5.841
E	3.664	-109.6

some of the cases studied here, the goal of this study is to assess the effect of the level-lumping strategy on the model results and not to model a specific experiment.

γ in equation (II.29) is here defined as:

$$N\frac{\gamma}{\gamma-1} = \sum_s n_s \frac{\gamma_s}{\gamma_s - 1} \tag{V.3}$$

where γ_s is the specific heat ratio of species s.

As in the previous work from our group[57], the specific heat ratio is here 1.67 for atomic species and 1.40 for diatomic molecules. For CO_2, we only have to take into account the heat capacity due to translational and rotational degrees of freedom, as well as the vibrational symmetric mode levels that are not described by an individual species. C_p can be expressed as in[57].

$$C_p = A + Bt + Ct^2 + Dt^3 + Et^{-2} \tag{V.4}$$

Where $t = T/1000[K]$. The coefficients A, B, C, D and E are shown in table V.1. We then use $\gamma_s = (1 - \frac{k_b}{C_p M_s})^{-1}$ to obtain γ_{CO_2}[57].

In sections V.3.1 and V.3.2, we consider a fixed temperature profile, increasing from 300 K to 3000 K in the plasma as shown in figure V.1. The maximum value of T_g = 3000 K, as well as the shape, are based on the predictions by our self-consistent model (see section V.3.3 below). The shape of the temperature profile is also similar to the typical shape obtained by 2D models of similar discharges[128], as we have also seen in chapter IV. The use of a temperature profile in sections V.3.1 and V.3.2 instead of a self-consistent calculation is motivated by the strong influence of the VDF on the gas temperature (see section V.3.3) and vice-versa. Thus, by applying a fixed temperature profile, this allows us, in a first step, to analyse the ability of the lumped-levels models to accurately describe the VDF for a given temperature.

Table V.2: Species described in the model.

Neutral ground states
CO_2, CO, O_2, O, C

Charged species
CO_2^+, CO_3^-, O^-, O_2^-, e^-

Excited states
[a]$O_2[v_{1-3}]$, $CO_2[v_{1-21}]$, $CO_2[v_a]$, $CO_2[v_b]$, $CO_2[v_c]$, $CO_2[v_d]$, CO_2^*

[a] The three levels $O_2[v_{1-3}]$ have only been considered for pressures of 200 mbar and above. For lower pressure, they were also negligible.

V.2.3 Reduction of the chemistry set

The chemistry set developed by[56;57], which will be referred to as "full set", is in a first step simplified by removing all the species that do not significantly contribute to the plasma chemistry. In order to determine which are the main species and processes to take into account, the model of[56;57] was implemented in ZDPlaskin[100]. Simulations are performed for a gas flow rate of 3 slm and a microwave power of 500 W, yielding a specific energy input (SEI) of 2.3 eV/molec. The gas temperature profile shown in figure V.1 is used. A comparison of the predictions given by the full and the reduced chemistry sets obtained in this way is given below in section V.3. The list of species that are considered in the reduced model considered in this chapter is shown in table V.2. The list of species in the full set is shown in tables III.1 and III.2. Note that no excited states have been kept for CO and only 3 vibrational levels have been kept at pressures of 200 mbar and above for O_2. The influence of the states removed from the full set was found to be negligible at these conditions, due to the relatively low number densities of CO and O_2 (see figure V.4 below). In cases where their number densities are higher, i.e. when the conversion is larger, the contribution of these vibrationally and electronically excited levels may not be negligible anymore, so in this case, the full chemistry set, or a reduced set with more species, should be used.

The list of the different reactions considered in the full and reduced sets is shown in appendix A.1.

V.2.4 Level lumping

The reduced model presented above is further reduced by grouping the asymmetric mode vibrational levels ($CO_2[v_{1-21}]$ in Table V.2) into l lumped levels. The symmetric mode vibrational levels (i.e., CO_2 [v_a, v_b, v_c, v_d] in Table V.2) are not further lumped together. The lumping of the asymmetric mode vibrational levels is realized by introducing n_{g_i}, the total number density of all the levels j within one lumped level i.

$$n_{g_i} = \sum_{j \in g_i} n_j \qquad i = 1, ..., l \tag{V.5}$$

It is then necessary to describe the distribution of the levels within the group g_i using a function $f(E_j, T_i)$, where E_j is the energy of the jth level within group g_i, and T_i is the temperature associated to the group g_i.

$$n_{j \in g_i} = n_{g_i} \frac{f(E_j, T_i)}{\sum\limits_{j \in g_i} f(E_j, T_i)} \tag{V.6}$$

In the case of a Boltzmann internal vibrational distribution where all the levels have the same degeneracy, this gives:

$$n_{j \in g_i} = \frac{n_{g_i} exp(-\frac{E_j}{k_b.T_i})}{\sum\limits_{j \in g_i} exp(-\frac{E_j}{k_b.T_i})} \tag{V.7}$$

Since the VDF is typically not a Boltzmann distribution, as discussed in section III.3, we recommend to use several groups when the VDF cannot be known in advance. In the case the user knows which VDF to expect, different inner-distribution functions can be chosen in order to limit the number of groups to be used. However, this limits the applicability of the method. Therefore, when the VDF is not known, the use of several groups, as presented here, makes the method more generally applicable.

In order to solve for the density of the group instead of the density of each individual level, we need to re-define the conservation equation II.28:

$$\frac{dn_{g_i}}{dt} = \sum_{j \in g_i} \frac{dn_j}{dt} = \sum_{j \in g_i} S_j \tag{V.8}$$

where S_j is the source term for each individual level j, i.e. the right-hand side of equation II.28. Additionally, for each group, another conservation equation is required to describe the inner-distribution within each group. In this work, we have chosen to solve for the mean group vibrational energy:

$$\overline{E_{g_i}} = \frac{1}{n_{g_i}} \sum_{j \in g_i} E_j n_j \tag{V.9}$$

where E_j is the energy associated to each vibrational level, obtained from the anharmonic oscillator approximation[106]. We can then define a conservation equation for $\overline{E_{g_i}}$, by taking the time-derivative of equation V.9 and using equation V.8:

$$\frac{d\overline{E_{g_i}}}{dt} = \frac{\sum\limits_{j\in g_i} E_j S_j - \overline{E_{g_i}} \sum\limits_{j\in g_i} S_j}{n_{g_i}} \tag{V.10}$$

Note that instead of solving for $\overline{E_{g_i}}$ other choices are also possible, such as solving for the density of one level within the group[155].

Obtaining the distribution of the levels within each group, based on a Boltzmann distribution, requires to know the temperatures T_i, as shown in equations V.6 and V.7. However, the model solves for the mean group energy $\overline{E_{g_i}}$. Therefore, for each group considered in the model, we need to use lookup-tables giving T_i as a function of $\overline{E_{g_i}}$. The relation between T_i and $\overline{E_{g_i}}$ is established by equation V.11.

$$\overline{E_{g_i}} = \frac{\sum\limits_{j\in g_i} E_j exp(-\frac{E_j}{k_b.T_i})}{\sum\limits_{j\in g_i} exp(-\frac{E_j}{k_b.T_i})} \tag{V.11}$$

Alternatively to the level lumping strategy, one can assume thermal equilibrium between the vibrational temperature and the gas translational temperature, which gives the following description of the VDF (see section III.3):

$$n_k = \frac{n_0 exp(-\frac{E_k}{k_b.T_g})}{\sum\limits_{0\leq j\leq 21} exp(-\frac{E_j}{k_b.T_g})} \qquad k = 1, ..., 21 \tag{V.12}$$

This will be referred to as 'thermal distribution model' in the following. n_0 refers to the density of the CO_2 ground state.

This level-lumping method is developed with the Comsol Multiphysics code. In this code, the rate coefficients of the electron impact reactions are calculated by means of the external Boltzmann solver, i.e., Bolsig+[65], as also done for argon in chapter IV. This is a necessary approximation, as a 2D-model solving the Boltzmann equation would be computationally expensive. For additional information, the effect of the vibrational collisions and the superelastic collisions on the EEDF is discussed in Pietanza *et al.*[50].

Table V.3: Asymmetric mode vibrational levels included within each group, for the different lumped-levels models developed

	Group 1	Group 2	Group 3
1G model	1-21	×	×
2G model	1-3	4-21	×
3G model	1-3	4-14	15-21

V.3 Results and discussion

As mentioned above, the first step of this study is the simplification of the chemistry set previously used, by identifying the main chemical processes taking place in this kind of discharge. We assess the validity of the reduced chemistry set over a range of pressures commonly used in the experiments (from 20 mbar to atmospheric pressure)[22;34;36].

In section V.3.1, we present a comparison of the model predictions using the full and the reduced chemistry set for the main model outputs: CO_2 conversion, VDF, electron temperature and density.

In section V.3.2, we show the influence of the number of lumped levels (or groups) considered in the level-lumping strategy on the accuracy of the description of the VDF. This is done using the temperature profile shown in figure V.1 in order to leave out the effects of the gas temperature on the VDF and to focus on the predictions of the VDF given by the lumped-levels model.

In section V.3.3, the most important plasma quantities, calculated with the various lumped-levels models using the self-consistent gas translational temperature calculation, will be compared to assess the validity of the lumped-level strategy.

Finally, in section V.3.4, we discuss the limitations of the lumped-levels model and its range of applicability.

Table V.3 shows the levels included within each group, for each of the lumped-levels models developed, i.e., one-group (1G), two-groups (2G) and three-groups (3G) model. This levels-repartition was chosen in order to fit the VDF predicted by the individual-levels model. The same groups are considered for all the conditions investigated in order to make the lumped-levels models as general as possible. We use a Boltzmann distribution to describe the distribution of levels within each group. However, this does not assume that the entire VDF follows a Boltzmann distribution, as the 2-groups and 3-groups models assume a different vibrational temperature for each group.

Finally, we will also study the effect of assuming simply a thermal vibrational distribution (as defined by the gas temperature), as well as no vibrational distribution of the asymmetric mode at all.

The definition of CO$_2$ conversion is given by equation (V.13).

$$X = 1 - \frac{v(z_{out})n_{CO_2,tot}(z_{out})}{v(z_0)n_{CO_2,tot}(z_0)} \tag{V.13}$$

where v is the gas velocity, z_{out} is the outlet axial position, and z_0 is the inlet axial position.

We also calculate the vibrational temperature of CO$_2$, as it provides an indication of the extent of vibrational population. The vibrational temperature is calculated from the population of the first asymmetric mode level of CO$_2$, since the contribution of the other levels to the total vibrational energy is typically low. It is obtained by assuming a Boltzmann distribution for the vibrational population, i.e.:

$$T_v = \frac{E_1}{ln(n_1/n_0)} \tag{V.14}$$

Where E_1 is the energy of the first asymmetric mode level (0.29 eV), n_1 is its density and n_0 is the ground state density.

V.3.1 Reduction of the chemistry set

This section discusses the effects of the first chemistry reduction performed on the set developed by Kozák and Bogaerts[56;57] and assesses its validity. Table V.4 shows the predicted CO$_2$ conversion for different pressures. It is clear that the consequences of the reduction of the chemistry set on the calculated CO$_2$ conversion at these conditions are small, especially considering the magnitude of the chemistry reduction, i.e., from 126 species to 36 or 39 depending on the pressure. The chemistry set could indeed be reduced to 36 species at a pressure of 100 mbar and below, while at 200 mbar and above, 39 species have to be considered. At these higher pressures, the 3 vibrational levels of O$_2$ are necessary in the reduced chemistry set to keep the difference in calculated CO$_2$ conversion below 5 %. Their role is found to be less important at 100 mbar and below. Keeping in mind the balance between accuracy and computational load, we judged it unnecessary to keep the 3 vibrational levels of O$_2$ at pressures of 100 mbar and below. At higher pressure, their presence enhances the recombination reaction of CO in CO$_2$ (i.e. N4 in table A.5), due to the lower activation energy of this reaction for a vibrationally excited state of O$_2$, thus affecting the calculated CO$_2$ conversion. This explains why the difference in predicted CO$_2$ conversion between the full set and the reduced set is larger at 100 mbar than at 200 mbar: the vibrational levels of O$_2$ still have a minor effect on the CO$_2$ conversion at 100 mbar and removing them slightly increases the error.

Table V.4: Comparison of the CO_2 conversion predicted by the full and the reduced chemistry sets at five different pressures and a SEI of 2.3 eV/molec

CO_2 conversion	Reduced set	Full set	Relative difference
20 mbar	1.01 %	1.0 %	1.1 %
100 mbar	15.3 %	14.9 %	2.6 %
200 mbar	26.8 %	26.6 %	0.7 %
500 mbar	11.7 %	11.5 %	1.2 %
1 bar	5.01 %	4.96 %	1.2 %

Figure V.2 shows the comparison of the VDF predicted by the full and the reduced chemistry sets, both in the plasma and in the afterglow at 20 mbar, 100 mbar and 1 bar. At 20 mbar, the reduced set predicts a slightly underestimated density in the plasma for the last three vibrational levels. At 1 bar, the reduced set slightly overestimates the last two levels in the plasma. However, the VDFs determined by the reduced set are overall in very good agreement with the VDFs predicted by the full set, in the entire range of pressures investigated, both in the plasma and in the afterglow. As the reduced chemistry set does not account for the CO vibrational levels, in contrast to the full chemistry set, which considers 63 CO vibrational levels, this shows that, under these conditions, the contribution of the CO vibrational level population to the CO_2 VDF is negligible. Not taking them into account only has a minor influence. A more detailed description of the VDF will be given in the next section.

In the full model, various positive ions were included, but the role of the individual ions in the actual CO_2 conversion is minor, both directly and indirectly (through determining the electron density). Therefore, in the reduced model, only 1 type of positive ion is kept, i.e., CO_2^+. Figure V.3 shows a comparison between the full model and the reduced model for the total positive ion density, the densities of the two major negative ions, i.e., CO_3^- and O^-, and the electron density, at 20 mbar, 100 mbar and 1 bar.

At 20 mbar, the model using the full set predicts a fast rise of the electron density at the beginning of the plasma ($z = 10$ cm). The electron density keeps rising until $z = 12$ cm and then drops. In the afterglow ($z > 15$ cm), the electron density drops slowly and has values in the order of 10^{15} m^{-3}. The model with the reduced chemistry set predicts the same rise, but a faster drop in the electron density, so that the maximum electron density is lower, and reached at an earlier position, than in case of the full set. This will be explained below.

At 100 mbar and 1 bar, the model with the full set also predicts a fast rise of the electron density at the beginning of the plasma ($z = 10$ cm), but the maximum is reached at a somewhat later position ($z = 12.5$ cm), and the density initially also drops

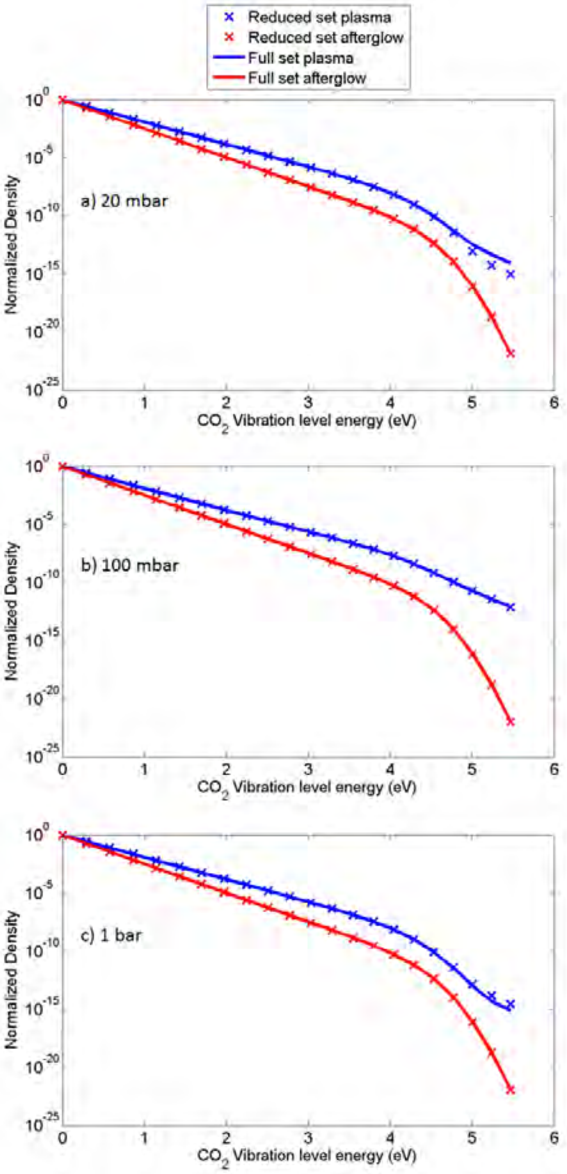

Figure V.2: Comparison of the VDFs predicted in the plasma (blue) at z = 12.5 cm and in the afterglow (red) at z = 22.5 cm, by the full chemistry set (lines) and the reduced set (crosses), at p=20 mbar, 100 mbar and 1 bar and a SEI of 2.3 eV/molec more slowly than at 20 mbar, but at the end of the plasma it drops rapidly. In the afterglow (z $>$ 15 cm), the electron density drops slowly at 100 mbar, and has values in the order of 10^{14} m^{-3}, while at 1 bar, the electron density drops faster and quickly reaches low values, in the order of 10^{13} m^{-3}. The model with the reduced set predicts the same electron density profiles at both 100 mbar and 1 bar.

As observed in figure V.3 (a), the agreement between full set and reduced set is not so good at 20 mbar. This is attributed to the removal of several ions in the reduced set, which has a considerable effect on the electron density at this pressure. However, the overall CO_2 conversion calculated by the reduced and full set is still in good agreement at 20 mbar. This can be explained by the importance of thermal dissociation when using the gas temperature profile plotted in figure V.1, making the electron excitation of the vibrational levels less important at this pressure. At 100 mbar and 1 bar, the agreement for the electron density is much better.

At 20 mbar, the total positive ion density is much lower with the reduced set than with the full set from z = 11.5 cm. Consequently, the electron density and also the negative ion densities are lower. At 100 mbar, the agreement between the different ion densities is almost perfect. The removal of several ions thus has only very little effect on the charged particles kinetics at this pressure. At 1 bar, from z = 10.5 cm to z = 12.5 cm, the reduced set underestimates the density of both positive and negative ions. However, the difference between them, giving the electron density, remains very close to what is predicted by the full set. In the rest of the simulation region, a very good agreement between the different charged particle densities is reached. Most of the applications of CO_2 conversion using microwave plasma use pressures of 100 mbar or more[62]. Moreover, the ions have very little direct effect on the CO_2 conversion and are therefore only important for the determination of the electron density. That is why we did not judge it necessary to keep more ions in the reduced chemistry set.

Figure V.4 illustrates the axial density profiles of CO, CO_2, O and O_2 calculated by the full and the reduced sets at p = 20 mbar, 100 mbar and 1bar. At 20 mbar and 100 mbar, since the conversion remains rather low (less than 20 %, see table V.4), the CO_2 profile follows more or less the inverse of the gas temperature profile. Indeed, the model ensures that the densities comply with the ideal gas law. At 1 bar, we see an additional drop in the CO_2 density around z = 13 cm, which is explained by the large local conversion of CO_2 at this position. However, due to the recombination of CO with O and O_2, the density of CO_2 increases again later, explaining the rather low overall conversion.

In all three cases, the CO density greatly increases in the plasma, as a result of the CO_2 conversion. At 100 mbar, it stays constant in the afterglow (i.e. z $>$ 15 cm), while it keeps on increasing slightly at 20 mbar due to the thermal conversion of CO_2 and it

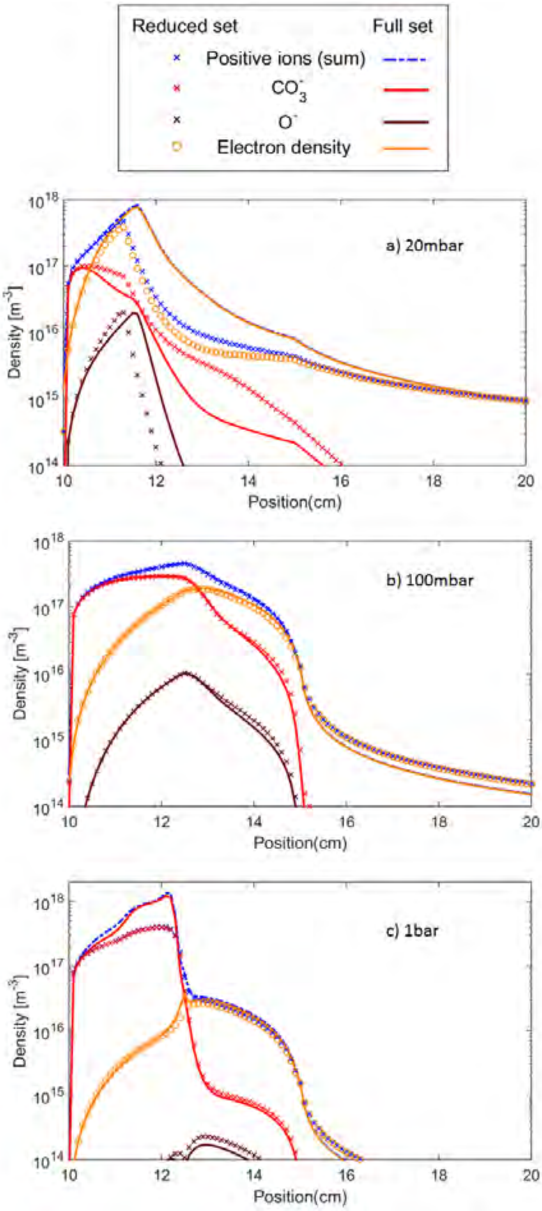

Figure V.3: Comparison of the axial density profiles of the main charged species predicted by the full set (lines) and the reduced set (symbols) at p=20 mbar, 100 mbar and 1 bar and a SEI of 2.3 eV/molec decreases at 1 bar due to the recombination of CO with O, mentioned above.

The O and O_2 density profiles follow more or less the CO density profiles at all pressures, since they all originate from the CO_2 dissociation. Nevertheless, the O density is found to be higher than the O_2 density in the plasma at 20 mbar, while it is only higher than O_2 in the first half of the plasma at 100 mbar and between z = 10 cm and z = 11 cm at 1 bar.

Comparing the results given by the model using the full set and the reduced set, we can see that the agreement in the predicted density profiles is very good at 100 mbar and at 1 bar. At 20 mbar, the agreement is also reasonably good at the end of the plasma and in the afterglow, but the model with the reduced set somewhat overestimates the O_2 density and underestimates the O density in the plasma itself. However, these densities are several orders of magnitude lower than the CO_2 density, and this deviation does not really affect the CO_2 conversion, which is the most important outcome of the model.

At 100 mbar, a small underestimation of the O density using the reduced set is found in the afterglow. This can be explained by the fact that the vibrational levels of O_2 are not included at this pressure, leading to a lower dissociation rate of O_2. As this has no major influence on the CO_2 conversion, it was decided to leave these levels out at this pressure, to reduce the chemistry set as much as possible, in order to enhance its compatibility with more-dimensional models.

From these results, we can conclude that this first chemistry reduction has very little effect on the model predictions, certainly at 100 mbar and above, i.e. at the conditions studied in this work.

V.3.2 Influence of the lumped-level strategy on the VDF and CO_2 conversion at fixed gas temperature

As previously mentioned, the results shown in this part are obtained using the temperature profile described in figure V.1 and the reduced chemistry set. The model describing each vibrational level separately will be referred to as the "individual-levels" model. The predictions of the 3 different lumped models listed in table V.3 as well as the model assuming a thermal vibrational distribution, called the "thermal distribution model", are compared to those of the individual-levels model. The accuracy of the level lumping method is tested in the entire pressure range between 20 mbar and 1 bar.

Figure V.5 (left panel) shows the VDFs obtained by the different models at the beginning of the plasma (z = 10.2 cm), where the gas temperature is low (around 500K) and there is strong non-equilibrium, for pressures of 20 mbar (a), 100 mbar (b) and 1 bar (c). The shape of the VDF predicted by the individual-levels model is very similar to our previous results obtained with the full chemistry set[56;57] .

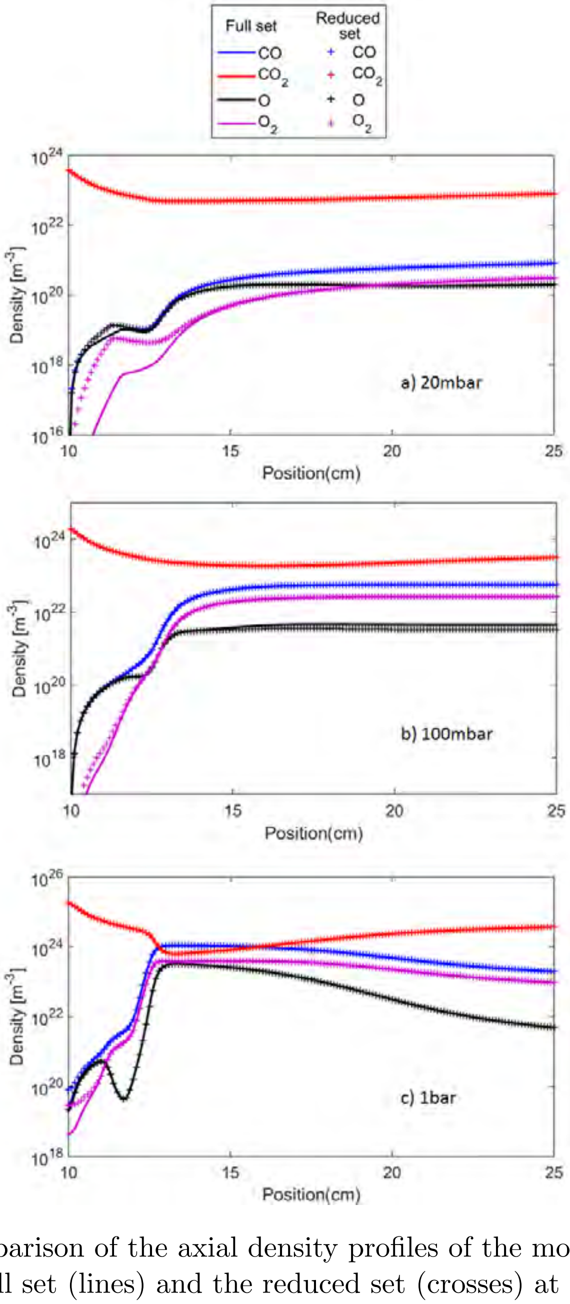

Figure V.4: Comparison of the axial density profiles of the most important species predicted by the full set (lines) and the reduced set (crosses) at p=20 mbar, 100 mbar and 1 bar and a SEI of 2.3 eV/molec

In a Boltzmann energy distribution, the vibrational temperature is given by the slope of the VDF (on a logarithmic scale). When the VDF becomes more complex (i.e., not a straight line on a logarithmic scale), it is still possible to define several vibrational temperatures using the different slopes, which correspond to different groups within the vibrational level population. We can clearly identify three groups in the VDF calculated by the individual-levels model at the three pressures shown here. The first vibrational levels [v_1 - v_3] appear to be in close-to thermal equilibrium, with a vibrational temperature of about 580 K and 510 K, at 100 mbar and 1 bar, respectively. At 20 mbar, the vibrational temperature of the first levels is slightly higher, reaching about 840 K. A second part of the VDF [v_4 - v_{17}] is in non-equilibrium with vibrational temperatures several times higher than the gas temperature, i.e. from 5900 K to 6200 K. Finally, the last few levels [v_{18} - v_{21}] are overpopulated compared to a thermal VDF but the slope indicates that the vibrational temperature is here again close to the gas translational temperature, i.e. about 470 K when considering the last two levels. This typical shape in 3 parts with different vibrational temperatures in the plasma motivates our choice of a 3-groups model, described by 3 different temperatures.

To understand the advantage of such a model, we compare it with two other lumped models, using 1 and 2 groups (see table V.3), as well as a model yielding a thermal distribution. It should be noted that each extra group adds two extra equations to solve: one for the total number density of that group and one for the mean vibrational energy of that group, representing the inner-distribution of the levels within each group. Therefore, there is a balance between accuracy of the model predictions and computational cost. This is the reason why we have not tested models with 4 or more groups, as their advantage in terms of computational cost compared to the individual-levels model would be limited.

It is clear from the left panel of figure V.5 that the VDFs predicted by the 1-group model and the thermal distribution fail to reproduce the typical shape of the VDF in the beginning of the plasma and they result in a strong under-estimation of the population of the higher vibrational levels [v_5 - v_{21}]. The 2-groups model is able to reproduce the slope in the middle part of the VDF and thus it can be considered in reasonable agreement with the individual-levels model. However, the levels [v_{18} - v_{21}] are overestimated, as the last part of the VDF is not described by an extra group.

Finally, the VDF predicted by the 3-groups model yields quite good agreement with the individual-levels model, as it can reproduce the 3 parts of the VDF described above. A small deviation in the population of the highly excited vibrational levels is, however, still observed.

The right panel of figure V.5 shows the VDFs obtained at the end of the plasma (i.e. $z = 14$ cm), where the gas temperature is about 2900 K (see figure V.1 above) at

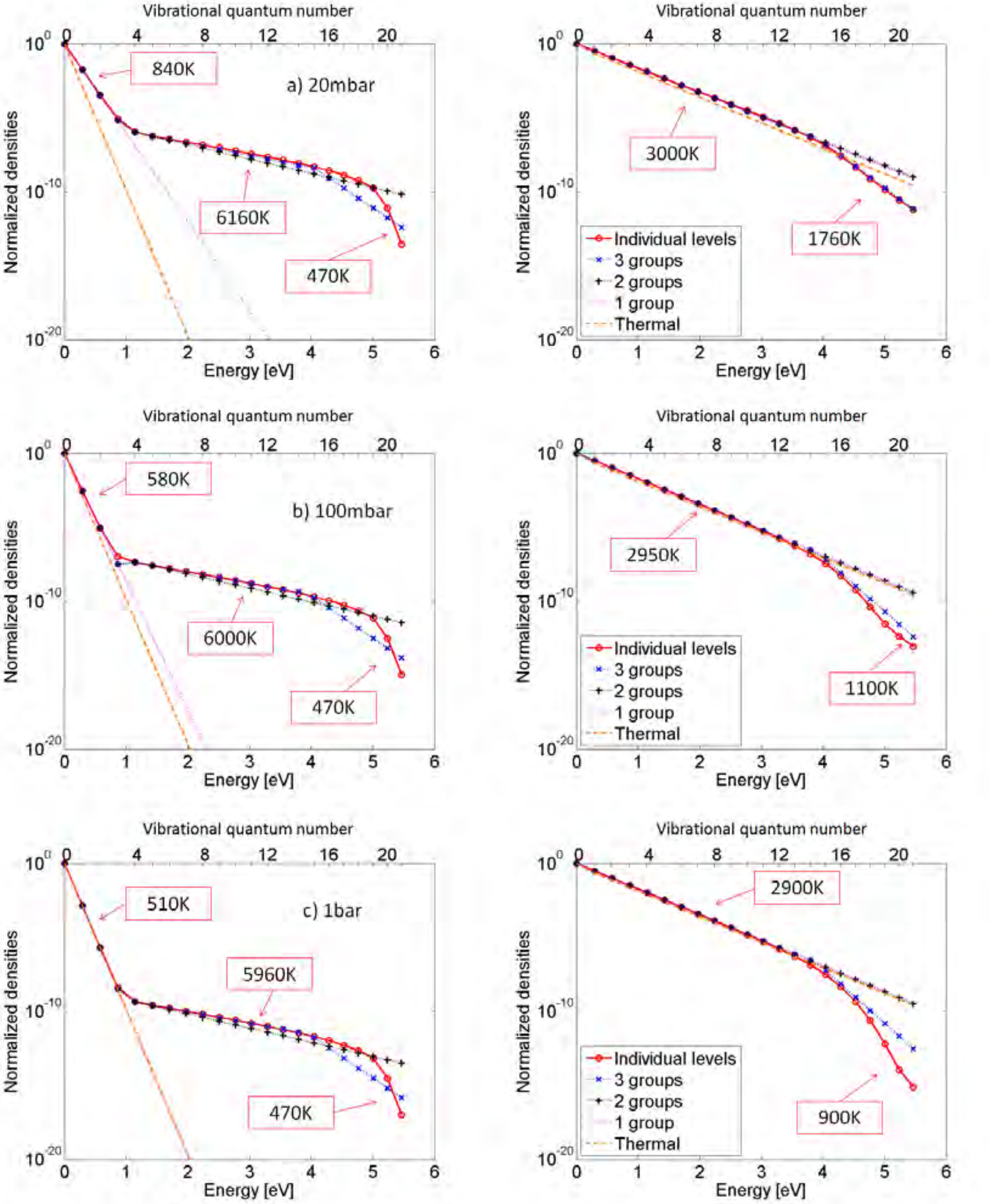

Figure V.5: Non-equilibrium VDF in the beginning of the plasma (left) at z=10.2 cm, and close-to-equilibrium VDF at the end of the plasma (right) at z = 14 cm, at 3 different pressures and a SEI of 2.3eV/molec. The vibrational temperatures corresponding to the different slopes of the VDF calculated with the individual-levels model are indicated. Comparison is made with the VDFs predicted by the different group models and the thermal distribution model.

the same pressures. The individual-levels model predicts that the levels [v_1 - v_{14}] can be described with one slope only, with a vibrational temperature close to the gas temperature. The levels [v_{15} - v_{21}] are underpopulated compared to a thermal distribution, which can be explained by the high dissociation rate of the highly excited vibrational CO_2 levels. Indeed, the CO_2 dissociation in a MW plasma mainly proceeds by vibrational excitation to the lower levels, followed by VV relaxation, gradually populating the higher vibrational levels (so-called vibrational pumping or ladder climbing), and the latter will be subject to the dissociation[62].

Looking at the definition of the groups in Table V.3 above, it is clear that the (one) group of the 1-group model, as well as both groups of the 2-groups model and the first two groups of the 3-groups model, adopt a vibrational temperature close to the gas temperature. Therefore, all the group models (1, 2 and 3-groups) manage to accurately reproduce the first thermal part of the VDF. The same applies to the model with the thermal distribution, which is quite logical. However, only the 3-groups model is able to reproduce rather accurately the last part of the VDF, as it considers a separate group for these last levels.

Note that it looks like the VDFs predicted by the 2-groups model and the 3-groups model exhibit only 1 and 2 slopes, respectively, but that is because both groups in the 2-groups model and the first two groups in the 3-groups model yield the same vibrational temperature, so their slopes coincide.

To evaluate whether the VDFs can be reproduced by the well-known Treanor distribution[123], we compare in Figure V.6 the VDFs calculated by the individual-levels model in the beginning of the plasma (i.e. z = 10.2 cm) and several Treanor distributions, using the gas temperature $T_g = 500$ K and several vibrational temperatures, as indicated in the legend. It is clear that the Treanor distributions all fail to reproduce the VDFs predicted by the model for any vibrational temperature and at any pressure. Indeed, only a vibrational temperature equal to the vibrational temperature of the first group can give a distribution reproducing accurately the first part of the VDF. However, the tail of the VDF is then overestimated. On the other hand, a larger vibrational temperature gives an overestimation of the first levels and can, in the more extreme cases, give an overestimation of the whole VDF (except the ground level). From these results, it seems that the Treanor distribution is a too rough approximation of the shape of the VDF, which stresses the need of using several groups with different vibrational temperatures, to accurately describe the actual VDF. More discussion on the Treanor distribution is shown in chapter VI.

Table V.5 shows the calculated CO_2 conversion of the different models at 5 different pressures (20, 100, 200 and 500 mbar, and 1 bar). The values given by the individual-levels model are in good agreement with the values given above, in table V.4. The

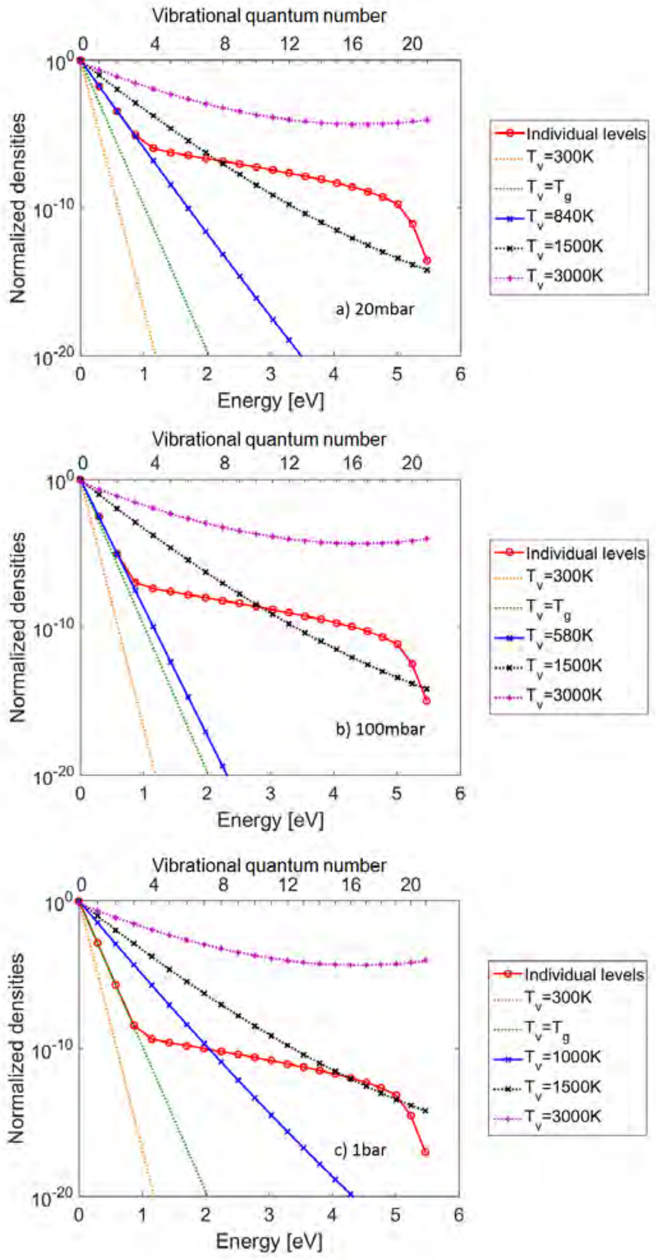

Figure V.6: Non-equilibrium VDF in the beginning of the plasma at z = 10.2 cm at 3 different pressures and a SEI of 2.3eV/molec. Comparison is made between the VDF predicted by the individual-levels model and several Treanor distributions using different vibrational temperatures.

Table V.5: Comparison of the CO_2 conversion predicted by the individual-levels model and the different lumped-levels models and the thermal distribution model at five different pressures and a SEI of 2.3 eV/molec, using the temperature profile of figure V.1. The relative errors given by the various lumped-levels models and the thermal distribution model, compared to the individual-levels model, are indicated between brackets, in %

	CO_2 conversion (%) and [Relative difference]				
Pressure	Individual-levels	3-groups	2-groups	1-group	Thermal
20 mbar	1.15	1.14 [-0.7%]	1.56 [+36%]	1.34 [+17%]	0.95 [-17%]
100 mbar	15.2	15.7 [+3%]	18.1 [+19%]	18.0 [+19%]	16.6 [+9%]
200 mbar	25.1	25.3 [+0.8%]	26.4 [+5.3%]	27.0 [+7.5%]	25.9 [+3.1%]
500 mbar	10.8	10.8 [+0.3%]	10.9 [+1.2%]	11.0 [+1.5%]	10.9 [+0.5%]
1 bar	4.57	4.58 [+0.2%]	4.63 [+1%]	4.76 [+4%]	4.58 [+0.2%]

small differences can be explained by the use of two different codes (i.e., ZDPlaskin for the chemistry reduction and Comsol Multiphysics for the level-lumping method) and the fact that the first code self-consistently solves the EEDF, while the second code uses an external Boltzmann solver, as explained in section V.2.4 above. As discussed in[50;51;53], in some cases, the effect of the EEDF on the CO_2 dissociation can be rather large and an a-priori calculation of the rate coefficients using an external Boltzmann solver can be a strong approximation when the EEDF greatly differs from a Boltzmann EEDF.

In all the cases tested here, the CO_2 conversion calculated with the 3-groups model is in reasonable agreement with the results of the individual-levels model. The 1 and 2-groups models and the model assuming a thermal distribution are not in good agreement with the individual-levels model for the pressures of 20 and 100 mbar. At 200 and 500 mbar, the agreement gradually becomes better, and at 1 bar, all the models are in quite good agreement with the individual-levels model. Indeed, at this pressure, the plasma is more or less thermal, and the CO_2 conversion mainly takes place at the end of the plasma, where the VDF approaches a simple Boltzmann distribution based on the gas temperature, at least up to level v_{14} (see right panel of figure 4(c)).

In the different models presented in this chapter, most of the CO_2 conversion is attributed to reactions N1, N2 and N5 (see table A.5). For pressures up to 200 mbar, these reactions mainly occur from the highly excited vibrational levels, which are easily populated by electron impact excitation and VV transfer. However, for the higher pressures, the electron temperature is slightly lower, and the electrons mainly populate the lowest vibrational levels, at least in the region where most CO_2 conversion takes place (i.e., at the end of the plasma; cf. the right panel of figure V.5c). Thus, for pressures above 200 mbar, the above-mentioned heavy-particle reactions mainly responsible for CO_2 dissociation, mostly occur from the CO_2 ground state, the symmetric mode vibrational levels and the first few asymmetric mode vibrational levels. Therefore, although only the 3-groups model is able to reproduce the VDF obtained by the individual-levels model, including the tail, it appears that at these conditions, the VDFs predicted by the other lumped-levels models , as well as by the thermal distribution model, are close enough to the real VDF to obtain a reasonable value for the CO_2 conversion, because the tail of the VDF plays a minor role.

It should be noted that the 2-groups model appears to give the worst agreement in CO_2 conversion at the lowest pressures, despite the fact that it better reproduces the VDF in the beginning of the plasma (cf. figure V.5; left panel) compared to the 1-group models and the model assuming a thermal distribution. This may seem counter-intuitive. However, it can be explained as follows. At all the conditions investigated, the 2-groups model tends to systematically over-estimate the VDF at the higher vibrational levels (see e.g. figure V.5 above). This results in an overestimation of the CO_2 conversion, because of the major role of the highest CO_2 vibrational levels in the CO_2 dissociation at low pressure (cf. above). On the other hand, the 1-group model and the model assuming a thermal distribution underestimate the VDF in the non-equilibrium part and overestimate it in the thermal part of the discharge (see figure V.5: left and right panel, respectively). These two effects tend to compensate each other for predicting the overall CO_2 conversion, but the agreement can therefore not be considered better than with the 2-groups model.

For the same reason, the thermal model appears to give somewhat better results than the 1-group model: while the differences in the predicted VDFs are barely visible on the log-scale in figure V.5, the vibrational temperature predicted by the 1-group model is systematically higher than the gas temperature. Therefore, the 1-group model predicts asymmetric mode vibrational level populations that are slightly higher than the thermal model, explaining why the thermal model predicts a conversion slightly lower than the 1-group model. Again, the agreement given by the thermal model can therefore not be considered better than with the 1-group model.

V.3.3 Influence of the lumped-level strategy on the various plasma characteristics and CO_2 conversion in a self-consistent calculation

In this section, we assess the validity of the lumped-levels models, by comparing the calculated gas temperature, electron density, electron temperature and VDF in the plasma, as well as the obtained CO_2 conversion, with the results of the individual-levels model. Furthermore, we also compare to the model assuming a thermal distribution and a model not considering the asymmetric mode vibrational excitation (i.e. the CO_2v_i levels) at all. For this assessment, we self-consistently calculate the gas translational temperature T_g using equation (II.29).

V.3.3.1 Effect on the gas temperature profile

Figure V.7 (left panels) shows the axial profile of the gas temperature, calculated by the different models, at pressures of 20 mbar, 100 mbar and 1 bar. At 20 mbar and 100 mbar, the individual-levels model predicts a peak in the gas temperature profile of T_g = 3280 K and T_g = 2920 K at about z = 14.5 cm and z = 13.5 cm, respectively. The fact that the gas temperature is slightly lower at higher pressure is counter-intuitive, but can be explained from the relative importance of various (exothermic and endothermic) heavy particle reactions, as outlined below. Subsequently, the gas temperature starts to drop slowly, indicating that part of the translational energy goes to the vibrationally excited levels. At 1 bar, the gas temperature increases from the beginning of the plasma to approximately z = 13 cm and then forms a plateau at T_g = 2420 K. This shape, as well as the lower gas temperature at this higher pressure, can be explained as follows.

Figure V.7 (right panels) shows the heat released (positive value) or absorbed (negative value) by the different reactions, as calculated by the individual-levels model, at pressures of 20 mbar, 100 mbar and 1 bar.

In each case, VT relaxation is the main source of translation energy for the heavy particles, and thus the main reason for gas heating. At 20 and 100 mbar, our calculations reveal that this is the case from the beginning of the plasma to z = 14 cm. At this stage, the dissociation of CO_2 by heavy particle impact (Reaction N1 in table A.5) starts playing a more important role and explains why the gas temperature drops, as this reaction is endothermic. On the other hand, at 1bar, VT relaxation is only the major source of translational energy for the heavy particles (and thus of gas heating) until z = 13 cm. At this position, reaction N1 starts counterbalancing the effect of VT relaxation, explaining why the temperature stops increasing. However, from z = 13.5 cm, the exothermic recombination reactions (N3, N4 and N16 in table A.5) become non-negligible. The VT energy exchanges eventually give a negative contribution to the gas heating, as the tail of the VDF is underpopulated. Thus, the VT relaxation and the various heavy particle endothermic and exothermic reactions balance each other and the variation of gas temperature becomes very small. This explains why the gas temperature at 1 bar becomes constant from z = 13 cm to the end of the simulation region.

The 1-, 2- and 3-groups models almost perfectly manage to reproduce this behavior, although a slight deviation is seen for the 1- and 2-groups models at 20 mbar.

The model without vibrational excitation (see green curve in figure V.7) shows a slower rise of temperature, followed by a plateau at $T_g = 1280$ K, $T_g = 1780$ K and $T_g = 1930$ K, for p = 20 mbar, p = 100 mbar and p = 1 bar, respectively, indicating that the gas temperature stays constant in the post-plasma region. Since the asymmetric mode vibrational excitation is not taken into account in this model, the main source for the gas temperature is VT relaxation from the 4 symmetric mode levels taken into account. Moreover, the reactions mentioned before (i.e. N1, N3, N4 and N16 in table A.5), have a negligible contribution to the gas temperature in this case. Indeed, N1 can only occur from the ground state of CO_2 in this model, and thus it is of minor importance because of the high activation energy of this reaction (see exponential term in the rate coefficient). Furthermore, as the CO_2 dissociation is not very efficient without asymmetric mode vibrational excitation, yielding only a minor CO_2 conversion of less than 2% (see table V.6 below), the CO and O_2 densities remain small in the whole simulation domain, and the exothermic reactions N3, N4 and N16 play a negligible role.

A similar trend is predicted by the model assuming a thermal distribution, but the plateau is at a much lower temperature of $T_g = 590$ K and $T_g = 640$ K, for p = 20 mbar and p = 100 mbar, respectively. At p = 1 bar, this model predicts a maximum gas temperature of only 560 K, followed by a slow drop. The fact that this model cannot reproduce the gas temperature calculated by the individual-levels model can be explained by the influence of VT energy exchanges on the calculation of the gas temperature. Indeed, the 1-, 2- and 3-group(s) models solve for the density of the vibrational levels as well as the mean energy contained in the asymmetric mode vibrational excitation (i.e., by solving the equations for the total density and the mean energy of each group, which gives the slope of the VDF and thus the inner-distribution). Therefore, they guarantee that the total energy is conserved and they are able to accurately reproduce the gas temperature. The thermal distribution model, however, simply assumes that the population of the asymmetric mode vibrational levels is in thermal equilibrium with the gas temperature. As seen in figure V.5 above, this assumption is generally not valid for a CO_2 microwave plasma at the conditions investigated. The loss terms for the gas temperature and electron energy due to the energy transfer towards the vibrational levels are still present but they do not give rise to a larger vibrational energy. Therefore, the thermal distribution model does not guarantee conservation of energy, which results here in a loss of energy, explaining the lower gas temperature.

The model not considering the vibrational excitation obviously also does not account for the VT relaxation, and thus, this leads here to a lower gas temperature. On the other hand, it still guarantees energy conservation, so the gas temperature is still in somewhat better agreement with the individual-levels model, compared to the thermal distribution model.

These results show the importance of a correct description of the vibrational energy in a self-consistent model. Thus, we may conclude that the thermal distribution model and the model not taking asymmetric mode vibrational excitation into account cannot predict the correct gas temperature in a MW plasma. The 1-, 2- and 3-group(s) models, on the other hand, can well reproduce the gas temperature calculated by the individual-levels model. Nevertheless, it should be kept in mind that the CO_2 conversion is not well reproduced by the 1- and 2- group(s) models (see section V.3.2 and also below).

V.3.3.2 Effect on the electron density

Figure V.8 (left panels) shows the axial profiles of electron density for a pressure of 20 mbar, 100 mbar and 1 bar. The same behavior was also observed at the other pressures investigated. The electron density calculated by the individual-levels model shows a quasi-triangular profile with maxima of 7×10^{17} m^{-3}, 1.7×10^{17} m^{-3}, and 2.5×10^{16} m^{-3}, at 20 mbar, 100 mbar and 1 bar, respectively. A drop in electron density at rising pressure seems counter-intuitive, but can be explained because the length of the plasma (L in figure V.1) and the power deposition were kept constant in all the simulations. Thus, at constant power density, the electron temperature will be somewhat higher at lower pressure (see below), as the electrons lose less energy by collisions with the gas molecules. This higher electron temperature gives rise to more electron impact ionization, explaining the higher electron density at lower pressure. In reality, we might expect that the plasma length will decrease with rising pressure, so the power would be focused in a smaller volume at higher pressure, giving rise to a higher electron density. Radial contraction of the plasma at high pressure is also expected. However, this behavior is difficult to reproduce with a 0D model. Note, however, that the different electron attachment reactions also play a larger role at atmospheric pressure, reducing the electron density.

The fact that the electron density profile at 1 bar does not follow exactly the power-deposition profile, but keeps on rising until about z = 13.3 cm, is due to the presence of O_2^- and CO_3^- ions in relatively large amounts in the plasma. They keep on providing electrons, mostly through reaction (I38) followed by reaction (I58) (see table A.3).

This quasi-triangular profile is well-reproduced by the 1-, 2- and 3-group(s) models, both in shape and absolute value. On the other hand, the thermal distribution model and the model without asymmetric mode vibrational excitation are able to reproduce the shape of the electron density, which is mostly determined by the shape of the deposited power (see figure V.1 above), but they predict clearly different val-

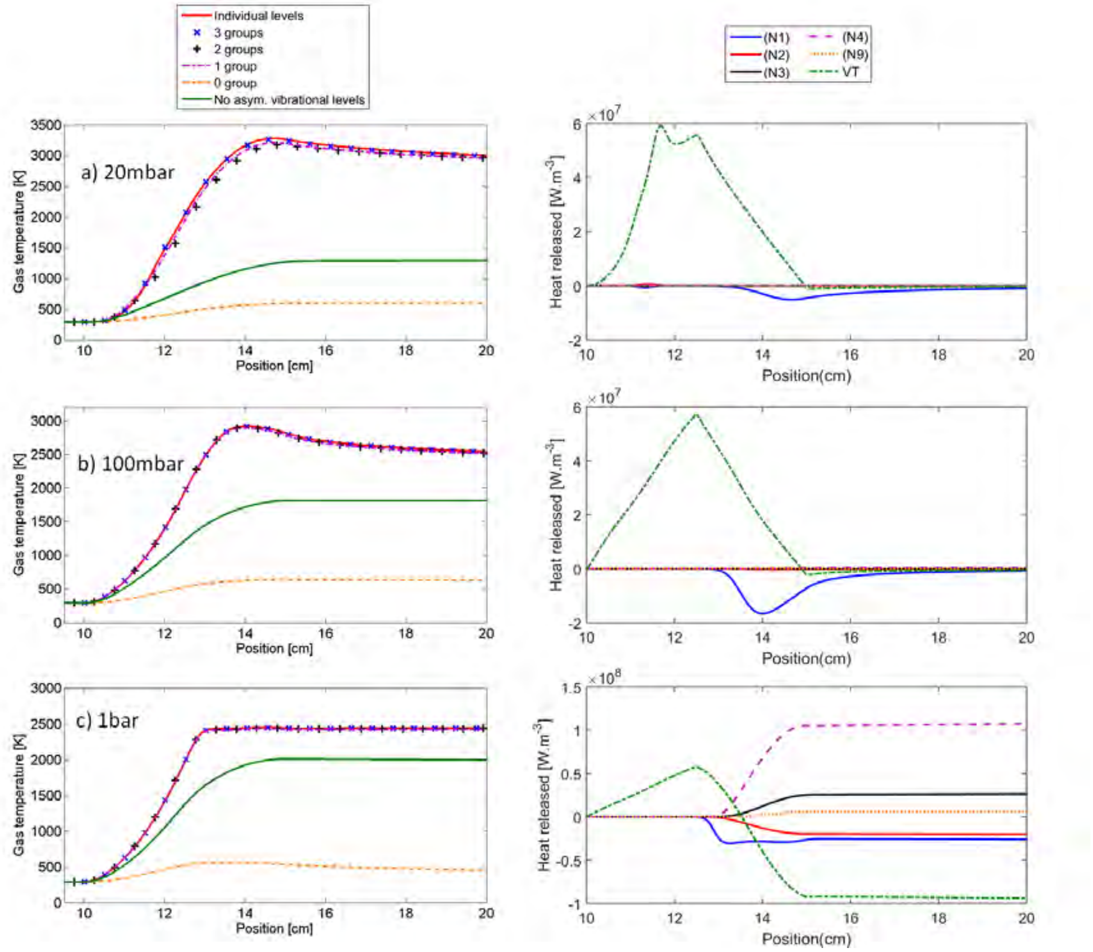

Figure V.7: Left panels: Axial profile of gas temperature, calculated by the different models (see legend) at three different pressures and a SEI of 2.3 eV/molec. Right panels: Heat released or absorbed by the most important reactions, calculated by the individual-levels model.

ues. Furthermore, at 1 bar, the maxima of electron density predicted by the thermal distribution model and the model without asymmetric mode vibrational excitation are shifted to the center of the plasma.

The electron density calculated by the thermal distribution model is a factor 3 - 4 too low at all pressures investigated, while the model without asymmetric mode vibrational excitation predicts an electron density which is approximately a factor 2, 3 and 4 too high, at 20 mbar, 100 mbar and 1 bar, respectively. As discussed above, the thermal distribution model does not guarantee conservation of energy, resulting in a loss of the total energy. Less energy is then available for the different ionization reactions, resulting in a lower electron density. On the other hand, the model which does not consider asymmetric mode vibrational excitation results in a somewhat larger electron energy density (or temperature; see below). Indeed, vibrational excitation is one of the main energy losses for the electrons due to its much lower energy threshold than electronic excitation and ionization processes. Since vibrational excitation to the asymmetric mode vibrational levels is not included in this model, this results in a somewhat larger electron energy density, thus yielding more electron impact ionization, and thus a larger electron density.

V.3.3.3 Effect on the electron temperature

The effect on the electron temperature can be seen in the right panel of figure V.8. The individual-levels model predicts an electron temperature of 0.8 eV in the beginning of the plasma (z = 10 cm) at all pressures investigated. It increases to 0.9 eV at 100 mbar and to 1.2 eV at 20 mbar, at around z = 13 cm, followed by a weak drop till z = 15 cm, which can be explained by the power deposition profile (see figure 1 above). At z = 15 cm, the power deposition stops, which results in a fast drop in the electron temperature. At p = 1 bar, the individual-levels model does not predict a rise in the electron temperature in the plasma, but values of T_e varying between 0.7 eV and 0.8 eV, followed again by a drop, which starts already at z > 12.5 cm. This is attributed to the fact that the electron density keeps on increasing even after the maximum power deposition density (i.e. at z = 12.5 cm) has been reached (see figure V.8 (c), left panel), leaving less energy to more electrons and thus reducing the electron temperature.

Again, the 1-, 2- and 3-group(s) models are more or less able to reproduce these calculated electron temperature profiles, although at 100 mbar and 1 bar, the 2-groups model predicts a somewhat lower electron temperature between z = 11 cm and z = 12 cm. On the other hand, the thermal distribution model and the model without asymmetric mode vibrational excitation fail to accurately reproduce the shape and absolute value of the electron temperature profiles at the different pressures investigated. How-

Table V.6: Comparison of the CO_2 conversion predicted by the individual-levels model, the different lumped levels models, the thermal distribution model and the model without asymmetric mode vibrational excitation, at five different pressures and a SEI of 2.3 eV/molec, using the self-consistent gas temperature calculation. The relative errors given by the lumped levels models, the thermal distribution model and the model without asymmetric mode vibrational excitation, as compared to the individual-levels model, are indicated between brackets, in %

	CO_2 conversion (%) and [Relative difference]					
Pressure	Individual-levels	3-groups	2-groups	1-group	Thermal	No CO_2v_i
20 mbar	14.4	9.99 [-30%]	23.4 [+63%]	13.8 [-4%]	0.1 [-99%]	1.55 [-89%]
100 mbar	16.5	16.5 [+0.3%]	17.9 [+8.5%]	16.8 [+2.3%]	0.07 [-99.6%]	1.5 [-91%]
200 mbar	15.7	15.9 [+0.3%]	17.0 [+8.5%]	16.1 [+2.3%]	0.06 [-99.6%]	1.1 [-93%]
500 mbar	17.6	17.5 [-0.5%]	18.4 [+4.6%]	18.9 [+7.3%]	0.06 [-99.7%]	1.0 [-94%]
1 bar	18.7	18.8 [+0.4%]	19.4 [+3.8%]	19.0 [+1.7%]	0.04 [-99.8%]	1.2 [-93%]

ever, the differences are smaller than for the gas temperature or the electron density. Indeed, in a microwave plasma, for a given pressure, the electron temperature tends to show little variation upon different conditions, as observed in Jimenez-Diaz *et al.*[132] and discussed more in detail in Schluter and Shivarova[125].

V.3.3.4 Effect on the CO_2 conversion

Table V.6 shows the CO_2 conversion predicted by the various models, as well as the relative differences with the individual-levels model. The results are clearly different from the comparison shown in table V.5. The reason is that the CO_2 conversion largely depends on the gas temperature, and the self-consistently calculated profiles (illustrated in figure V.7) differ to some extent from the temperature-profile shown in figure V.1, used to calculated the CO_2 conversion of table V.5. This strong temperature dependence of the CO_2 conversion stresses the importance of a correct temperature calculation in the model.

At 100 mbar, the CO_2 conversion predicted by both approaches is still in reasonable agreement, which is logical because the self-consistently calculated gas temperature profile (i.e., the second approach) is most similar to the profile assumed in the first approach (cf figure V.1 and figure V.7 b).

As is clear from table V.6, at a pressure between 100 mbar and 1 bar, excellent agreement is observed for the CO_2 conversions calculated by the individual-levels model and the 3-groups models. The agreement is worse for the 2-groups model, but again slightly better for the 1-group model (except at 500 mbar). This can again be explained by the fact that the 1-group model tends to underestimate the population of the highly excited levels in the non-thermal part of the plasma and to overestimate them in the

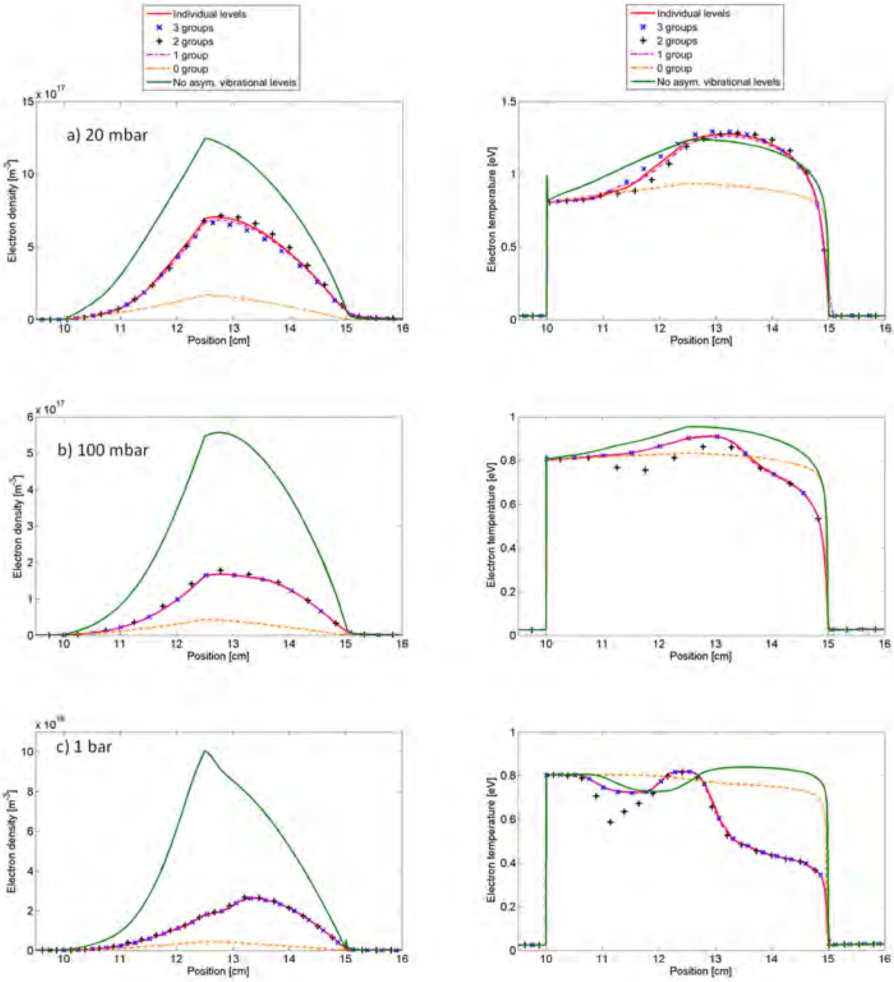

Figure V.8: Axial profile of electron density (left) and temperature (right) inside the plasma, calculated by the different models (see legend) at three different pressures and a SEI of 2.3 eV/molec.

close-to-thermal-equilibrium part (see section V.3.2 above and also next section), and these two effects compensate each other. The 2-groups model, on the other hand, tends to systematically over-estimate the population of the highly excited levels, resulting in a larger CO_2 conversion.

Due to the large differences in the calculated plasma characteristics (see previous sections) and the inaccurate or non-existent description of the vibrational energy contained in the asymmetric mode levels, the thermal distribution model and the model without asymmetric mode vibrational excitation are not able to reproduce the CO_2 conversion, predicted by the individual-levels model, at none of the pressures investigated. Indeed, the conversion predicted with these two models is far too low in each case, because they underestimate, or do not consider at all, the vibrational asymmetric mode levels. Furthermore, this also results in a lower gas temperature, as explained in section V.3.3.1 above (see also figure V.7 above). Therefore, they significantly underestimate both the conversion due to the ladder climbing effect mentioned above and the conversion due to purely thermal effects.

At 20 mbar, even the 3- and 2-groups models are not in good agreement with the individual-levels model, yielding an underestimation of the CO_2 conversion by 30% for the 3-groups model and an overestimation by 63% for the 2-groups model. The 1-group model appears to show a better agreement, with a CO_2 conversion underestimated by only 4%. However, this is again the result of the two competing effects, as explained below, and therefore, it does not mean at all that this model is more realistic. The reason why the 3- and 2-groups models do not yield a good agreement in the predicted CO_2 conversion at 20 mbar, in spite of the good agreement in calculated gas temperature, electron density and temperature, is because of the strong influence of the levels [v_{18}-v_{21}] on the CO_2 dissociation at this low pressure, and can be fully understood by looking at the VDFs calculated with the various models, as illustrated in the next section.

V.3.3.5 Effect on the VDFs

The left panel of figure V.9 shows the VDFs calculated by the different models in the plasma, at the axial position where the local CO_2 conversion reaches its maximum (i.e. $z = 11.5$ cm) at a pressure of 20 mbar. The VDFs calculated at 100 mbar and 1 bar will be presented below, but we first focus on the VDF at 20 mbar, to explain the discrepancy in the CO_2 conversion at this pressure.

The 3-groups model shows a somewhat better overall agreement with the individual-levels model than the 1- and 2-groups models. However, all the lumped-levels models underestimate the tail of the VDF, except for level v_{21}, which is overestimated by these models. The individual-levels model predicts that at this low pressure the dissociation of CO_2 from levels v_{18}, v_{19} and v_{20} directly contributes for more than 90% to the CO_2 dissociation at z = 11.5 cm. As these levels are underestimated by the 3-groups model, this explains the underestimation in the CO_2 conversion. The same effect also applies to the 1- and 2-groups models, but on the other hand, these models predict that the CO_2 dissociation from level v_{21} accounts for more than 90% of the total dissociation, since this level is overestimated by several orders of magnitude in these models. Moreover, although it is barely visible on a logarithmic scale, the density of the $CO_2[v_{21}]$ level is 1.6 times higher in the 2-groups model than in the 1-group model at this position, resulting in a larger overestimation of the CO_2 dissociation. In the 1-group model, the overestimation of the dissociation from level v_{21} coincidently compensates for the underestimation of the dissociation from levels v_{18}, v_{19} and v_{20}. In the 2-groups model, as the overestimation of the dissociation from v_{21} is stronger, it gives rise to a larger CO_2 dissociation. Therefore, the better agreement with the 1-group model is the result of two competing effects and it should be considered with caution, as it might not be so good at other conditions.

The right panel of figure V.9 illustrates the VDF at the end of the plasma (z = 14 cm), calculated by the different models. It is clear that the 3-groups model almost perfectly reproduces the VDF of the individual-levels model, while the 1-group and 2-groups models strongly overestimates the higher vibrational levels ($> v_{15}$) and the thermal distribution model strongly underestimates all levels.

To explain the better agreement in the CO_2 conversion calculated by the 3-groups model and the individual-levels model at the higher pressures, we illustrate in figure V.10 the VDFs at 100 mbar and at 1 bar, at an axial position of z = 10.2 cm, where the VDF is in strong non-equilibrium (left panels), and at an axial position of z = 14 cm, where most of the CO_2 conversion takes place at these conditions (right panels). As we have seen above in figure V.5, the VDF in the beginning of the plasma (left panels) is characterized by three different parts and the 3-groups model is the only model that can (more or less) reproduce this shape, although some underestimation of the tail of the VDFs is still visible.

Moreover, as is clear from the right panel of figure V.10 at z = 14 cm, the 3-groups model yields again the best agreement with the VDF predicted by the individual-levels model, although a small overestimation of the tail of the VDF is observed, especially at 1 bar.

Most of the conversion appears at the end of the plasma (around z = 14 cm) in this pressure range. As observed in section V.3.2, most of the CO_2 dissociation originates from the ground state, the symmetric mode vibrational levels and the first asymmetric mode vibrational levels. This explains why all the lumped-levels are able to predict a

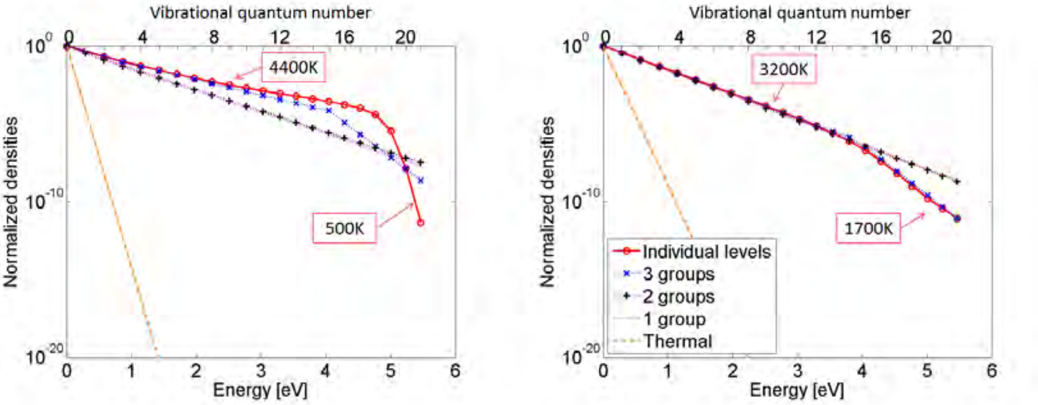

Figure V.9: Non-equilibrium VDF at the position in the plasma with local maximum CO$_2$ conversion, i.e. at z = 11.5 cm (left), and close-to-equilibrium VDF at the end of the plasma at z = 14 cm (right), for a pressure of 20 mbar and a SEI of 2.3eV/molec. The vibrational temperatures corresponding to the different slopes of the VDF calculated with the individual-levels model are also indicated. Comparison is made with the VDFs predicted by the different lumped-levels models and the thermal distribution model.

correct CO$_2$ conversion, despite their overestimation of the tail of the VDF. However, as the tail of the VDF still plays a (minor) role, the 3-groups model still gives the most accurate values for the CO$_2$ conversion (except at 20 mbar). It is interesting to note that because of the incorrect gas temperature calculated by the thermal distribution model, it is also not able to predict the shape of the VDF, even not the thermal parts. Therefore, when using a self-consistent gas temperature calculation, even in the case when CO$_2$ conversion also occurs in the close-to-thermal-equilibrium part of the discharge, the thermal distribution model cannot yield the right CO$_2$ conversion.

In certain conditions, especially at low pressure, the last levels of the VDF have a very strong influence on the CO$_2$ conversion as their vibrational energies are close to the dissociation energy. This shows that an accurate description of the tail of the VDF is crucial. In general, only the 3-groups model allows to (more or less) reproduce the tail of the VDF (except at the low pressure of 20 mbar around z = 11.5 cm; cf figure V.9 left panel). Hence we believe it is the only model that can predict the correct CO$_2$ conversion. A better agreement reached by a lower-group model, that is not able to reproduce the VDF, can therefore only be the result of two competing effects. At the low pressure of 20 mbar, in the middle of the plasma, even the 3-groups model seems to fail in reproducing the correct VDF, resulting in an underestimation of the CO$_2$ conversion.

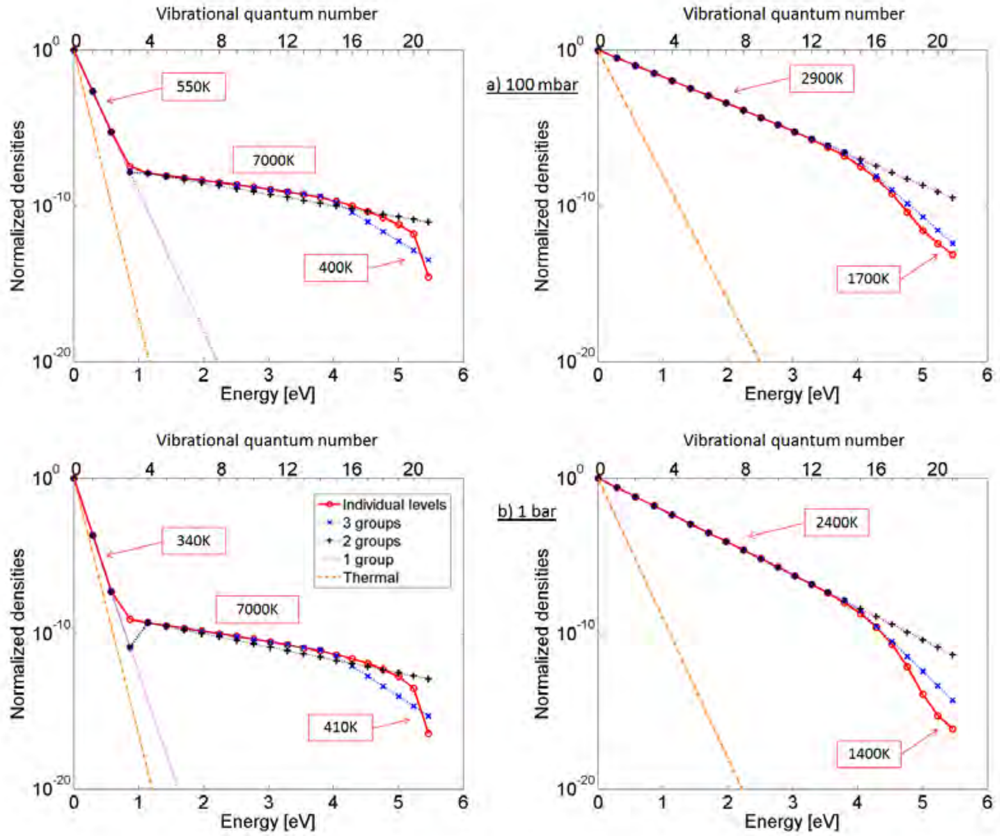

Figure V.10: Non-equilibrium VDF in the beginning of the plasma (left) at z = 10.2 cm, and close-to-equilibrium VDF at the end of the plasma (right) at z = 14 cm, at 100 mbar and 1 bar and a SEI of 2.3 eV/molec, computed using a self-consistent gas temperature calculation. The vibrational temperatures corresponding to the different slopes of the VDF calculated with the individual-levels model are also indicated. Comparison is made with the VDFs predicted by the different lumped-levels models and the thermal distribution model.

V.3.4 Range of validity of the level-lumping method

From the results above, it is clear that the level-lumping method, especially with 3 groups, is able to reproduce the results of a model solving for each vibrational level separately, at the conditions studied in this chapter. Only at 20 mbar, the agreement is not satisfactory, but this pressure is not so much of interest for CO_2 conversion applications. It is also clear from above that conservation of energy is a crucial point.

Counting for the number of equations to solve, only taking into account the chemical kinetics part of the model, the full chemistry set from Kozák and Bogaerts[56;57] requires to solve 126 equations while the reduced chemistry set requires to solve for 36 equations (at a pressure of 100 mbar and below), or 39 equations (at 200 mbar and above). A further computational load reduction is achieved by lumping the levels. Indeed, in this case, the 21 equations representing the 21 individual vibrational levels can be removed, yielding only 15 (or 18) equations, plus 2 equations for each of the lumped levels. In this way, a n-groups model requires to solve for $15 + 2n$ equations (or $18 + 2n$ at 200 mbar and above) for the chemical kinetics part.

In our 0D model, this computation time reduction caused by the level-lumping is not clearly visible, as the vibrational temperature can vary quite fast, counter-balancing the advantages of the reduction of the number of equations to solve. However, we expect the computational cost to significantly improve for a 1D, 2D or 3D model, as diffusion would smooth out the sharp peaks of the vibrational temperature seen in our 0D-model.

Despite the clear advantages of the level-lumping method, it should be stressed that it is not valid under all conditions that can exist in a CO_2 plasma.

Indeed, while studying the conditions presented above, we have also tested the validity of the method for more challenging conditions, to assess its range of applications. We noted that even the 3-groups model fails to accurately reproduce the VDF when the non-equilibrium part in the plasma is too strong, i.e. when the vibrational temperature is much larger than the gas-temperature. This effect was also apparent for the 20 mbar case above. Moreover, using several groups, it can happen that, at the junction between two groups, the model predicts $n_j < n_{j'}$ with $j < j'$, which is not a physical result. This is for example visible in figure V.10 (b) (left panel) for levels V_3 and V_4.

By analysing the equations of the lumped-levels model, we see that the contribution of the energy of each level to the mean group energy $\overline{E_{g_i}}$, defined by equation (V.9), depends on its population. If we now look at the ratio of the contribution β of two levels j < j' within one group i, we get:

$$\beta = \frac{E_j n_j}{E_{j'} n_{j'}} \simeq \frac{E_j}{E_{j'}} exp(\frac{E_{j'} - E_j}{k_B T_{v_i}}) \tag{V.15}$$

β exponentially increases when $E_{j'}$ increases for a given j. This means that the contribution of the highly excited levels of one group to the mean vibrational energy of that group is small, under usual conditions of vibrational temperature ($k_B T_{v_i} < 1$ eV). Changing the repartition of the levels between the different groups in a 3-groups model can help to describe more accurately the important parts of the VDF, as the population of the first levels of each group tends to be more accurately reproduced. Naturally, the optimal choice for this repartition (shown in table V.3) is case-dependent. However, at the conditions under study, which are common for MW plasmas used for CO_2 conversion, the level-lumping method works quite well. More specifically, using a 3-groups model, it is possible to reproduce the shape of the VDF and the predictions of the individual-levels model reasonably well. Even the 2-groups model and the 1-group model predict results in reasonable agreement with the results of the individual-levels model, in spite of the fact that the VDF is not properly reproduced, as they are still able to predict the mean energy contained in the asymmetric mode vibrational levels. However, as shown above, an accurate description of the tail of the VDF is also important for a correct prediction of the CO_2 conversion. As the last levels of the VDF have small populations in comparison with the first levels, it is necessary to describe them using a separate group.

Finally, this (n-groups) level-lumping model only requires to solve n extra energy conservation equations, to determine the vibrational temperatures of the n groups, and n continuity equations for the corresponding number densities, which can be added to a standard plasma fluid model. It is thus very easy to implement in an existing code, which is one of its main advantages.

V.4 Conclusion

In this chapter, a reduced chemistry set to model CO_2 non-equilibrium discharges, with special focus on the CO_2 vibrational levels, is presented and compared to the complete chemistry set previously developed by Kozák and Bogaerts[56;57]. Furthermore, a lumped-levels model is developed to avoid the need of solving equations for all individual CO_2 vibrational levels. The proposed chemistry reduction and level-lumping make this chemistry set compatible with the use in large-dimensional models (i.e. 1D, 2D and 3D) by drastically reducing the number of equations to solve, leading to a significant reduction of the calculation time.

We demonstrated that a 3-groups model is able to (more or less) reproduce the asymmetric mode vibrational distribution function of CO_2. Furthermore, this model also yields a good agreement with the full model for the different plasma quantities calculated (i.e., electron density and temperature, and gas temperature) as well as for the CO_2 conversion, in a range of different pressures, typically used in MW plasmas, i.e., between 100 mbar and 1 bar. However, both the reduction of the chemistry set and the level lumping are not entirely valid anymore at lower pressures (i.e. 20 mbar). This should not be considered a big problem, as such low pressure is not really of interest for CO_2 conversion applications.

Also a 2-groups and 1-group model yield a very good agreement with the full model for the gas temperature and the electron density and temperature, and the agreement for the CO_2 conversion is still reasonable (at pressures of 200 mbar and above), in spite of the fact that the VDF is not fully reproduced. At 1 bar, these models also yield good agreement for the CO_2 conversion, because most of the conversion takes place in the part of the plasma where the VDF is in close-to-thermal equilibrium. There, the VDF resembles a simple Boltzmann distribution, except for the tail which appears to become less important at this high pressure. A further reduction of the number of equations to solve (i.e., by applying a thermal distribution model or a model without asymmetric mode vibrational excitation) leads to inaccurate results. This demonstrates the strong influence of vibrational excitation on the plasma characteristics. The balance between accuracy and computation time is here an important point.

Finally, our study reveals that the CO_2 conversion largely depends on the gas temperature. Indeed, the results obtained with the model assuming a fixed temperature profile are clearly different from the results obtained with the self-consistently calculated temperature. This indicates that the conversion, at these conditions, is partially due to thermal effects. A high gas temperature increases the population of all the vibrationally excited states, as well as the rate coefficients of the different (heavy particle) dissociation reactions. Both effects lead to a higher CO_2 conversion.

We also discussed the range of validity of the level-lumping method in CO_2 and we suggested possible ways to overcome the limitations. We believe that this level-lumping method can enable the modeling of CO_2 conversion in 2D or 3D microwave discharges, as it is quite easy to implement in an existing discharge code, such as the model presented in chapter IV.

CHAPTER VI

Dissociation processes in a microwave discharge: how to improve the energy efficiency?

The results presented in this chapter were published in[158]:

- A. Berthelot and A. Bogaerts. Modeling of CO_2 Splitting in a Microwave Plasma: How to Improve the Conversion and Energy Efficiency. *The Journal of Physical Chemistry C*, 121(15):8236–8251, 2017. DOI: 10.1021/acs.jpcc.6b12840

VI.1 Introduction

While it was reported that the best energy efficiencies in MW plasmas are obtained between 100 and 200 mbar[22], it would be particularly interesting for industrial application to use a process working at atmospheric pressure. Indeed, the energy efficiencies usually reported in the literature only take into account the energy consumed by the plasma and not the total energy consumption. In a real chemical installation, different extra energy costs have to be taken into account and the energy consumption of a vacuum installation is typically not negligible.

In spite of the previous investigations on CO_2 conversion, there is still a lack of detailed understanding of the most important plasma parameters in a MW discharge, such as the pressure, the power density and the gas temperature. These parameters have a strong influence on the conversion and energy efficiency in a MW plasma and are thus particularly relevant to gain a better understanding of the underlying mechanisms, and to improve the process of CO_2 conversion.

The aim of the research presented in this chapter is thus to provide more insights in the relevant dissociation and recombination mechanisms of CO_2 in a MW discharge, in a wide range of conditions of pressure, power deposition and gas temperature. In particular, we will focus on the role of vibrational excitation, because of its importance for energy efficient CO_2 splitting. This chapter is organized as follows.

In section VI.2, we present the conditions which are considered in the model. The results section VI.3 is divided into two main parts. First, we present a self-consistent gas temperature calculation and we investigate the conversion and energy efficiency in a wide range of discharge conditions (section VI.3.1). Then, we consider a simplified case with a fixed gas temperature to better understand the effect of vibrational excitation (section VI.3.2) and of the relative importance of the different dissociation and recombination mechanisms for CO_2 splitting (section VI.3.3), making the link with the results shown in section VI.3.1. Furthermore, in section VI.3.4, we propose some possible ways to improve the experiments based on all these findings. Finally, conclusions are given in section VI.4.

VI.2 Model description

The model considered in this chapter is a 0D model developed using the code ZDPlasKin[100], described in section II.4.1. This model uses the full chemistry set and the species considered are presented in tables III.1 and III.2. The reactions are listed in appendix A.1. The model solves for the density of each species (equation (II.28)) and the EEDF, using Bolsig+[65].

The gas temperature is either solved using equation (II.29), in section VI.3.1, following the procedure described in section V.2.2, or considers a constant gas temperature, in sections VI.3.2 and VI.3.3. Contrary to the model presented in chapter V, the wall cooling term of equation (II.29) is considered in section VI.3.1, as this section focuses on predicting realistic values of conversion and energy efficiency, which may be influenced by the cooling term.

The power deposition profile is either triangular, in section VI.3.1, as described by figure V.1, or a constant value, in sections VI.3.2 and VI.3.3. Given the lack of experimental data and the complex physics giving rise to plasma contraction (in both the axial and radial direction), it is difficult to estimate a priori the average power deposition density. In order to take into account the effect of pressure on the power deposition, we decided to take a maximum power deposition proportional to the pressure. The effect of power deposition will be discussed in more detail in sections VI.3.1, VI.3.2.1 and VI.3.3.1 below. The effect of radial contraction of the plasma is not studied here, due to the limitations of the 0D approach, which are discussed in more detail in section VI.3.4.

Post-processing of the results The energy efficiency of the conversion is expressed from the value of conversion (equation (V.13)) and the SEI (equation (V.2)) as:

$$\eta = X(\%)\frac{2.93\text{eV/molec}}{\text{SEI(eV/molec)}} \tag{VI.1}$$

Where X, the CO_2 conversion, is calculated by equation (V.13), 2.93 eV/molec is the energy cost of splitting one CO_2 molecule into CO and 1/2 O_2 at a temperature of 300 K (see section I.1.3). Furthermore, the model also provides information on the relative contribution of the various vibrational levels to the dissociation mechanisms of CO_2. The relative contribution of a given level i is defined as:

$$\Theta(\%) = 100\% \times \frac{\sum_{i\in j}\int_0^\tau R_i \mathrm{d}t}{\sum_j \int_0^\tau R_j \mathrm{d}t} \tag{VI.2}$$

Where the definition of τ, the integral upper bound, is explained in the text below. The index j refers here to all the dissociation reactions. The index i refers to all the reactions taking place from level v_i. In section VI.3.1, the contributions indicated in the text are the result of an integration from t = 0 to the end of the simulation (i.e. when z = 30 cm).

VI.3 Results and discussion

VI.3.1 Self-consistent calculation of the CO_2 conversion and energy efficiency

It is known that the gas temperature plays a very important role for energy-efficient CO_2 conversion, as will also be shown in sections VI.3.2 and VI.3.3 below. However, in practice, the gas temperature cannot easily be controlled, since it is the result of the heat produced and absorbed by the plasma. Given its importance for the conversion and in order to mimic real experimental conditions, and particularly to predict the energy efficiency for CO_2 conversion, it is necessary to include a self-consistent description of the gas temperature, as we did in the previous chapter V. Therefore, in this section, we perform self-consistent calculations of the plasma behavior, and we calculate the CO_2 conversion and corresponding energy efficiency as a function of pressure. The gas flow rate is kept constant in all the simulations, i.e., ϕ=10 slm. Also the SEI is kept constant, i.e., 2 eV/molec, which implies that the total power is also kept fixed. The goal of this section is to understand the different processes taking place in a realistic calculation, in order to understand what causes the limitations of the CO_2 conversion and energy efficiency. The individual effects of gas temperature, power deposition and pressure will be studied in more detail in sections VI.3.2 and VI.3.3.

Figure VI.1 shows the calculated CO_2 conversion and the energy efficiency as a function of pressure. The maximum power density Q_{max} is taken proportional to the pressure, ensuring that each CO_2 molecule receives the same amount of energy per time unit. We do not know the exact relationship between both, as it depends on the plasma volume, and the latter is not exactly known, so each curve corresponds to a different proportionality coefficient. For the red curve, Q_{max} = 50 W.cm^{-3} at 50 mbar and Q_{max} = 1 kW.cm^{-3} at 1 bar, while for the other curves, we used a higher power density, by multiplying the latter with a factor 2, 5 or 10, to investigate the effect of a higher power density. Since the total power input (and the SEI) are kept constant (i.e., SEI = 2 eV/molec), increasing the power density by a certain factor makes the plasma volume shrink by the same factor. Finally, the green curve shows the calculated CO_2 conversion when the cooling term (last term of equation (II.29)) is multiplied by 10 in the afterglow (i.e. after the power deposition stops), for the normal power density profile (see detailed discussion below).

The conversion and energy efficiency in figure VI.1 are linearly proportional to each other in this case, which is logical because the SEI is kept constant, and the energy efficiency is calculated from the conversion and the SEI (see equation (VI.1) above). Thus, the conversion and energy efficiency show exactly the same dependency

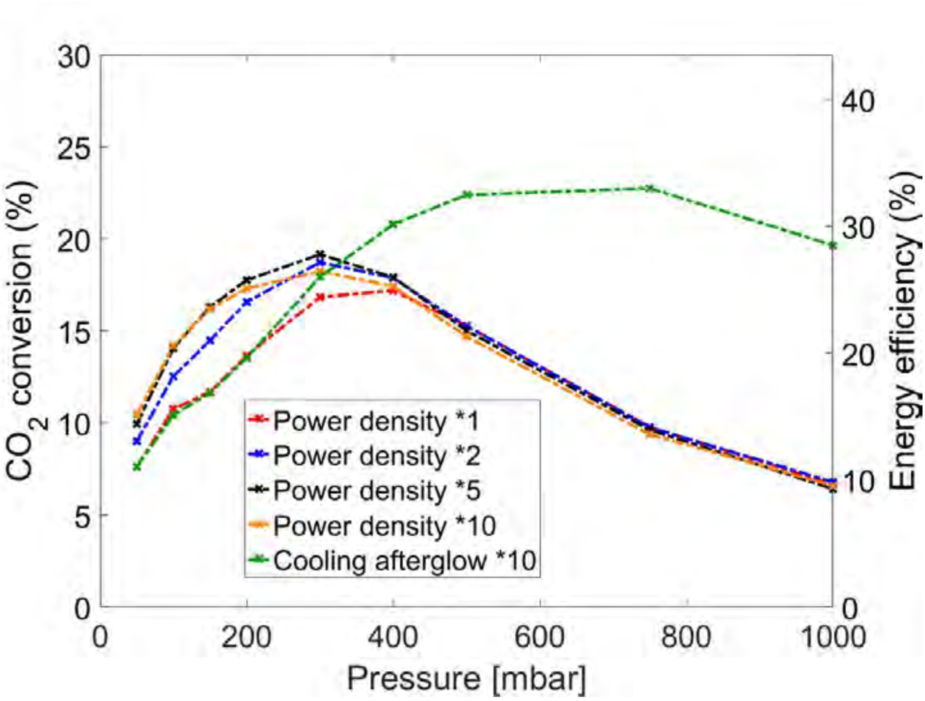

Figure VI.1: CO$_2$ conversion and corresponding energy efficiency as a function of pressure for different power deposition densities (see text) and for an increased cooling term in the afterglow (with the standard power density). ϕ = 10 slm; SEI = 2 eV/molec.

with pressure. The model predicts a maximum conversion and energy efficiency at 400 mbar for the normal power deposition density (red curve), and at 300 mbar for the other power deposition density profiles. This trend is in agreement with previous experiments[22]. For all the cases considered here, the conversion thus increases with pressure at low pressure, reaching between 13 and 20 % conversion between 200 and 300 mbar, followed by a slow drop, reaching 6 to 7 % at atmospheric pressure. The corresponding energy efficiency is 1.45 times this value, i.e. between 19 % and 30 % at a pressure between 200 and 300 mbar, followed by a slow drop, reaching 11 % to 15 % at atmospheric pressure. These value are slightly lower than the measurements of Bongers *et al.*.[34] where energy efficiencies of about 40 % have been found in a range between 150 and 400 mbar and for a SEI of 1.7 eV/molec. This difference may be partly explained by the complexity of the flow pattern in their setup, which makes a more detailed comparison difficult. The different approximations made in this chapter and their effect are discussed in section VI.3.4.

The effect of the power deposition density is important at low pressure and we see that a higher power deposition density increases the conversion and energy efficiency, in spite of the fact that the total power deposition, and thus the SEI, is kept constant. This indicates that at low pressure, a higher power density seems more important in determining the conversion and energy efficiency than a larger plasma volume. When the pressure increases, the difference between the different power densities becomes rather small and increasing the power deposition density even has a slightly negative impact on the conversion and energy efficiency.

We also investigated the effect of faster cooling in the afterglow, as this will affect the recombination of CO back into CO_2 (see details in sections VI.3.2 and VI.3.3 below), and thus the overall CO_2 conversion and energy efficiency. It is clear from figure VI.1 that, in contrast to the effect of power deposition density, the effect of a faster cooling is almost negligible at pressures below 200 mbar but it becomes particularly beneficial at pressures of 300 mbar and above. The maximum conversion and energy efficiency are then shifted between 600 and 800 mbar and they reach 23 % conversion, with 33 % energy efficiency. At atmospheric pressure, when applying this faster cooling, the conversion reaches 20 %, with 29% energy efficiency, while it was only 6 % (with 10 % energy efficiency) with the normal cooling term. This clearly illustrates that faster cooling in the afterglow can indeed drastically improve the CO_2 conversion and corresponding energy efficiency. The latter result is of great interest for practical applications. This faster cooling might be realized by applying a supersonic gas flow, which has indeed been demonstrated to give rise to more energy efficient CO_2 conversion[33].

To understand the trend of CO_2 conversion and energy efficiency with rising pressure, we study in detail the dissociation and recombination processes. Figure VI.2 illustrates the reaction rates of the three main dissociation and two main recombination mechanisms. The results are shown for three different pressures (100 mbar, 300 mbar and 1 bar) and for two different power deposition density profiles each, corresponding to the red curve of figure VI.1 (i.e., Figure VI.2 a, b, c) and to the black curve of figure VI.1 (i.e., Figure VI.2 d, e, f). The time t = 0 is chosen as the beginning of the plasma, i.e., where the MW power is first applied (see figure V.1 in chapter V). The end time of the plasma is easily identifiable by looking at the electron impact dissociation rate (red curve), since this rate drops right after the plasma (i.e., when the MW power deposition drops to zero) and is negligible in the afterglow.

The residence time naturally depends mostly on the size of the plasma. As the power deposition density is a factor 5 higher in the right panels (Figure VI.2 d, e, f) than in the left panels (Figure VI.2 a, b, c), the plasma volume is a factor 5 lower, at constant total power (and SEI). This explains why the residence time is about a factor 5 shorter in the right panels. It is not exactly a factor 5, since the gas temperature

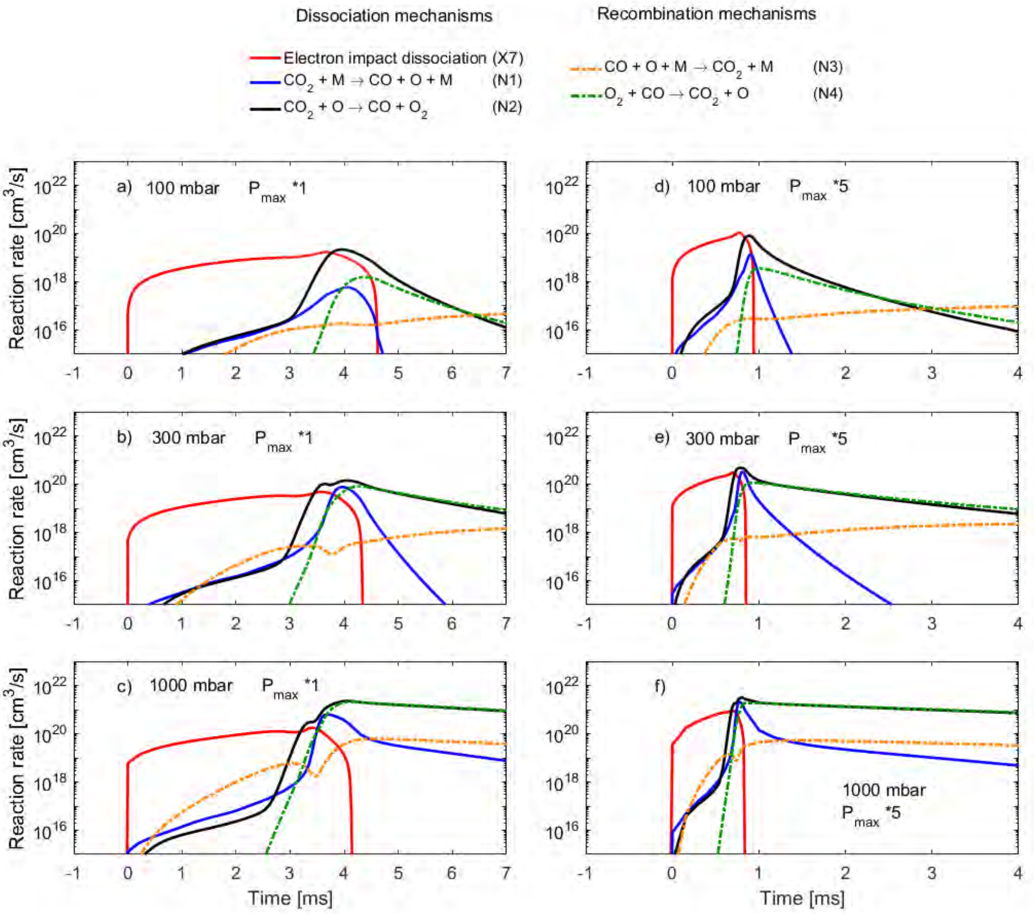

Figure VI.2: Reaction rates of the three main dissociation mechanisms (full lines) and two main recombination mechanisms (dashed lines), as a function of time, for three different pressures: 100 mbar (a and d), 300 mbar (b and e) and 1 bar (c and f), and for a regular power density profile (a, b and c) and a 5 times higher power profile corresponding to a plasma contracted by a factor 5 (d, e and f).

is self-consistently calculated and also plays a role in determining the residence time. Note that the time in figure VI.2 can easily be transferred to the position in the plasma, by looking at figure V.1 in chapter V.

The dissociation rates are strongly correlated with the evolution of other plasma parameters, such as the electron density, the gas temperature and the vibrational temperature. Figure VI.3 shows the evolution of the electron density (left y-axis), as well as of the gas temperature T_g and the vibrational temperature T_v (right y-axis) as a function of time. The results are again shown for three different pressures (100 mbar,

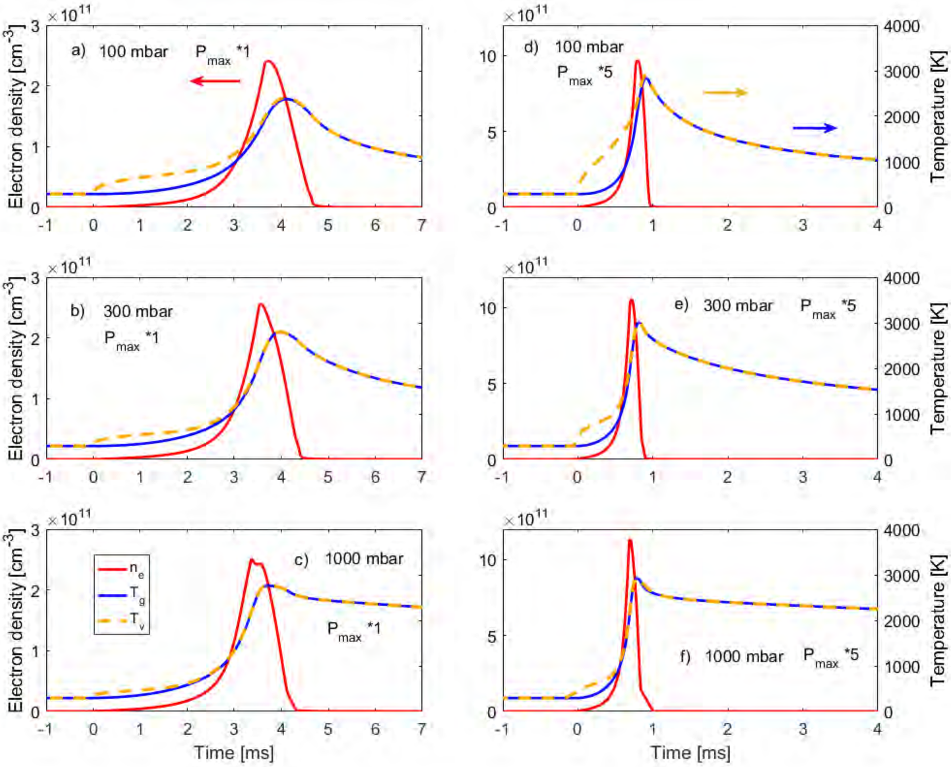

Figure VI.3: Evolution of the electron density n_e (red curve, left axis), the gas temperature T_g (blue curve, right axis) and the vibrational temperature T_v (orange curve, right axis), as a function of time, for three different pressures: 100 mbar (a and d), 300 mbar (b and e) and 1 bar (c and f), and for a regular power density profile (a, b and c) and a 5 times higher power profile corresponding to a plasma contracted by a factor 5 (d, e and f). Note the different y axis values for the electron density between the left and the right panels.

300 mbar and 1 bar) and for two different power deposition density profiles each, i.e. the same conditions as in figure VI.2 and with the normal cooling term.

In all the cases shown here, electron impact dissociation is the dominant dissociation mechanism in the first part of the plasma, i.e. before the gas temperature increases. Further in the plasma region, i.e., at later times, the gas temperature increases due to VT relaxation and thus the rates of the neutral reactions rise. As a consequence, the two other main dissociation mechanisms (N1 and N2, see appendix A.1) become relatively more important. The gas temperature starts decreasing before the end of the plasma, since the power deposition density drops (cf. the triangular profile illustrated in figure V.1 in chapter V). At 1 bar, the gas temperature decreases more slowly, because the recombination reactions become more important (cf. figure VI.2) and they are exothermic, and also because the gas has a larger heat capacity at higher pressure. The dissociation of CO_2 upon collision with O atoms, i.e., reaction N2 in appendix A.1, is the main dissociation mechanism at the end of the plasma and in the afterglow. For high power depositions (figure VI.2 d, e and f), the role of reaction N1 becomes slightly more important, although at 300 mbar (Figure VI.2 b) and 1 bar (Figure VI.2 c), it plays a non-negligible role in the case of the lower power deposition too. At 100 mbar (Figure VI.2 a), electron impact dissociation is overall clearly the main dissociation mechanism. When the pressure increases, its role becomes less and less important compared to the role of reactions N1 and N2. More specifically, at 100 mbar, electron impact dissociation accounts for 66 % of the entire CO_2 dissociation with both power deposition profiles. The relative contribution of electron impact dissociation clearly decreases upon increasing pressure and is only around 4 % at atmospheric pressure in both cases. Reaction N1 accounts for 2 %, 11 % and 5 % of the total dissociation at the regular power deposition profile, at 100, 300 mbar and 1 bar, respectively. Finally, reaction N2 contributes for 33 %, 59 % and 91 % to the total dissociation at 100 mbar, 300 mbar and 1 bar, respectively. On average, the relative importance of these different mechanisms is not much influenced by the choice of power deposition. However, the absolute value of the dissociation reaction rates is higher when increasing the power density, especially at low pressure. It is clear that reaction N2 is by far the most important dissociation mechanism at atmospheric pressure. However, as mentioned above, the O atoms which contribute in reaction N2 mainly originate from the reverse reaction N4, which indicates that both reactions reach a sort of equilibrium, thereby limiting the conversion at atmospheric pressure. It also explains why the cooling in the afterglow has a beneficial effect on the conversion at higher pressure. Indeed, recombination is a strong limiting factor at higher pressure and a faster cooling partly prevents these reactions from happening, as we will see below.

The vibrational temperature profiles, shown in Figure VI.3, show that the level of non-equilibrium (characterized by T_v/T_g) is higher at low gas temperatures, low pressures and high power densities. Indeed, at 100 mbar, the maximum of T_v/T_g is 2 at t = 0.9 ms with the regular power deposition profile, while it reaches 3 at t = 0.3 ms with the 5 times higher power deposition. At 300 mbar, the maximum T_v/T_g is 1.62 (at t = 0.7 ms) and 2.2 (at t = 0.15 ms), for the normal power deposition and the 5 times higher power deposition, respectively. At 1 bar, it is 1.37 (t = 0.5 ms) and 1.71 (t = 0.16 ms) at the normal and 5 times higher power deposition, respectively. However, in all these cases, as soon as the gas temperature increases, the ratio T_v/T_g becomes close to 1, indicating that the vibrational distribution becomes thermal in all cases investigated. Therefore, it seems that the non-equilibrium is better exploited with low pressures and high power deposition, but even in these cases, it is only present when the gas temperature remains low. The next two sections (VI.3.2 and VI.3.3) are dedicated to understand how to better exploit the non-equilibrium of the discharge and why some conditions (higher power deposition, and cooling in the afterglow) give a better conversion and energy efficiency.

VI.3.2 Vibrational distribution function (VDF)

In order to better understand the above results, we study here the effect of the different parameters (i.e., power deposition, pressure and temperature) on the vibrational distribution function (VDF). We assume here that the power deposition rises immediately from 0 to the indicated Q_{max} at t = 0. The gas temperature is taken as a constant. At t = 0, the gas is pure CO_2 and the VDF is taken as a Boltzmann distribution (see section III.3). In this section and in section VI.3.3, since all the required inputs are fixed as a function of time, it is not necessary to use the plug-flow approximation. Instead, we assume that a certain power deposition Q_{max} is applied to a volume of gas V at a temperature T_g from a time t=0 to t = τ.

VI.3.2.1 Effect of power deposition on the VDF

Figure VI.4 shows the VDF at a pressure of 100 mbar for two different power densities (Q_max = 100 W.cm^{-3} and Q_max = 500 W.cm^{-3}) and two gas temperatures, i.e., 300 K (Figure VI.4 a) and 2000 K (Figure VI.4 b). The temperature in a MW plasma is typically between 2000 K and 3000 K[37]. However, it is generally known that a lower gas temperature can give rise to a (relatively) higher vibrational excitation and it is thus interesting to study the effect of temperature on the VDF. The VDFs are shown for different times: t = 0, t = 1 μs, t = 10 μs and t = 100 μs, which are characteristic times in the temporal evolution of the plasma (see below). In most cases, a quasi-equilibrium is reached at t = 100 μs (or before). The VDF at t = 0 is assumed to be a Boltzmann distribution (straight line on the y-log plot) with vibrational temperature being equal to the gas temperature. When applying microwave power, the vibrational level population gradually increases. The higher the power deposition density, the faster the increase of the vibrational population. The vibrational excitation eventually saturates, to a level that depends on the conditions.

At a gas temperature of 300 K, for both power deposition values, a quasi-steady state is reached at around 100 μs (orange curves). In case of a power deposition of 100 W.cm^{-3}, the vibrational temperature reaches 1050 K at t = 100 μs, while in case of a power deposition of 500 W.cm^{-3}, the vibrational excitation is much more pronounced and the vibrational temperature reaches 2120 K. Note that these values are much

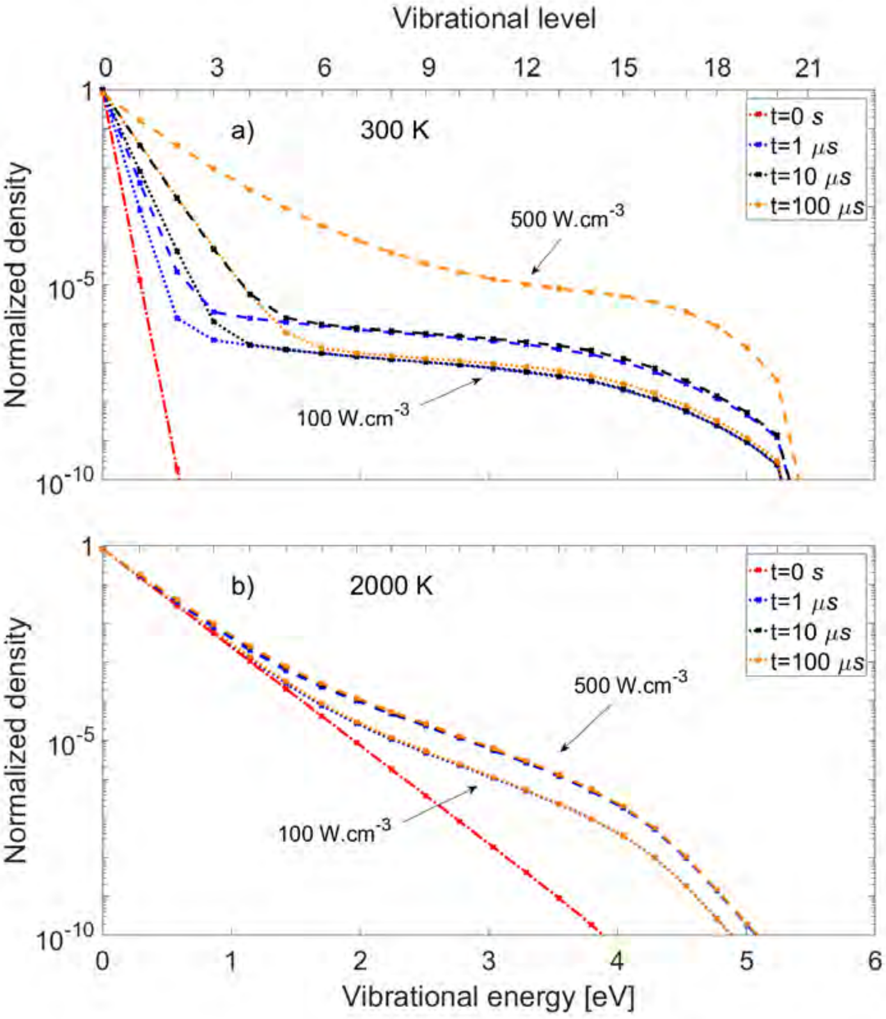

Figure VI.4: Vibrational distribution functions at different times (see legend) for a gas temperature of 300 K (a) and 2000 K (b) and a pressure of 100 mbar. The results are shown for two different power densities: $Q_{max} = 100$ W.cm^{-3} (dotted lines) and $Q_{max} = 500$ W.cm^{-3} (dashed lines).

higher than the gas temperature of 300 K, clearly demonstrating the non-equilibrium character of the MW plasma at these conditions. The intermediate vibrational levels from v_5 to v_{15} more or less form a plateau and thus have very similar populations. This is due to the effectiveness of energy exchange between two vibrational levels (i.e., so-called VV relaxation), as described in Treanor *et al.*[123]. For levels with higher energies (i.e., above v_{15}), the dissociation rate coefficients are much higher (due to a lower activation energy). Therefore, the population of these levels is lower since their lifetime is much shorter. This phenomenon is described in more detail in section VI.3.2.3 below. The difference in vibrational excitation with power deposition can easily be explained: the higher the power deposition, the higher the electron density, since more energy is available to ionize the CO_2 molecules. Indeed, at t = 100 μs, the electron density is calculated to be 2.3×10^{16} m^{-3} and 1.2×10^{17} m^{-3} for a power deposition of 100 $W.cm^{-3}$ and 500 $W.cm^{-3}$, respectively. It is interesting to note that the electron density is almost proportional to the power deposition for a given pressure and gas temperature. The electron temperature stays, however, practically the same at around 1.8 eV. Indeed, the higher power density gives rise to a higher electron density, so the applied energy has to be distributed over more electrons, explaining why their mean energy does not rise with higher power density. Note that the values of electron density that are self-consistently calculated here are lower than the ones used in Kozák, and Bogaerts[57]. Indeed, in Kozák, and Bogaerts, relatively high values, above the range that would be expected for typical MW plasma conditions, were used as a way to show how to optimize vibrational excitation for a given pressure and E/N, but they were not self-consistently calculated in the model.

At 2000 K, the population of the vibrational levels in a Boltzmann distribution, i.e., at t = 0, is of course much higher than at 300 K, because more energy is available for populating these levels thermally. Therefore, the effect of the plasma on the VDF is less obvious, although some overpopulation for levels v_5 and higher is still clearly visible. Furthermore, a quasi-equilibrium is reached faster (i.e., within less than 1 μs; see figure VI.4 b) for both power deposition values. Because the energy exchange upon collision between vibrational levels and ground state molecules, which depopulates the vibrational levels, i.e., so-called VT relaxation, increases with gas temperature, the VDF tends to become more thermalized at higher gas temperature. Starting from t = 1 μs, the vibrational temperature is calculated to be 2060 K and 2290 K for a power deposition of 100 $W.cm^{-3}$ and 500 $W.cm^{-3}$, respectively. These values are only slightly higher than the gas temperature, indicating that the MW plasma tends to be close to thermal equilibrium at these conditions. In summary, we can state that a higher power deposition gives rise to more vibrational excitation, whereas a higher gas temperature tends to thermalize the VDF. This is consistent with our previous findings (Figure VI.3), where we saw that the value T_v/T_g is higher in those regions of the discharge characterized by a low gas temperature is low and a high power deposition.

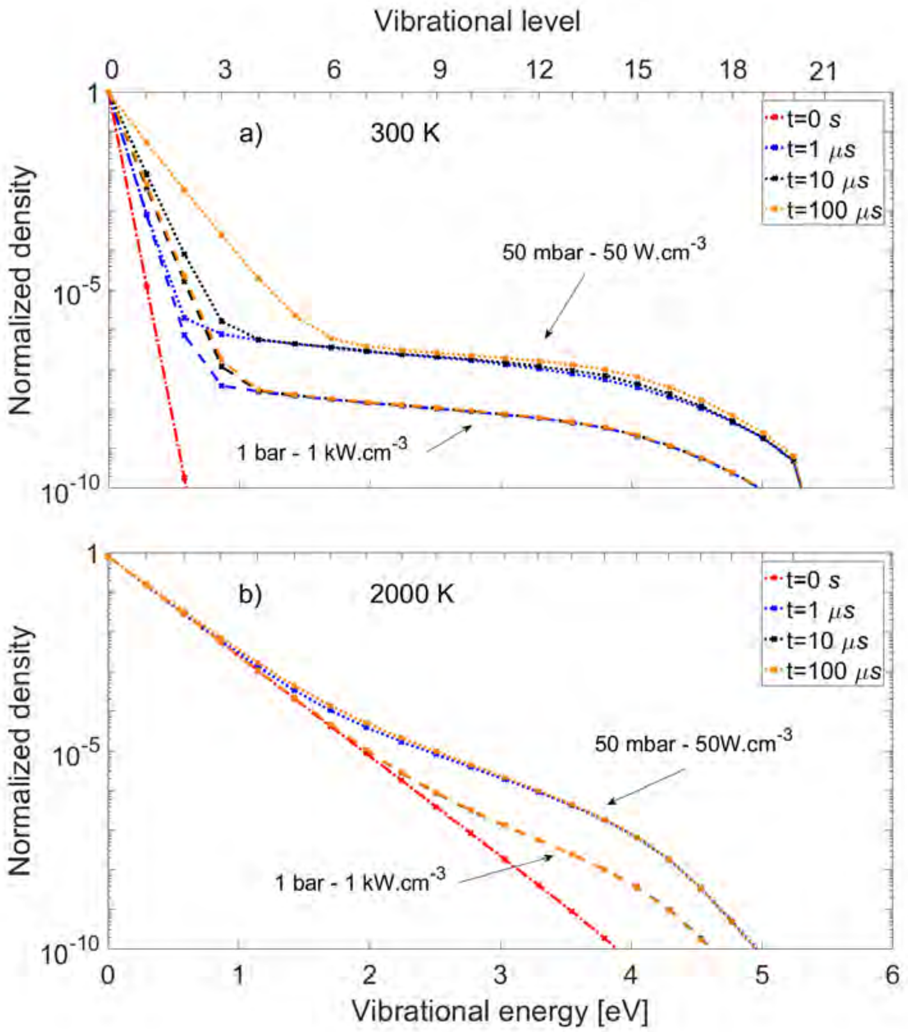

Figure VI.5: Vibrational distribution functions at different times (see legend) for a gas temperature of 300 K (a) and 2000 K (b). The results are shown for two different pressures and power densities: p = 50 mbar and Q_{max} = 50 W.cm^{-3} (dotted lines) and p = 1 bar and Q_{max} = 1 kW.cm^{-3} (dashed lines).

VI.3.2.2 Effect of pressure on the VDF

Figure VI.5 shows the VDF at different times (t=0, t = 1 μs, t = 10 μs and t = 100 μs), again for a gas temperature of 300 K (Figure VI.5 a) and 2000 K (Figure VI.5 b). Two different pressures and corresponding power densities are considered, i.e., 50 mbar at 50 W.cm^{-3} and 1 bar at 1 kW.cm^{-3}. Note that we again assume the power deposition to be proportional to the pressure, ensuring that each CO_2 molecule receives the same amount of energy per time unit, so that we can better evaluate the effect of pressure.

At a gas temperature of 300 K and atmospheric pressure (1 bar), the VDF reaches a quasi-steady state after 10 μs. The vibrational temperature reaches 620 K, despite the high power deposition. At lower pressure (50 mbar), a quasi-steady state is reached only after approximately 100 μs. The shape of the VDF is similar to the VDF in the 1 bar case. However, the vibrational temperature reaches 1170 K, indicating that the MW plasma is more out-of-equilibrium at lower pressure. For comparison, at 100 mbar and 100 $W.cm^{-3}$, the vibrational temperature was calculated to be 1050 K (see previous section), hence in between the results at 50 mbar and 1 bar, clearly illustrating the effect of the pressure. At 50 mbar, the plateau is also present but with a population about 1 order of magnitude higher than at atmospheric pressure. This is mainly due to the higher VT vibrational energy losses in the plasma at atmospheric pressure, resulting in a less pronounced degree of vibrational excitation. At a gas temperature of 2000 K, the VDF reaches again a quasi-steady state much faster, in less than 1 μs. The difference with a Boltzmann distribution is only significant from level v_5 at 50 mbar and from level v_8 at 1 bar. The overpopulation from the Boltzmann distribution, or in other words, the degree of non-equilibrium, is again obviously less important compared to the 300 K case. However, the normalized density of the vibrationally excited levels is higher at 2000 K than at 300 K, both at 50 mbar and at 1 bar, because the levels are also partially thermally populated.

Thus, we can conclude that a higher pressure, just like a higher temperature, tends to make the VDF thermalize faster and it is thus detrimental for the vibrational excitation. This is also consistent with our previous results (Figure VI.3), which revealed that the ratio T_v/T_g was maximum at low pressures and low gas temperatures.

VI.3.2.3 Effect of dissociation and vibrational-translational (VT) relaxation reactions on the VDF

It is known that the Treanor distribution has a higher population of the highest vibrational levels, and this would be beneficial for CO_2 splitting, because these levels tend to dissociate easily. However, the VDFs shown above do not exhibit this Treanor distribution. The reason is that the classical Treanor distribution is derived for the case of anharmonic molecules without dissociation reactions and VT relaxation. To demonstrate this, we show here the effect of the dissociation reactions and VT relaxation on the VDF. For this purpose, we considered a chemistry set without dissociation reactions (i.e. the reactions N1, N2, N5, X3, X4, X5, X6 and X7 from table A.1 and table A.5 in appendix A.1 are removed, as well as all the reactions from table A.3 involving the

CO_2 molecules) and a set without dissociation reactions and VT relaxation (reactions V1, V2a, V2b and V2c from table A.4).

We compare the results with those obtained using the full chemistry set. Figure VI.6 shows the VDF obtained using the full chemistry set and the chemistry set without dissociation reactions at t = 300 μs, for a gas temperature of 300 K, a pressure of 50 mbar and a power deposition density of 200 W.cm^{-3}. At this time of 300 μs, a quasi-equilibrium has been reached for the VDF. Note that this quasi-equilibrium is reached after a longer time in the case without dissociation. We also compare with the corresponding Boltzmann distribution at a temperature of 300 K and with the Treanor distribution at a gas temperature of 300 K and a vibrational temperature of 3010 K. The latter corresponds to the vibrational temperature of the actual VDF calculated without dissociation reactions (see below). Note that a relatively high power density, a low pressure and a low gas temperature are used for this comparison, in order to clearly show the Treanor effect. Indeed, with a lower power density and a higher gas temperature and pressure, as shown above, the vibrational excitation is weaker, and both the actual VDF and the Treanor distribution are then closer to a Boltzmann distribution. It is thus more difficult to observe the Treanor effect.

The comparison between the two VDFs obtained with and without dissociation reactions shows that without dissociation, the highly excited levels are more populated than when dissociation is considered. This is very logical, and attributed to the large dissociation rate coefficients associated with these levels, since the activation energy of the different dissociation reactions is significantly lower for the highly excited levels. It is interesting to note that when neglecting dissociation, the highest levels of the VDF are even more populated than the intermediate levels, as is also the case for the Treanor distribution. The vibrational temperature is calculated to be 2500 K with dissociation and 3010 K without dissociation reactions. The VDF calculated without dissociation reactions is in reasonable agreement with the analytical predictions of Treanor *et al.*[123], in which the dissociation reactions were also not considered. A large difference is still visible for the highly-excited levels, as the Treanor distribution predicts a higher population of these levels. However, in reality, dissociation of CO_2 does take place, and thus, it is clear from figure VI.6 that the Treanor distribution greatly overestimates the real VDF, and can thus not be used to predict CO_2 splitting in a plasma in a realistic way.

Finally, the VDF calculated without dissociation and VT relaxation reactions (green curve in figure VI.6) has a similar shape as the one without dissociation (black curve in figure VI.6) but its vibrational temperature is much higher (i.e., 4300 K compared to 3010 K), clearly demonstrating that VT relaxation is also responsible for the loss of vibrational energy.

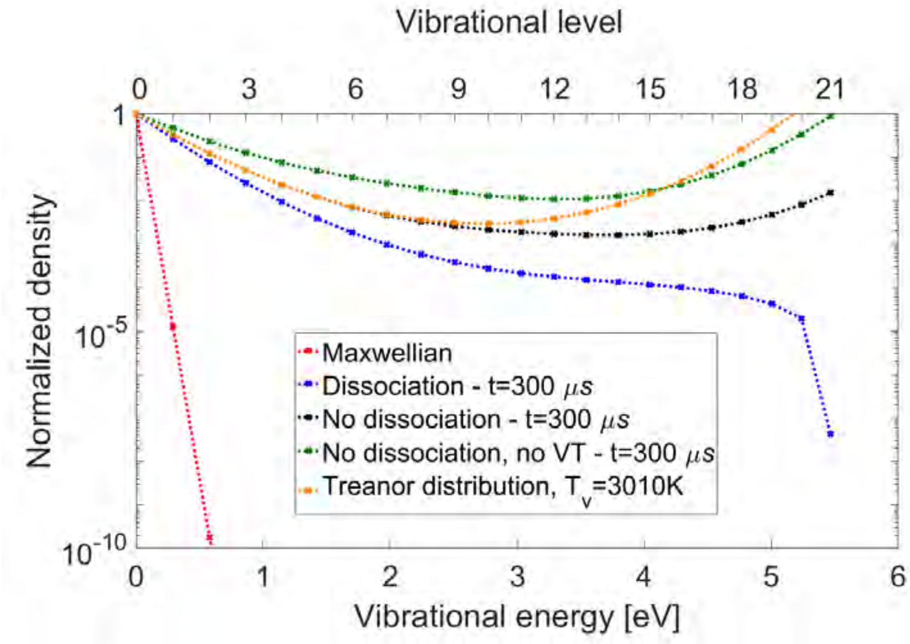

Figure VI.6: Vibrational distribution functions at a pressure of 50 mbar, a power density of 200 W.cm^{-3} and a gas temperature of 300 K. The blue curve corresponds to the VDF obtained using the full chemistry set. The black curve was obtained by neglecting the dissociation reactions. The green curve was obtained by neglecting the dissociation reactions and the VT relaxation reactions. The orange curve is calculated using the analytical formula of a Treanor distribution, while the red curve shows a Boltzmann distribution at 300 K.

VI.3.3 Dissociation and recombination mechanisms of CO_2

Now that we understand how the VDF varies with the operating conditions, we want to investigate the effect on the dissociation and recombination mechanisms of CO_2, to better understand the self-consistently calculated CO_2 conversion and energy efficiency in the range of conditions investigated in section VI.3.1. The same conditions as in the previous section (VI.3.2) are considered here: at t = 0 the VDF is a Boltzmann distribution and the power deposition rises from 0 to Q_{max}, also at t = 0. In all the conditions tested here, our calculations predict that the main dissociation mechanisms of CO_2 are electron impact dissociation, and dissociation upon collision with O atoms or any other molecule (denoted as M), i.e., reaction X7 (CO_2 + e → CO + O + e-) in table A.1 in appendix A.1, and reactions N1 (CO_2 + M → CO + O + M) and N2 (CO_2

+ O → CO + O_2) in table A.5 in appendix A.1. The reaction rates shown here are taken as the sum of the reaction rates from the ground state and vibrationally excited states. To compare the data, we introduce the quantity τ, which is the time after which each molecule in the considered volume has received an energy of 1eV in average:

$$\tau = \frac{p}{T_g Q_{max}} \frac{e}{k_B} \tag{VI.3}$$

This allows us indeed to compare the average reaction rates in a period during which each CO_2 molecule has received the same amount of energy, so that the latter is kept constant. τ can thus be considered as a characteristic time of the plasma, which would be the residence time in a discharge with a SEI of 1 eV/molec. The rates are thus averaged in the plasma only, and not in the afterglow, although the variations of the rates in the afterglow with the gas temperature can be inferred from these results. This averaging is necessary to compare the different data. However, since the time τ varies with the conditions, this averaging can have some consequences on the results, which are indicated in the text.

VI.3.3.1 Effect of power deposition on the dissociation and recombination mechanisms

Figure VI.7 shows the reaction rates of the three main dissociation processes of CO_2, as well as the two main recombination processes, forming again CO_2, for different values of power deposition and gas temperature, at a pressure of 100 mbar. The reaction rates are averaged from t = 0 to t = τ. Note that the density of the gas molecules changes with the gas temperature (according to the ideal gas law), thus the absolute value of the reaction rates also changes, since it depends on the density of the reactants.

At $T_g = 300$ K (Figure VI.7 a), electron impact dissociation is the main dissociation process for low power deposition: from 50 to 200 W.cm^{-3}, reactions N1 and N2 are negligible. However, when the power density increases, these two reactions become increasingly important and end up contributing even slightly more than electron impact dissociation. At $T_g = 1000$ K (Figure VI.7 b) and $T_g = 2000$ K (Figure VI.7 c), electron impact dissociation is by far the main dissociation mechanism, while reactions N1 and N2 are almost negligible. Finally, at $T_g = 3000$ K (Figure VI.7 d), electron impact dissociation is not so important at low power deposition (i.e., below 200 W.cm^{-3}), but it becomes increasingly important upon higher power deposition, while the importance of N1 and N2 stays almost constant with increasing power deposition.

Note that in all the cases shown here, the average value of the electron impact dissociation rate linearly increases with power deposition. This can be explained by the fact that the electron density also linearly increases with power deposition, while the

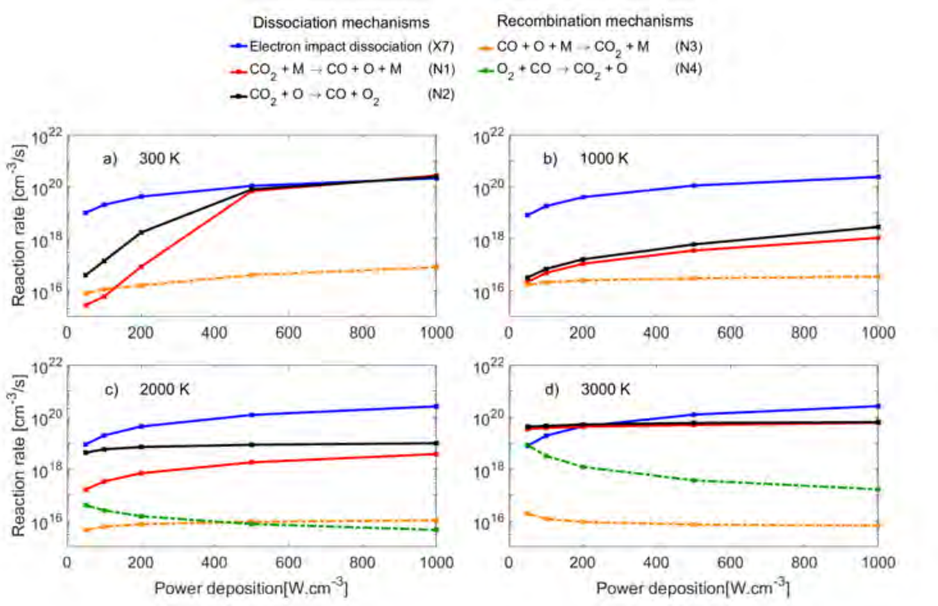

Figure VI.7: Reaction rates of the three main dissociation mechanisms of CO_2 (X7, N1, N2; solid lines) and the two main recombination mechanisms forming again CO_2 (N3, N4; dashed lines), averaged from t = 0 to t = τ, as a function of the power deposition, for a pressure of 100 mbar, and a gas temperature of 300 K (a), 1000 K (b), 2000 K (c) and 3000 K (d).

electron temperature stays constant and thus the rate coefficient stays almost constant.

At all the conditions shown here, the two major recombination reactions forming again CO_2, i.e., the three-body recombination of CO with O atoms (reaction N3 from table A.5) and the two-body recombination of CO with O_2 molecules (reaction N4 from table A.5), are almost negligible compared to the dissociation reactions at this low pressure of 100 mbar. This means that no equilibrium has been reached yet between the dissociation reactions and their reverse recombination processes. Only at T_g = 3000 K, reaction N4 has a reaction rate comparable to electron impact dissociation for low power deposition values. However, the average rate of this recombination process clearly decreases with increasing power deposition. This is caused by the fact that τ drops upon rising power deposition. Therefore, the rate is averaged over a shorter time, at the beginning of the conversion. During this time τ, the reaction products of CO_2 splitting (CO and O_2) do not have time to build up yet. Indeed, since most of the conversion is thermal in this case, the rise in CO_2 dissociation with power deposition is not important enough to counter-balance the decrease of the averaging time τ.

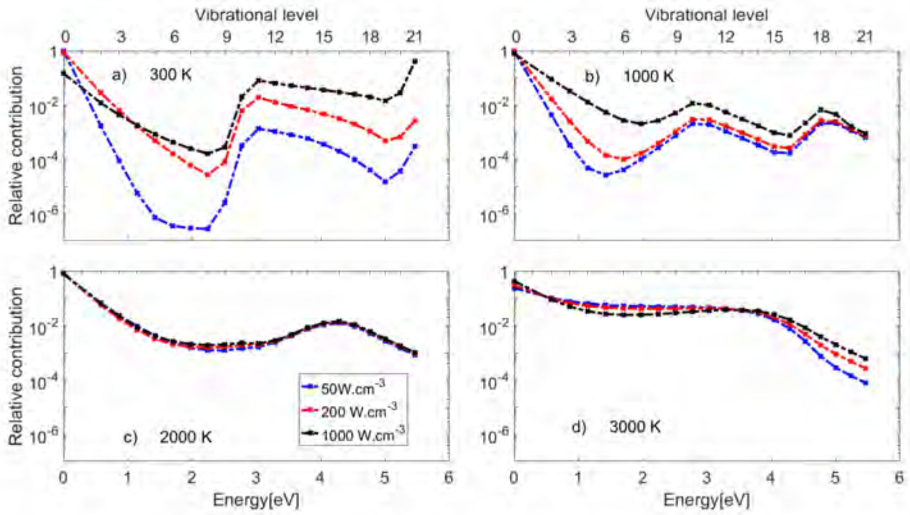

Figure VI.8: Relative contribution of the vibrational levels to the overall CO_2 dissociation at a pressure of 100 mbar, for different values of power density (see legend) and different gas temperatures, i.e., 300 K (a), 1000 K (b), 2000 K (c) and 3000 K (d).

To understand the behavior of the dissociation reaction rates of X7, N1 and N2 as a function of power deposition and gas temperature, it is interesting to look at the effect of vibrational excitation on the overall dissociation. Indeed, since the dissociation reactions have much larger probabilities to occur from a highly excited vibrational state, the total rate of a given dissociation reaction also depends on the vibrational excitation. Figure VI.8 shows the relative contributions of all the vibrational levels to the overall dissociation at a pressure of 100 mbar. The contributions are again averaged from t = 0 to t = τ.

At a gas temperature of 300 K (Figure VI.8 a), the highly excited vibrational levels of the asymmetric mode are not important for dissociation at low power deposition, but they become increasingly important for high power deposition, as could also be deduced from figure VI.4 a above. This explains why the dissociation reactions upon impact by O atoms or any molecules M (i.e., reactions N1 and N2) become increasingly important at higher power deposition, because at low gas temperatures these reactions only occur for the highly excited vibrational levels, due to their high threshold energies. The shape of the curves in figure VI.8 a can easily be understood by looking at figure VI.4 a: the activation energy of these dissociation reactions decreases with rising vibrational energy and thus the corresponding rate coefficient increases exponentially. The plateau described previously in the VDF, with practically constant populations of the vibrational levels, then gives rises to a large contribution of the highly-excited levels. This plateau is responsible for the sudden increase of the contribution of the excited levels around level v8. On the other hand, the intermediate levels do not have a large enough population to contribute significantly to dissociation, given the high activation energies of the reactions taking place from these levels.

At a gas temperature of 1000 K and 2000 K (Figure VI.8 b and figure VI.8 c), the model predicts a quasi-negligible role of the vibrational levels with energies above 1 eV (i.e., level v_4 and higher). The dissociation almost exclusively originates from the first levels of the VDF, due to electron impact (see figure VI.7 b,c), and the contribution of vibrational excitation to the dissociation is not important.

Finally, at 3000 K (Figure VI.8 d), the lowest levels are still more important, but almost all the levels, except for the highest ones, have a significant contribution to the total dissociation. This is mainly because these levels are thermally populated at this high gas temperature.

As shown in figure VI.4a, at $T_g = 300$ K, the plasma significantly affects the VDF, especially for high power deposition densities. Therefore, despite the low gas temperature and the high activation energies of reactions N1 and N2, as well as the high energy threshold for X7, vibrational excitation can become high enough to significantly enhance the probability of reactions N1 and N2 (and X7) to occur. Indeed, the energy of the highly-excited vibrational levels is comparable to the activation energy of reaction N1 (5.6 eV) and even higher than the activation energy of reaction N2 (1.43 eV). The limiting factor for reaction N2 to occur is thus mainly the presence of O atoms.

On the other hand, at higher gas temperatures, the contribution of the plasma to the vibrational excitation gradually drops, as was clear from figure VI.4 b above. At 1000 K and 2000 K, the gas temperature is not yet high enough to overcome the activation energy of reactions N1 and N2. Yet, at these higher gas temperatures, the VT vibrational energy losses are larger, reducing the role of the vibrational levels. This makes electron impact dissociation by far the main source of dissociation. Given the relatively low population of the highly excited vibrational levels at these temperatures, electron impact dissociation is much more likely to happen from the CO_2 ground state.

At 3000 K, the VDF does not depend much on the plasma either. However, due to the high gas temperature, the vibrational levels are more populated even at close-to-equilibrium conditions, and the probability of reactions N1 and N2 becomes more important, both from the ground state and from vibrationally excited states. Therefore, the contribution of almost all the levels to the CO_2 dissociation becomes significant.

This explains why the reaction rates of reactions N1 and N2 do not depend much on the power deposition density at high gas temperatures, since the VDF is not so much influenced by the plasma.

In summary, at low gas temperature, electron impact dissociation, mainly from the CO_2 ground state, is the major dissociation mechanism at low power density, but at higher power densities, the dissociation reactions upon impact of O atoms or other molecules with the highly excited vibrational levels of CO_2 become increasingly important. Upon increasing gas temperature, i.e., 1000 and 2000 K, electron impact dissociation, mainly from the CO_2 ground state, is most important at all power densities, because the CO_2 vibrational levels are not enough populated, and consequently, the heavy particle reactions (N1 and N2) are not important. Finally, at a gas temperature of 3000 K, dissociation upon impact of O atoms or any other molecules (N1, N2) with the excited vibrational levels is comparable to electron impact dissociation, but in this case, the VDF is nearly thermal, so we do not really exploit the non-equilibrium conditions of the plasma. Therefore, in order to exploit the non-equilibrium aspect of the plasma, it is better to design a setup that would limit the gas temperature increase, while giving a strong power density that would enable a large vibrational excitation. This corresponds to our previous observations (Figures VI.2 and VI.3), where we saw that the non-equilibrium was favored at low gas temperatures and high power deposition.

VI.3.3.2 Effect of pressure on the dissociation and recombination mechanisms

Figure VI.9 shows the reaction rates of the three main dissociation processes and the two main recombination processes for different values of pressure and gas temperature. The power density again proportionally increases with pressure such that each CO_2 molecule receives the same amount of energy per time. More specifically, the power density is 50 W.cm^{-3} at 50 mbar, and rises to 1 kW.cm^{-3} at 1 bar. Note that these power densities correspond to the low range of power densities used above, where the pressure was kept constant at 100 mbar (so the corresponding power density is then 100 W.cm^{-3}; hence in the lower range of power density values of figure VI.7 above). The reaction rates are again averaged from t = 0 and t = τ.

At T_g = 300 K (Figure VI.9 a) and T_g = 1000 K (Figure VI.9 b), electron impact dissociation is the main dissociation mechanism, by several orders of magnitude, and the heavy particle reactions (N1, N2) are not important in the entire pressure range, which is attributed to the relatively low values of the power density used here (cf. figure VI.7 above). Indeed, at low power density, vibrational excitation is limited, and the heavy particle reactions (N1, N2), which mainly occur with the vibrational levels, are thus not important. At higher power densities, these reactions become gradually more

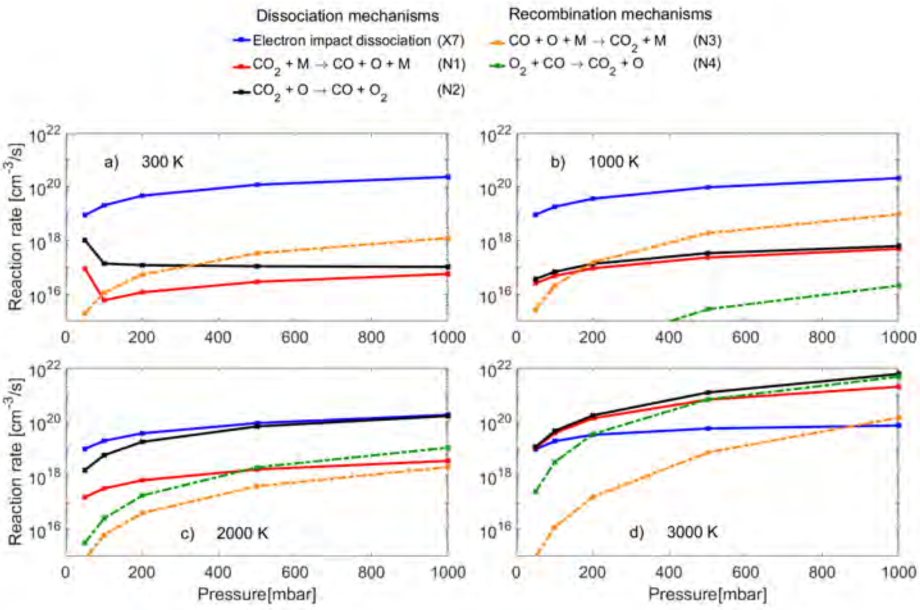

Figure VI.9: Relative contribution of the vibrational levels to the overall CO_2 dissociation at a pressure of 100 mbar, for different values of power density (see legend) and different gas temperatures, i.e., 300 K (a), 1000 K (b), 2000 K (c) and 3000 K (d).

important, as was obvious from figure VI.7. At $T_g = 2000$ K (Figure VI.9 c), reaction N2 becomes more and more important and is of the same order of magnitude as electron impact dissociation. At $T_g = 3000$ K (Figure VI.9 d), electron impact dissociation becomes of lower importance, especially with increasing pressure, while reaction N2 has the largest reaction rate. The recombination reactions have increasing reaction rates with increasing pressure. However, from $T_g = 300$ K to $T_g = 2000$ K, their rates are clearly lower than the total dissociation rate. On the other hand, at $T_g = 3000$ K (Figure VI.9 d) and for high pressures (above 500 mbar), the recombination reaction N4 plays a significant role and has a rate larger than N1, and comparable to N2. The O atoms consumed by reaction N2 actually originate from the recombination of O_2 and CO. This suggests that an equilibrium has been reached between the dissociation reaction (N2) and the recombination reaction (N4), limiting the CO_2 conversion at high temperature and atmospheric pressure

Figure VI.10 shows the relative contributions of the vibrational levels to the dissociation reactions (X7, N1 and N2) at three different pressures and four different

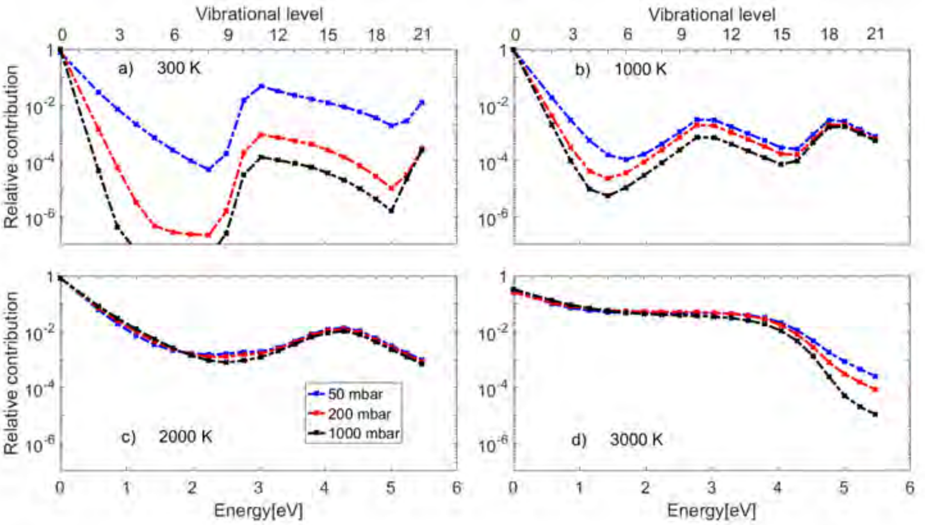

Figure VI.10: Relative contribution of the vibrational levels to the overall dissociation for different values of pressure (see legend) and different gas temperatures, i.e., 300 K (a), 1000 K (b), 2000 K (c) and 3000 K (d).

temperature values. The contributions are again averaged from t = 0 to t = τ. At T_g = 300 K (Figure VI.10 a), most of the dissociation takes place from the ground state. However, the highly-excited states also play a non-negligible role, as in figure VI.8, especially at 50 mbar. At T_g = 1000 K (Figure VI.10 b) and T_g = 2000 K (Figure VI.10 c), the contribution of the highly excited levels is not very important to the total dissociation, as also seen before in figure VI.8. At T_g = 3000 K (Figure VI.10 d), the contribution of all the vibrational levels is more important, except for those with the highest energies. As explained before, this is due to the fact that the conversion is mainly caused by thermal processes rather than by plasma processes.

For all the cases shown here, the role of vibrational excitation is more important at lower pressure than at atmospheric pressure. This can be understood again by looking at figure VI.5, which shows that upon increasing pressure the VT relaxation rises, and tends to thermalize the VDF. On the other hand, as seen in figure VI.9 d, a higher pressure favors the heavy particle dissociation reactions more than electron impact dissociation for high gas temperatures. We can thus conclude that a lower pressure tends to make the plasma more non-equilibrium and improves the role of vibrational excitation. Furthermore, the role of recombination reactions is also reduced at lower pressures. Both effects are beneficial for the CO_2 conversion.

These results explain the dependence of the conversion to the different parameters observed in figure VI.1. Indeed, as seen from figures VI.2,VI.3 and figure VI.9, at low pressure, despite the larger vibrational excitation, electron impact dissociation is the main dissociation process, which is not very efficient, and the heavy particle reactions N1 and N2 only account for a small fraction of the total dissociation. The role of these two reactions increases with pressure, especially at relatively high gas temperatures. On the other hand, an increase in pressure has two detrimental effects on the conversion:

(*i*) the vibrational distribution thermalizes faster and (*ii*) recombination reactions become more important. Hence, the CO formed in the discharge recombines in the afterglow due to the large recombination reaction rates and the slower drop in gas temperature.

This explains why increasing the cooling in the afterglow has a beneficial effect on the conversion at high pressure (see green curve in figure VI.1):

(*i*) at low pressure, recombination is not so important and a faster cooling is thus not particularly beneficial, while (*ii*) at high pressure, a large fraction of the CO formed in the discharge recombines in the afterglow, which can be partly prevented with a better cooling.

Our results also indicate that a higher power density yields more pronounced vibrational excitation (see figure VI.4) and gives a stronger weight to the heavy particle reactions (N1 and N2) in the dissociation process, especially at low gas temperatures.

VI.3.4 Limiting factors and how to take optimal advantage of the non-equilibrium in a MW discharge

The above results are very interesting, but we would like to point out the limitations of the model in order to better understand these results and how they compare to experiments. First, the approximations required by the 0D approach are not necessarily valid in all cases. In reality, the power deposition and the gas temperature also depend on the radial coordinate and the complexity of these gradients cannot be reproduced here. Moreover, at high pressures, the plasma also tends to contract in the radial direction, resulting in a layer of gas around the plasma, which has a large influence on the gas temperature gradients. This contraction makes the plasma smaller and therefore it increases the power density. According to experimental data[37], increasing the pressure causes a sharp transition from diffuse to contracted regimes. These effects are obviously not captured by our 0D approach.

Furthermore, the chemistry set also contains some approximations. The rate coefficients are not always well known, which might hinder the accuracy of the results. Our modeling work would greatly benefit from more in-situ experimental measurements (electron density, gas temperature, . . .) in order to benchmark our results. It should also be pointed out that the effect of the CO_2 vibrational levels of the symmetric mode at high vibrational energies is not considered. In reality, the levels become so close to each other that they form a quasi-continuum close to the dissociation limit. The role of energy transfer within this continuum is not well known and it would be interesting to investigate this in the future.

Nevertheless, we believe that the trends observed here give valuable information on the CO_2 conversion and on the vibrational excitation of CO_2 in a MW plasma. Our results indicate that the best conversion and energy efficiency are obtained at reduced pressure (i.e., around 300 mbar), in order to enhance vibrational-induced dissociation (mainly by reaction N1), since vibrational excitation is more effective at low pressures. This corresponds to important results obtained in literature[22;33]. Indeed, the best conversion and energy efficiency reported so far were obtained using a supersonic flow in a Laval nozzle[22;33]. According to our study, this supersonic flow can be beneficial for two reasons:

(*i*) it creates a low pressure zone where vibrational excitation is more efficient and (*ii*) the gas temperature stays low, which prevents recombination upon increasing pressure, which we have seen to be particularly important in the afterglow. Indeed, our model predicts that low gas temperatures are beneficial for the vibrational excitation and thus enhance the non-equilibrium character of the plasma. Furthermore, this supersonic flow does not require a pumping system, which is also beneficial for the overall energy efficiency.

It is clear that enhancing the vibrational excitation can improve the energy efficiency. According to our model predictions, there are several ways to achieve this: using lower pressures, higher power densities (i.e. contracting the plasma) and reducing the gas temperature. Therefore, we believe that efforts should be made in designing more complex plasma discharges that manage to combine these properties, because conventional MW discharges operating at atmospheric pressure do not seem to take sufficient advantage of the non-equilibrium aspect of the plasma. As stated above, the Laval nozzle supersonic flow discharge seems very promising in that sense. Other paths are also being investigated, such as applying a vortex gas flow[34], which is thought to be beneficial for gas cooling. Furthermore, pulsing the plasma power could also be beneficial for the conversion, as it prevents the gas from heating. More investigations in that direction are necessary. To summarize, this study shows that experiments do not systematically take advantage of the non-equilibrium aspect of the plasma and efforts should thus be made in that direction.

While this study was made for MW plasma discharges, we believe that the trends observed here are also valid for other types of plasmas, particularly gliding arc discharges, where vibrational excitation is also stated to be responsible for energy efficient

CO_2 conversion[39;159].

Additionally, we would like to point out that, when comparing different CO_2 dissociation techniques, the extra energy costs of the whole installation should be taken into account. A blower would typically be needed, as well as a vacuum pump to work at low or intermediate pressures. A cooling system may also be required if the discharge produces too much heat. In experimental setups, the power consumed by a vacuum pump alone can be comparable to the plasma power, which makes it far from negligible. A study detailing the energy consumption of the different setups would be of great interest for potential industrial application of CO_2 dissociation.

VI.4 Conclusion

We have used in this chapter a zero-dimensional chemical kinetics model to describe the CO_2 conversion in a MW plasma. This model includes a detailed description of the vibrational kinetics of the asymmetric mode of CO_2 and the first levels of CO and O_2, as well as the energy transfers between these levels.

In a first step, we used a self-consistent gas temperature calculation to understand the effect of pressure and power density on the CO_2 conversion and energy efficiency, as well as the advantages of a faster cooling in the afterglow. Our model predicts that the conversion and energy efficiency reach a maximum of about 17% and 25%, respectively, between 300 and 400 mbar and with the standard power deposition profile (figure VI.1, red curve). A higher power density has a beneficial effect on the conversion and energy efficiency at low pressure, which can reach up to 28% when the power deposition is 5 or 10 times denser, but almost no effect at high pressures. On the other hand, an increased cooling in the afterglow yields a higher conversion at 300 mbar and above, reaching up to 22% conversion, at 32% energy efficiency, at 500 mbar. The effect of cooling is particularly important at high pressure, when recombination plays a major role, while it is negligible at low pressure due to the little effect of recombination.

In a second step, we used the model to investigate the individual effect of power density, pressure and gas temperature on the vibrational distribution function of CO_2, and on the most important dissociation and recombination mechanisms, and we made a link between both, by determining the relative contribution of the individual vibrational levels to the overall dissociation.

The model predicts a larger vibrational excitation with increasing power deposition density and with decreasing pressure and temperature. A higher power deposition gives a higher electron density, which in turn enhances the transfer of electron energy to vibrational excitation. On the other hand, a higher pressure enhances the VT relaxation processes, so that the vibrational energy is lost again more quickly. Finally, the gas temperature was also identified as a key parameter. A higher gas temperature also results in more pronounced VT transfers, making the vibrational levels thermalize faster. It is clear that we should exploit the strong non-equilibrium character of the MW plasma, with a pronounced vibrational excitation, as the latter is important for energy efficient CO_2 conversion. To realize this, it would be most beneficial to operate at reduced pressure, but still at sufficiently high power densities, while keeping the temperature under control.

We investigated the role of the most important dissociation and recombination mechanisms of CO_2, in the same range of operating conditions, i.e., power density, pressure and temperature. At low power densities, electron impact dissociation is the main dissociation mechanism, since the vibrational excitation is not significant enough to overcome the activation energy of the other dissociation reactions involving neutral species. At high power densities, the vibrational excitation is sufficient to overcome the activation energy of the neutral reactions that lead to dissociation of CO_2, i.e., upon collision with any neutral molecule or with O atoms (reactions N1 and N2 of table A.10 from the appendix A.1). We also find that a higher gas temperature tends to favor the heavy particle dissociation reactions (N1 and N2), but the effect of the plasma-induced vibrational excitation becomes lower. Hence, a higher gas temperature is expected to be detrimental to the CO_2 conversion and energy efficiency. The same trend is observed with pressure: a higher pressure gives rise to more VT relaxation and is thus detrimental for the vibrational excitation. It is thus quite logical that a higher pressure reduces the CO_2 conversion and energy efficiency.

These observations help to explain the increase in conversion at low pressure. Indeed, an increase of power density has a positive effect on the vibrational excitation, especially at low pressure. This positive effect enhances in turn the dissociation through reactions N1 and N2, counterbalancing the importance of electron impact dissociation at low pressure. On the other hand, at high pressures, the gas tends to lose its vibrational excitation faster and the dissociation becomes more and more thermal. Therefore, the effect of the vibrational excitation is less important. The recombination reactions were also found to have an important effect at high gas temperatures and high pressures, especially in the afterglow. They are one of the main reasons of the decrease of conversion and energy efficiency at pressures close to atmospheric pressure. This explains why a higher cooling rate in the afterglow is particularly beneficial for the conversion and energy efficiency at high pressure.

In general, our model predicts that a higher pressure and gas temperature, especially in the afterglow, have a negative effect on the conversion and energy efficiency, while a higher power density is beneficial. These findings can explain the high energy efficiencies obtained with a supersonic gas flow, as the latter setup combines a reduced pressure and temperature with high power density.

The model provides interesting suggestions to enhance the CO_2 conversion and energy efficiency by identifying the limiting factors and how to take optimal advantage of the non-equilibrium in a MW discharge, either by applying a supersonic gas flow or a vortex flow, which leads to gas cooling, or by applying pulse power. Exploiting the non-equilibrium character of the MW plasma will increase the energy efficiency, which is a crucial aspect for the application. The trends observed in this chapter are also valid more in general, for other types of discharges. Chapter VIII focuses, more specifically, on the energy transfers occurring in a CO_2 plasmas.

CHAPTER VII

Uncertainties in the modeling results

The results presented in this chapter were published in [160]:

- A. Berthelot and A. Bogaerts. Modeling of CO_2 plasma: effect of uncertainties in the plasma chemistry. *Plasma Sources Science and Technology*, 26(11):115002, 2017. DOI: 10.1088/1361-6595/aa8ffb

VII.1 Introduction

One of the main issues encountered when developing kinetics models is the reliability of the rate coefficients and cross sections used. This issue was first brought to the attention of the plasma community by M. Turner[161–163] for a helium-oxygen mixture. The large uncertainty that exists in some of the rate coefficients leads to an uncertainty in the modeling results, which hinders their predictive capacities. Moreover, most papers refer to other papers using the rate coefficients cited in these papers and they do not refer to (or check) the original references where the expressions for these coefficients were determined. This leads to an increase in the chance of making a copy error.

Following this, several groups started verifying the rate coefficients and cross sections used for CO_2 modeling. Grofulović *et al.*[104] proposed a set of cross sections for CO_2 plasmas by comparing swarm parameters to the results of a two-term Boltzmann solver and the available experimental data. In particular, they recommended, along with Bogaerts *et al.*[64], to use the Phelps 7eV excitation cross section[109] as a dissociation cross section, which we use in this chapter. Koelman *et al.*[60] performed a first step toward the verification of the rate coefficient data and compared the results of two different global models using the same chemistry set.

The aim of this chapter is to find the original source of the rate coefficients that we use in our CO_2 kinetics model and to understand how the uncertainty in the input rate coefficients and cross sections leads to uncertainties on the model output, thus giving an idea on the reliability of the model, both qualitatively and quantitatively, following the method proposed by M. Turner[161]. A statistical treatment of the data is used to pinpoint which rate coefficient has most effect on different outputs. This chapter should be seen as a first step towards building a more reliable database for CO_2 plasma kinetics. It stands as the continuation of the work initiated by Koelman *et al.*[60]

This chapter is organized as follows. In section VII.2, we first describe the model, and the conditions used in the model (in section VII.2.1) as well as the chemistry set considered in this chapter (section VII.2.2). In section VII.2.3, we explain the procedure used to determine the uncertainty in the output and in section VII.2.4, we explain the statistical treatment used to treat the data. The results are presented in section VII.3. This section contains two subsections. In section VII.3.1 we show the uncertainty in different model outputs (electron temperature and density, vibrational distribution function of the asymmetric stretch mode of CO_2 and CO_2 conversion) for different conditions. In section VII.3.2, we illustrate which rate coefficients are mainly responsible for the uncertainty of the various model results and we give some recommendations for good practice in chemical kinetics modeling. Finally, conclusions are given in section VII.4.

VII.2 Model description

VII.2.1 Plasma model

A zero-dimensional chemical kinetics model using the code ZDPlasKin[100] is developed, using the reduced chemistry set presented in table III.1 in chapter III. The density of each of the plasma species n_s is calculated using equation (II.28) in chapter II. The chemical kinetics part is here also coupled, within the ZDPlasKin framework, to the Boltzmann solver BOLSIG+[65].

The electron energy distribution function (EEDF) is calculated using the same set of cross sections used for the kinetic part (Table A.6 in appendix A.2), including superelastic collisions. The electron mean energy is obtained from the EEDF, providing also the electron temperature. During the simulation, the EEDF is regularly updated to reflect the changing chemical composition due to CO_2 conversion into CO and O_2 and the change in the value of the reduced electric field. Namely, the EEDF is updated if the gas temperature or the electron density change more than 3%, or if the reduced electric field or the density of a species reacting with electrons change more than 0.1 %. Calculating the EEDF is computationally expensive and updating it more often would result in a much longer computational time, which this kind of study cannot afford.

The model starts with pure CO_2 and a Boltzmann vibrational distribution function at t=0. A power deposition P_{dep} is applied until the Specific Energy Input (SEI) reaches 1 eV/molec and then drops to 0. The gas temperature T_g and the pressure p are kept constant and are considered as parameters in this study. The power density is taken proportional to the pressure, as in the previous chapter VI. This is done to ensure that the ratio between power density and pressure is constant, so that the data is comparable over different pressures. Naturally, we expect the situation in reality to be more complex.

The plasma-on time can be defined as:

$$\tau = \frac{e}{k_B} \frac{p}{P_{dep} T_g} \times 1[eV/molec] \tag{VII.1}$$

where e, the elementary charge, is used to convert eV to J. Since P_{dep} is chosen proportional to the pressure p in all cases, τ does not depend on the pressure.

The CO_2 conversion is here calculated following:

$$X(t)(\%) = \frac{n_{CO}(t)}{n_0 - \frac{1}{2} n_{CO}(t)} \tag{VII.2}$$

where $n_{CO}(t)$ is the total CO density (all CO species) at a time t and $n_0 = \frac{p}{k_B T_g}$

is the initial CO_2 density. The second part of the denominator originates from the gas expansion[164]. Since the model considers an isobaric process, the volume is not fixed and this needs to be taken into account when calculating the conversion. Note that equation (V.13) cannot be used here, since the model does not consider the plug-flow approximation.

VII.2.2 Chemistry set

The chemistry set used in this chapter contains the species listed in table III.1 in chapter III. It is important to note that this chemistry set has been reduced compared to the previous chapter VI, based on our previous chemistry reduction in chapter V. This simplification of the chemistry set is justified by the fact that some species only have a minor contribution to the outcome of the model. Therefore, they do not bring additional important information, given the uncertainty existing on the different outputs of the model (see results), while making the task of retrieving all the original sources much more complex. More generally, we would like to point out that adding more complexity in the plasma kinetic models does not necessarily give a better outcome of the simulation, since the chemistry of the more rare species is usually poorly known. Moreover, although included to some extent, the chemistry of CO and O_2 is described in less detail in this model than the chemistry of CO_2, which is justified because of the low CO_2 conversion at the conditions under study. A more detailed description of these species might be needed at conditions where these species are present in higher densities (i.e. higher CO_2 conversion).

The list of the different reactions considered in this chapter is given in appendix A.2. The reaction rates have often been updated after a source verification (see section VII.2.3), compared to the previous chemistry set shown in appendix A.1.

Table A.6 shows the electron impact reactions that use cross section data to retrieve the rate coefficients. Table A.7 presents the electron impact reactions described by analytic expressions for the rate coefficients. Table A.8 shows the list of reactions involving ions. Table A.10 presents the reactions between neutral molecules, and finally table A.9 lists the reactions between the different vibrational levels. The procedure used to calculate the rate coefficients of the reactions involving vibrationally excited molecules is described in detail in chapter III.

VII.2.3 Uncertainty determination and computational procedure

Most experimentally derived expressions for the rate coefficients are given in the form of Arhenius expression VII.3.

$$k = AT_g^B exp(-E_a/k_B T_g) \tag{VII.3}$$

where k is the rate coefficient, k_b is the Boltzmann constant, T_g the gas temperature. E_a the activation energy, and A and B are coefficients that are experimentally or theoretically determined. Note that reactions that involve electrons typically show an additional dependence to the electron temperature. One of the most important parts of this work was to retrieve the original source for each expression. We have done this as much as possible in order to estimate the uncertainty in the rate coefficients. Naturally, our choice of sources is also subject to errors and we invite the reader to form a critical opinion and to systematically check the primary source of the data.

The uncertainty can be considered to be contained in the parameter A, as long as the rate coefficient is used in the parameter range considered in the determination of the analytical expression, i.e. $\frac{\Delta k}{\overline{k}} = \frac{\Delta A}{\overline{A}}$, where ΔX refers to the uncertainty in a quantity X and $\overline{X}$ refers to its mean value.

The procedure used in this chapter is very similar to the initial work of M. Turner on this matter[161]. First, we assume that the probability of each rate coefficient for having a certain value can be derived from a log-normal distribution. As pointed out in Turner[161], this choice is debatable as some of the extreme values for the rate coefficients may be non-physical. Nevertheless, we believe that it gives a good estimation of the uncertainty of the model and this study focuses on the different quantiles in the outcome of the simulations, in order to avoid these non-physical values. The probability $f(A_n = x_A; \Delta A, \overline{A})$ that the coefficient A in expression VII.3 has a value x_A, given its uncertainty ΔA, is given by a log-normal distribution[165]:

$$f(A_n = x_A; \Delta A, \overline{A}) = \frac{1}{x_A \sigma \sqrt{2\pi}} exp(-\frac{ln(x_A - \mu)^2}{2\sigma^2}) \tag{VII.4}$$

where μ and σ are parameters that contain the mean value of A ($\overline{A}$) and the error ΔA:

$$\mu = ln(\frac{\overline{A}}{(\Delta A)^2 + \overline{A}^2}) \sigma = \sqrt{(ln(1 + (\frac{\Delta A}{\overline{A}})))} \tag{VII.5}$$

Then, we create a large number (N = 400) of different combinations of rate coefficients. Each rate coefficient k_n of a given combination n is chosen randomly based on the probability density described in equation VII.4. For rate coefficients k' that are derived from another rate coefficient k (scaling laws, see section III.2), we multiply the scaled rate coefficient $\overline{k'}$ by a factor $\frac{k_n}{\overline{k}}$, i.e. $k'_n = \overline{k'} \frac{k_n}{\overline{k}}$ for each chemistry set n.

The model is ran using each combination of rate coefficients (i.e. 400 different inputs) and the different outcomes are compared, which gives an estimation on the error of the calculation results. An analysis of the correlation between the input value taken for a rate coefficient and a certain output gives us an indication of which reaction is important for this output.

It is important to note that only the uncertainty in the original rate coefficients is considered here. The uncertainty in the model results is in reality likely to be larger due to possible systematic errors, especially the error made when using the different scaling laws and the fact that not all vibrational states are considered in the model. The goal of this research is to understand how, and to which extent, the error on the rate coefficients propagates to the results of the model.

VII.2.4 Statistical treatment

This study has two main goals: (i) to quantify the uncertainty in the modeling results due to the uncertainty in the rate coefficients and (ii) to identify the main sources of uncertainty.

For the first part, the results will be shown using different colors delimiting the different chosen quantiles. This illustrates the distribution of the data at any given abscissa. The median value will be presented by a black line.

When comparing different conditions, error bars have been drawn. They delimit the data within a confidence interval of 70 %, determined by the quantiles corresponding to the first 15 % and 85 % of the data (X_{15},X_{85}). For simplicity, we call the quantile delimiting the first p % of the data X_p in this study. The relative difference between upper and lower quantiles is also shown, as it gives a good estimation of the relative error for a given confidence interval (see VII.3.1). Note that the distribution of the data within the interval $[\overline{X}\text{-}\sigma_X,\overline{X}+\sigma_X]$ in a normal distribution, where σ_X is the standard deviation, is about 68 %. This explains our choice of a confidence interval of 70 %, although the distribution of the data is not symmetrical in our case.

For the second part of this study, the built-in Matlab® tools for correlations are used to rank which input is mostly correlated with which output. This information together with the uncertainty in the corresponding rate coefficients allows us to identify the main sources of uncertainty in a given output (see VII.3.2). In particular, the Spearman's ρ rank correlation coefficient is used[166]. It is the common linear correlation coefficient, using the rank variables instead of the variables themselves.

It measures how monotonic a particular model output f(x) is as a function of a model input x. It has the advantage, in comparison to a standard correlation coefficient, to also detect non-linear correlations. ρ varies between -1 and +1. A value of 0 means that there is no monotonic relationship between the input and the output. An absolute value of 1 means that the function f(x) is perfectly monotonic with x. The sign of ρ gives information on whether the function is increasing (positive ρ) or decreasing (negative ρ). In this chapter, following several estimations, we considered that only an absolute value of ρ larger than 0.3 is significant.

VII.3 Results and discussion

VII.3.1 Quantification of the uncertainty in the plasma variables

As mentioned earlier, it is crucial for the reliability of a model to know the uncertainty in its output. These uncertainties can for sure hinder the quantitative predictive capacities of a model, but they might also have an influence on the qualitative predictions. This section aims at understanding the effect of the uncertainties of the rate coefficients on several outputs of our CO_2 0D chemical kinetics model, namely the electron temperature (figure VII.1), the electron density (figure VII.2), the vibrational distribution function (VDF, figures VII.3 and VII.4) and the CO_2 conversion (figures VII.5 and VII.6).

Showing the solutions of the model for the N=400 combinations of rate coefficients is obviously not desirable. Therefore, in figures VII.1, VII.2, VII.3 and VII.5 we opted for a representation using different colors. Each color delimits a confidence interval. The confidence intervals of 90%, 70%, 50 % and 25 % are represented in yellow, orange, red and dark red, respectively. They correspond to the following intervals, respectively: [X_5,X_{95}], [X_{15},X_{85}], [X_{25},X_{75}], [$X_{37.5}$,$X_{62.5}$]. The black curve shows the median value.

Additionally, in order to quantify more precisely the dispersion of the data, we show the relative difference $(X_U - X_L)/X_{50}$ between the upper quantile X_U and the lower quantile X_L, using the right y-axis. The dotted line gives the relative difference for the interval [X_{15},X_{85}], hence a confidence interval of 70 %, while the dashed line gives the relative difference for the interval [$X_{37.5}$,$X_{62.5}$], hence a confidence interval of 25 %.

Since the uncertainty is typically condition-dependent, figures VII.1, VII.2 and VII.5 show the results for four different conditions:

a) Basic case: 200 mbar, 200 $W.cm^{-3}$, 300 K, τ = 3.87 ms

b) Higher pressure: 1000 mbar, 1000 $W.cm^{-3}$, 300 K, τ = 3.87 ms

c) Higher power density: 200 mbar, 1000 $W.cm^{-3}$, 300 K, τ = 0.77 ms

d) Higher temperature: 200 mbar, 200 $W.cm^{-3}$, 2000 K, τ = 0.58 ms

The residence time τ varies upon the parameters chosen, as the latter is defined by the time needed to reach an SEI of 1eV/molec, cf equation VII.1. The letter of the different panels corresponds to the letters of this list. These conditions correspond to typical conditions encountered in microwave plasmas or in other types of discharges, and were used in the previous chapter VI as well.

More specifically, figure VII.1 shows the electron temperature T_e for these four conditions. The end of the power pulse (τ) is indicated by the vertical dash-dot black line. At 300 K (figure VII.1 a, b and c), T_e shows the same behavior: a very short and sharp increase at t = 0, followed by a decrease until approximately t = 0.1 ms (barely visible in the figure) and a slower increase until a stable value is reached. T_e then drops almost immediately to 0 at the end of the power pulse. The uncertainty (defined as the relative difference between the values lying 35 % above or below the median value, i.e., a confidence interval of 70 %; see above) is here between 10 % (figure VII.1 a, b) and 15 % (figure VII.1 c) in the plasma (dotted line).

At 2000 K (figure VII.1 d), the behavior is slightly different: T_e increases sharply at t = 0 and then decreases for about 0.1 ms. Then, it reaches a rather stable value around 1 eV until the end of the plasma. The uncertainty is lower, around 5% in the plasma.

It is important to note that while the error on the electron temperature may appear small, it can have a major effect on the electron impact rate coefficients, since they are particularly sensitive to the electron energy.

Figure VII.2 shows the calculated electron density n_e. The absolute value of the electron density depends on the conditions. However, the four curves follow a similar trend: n_e rises quickly at the beginning of the power pulse and reaches a stable value after less than 0.1 ms. At the end of the power pulse, the electron density decreases exponentially. The error is typically 10 % or below in the plasma. In the afterglow, particularly in the beginning at 300 K, we see a sharp increase of the uncertainty, reaching up to 90 %. With decreasing electron density, the uncertainty decreases as well, to values ranging from 20 to 50 %. This sharp increase in the uncertainty is caused by the fact that a different choice of rate coefficients has a large effect on the decay time of the electron density. However, the electron density in the afterglow does not play a significant role in the CO_2 conversion at this relatively high pressure, so this uncertainly will be of minor importance to the overall uncertainty of the model.

At 2000 K, the uncertainty remains rather low and increases from about 5 % to a bit more than 15 %.

Figure VII.3 shows the VDF at the beginning of the plasma (t = 0.1 ms, figure VII.3a and b) and at a later stage of the plasma (t = 2 ms in figure VII.3c and t = 0.5 ms in figure VII.3d). Only two conditions are presented here: the basic case (200

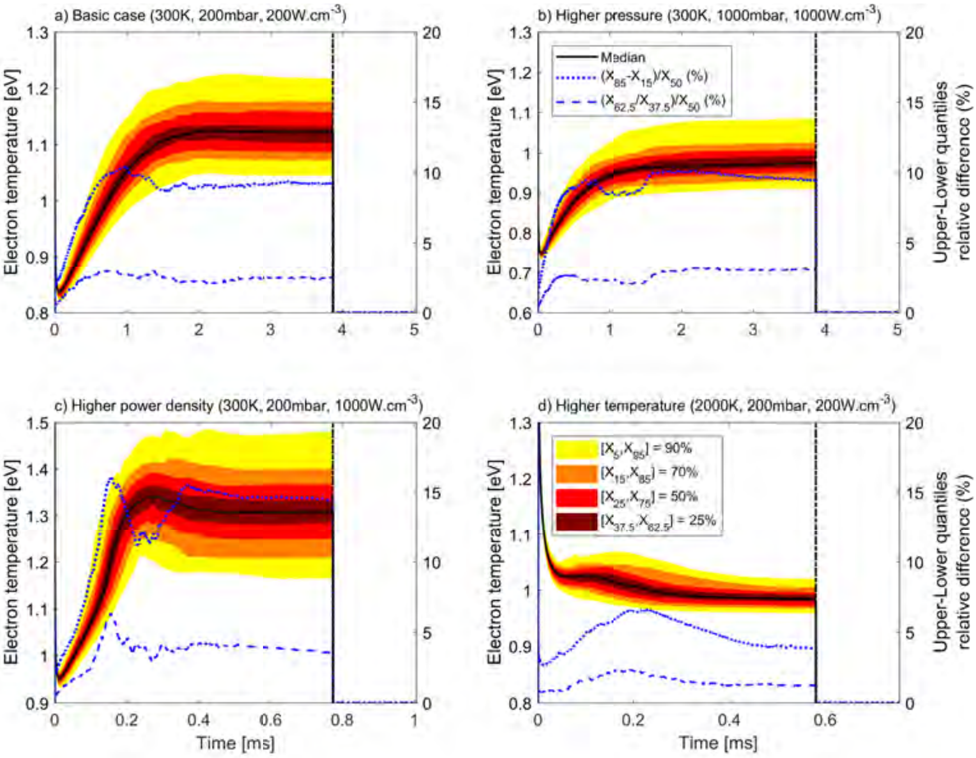

Figure VII.1: Electron temperature (left y-axis) as a function of time for four different cases. The different colors delimit different quantiles of the N = 400 solutions at each time. The median value is shown by the black curve. From lighter to darker, they correspond to 90%, 70%, 50% and 25% of the solutions. The end of the pulse is represented by the vertical dashed black line. The relative difference between the upper and the lower quantiles (right y-axis) are shown with the dotted blue line (corresponding to the orange zone; confidence interval of 70 %) and the dashed blue line (corresponding to the dark red zone; confidence interval of 25 %).

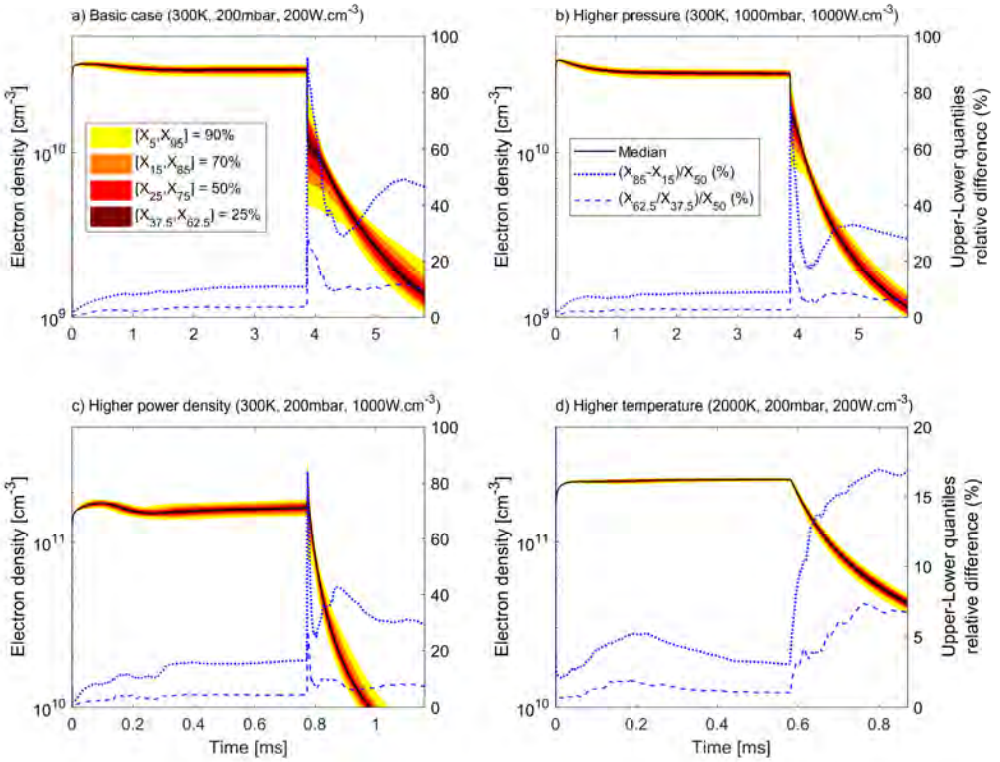

Figure VII.2: Electron density (left y-axis) as a function of time for four different cases. The different colors delimit different quantiles of the N = 400 solutions at each time. The median value is shown by the black curve. From lighter to darker, they correspond to 90%, 70%, 50% and 25% of the solutions. The relative difference between the upper and the lower quantiles (right y-axis) are shown with the dotted blue line (corresponding to the orange zone; confidence interval of 70 %) and the dashed blue line (corresponding to the dark red zone; confidence interval of 25 %).

mbar, 200 W.cm^{-3}, 300 K, τ = 3.87 ms) and the higher temperature case (200 mbar, 200 W.cm^{-3}, 2000 K, τ = 0.58 ms). Indeed, the results at higher pressure or power density are similar to those of the basic case.

The typical non-equilibrium shape of the VDF described in the previous chapter VI is present for the basic case (figure VII.3 a and c), i.e. at low gas temperature. The increasing population of the vibrationally excited states over time is visible by comparing figure VII.3a and figure VII.3c. Using the population of the first asymmetric mode, we can associate a vibrational temperature to the VDF, giving an estimation of the extent of vibrational excitation. At t = 0.1 ms (figure VII.3a), the vibrational temperature varies between 830 K and 978 K (for a confidence interval of 70 %), with a median value of 900 K (hence an uncertainty of 16 %). At t = 2 ms (figure VII.3c), it varies between 1275 K and 1703 K (for the same confidence interval), with a median value of 1472 K (hence, an uncertainty of 29 %).

The uncertainty in the VDF also increases with time, ranging from 50 % to 300 % for the population of different energy levels at t = 0.1 ms and between 50 % and 1400 % at t = 2 ms. Indeed, the error on the densities on the vibrational levels builds up over time and there are no mechanisms that compensate this build-up, which explains the increase of the uncertainty. The uncertainty in the VDF is thus large and can reach more than an order of magnitude. This is expected since many reactions occur between the vibrational levels and they are particularly important in determining the VDF. Thus, a small error on the original VT and VV rates coefficients can have much larger consequences on the VDF.

On the other hand, at a temperature of 2000 K (figure VII.3 b and d), the VDF stays rather constant and resembles a Boltzmann distribution. This behavior was also observed previously (chapter VI) and is attributed to the fast VT relaxation occurring at high gas temperature. The vibrational temperature is about 2000 K at all time, with no significant dispersion of the results. Since the large VT transfers bring the VDF back to a Boltzmann distribution, the uncertainty is here much lower. It ranges from 5 % to 45 % and does not really change over time.

Similarly, using the population of the 4 symmetric states, we can obtain a vibrational temperature for the symmetric states. At t = 0.1 ms and with a gas temperature of 300 K, a pressure of 200 mbar and a power density of 200 W.cm^{-3}, corresponding to the basic case, we obtain the following median temperatures for the vibrational symmetric mode levels v_a, v_b, v_c and v_d: $T_{va} = 320K$, $T_{vb} = 472K$, $T_{vc} = 565K$ and $T_{vd} = 519K$. Using a confidence interval of 70 %, the uncertainties are 10 %, 13 %, 12 % and 6 %, respectively. At t = 2 ms, the symmetric temperatures are $T_{va} = 1111K$, $T_{vb} = 1346K$, $T_{vc} = 1386K$ and $T_{vd} = 795K$. The uncertainties are 92 %, 67 %, 60 % and 22 %, respectively. Note that the vibrational energy of the symmetric levels is rather low.

Their population is thus comparable to the ground state population, which explains the high sensitivity of their temperatures to the uncertainties of the rate coefficients. At this high level of symmetric excitation, inter-mode energy exchanges can become important[167]. These non-linear effects are partly included in the model for the low-energy levels through reaction V5 (see table A.9 in appendix A.2), but not for the higher energy levels, as this would lead to a complexity that is beyond this study.

Thus, the uncertainty in the VDF depends a lot on the conditions, as seen in figure VII.3. Given the magnitude of the uncertainty, one question then arises: to which extent are the trends observed in the calculations for different conditions still valid, keeping in mind the uncertainties? Figure VII.4 shows the vibrational distribution function for the four different conditions studied here at a time t = 0.1 ms (figure VII.4a) and t = 0.5 ms (figure VII.4b). Error bars are added, corresponding to a confidence interval of 70 %, i.e. delimiting the interval $[X_{15},X_{85}]$.

At t = 0.1 ms (figure VII.4 a), we see that the high pressure case and the high gas temperature case exhibit a smaller uncertainty. Indeed, the VDF is then closer to equilibrium and is thus easier to predict. In typical experimental cases, because of the high gas temperature, extreme non-equilibrium conditions are very difficult to reach. On the other hand, for the basic case and particularly for the high power density case, the uncertainty can become very large, even at the beginning of the simulation. It is also interesting to note that in the high pressure case, the uncertainty is maximum for the highly excited vibrational levels.

Nevertheless, the trends observed previously (chapter VI), namely that the importance of higher vibrational levels increases with power density and decreases with temperature and pressure, are still visible and the difference between the VDFs is still significant.

At t = 0.5 ms (figure VII.4 b), the trends are still the same, although vibrational excitation has had time to build up, which is particularly visible on the curve showing the high power density case. It is especially interesting to see that the uncertainty increases for the basic case but is drastically reduced for the high power density case.

This can be explained by the fact that vibrational excitation (i.e., vibrational ladder climbing) is building up at t = 0.1 ms. There, the results are thus very sensitive to the chosen combination of rate coefficients and very large uncertainties can occur. However, once the vibrational ladder climbing has built up and has reached a sufficient population, the CO_2 molecules begin to dissociate very quickly, which seems to significantly reduce the uncertainty.

Figure VII.5 shows the CO_2 conversion as a function of time for the four different conditions listed above. The end of the power pulse is indicated by the vertical black dotted line. The trends are rather similar in all cases: the CO_2 conversion increases

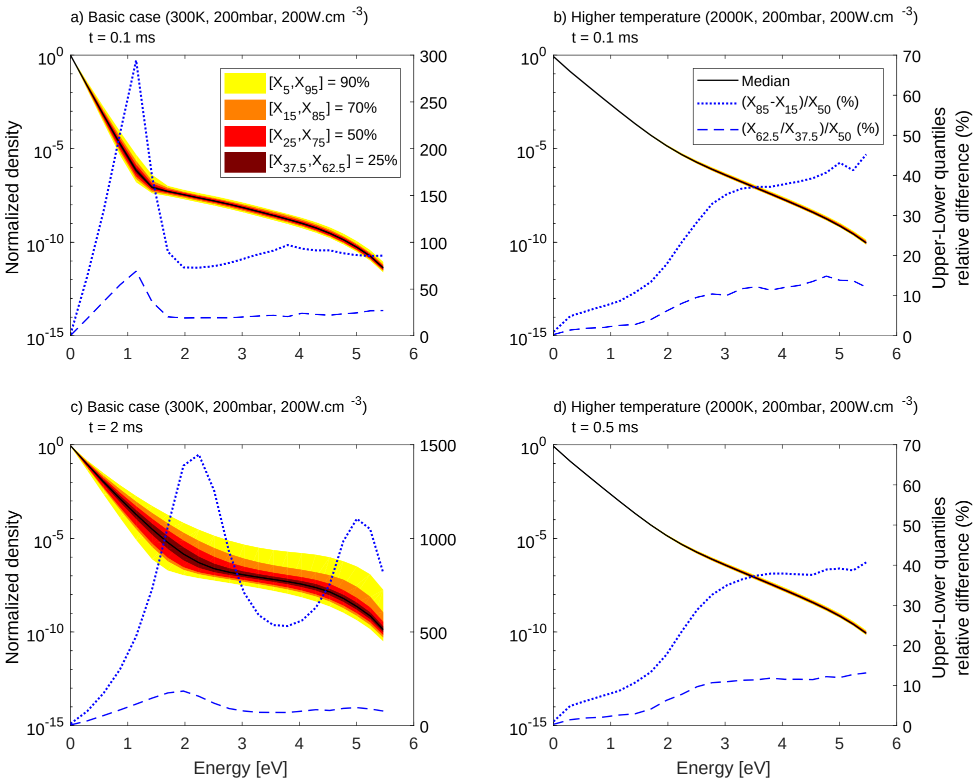

Figure VII.3: Vibrational distribution function (left y-axis) at the beginning of the power pulse (t = 0.1 ms, panels a and b) and at a later stage in the power pulse (t = 0.5 and 2 ms, panels d and c, respectively) for the basic case (panels a and c) and the higher temperature case (b and d). The median value is shown by the black curve. The different shades delimit different quantiles of the N = 400 solutions. From lighter to darker, they correspond to 90%, 70%, 50% and 25% of the solutions. The relative difference between the upper and the lower quantiles (right y-axis) are shown with the dotted blue line (corresponding to the orange zone; confidence interval of 70 %) and the dashed blue line (corresponding to the dark red zone; confidence interval of 25 %).

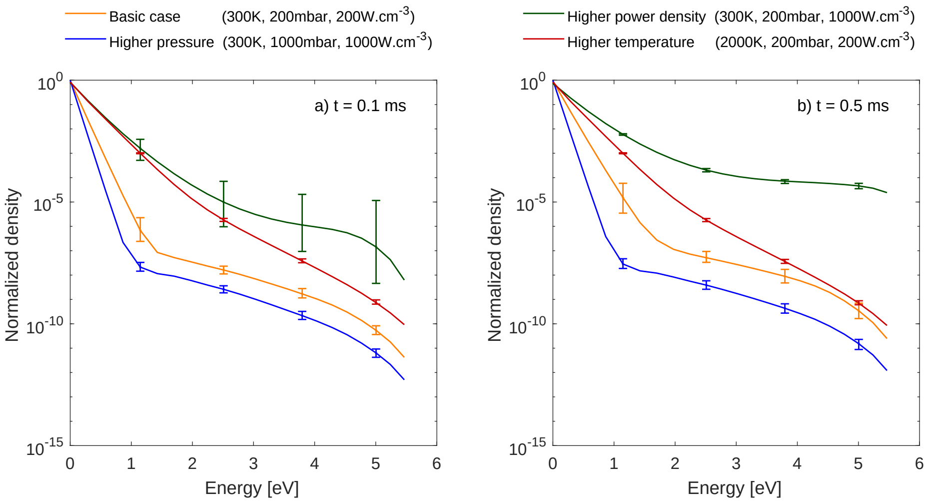

Figure VII.4: Median value of the vibrational distribution function at t = 0.1ms (panel a) and at t = 0.5 ms (panel b) for different conditions (see legend). The error bars delimit the interval [X_{15},X_{85}], corresponding to a confidence interval of 70%.

linearly inside the plasma and then stays constant, although it slowly increases in the 2000 K case (figure VII.5 d). This slow increase at 2000 K is due to thermal conversion, that does not require plasma. Note that at low gas temperature (figure VII.5 a, b and c), the conversion starts with a short delay after the beginning of the power pulse (at t = 0). This is particularly visible in figure VII.5c, and it is due to the time that the vibrational levels require to be populated first, before they can give rise to conversion.

The uncertainty is quite large and relatively constant in figure VII.5 a, b and d, between 70% and 110 %. In figure VII.5 c, it reaches more than 250 % at the beginning of the conversion and then stabilizes at a bit more than 50%. This can be understood by knowing that most of the conversion originates from vibrationally excited CO_2 in this case. Since the build-up time of the vibrational population is not the same with all combinations of rate coefficients, as mentionned above, there is a delay between the beginning of the conversion from one simulation to the other. This means that simulations with practically zero conversion in the beginning are compared to simulations where the conversion is already non-negligible, causing a large uncertainty. Eventually, as we have seen in figure VII.4 b, since the vibrational excitation becomes very large in the vast majority of the simulations, the conversion happens and the uncertainty reaches more reasonable values, although it is still quite large.

The different values of conversion, calculated long after the end of the plasma pulse,

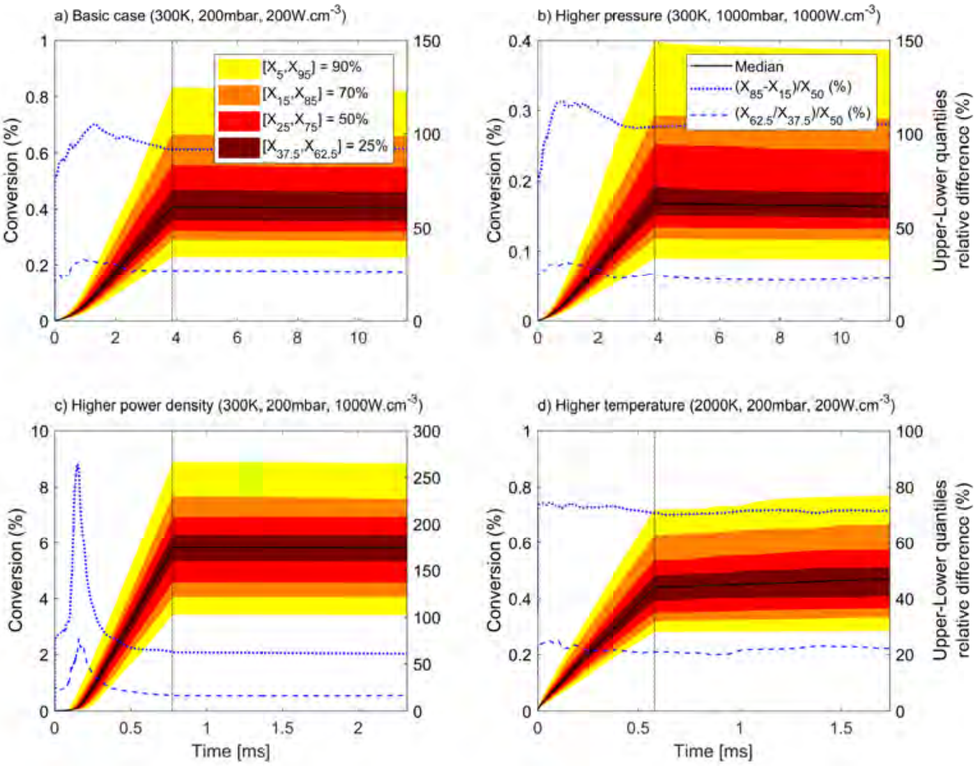

Figure VII.5: CO_2 conversion as a function of time for four different cases. The different colors delimit different quantiles of the N = 400 solutions at each time. The median value is shown by the black curve. From lighter to darker, they correspond to 90%, 70%, 50% and 25% of the solutions. The relative difference between the upper and the lower quantiles (right y-axis) are shown with the dotted blue line (corresponding to the orange zone) and the dashed blue line (corresponding to the orange zone; confidence interval of 70 %) and the dashed blue line (corresponding to the dark red zone; confidence interval of 25 %).

at t = 50 ms, are plotted as a function of pressure in figure VII.6. In the basic case, as we have also seen in figure VII.5, the conversion is very low: it drops from 1.4 % at 100 mbar to 0.5 % at 1000 mbar. The conversion in the high temperature case is around 0.7 %, independent from the pressure. The higher power density yields a much larger conversion at low pressure, reaching 8 % at 100 mbar, but decreasing to 0.5 % at 1000 mbar. The uncertainties are particularly important for low pressures and high power deposition, at low gas temperature.

These results indicate that there is a threshold of power density above which vibrationally-induced dissociation becomes important. This threshold depends on pressure and on gas temperature, as we have also seen previously (chapter VI). Under this threshold, dissociation is either due to electron impact dissociation or to thermal processes and the non-equilibrium aspect of the plasma is not fully exploited. This also has an effect on the uncertainties: vibrationally-induced dissociation is a complex mechanism and an accurate prediction of its magnitude requires using multiple reactions. The most important reactions are vibrational-translational (VT) relaxations, vibrational-vibrational (VV) relaxations and electron-vibration energy transfers (e-V). Naturally, the uncertainty in all these reactions builds up on the final result. On the other hand, electron impact dissociation and thermal dissociation are the result of much simpler processes, which allows for more accurate predictions.

Note that the values of conversion appear to be low in comparison to experiments, especially in the basic and the high temperature case. It is worth mentioning that these test scenarios cannot be transposed to complex experimental cases, due to their simplicity. They are chosen to be simple in this study on the uncertainties of our CO_2 chemical kinetics model in order to be able to analyze the data and to understand the source of the uncertainties.

VII.3.2 Correlations between uncertainties in the model results and responsible reactions

The aim of this section is to understand which reactions have a substantial effect on the model results. We focus here on the CO_2 conversion and the vibrational excitation, as they are very important for the application and they are characterized by the largest uncertainties, as seen in section VII.3.1 above. Indeed, for those calculation results with lower uncertainties, like the electron temperature and density, it was found difficult to draw meaningful conclusions about the effect of specific reactions.

To grasp the concept of the Spearman's rank correlation coefficient described in section VII.2.4, figure VII.7 shows the values of the calculated CO_2 conversion as a function of the relative value of the rate coefficient for electron impact excitation to the

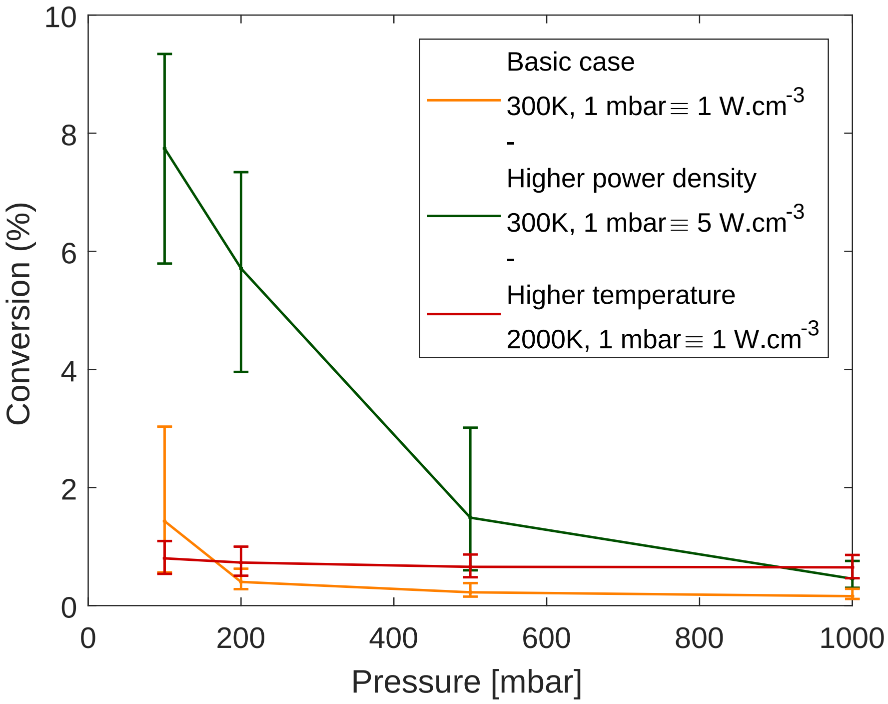

Figure VII.6: Calculated conversion as a function of pressure for different conditions: two different gas temperature, $T_g = 300K$ (yellow and green curve) and $T_g = 2000K$ (red curve); two different power depositions, low (orange and red curves) and high (green curve). The error bars delimit the interval [X_{15},X_{85}], corresponding to a confidence interval of 70%. The conversion is calculated at t=50ms.

asymmetric mode vibrational levels (any of the levels), for two conditions: the basic case (igure VII.7 a) and the high power density case (figure VII.7 b). The same data was used in figure VII.6: each scatter plot in figure VII.7 corresponds to one conversion data point and error bar in figure VII.6.

The Spearman's ρ coefficient is calculated to be 0.15 and 0.69, in the basic and the high power density case, respectively. Indeed, figure VII.7 shows that the correlation between the calculated CO_2 conversion and the rate coefficient for vibrational excitation is obvious in the high power density case, while no trend stands out in the basic case.

This information is summarized, and extended also to other reactions, in figure VII.8, which shows the Sperman's ρ coefficient for the four conditions indicated, between the CO_2 conversion and the rate coefficients of seven important reactions. The other rate coefficients did not show any noticeable trend (i.e. $\rho < 0.3$). The results for the basic case and the higher pressure case are similar. In both cases, electron

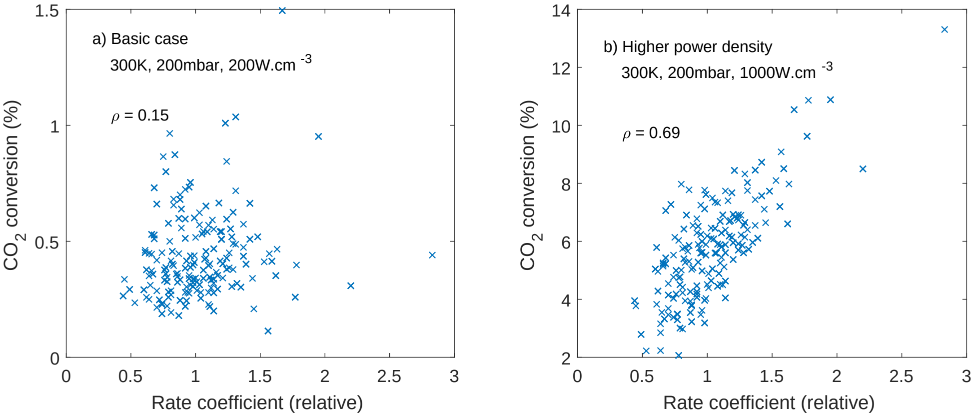

Figure VII.7: Scatter plot of the CO_2 conversion calculated at t=50ms as a function of the relative rate coefficient for electron impact vibrational excitation to the asymmetric mode levels, i.e. $k_n/\overline{k}$ for two different conditions (a: basic case - b: high power density case). In each panel, each of the N=400 points corresponds to a simulation made with a different choice of rate coefficients. The Spearman's ρ correlation coefficient is indicated in both cases.

impact dissociation (X4) is, by far, the main source of uncertainty. Reaction (I9), i.e. a formation process of CO_2 upon collision of a negative ion with O atoms, is the second source of uncertainty. Indeed, since electron impact dissociation is the main dissociation mechanism at these conditions, the ion kinetics, which is strongly related to the electron kinetics, is also important. No other significant correlations were found.

At higher temperature, electron impact dissociation (X4) is still the main source of uncertainty, followed by CO_2 dissociation upon O atom impact (N2). Kozák and Bogaerts[57] also reported that modifying the activation energy of this reaction has a large effect on the conversion. The uncertainty in this rate coefficient is large, causing a large effect on the CO_2 conversion.

At higher power density, more reactions were found to be significant. The main correlation was found with electron impact asymmetric mode vibrational excitation (X7) (also shown in figure VII.7 b), followed by electron impact symmetric mode vibrational excitation to CO_2v_a and CO_2v_b, (X6a) and (X6b), respectively. Increasing the rate coefficient of reaction (X4), (N2) and (X7) has a beneficial effect on the conversion. The correlation coefficient for the other rate coefficients is too low (< 0.3) to draw reliable conclusions about their effect on the CO_2 conversion

It is also found that increasing the VT reaction rate coefficient (V1) has a detrimental effect on the CO_2 conversion in the high power density case. These trends

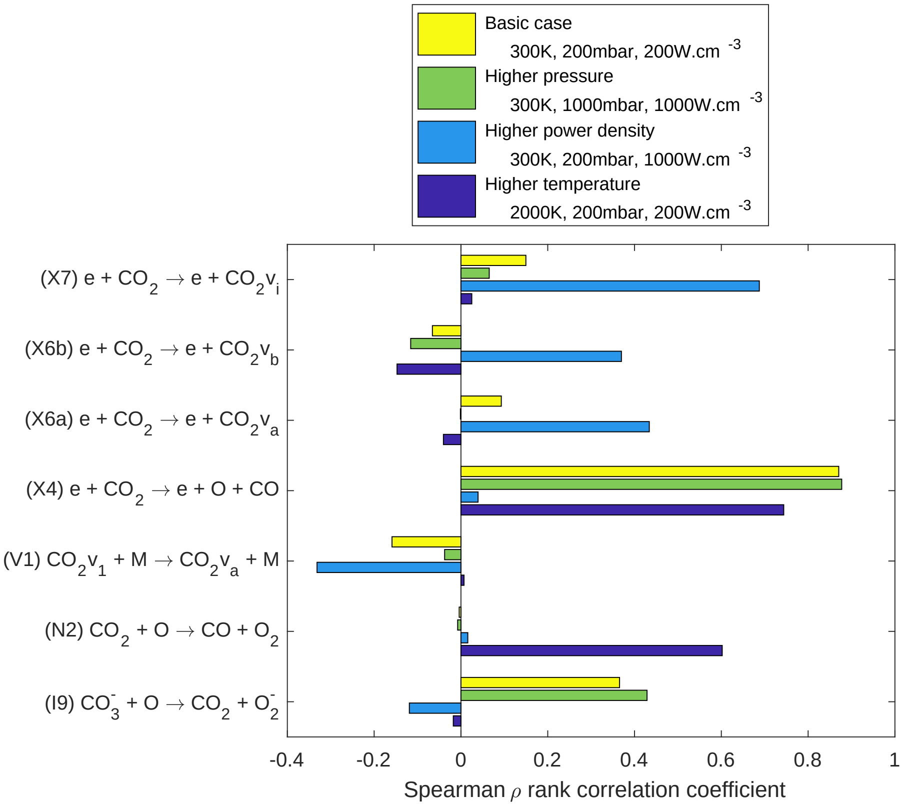

Figure VII.8: Spearman's ρ rank correlation coefficient between the calculated CO_2 conversion at t=50ms and the rate coefficients of different reactions for four different conditions (see legend). The coefficients are only shown when the CO_2 conversion exhibits a clear dependence on the rate coefficient of that reaction, i.e. if $\rho > 0.3$ for one of the conditions.

correspond to our previous observations, showing that at higher power density, the dissociation mainly originates from vibrationally excited levels. Therefore, the main source of uncertainty arises from the reactions that are needed to obtain the VDF.

Figure VII.9 shows the obtained Sperman's ρ coefficient for the four conditions indicated between the density of one of the highest asymmetric mode vibrational levels of CO_2, i.e. CO_2v_{20}, and the rate coefficients that are found to yield the most significant correlations. Figure VII.9a considers the CO_2v_{20} density at t = 0.1 ms while figure VII.9 b shows the CO_2v_{20} density at t = 0.5 ms, corresponding to figure VII.4a and b, respectively.

This particular asymmetric mode vibrational level was chosen since its determination leads to a large uncertainty, particularly in the high power density case at t = 0.1 ms, as observed in figure VII.4a.

At t = 0.1 ms (figure VII.9a), the basic case, the higher pressure case and the higher power density case show similar correlations. The main source of uncertainty is found to be reaction (X7), i.e., electron impact vibrational excitation. Increasing the rate coefficient of this reaction clearly enhances the density of CO_2v_{20}, which is logical. The VT relaxation reaction (V5) comes second, with a negative ρ coefficient, which is again logical. At higher temperature, X7 has again the main influence, but some more reactions play a role. Reactions N1, V1 and V2b show a similar negative correlation coefficient and X6c is found to have a clear positive correlation. The influence of N1 at higher temperature can be easily understood: for a highly excited level, the activation energy of dissociation reactions is lowered. Therefore, the activation energy of CO_2v_{20} is similar to the (relatively high) gas temperature, leading to a very high probability of dissociation by reaction N1.

At t = 0.5 ms (figure VII.9 b), similar correlations are observed for the basic and the high pressure case, although V1 seems to be more important than at t = 0.1 ms. The correlations for the high power density case are quite different from what we have seen above. N2 is now the main depopulating mechanism, followed by V1. The influence of X7 is lower here. At 2000 K, the observations made in figure VII.9 a are still valid. Indeed, at 2000 K, the VDF thermalizes very quickly and thus, there is no important change in the kinetics between the beginning and the end of the plasma.

To summarize our results, we see that the uncertainty in the model results clearly depends on the conditions and the type of output. Knowing the magnitude of the uncertainties is necessary for a valid interpretation of the modeling results. This study shows that the absolute values predicted by the model are subject to quite large uncertainties. The CO_2 conversion and vibrational excitation have been identified as particularly sensitive to the uncertainties on the rate coefficients. This is perfectly understandable since obtaining these values requires to calculate several other quantities, which are themselves subject to uncertainties. In other terms, these "final" outputs combine all the uncertainties from the other quantities.

Despite these findings, it is important to note that the trends observed previously (chapter VI) and in the previous work from our group[56;57] are still found back in the current study, accounting for the uncertainties. Given the complexity of the kinetics, this is a rather positive message. Indeed, when analyzing the results of a kinetic model, especially the more complex ones, one should be aware that the absolute values are subject to large uncertainties and the predictive power of such models is thus hindered. However, the trends that are predicted by the models seem to be valid and also contain very useful information.

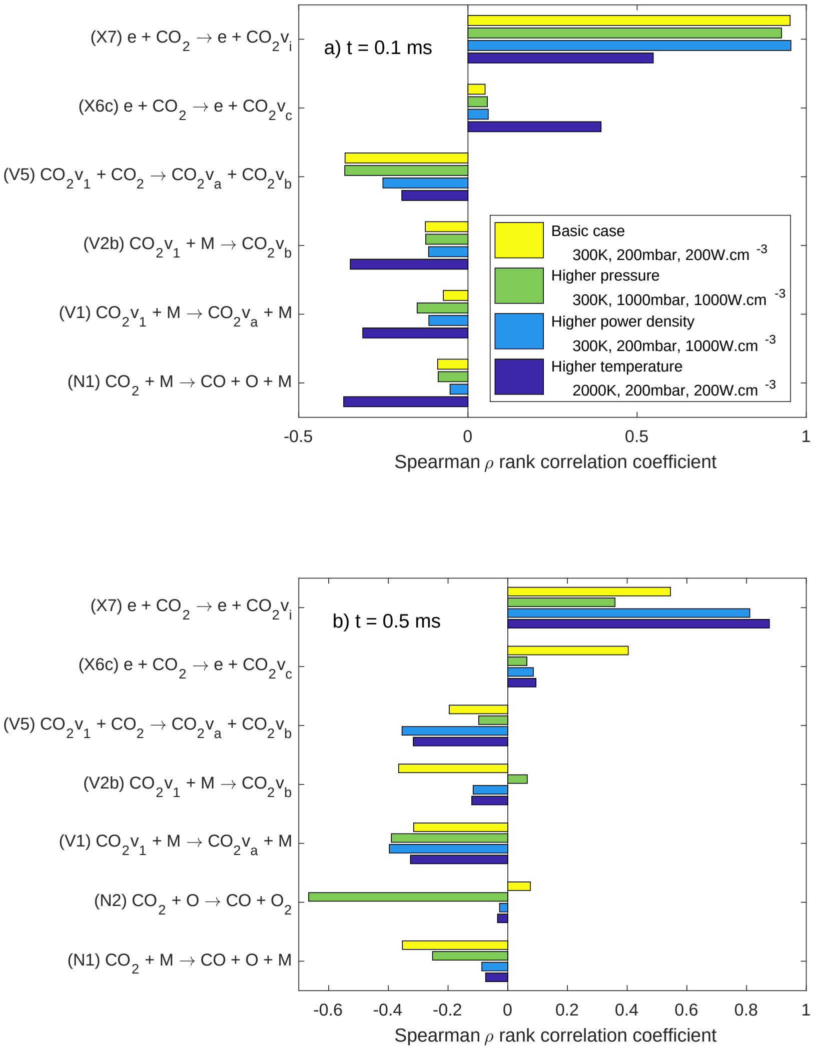

Figure VII.9: Spearman's ρ rank correlation coefficients between the calculated CO_2v_{20} density and the rate coefficients of different reactions for different conditions (see legend) at t = 0.1 ms (panel a) and at t = 0.5 ms (panel b). The coefficients are only shown when the CO_2v_{20} density exhibits a clear dependence on the rate coefficient of the reaction, i.e. if $\rho > 0.3$ for one of the conditions.

Note that, as mentioned earlier, this study is only a first step in the direction of the Verification and Validation (V&V) of the kinetic modeling results, which was described by Turner[163]. Naturally, the rate coefficients are not the only source of uncertainty in the model and more systematic errors may be present, such as the influence of the different scaling laws that are used. Errors in the code may also still be present, despite our best efforts to ensure that there are none.

In accordance with Turner, we recommend a (non-exhaustive) number of 'good practices' that should be adopted by the low-temperature plasma modeling community. First, and probably most importantly, the original source of the rate coefficient data should be cited as much as possible, along with mentioning the uncertainty of the data. We have tried to do this as much as possible in this chapter, although it is sometimes not possible to access the original sources. Second, a large database of verified rate coefficients would be particularly useful for the plasma modeling community. These databases exist in other fields, such as the UMIST database[168] for astrophysics or the NIST chemistry webbook[23] to some extent. This work is started in the plasma community by LxCat[169], which is an extensive database of electron and ion scattering cross sections, swarm parameters, etc. Third, this type of study is highly necessary so that the modeling results can be analyzed in light of the uncertainties that exist. Note that the calculation time might be a problem in more complex cases here, since the model needs to run for several hundreds of combination of rate coefficients, instead of just one.

Finally, when possible, we would recommend a more systematic attempt to validate the modeling results and the chosen rate coefficients against experimental values, particularly species and electron densities, in a rigorous manner. In order to validate the rate coefficients over a wider range of parameters, it would be beneficial to control parameters, such as the gas temperature and the reduced electric field, in these experiments. Thus, the experiments should be carried out in a simple design, like a glow discharge with parallel electrodes, not optimized for CO_2 conversion studies in terms of conversion or energy efficiency, but for controlled experiments. Moreover, using various conditions in these experiments would allow to benchmark (or discard) different rate coefficients at these different conditions, since the dominant mechanisms depend on the conditions considered.

VII.4 Conclusion

In this chapter, we have evaluated the effect of uncertainties in the rate coefficients on various calculation results, such as the electron density and temperature, the CO_2 conversion and the VDF. Using the uncertainty in the rate coefficients, which is typically in the order of 10-30 %, but can rise up to 100 % or even 200 %, a probability distribution was calculated for the rate coefficient of each reaction. Based on these probability distributions, 400 different combinations of rate coefficients have been created and used in the model for different conditions of pressure, power density and gas temperature to predict the uncertainty in the calculation results of the model. This method indeed shows how the uncertainty present on the rate coefficients propagates to the final results.

The electron density and electron temperature show relatively small errors, in the range of 15 % inside the plasma. The error on the electron density in the afterglow is more important, reaching up to 90 %, but will not be very critical due to the lower values of the electron density. The error on the population of the vibrational levels is much larger, reaching up to two orders of magnitude. This error is smaller when increasing the gas temperature and/or the pressure, i.e. conditions closer to equilibrium. The CO_2 conversion is also strongly affected by the uncertainties, whith errors ranging between 50 % and 110 % depending on the conditions.

By analyzing the correlations between the model results and the rate coefficients of the individual reactions, we can reveal which reactions contribute most to the uncertainty in the model results. Typically, the results that are sensitive to other calculated quantities, such as the VDF and the CO_2 conversion, seem to be particularly subject to uncertainties, since they combine all the uncertainties of the quantities needed to calculate them. The reactions that can contribute most to the uncertainty in the VDF are the electron impact asymmetric mode excitation and the VV and VT reactions. Electron impact dissociation contributes most to the uncertainty in the CO_2 conversion, except in cases with strong vibrational excitation, where the reactions contributing to the uncertainty in the VDF also contribute to the uncertainty in the CO_2 conversion.

Finally, we recommend a number of "good practices" to improve the reliability of plasma kinetic modeling, in line with earlier recommendations by Turner[163]. Probably the most important is to systematically refer to the original sources of the data used. Creating a large database of verified rate coefficients would largely contribute to the improvement of the reliability as well. Validating the results of kinetic modeling using a certain series of rate coefficients against experiments would also be of great help for the community.

These aspects should be borne in mind when analyzing the calculation results of a chemical kinetics model. The main message emerging from this study is that the absolute value of certain model outputs has to be interpreted with caution. However, the trends still seem to be valid in the majority of the cases, and they also contain very useful information. Therefore, in the absence of certainty over the rate coefficients, kinetic modeling should focus more on trends and the model results should be evaluated critically, both by the researchers and the readers.

CHAPTER VIII

Tracking the energy pathways in a CO_2 discharge

The results presented in this chapter were submitted to the Journal of CO_2 Utilization as:

- A. Berthelot and A. Bogaerts. Pinpointing energy losses in plasma-based CO_2 conversion. *Journal of CO_2 Utilization*, 2018. In press

VIII.1 Introduction

In this chapter, we investigate, using a 0D chemical kinetics model, the way in which energy transfers take place inside the plasma. Indeed, energy efficiencies reported for plasma-driven CO_2 conversion reach up to 90 % for a MW plasma operating with a supersonic flow[22;33], where the plasma is formed in the low pressure zone of the flow. Modeling, on the other hand, has only reached energy efficiencies in the vicinity of 30 % at best[57], as also seen in figure VI.1. The record energy efficiencies of the early experiments carried out in the former Soviet Union[22;33] have not been reproduced since then. However, energy efficiencies reaching up to 48 % have been reported in experiments carried out recently at DIFFER[34]. Therefore, we want to check in this chapter which energy losses might be present in the model, and/or which processes limit the theoretical energy efficiency. This should allow us to understand the limitations to energy efficient CO_2 conversion, both in the model and in general.

Therefore, we use conditions that were previously found to be ideal for CO_2 conversion (chapter VI). In continuation of our work on the uncertainties of the rate coefficients, we investigate here also the effect of the parameters chosen in the scaling laws on dissociation reaction rate coefficients, as well as the effect of the activation energy of the reaction $CO_2 + O \rightarrow CO + O_2$, as these two parameters are expected to limit the energy efficiency of CO_2 conversion.

Furthermore, to investigate the effect of different plasma operating conditions on energy efficient CO_2 conversion, we also consider different values of the reduced electric field, as well as different gas temperatures and different ionization degrees. These correspond to the parameters that can be improved by optimizing the design of the discharge setup. Some of these conditions might be difficult to currently reproduce experimentally, but can be considered as recommendations towards future experiments.

The chapter is organized as follows. In section VIII.2, the model is described, as well as the chemistry set considered. The results are shown in section VIII.3. In section VIII.3.1, the CO_2 conversion and energy pathways are analyzed for different conditions of reduced electric field, gas temperature and ionization degree. Section VIII.3.2 is dedicated to the verification of the rate coefficients and scaling laws used for the two main neutral dissociation reactions, to elucidate their effect on the calculated CO_2 conversion and energy efficiency. Section VIII.3.3 attempts to define a general expression for the maximum energy efficiency that can be obtained with plasma. Finally, conclusions are given in section VIII.4.

VIII.2 Model description

VIII.2.1 Chemistry set and scaling laws

This model uses the same chemistry set as the one in chapter VII, so it considers the species listed in table III.1 in chapter III. The list of reactions included in the model is shown in appendix A.2. Tables A.6 and A.7 present the list of electron impact reactions considered, described by cross section data and analytical rate coefficients, respectively. Tables A.8 and A.10 show the reactions involving ions, and neutral molecules and atoms, respectively, while table A.9 lists the reactions consisting in energy transfers between the molecules considered.

The scaling laws used to determine the various rate coefficients of reactions involving vibrational levels were presented in section III.2.

Note that in the case of reaction N1 (see table A.10 in appendix A.2), an endothermic CO_2 dissociation reaction, the activation energy determined experimentally (E_a(N1) = 4.53 eV) is lower than the reaction enthalpy (5.52 eV), which is a theoretical minimum. This is probably due to the difficulty to experimentally determine the rate coefficient of this reaction with a high energy barrier, especially at low gas temperatures. This was not the case with the rate coefficient considered in chapters V and VI (see table A.5 in appendix A.1), but this rate coefficient could not be verified in the study of chapter VII.

To avoid this anomaly, and since equation (III.5) obviously does not take this case into consideration, we use a value $\alpha_M = 0.82$ instead of using equation (III.5). This value is derived from $E_a(\mathrm{N1}) - \alpha_M E_v = 0$, taking $E_v = \Delta H^\circ(\mathrm{N1})$. This choice of α_M ensures that CO_2 molecules with a vibrational energy equal to the enthalpy of the reaction see no activation energy barrier for reaction N1.

Hence, this way, we ensure that only the molecules with vibrational energies equal to or higher than the enthalpy of the reaction can effectively react through reaction N1 in the absence of significant translational energy. Using a value of α_M above 0.82 (i.e. closer to 1) may result in lack of energy conservation, since it would allow CO_2 molecules with vibrational energies similar to the activation energy (i.e. below the reaction enthalpy) to react, without the need to provide extra thermal (translational) energy. This will be explained in more detail in section VIII.3.2.1.

As also explained in section VIII.3.2.1, the model is quite sensitive to the value of α_M. Note that in theory, α_M should be close to one with $E_a(\mathrm{N1}) \simeq \Delta H^\circ(\mathrm{N1})$. More experimental investigation is thus required to verify this rate coefficient and in particular its activation energy.

In section VIII.3.2.1, we will investigate the effect of the α parameters of the two main dissociation reactions (N1 and N2, see table A.10 in appendix A.2) on the calculated CO_2 conversion and energy efficiency and the underlying mechanisms, in order to find out the maximum theoretical energy efficiency that the model can predict for various conditions. Likewise, in section VIII.3.2.2, we will discuss the effect of the activation energy linked with the α parameter of reaction N2 on the calculation results.

VIII.2.2 Plasma model

Again, the code ZDPlasKin[100] is used in this chapter. The densities of all species n_s are solved as a function of time using equation (II.28) The electron energy distribution function (EEDF) is here also calculated using the Boltzmann solver Bolsig+[65].

The model starts at $t = 0$ with pure CO_2, and a Boltzmann vibrational distribution. At $t = 0$, the plasma starts with a given DC reduced electric field E/N (where E is the electric field and N is the gas number density). The power density applied to the plasma is simply calculated using Joule's law $P = \sigma E^2$, where σ, the conductivity, is given by $\sigma = e n_e \mu_e$ (see section II.3.1). μ_e is the electron mobility, obtained from the Boltzmann solver, and e is the elementary charge. The electron density n_e in the plasma is fixed to a value determined by the ionization degree η_{ion}. The plasma stops when the power applied to the gas has reached a specific energy input (SEI) value of 2eV/molec.

We keep the gas temperature T_g and pressure p constant throughout the whole simulation. We perform calculations for 300 K, 1000 K and 2000 so that we can study more in detail the effect of gas temperature on the various reaction mechanisms. Moreover, we have seen in chapter VI that a low gas temperature (in the order of 300 K) is required to have a significant vibrational over-population and a better energy efficiency, as will also be discussed below.

We chose here a fixed pressure of 100 mbar, as it is representative for MW plasma experiments yielding a good energy efficiency[33;34;37] and it allows us to study non-equilibrium phenomena, as seen in chapter VI.

Note that plasmas for CO_2 conversion often operate at atmospheric pressure as well, but they typically give rise to lower energy efficiency, due to either negligible vibrational kinetics (like in DBD[56]) or a VDF too close to thermal equilibrium (like in MW or GA plasmas, see chapter VI). Therefore, atmospheric pressure is less suitable to study the non-equilibrium phenomena, and to pinpoint the energy transfers in the plasma in order to predict the maximum theoretical energy efficiency.

Ionization degrees η_{ion} between 10^{-6} and 10^{-4} are considered here. The typical value of η_{ion} in a CO_2 MW or GA plasma is indeed[37;171] around 10^{-6}, while it can reach up to 10^{-4} in some DBD setups[64]. The electron density n_e is fixed to a very low value ($\eta_{ion} = 10^{-16}$) outside of the plasma zone, in order to ensure that no power is deposited there.

The CO_2 conversion is calculated as explained by equation (VII.2). The energy efficiency η of the CO_2 conversion is calculated by equation (VI.1).

We will mostly present the calculated CO_2 conversion at the end of the simulation, i.e. 10 ms after the end of the plasma. Indeed, after 10 ms, most of the radicals will have recombined at the pressure considered here, and the gas will be close to chemical equilibrium.

VIII.3 Results and discussion

VIII.3.1 CO_2 conversion and energy transfers in the plasma

VIII.3.1.1 Calculated CO_2 conversion and energy efficiency

Figure VIII.1 shows the CO_2 conversion (left y-axis) and corresponding energy efficiency (right y-axis) as a function of the reduced electric field E/N for different gas temperatures (300 K, 1000 K and 2000 K) and different ionization degrees α_i for an SEI of 2 eV/molec. The energy efficiency is calculated based on the energy acquired by the electrons from the electric field: the energy necessary to heat the gas is not taken into account here. Thus the energy efficiency is here more an indicative value, since the gas temperature is not self-consistently calculated. Note that at gas temperatures of 2000 K and below, purely thermal conversion is a negligible process[21;40]. A rise in gas temperature within this range actually has a detrimental effect on the conversion, as discussed below.

It should also be realized, as pointed out previously (chapter VII), that the uncertainty on the conversion predicted by the model can be substantial and therefore, the focus should be on trends rather than on absolute values. The absolute values of various quantities (CO_2 conversion and energy efficiency, relative contribution to dissociation, ...) presented in this chapter should be considered as an indication of the differences caused by a change of conditions.

At $T_g = 300$ K, and $\alpha_i = 10^{-5}$ or $\alpha_i = 10^{-6}$, the CO_2 conversion reaches a maximum value of 31% and 29% for an E/N of 30 Td and 45 Td, respectively. On the other hand, with $\alpha_i = 10^{-4}$, the CO_2 conversion decreases monotonously with E/N, reaching up to 32 % for an E/N of 10 Td. Above 50 Td, the differences between different ionization degrees become negligible. At 200 Td, the CO_2 conversion has dropped to about 13 % for all ionization degrees.

At $T_g = 1000$ K and with $\alpha_i = 10^{-6}$, the CO_2 conversion increases with E/N, from zero at 40 Td to approximately 7 % at E/N = 100 Td and above. At $\alpha_i = 10^{-5}$ and

$\alpha_i = 10^{-4}$ a maximum conversion of 11 % at 90 Td and 16 % at 50 Td is reached, respectively.

Finally, at $T_g = 2000$ K, the CO_2 conversion shows a similar behavior for all values of α_i, although $\alpha_i = 10^{-4}$ gives a slightly higher conversion. The CO_2 conversion starts increasing from around 50 Td to reach a maximum around 130 Td, and slowly decreases for E/N > 150 Td. For high values of E/N, a gas temperature of 2000 K with an ionization degree above 10^{-5} can give slightly higher conversion than at 1000K.

To link these values to the experiments, note that MW and GA discharges typically operate at E/N values of 100 Td and below, while DBDs typically operate at 200 Td and above.[21;62] It is however difficult to sustain a plasma with low values of E/N (50 Td and below), since attachment reactions are more important than ionization reactions at low E/N, due to the difference in the energy threshold of the two cross sections[109;172]. Nevertheless, it is possible to work around this, by using two different energy sources: one with a large E/N (ionization source) and one with a lower E/N, as shown in a CO_2 plasma by Andreev *et al.*[67].

In general, the conversion drops drastically upon higher gas temperature, while a higher ionization degree is beneficial for the conversion. The effect of E/N depends on the value of the gas temperature. These trends will be explained in more detail in the next sections.

The energy efficiency follows exactly the same behavior as the conversion, which is logical from equation (VI.1) as the SEI is kept constant. It is a factor 1.46 higher than the conversion (i.e. ΔH° / SEI = 2.93 / 2.0). Thus, the highest energy efficiency reached at these conditions is 45 %, at 300 K, E/N = 10 Td and $\alpha_i = 10^{-4}$.

In literature a wide range of energy efficiencies has been reported, depending on the type of discharge and the setup[21]. DBD plasmas typically have energy efficiencies of 15 % or below[43;76;77], which corresponds well to the energy efficiencies predicted here at high E/N, i.e. values typical of DBDs. MW and GA plasmas, on the other hand, reach higher energy efficiencies. Values of η up to 90 % have been reported in literature from the former USSR in supersonic flow MW plasmas[33], while most recent experiments give values up to 50 % for MW plasmas[34;37] and GA plasmas[39;40]. The experimental maximum energy efficiencies thus correspond to the highest values obtained here (figure VIII.1), or are even slightly higher, although they were typically not obtained at ideal conditions, while the conditions presented here are somehow optimal, and thus higher values of energy efficiency would be expected from the model.

Therefore, the following two sections, VIII.3.1.2 and VIII.3.1.3, focus on the energy transfers taking place within the plasma, in order to explain the results shown in figure VIII.1. The theoretical limitations of the energy efficiency in the model will also be discussed below.

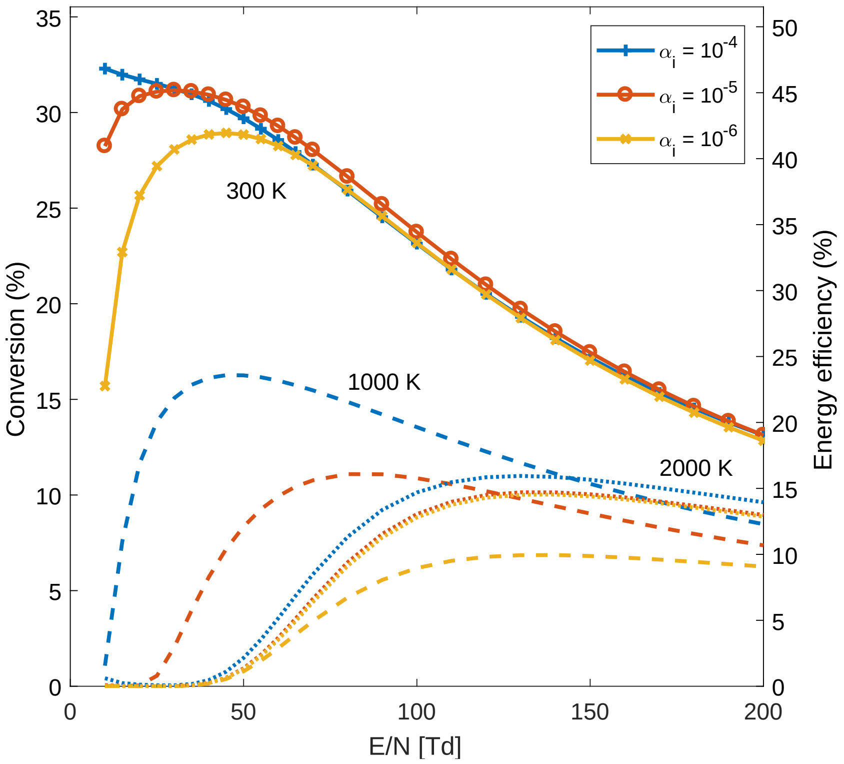

Figure VIII.1: CO_2 conversion (left y-axis) and corresponding energy efficiency (right y-axis) as a function of the reduced electric field E/N, for three different ionization degrees (10^{-6}, 10^{-5}, 10^{-4} in blue, orange and yellow, respectively) and three different gas temperatures (300 K, 1000 K, 2000 K, shown with full lines, dashed lines and dotted lines, respectively.)

VIII.3.1.2 Time-dependent behavior of the energy transfers in the plasma

In this section, we first show the electron energy loss mechanisms as a function of time and for various conditions. Indeed, the energy from the electric field will in first instance entirely go to the electrons. The electrons then redistribute this energy to the other particles, through various processes. Vibrational excitation is known as the key to high energy efficiencies and thus we will later focus on the CO_2 vibrational energy transfer mechanisms. The goal is to investigate how much of the plasma power effectively goes into CO_2 dissociation and to identify the energy loss mechanisms for various conditions.

Figure VIII.2 shows the electron energy losses in the plasma for a gas temperature of 300 K, an ionization degree of 10^{-6} and a reduced electric field of 50 Td (figure VIII.2 a) and 150 Td (figure VIII.2 b). The electron energy losses are normalized to the maximum value of the energy applied to the electrons. Note that the energy losses due to elastic collisions between electrons and neutrals are included in the model, but are several orders of magnitude lower than the inelastic energy losses, at the conditions considered here. The time dependent CO_2 conversion is plotted against the right y-axis. Note that the time dependent CO_2 conversion after the plasma may be slightly higher than the CO_2 conversion at the end of the simulation (plotted in figure VIII.1) due to the back reaction N4 (see table A.10 in appendix A.2) occurring after the plasma due to the presence of O atoms.

In general, the electron energy pathways are mainly determined by the value of E/N and the gas chemical composition. Gas temperature and ionization degree have thus only an indirect effect. Therefore, the results are only shown for one gas temperature and one value of the ionization degree.

At E/N = 50 Td, by far the dominant electron energy loss is CO_2 vibrational excitation, accounting for more than 90 % of the electron energy losses. The other energy losses only contribute for a few %.

At E/N = 150 Td, CO_2 vibrational excitation is still the main electron energy loss, and accounts for 58 % of the losses at the beginning of the plasma and 32 % at the end of the plasma. However, CO_2 electronic excitation and dissociation are also significant energy losses, accounting for between 21 % and 26 %. Furthermore, CO electronic excitation also becomes increasingly important as energy loss process as time evolves, i.e., due to the increasing CO density (upon conversion of CO_2), and it contributes for up to 15 %.

The difference between 50 and 150 Td is explained by the average electron energy, which is about 0.9 eV at 50 Td and about 2.6 eV at 150 Td. As this is the average electron energy, there are of course electrons with higher energy in the tail of the distribution. Still, at 50 Td, there are not many electrons with sufficient energy to overcome the large thresholds of electronic excitation and dissociation reactions (i.e., 10.5 eV and 7 eV, respectively). On the other hand, at 150 Td, there is a competition between different processes. Moreover, the vibrational excitation cross sections show a maximum at relatively low electron energies (0.38 eV for $CO_2 + e \rightarrow CO_2v_1 + e$), which means that the chance to transfer the electron energy to vibrational levels will decrease with increasing electron energy.

The total energy lost by the electrons to inelastic collisions varies with time, although E/N and n_e are fixed, which may seem counter-intuitive. However, the electron energy loss mechanisms also depend on the gas composition. Therefore, at the beginning there is a sharp peak of electron energy loss, due to the lack of superelastic collisions at the beginning of the plasma, which can be explained from the time required for the population of vibrationally excited states to build up. Once their concentration is higher, they release back part of their energy to the electrons through superelastic collisions, which decreases the total electron energy loss. Moreover, in figure VIII.2 a, we see that the electron energy loss decreases continuously with time. This is caused by the increasing CO concentration, as the electrons lose their energy more easily to CO_2 than to CO. This also leads to a higher electron temperature over time (from 0.65 eV at the very beginning of the plasma to 1.05 eV at the end) since the electrons will thus store more energy. Indeed, the electron temperature is more or less inversely proportional to the total electron energy loss.

It is also interesting to note that CO vibrational excitation is not an important energy loss mechanism, despite the relatively high CO concentrations at the end of the plasma (i.e. molar concentrations up to 25 % for a conversion of 29 % at 50 Td). This is due to the important energy transfer between the vibrational levels of CO_2 and CO (reaction V8, table A.9 in appendix A.2). This creates a large vibrationally excited CO population, giving rise to important superelastic CO vibrational excitation reverse reactions (i.e. vibrational deexcitation), which almost entirely compensate for the forward reactions. This behavior is of course only significant with large CO_2 vibrational populations and high CO concentrations (i.e. E/N of 50 Td or below and gas temperature of 300 K).

The results shown in figure VIII.2 are representative for other conditions as well, since the electron energy loss mechanisms almost only depend on the value of E/N and the gas composition, in particular the CO density. Therefore, the results for other conditions of ionization degree and gas temperature are very similar, with the exception of the energy losses to CO that depend, of course, on the CO density. The behavior of the electron energy losses as a function of E/N is described in more detail below.

As can be concluded from figure VIII.2, vibrational excitation is the main electron energy loss mechanism. It is therefore interesting to see where the energy stored in the CO_2 vibrational levels of CO_2 effectively goes, and in particular how much of it effectively goes to CO_2 dissociation.

Figure VIII.3 shows the main vibrational energy loss processes for a reduced electric field of 50 Td, an ionization degree of 10^{-6} and a gas temperature of 300 K (Figure VIII.3 a) and 1000K (Figure VIII.3 b). The vibrational losses are calculated from the balance of vibrational energy before and after the reaction. These losses are normalized to the maximum energy that the vibrational levels received from the electrons (i.e. purple curve in figure VIII.2 a, for the $T_g = 300$ K case). Note that the sum of the energy losses by the individual processes must not be equal to the vibrational energy received from the electrons at each moment in time, since the vibrational levels can store energy and redistribute it back later. However, integrated over the whole simulation time, the total vibrational energy loss is of course equal to the total vibrational energy

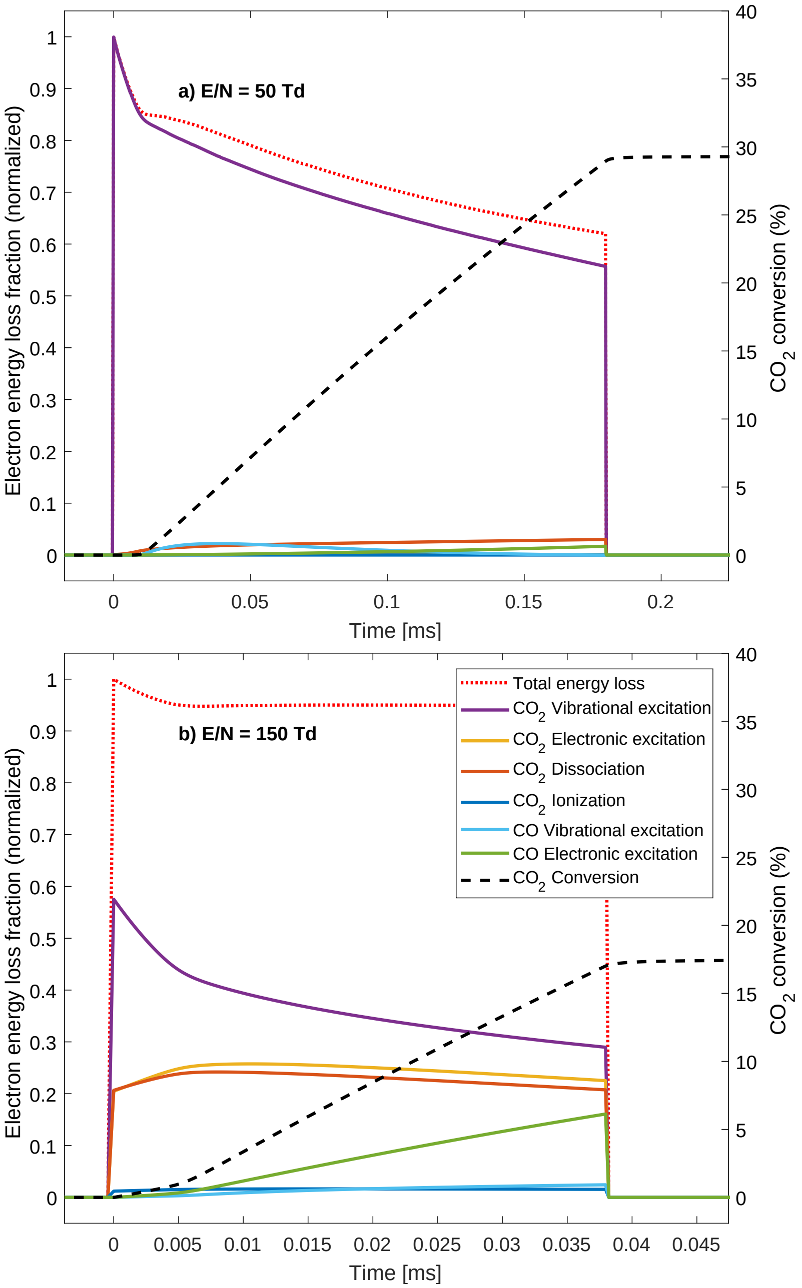

Figure VIII.2: Electron energy loss fractions (left y-axis) and CO_2 conversion (right y-axis) as a function of time for a gas temperature of 300 K, an ionization degree of 10^{-6}, a pressure of 100 mbar and a reduced electric field of 50 Td (panel a, top) and 150 Td (panel b, bottom). The energy losses are normalized to the maximum of the total energy applied to the electrons.

received from the electrons.

The time dependent CO_2 conversion is again plotted against the right y-axis. The results are now shown for two different gas temperatures and only one value of E/N, since the vibrational energy pathways depend mostly on gas temperature and gas chemical composition. The E/N and ionization degree have thus only an indirect effect.

At $T_g = 300$ K, CO_2 dissociation upon impact with any neutral molecule M (i.e. reaction N1), is the main vibrational energy loss process, especially at the beginning of the plasma, accounting for up to 75 % of the vibrational energy losses. The delay time between the start of the plasma and the effective start of dissociation processes is due to the time required for a significant vibrational population to build up. The second energy loss process is dissociation upon impact with O atoms in the plasma (i.e. reaction N2). At the beginning of the plasma, however, the contribution of N2 is negligible. This is because first O atoms need to be formed by reaction N1 or electron impact dissociation. At the end of the plasma, the vibrational energy dissipated by reaction N2 reaches 35 % of the total vibrational energy losses.

VV energy exchanges between CO_2 molecules (i.e. reactions V5 and V6 in table A.9 in appendix A.2) are also non-negligible energy loss mechanisms. While the reaction rates of VV reactions between CO_2 molecules can be extremely high, the energy lost in each reaction is rather small. The energy loss in VV reactions is due to the anharmonicity between the energies of the vibrational levels. Because of the small energy losses, VV reactions only account for between 10 % and 15 % of the vibrational energy losses, in spite of their high reaction rates.

In a similar fashion, VV energy exchange between CO_2 and CO molecules (i.e. reaction V8 in table A.9 in appendix A.2) is non-negligible, and becomes increasingly important with time, due to CO_2 conversion into CO, hence giving rise to a higher CO density. As mentioned earlier, this process can create a large population of CO vibrationally excited states. It is thus important to consider the CO vibrational kinetics in this type of modeling, as also pointed out by Pietanza *et al.*[173].

Pure VT transfers (reactions V1, V2a, V2b and V2c in table A.9 in appendix A.2) cause only a small vibrational energy loss, due to the relatively low gas temperature considered here (300 K). Finally, since CO_2 electron impact dissociation occurs mainly from ground state CO_2 (as explained below) and is not a process likely to happen at low E/N, it is only a minor vibrational energy loss process here.

At $T_g = 1000$ K, the situation is very different, because VT energy transfer processes account for almost all the vibrational energy loss. Indeed, the rate coefficient of VT reactions (reactions V1, V2a, V2b and V2c in table A.9 in appendix A.2) increases rapidly with gas temperature. VV exchanges between CO_2 molecules are only a minor process, and the other processes are completely negligible. Indeed, as also pointed out in chapter VI, with increasing gas temperatures, VT transfers become so important that vibration-induced dissociation becomes of minor importance.

To conclude this section, we have investigated the time-dependent behavior of the electron and vibrational energy loss pathways. We showed that at low E/N (50 Td), most of the electron energy effectively goes to CO_2 vibrational excitation, while at a higher E/N (150 Td), more energy-demanding processes such as electronic excitation and electron impact dissociation become important energy loss pathways as well. The vibrational energy is subsequently mostly lost to dissociative processes at low gas temperature (300K), while at higher gas temperature (1000 K), VT vibrational energy loss processes become more important and dissipate the vibrational energy much faster.

As discussed below in more detail, the different energy transfers taking place in the plasma can explain the trends observed in figure VIII.1. Indeed, we see that a high temperature quickly dissipates the vibrational energy, rendering vibration-induced dissociation unlikely. On the other hand, a low E/N value favors vibrational excitation, and thus also vibration-induced dissociation (at least at low gas temperature).

VIII.3.1.3 Time-integrated behavior of the energy transfers in the plasma

Figures VIII.2 and VIII.3 present the time-dependent behavior of the different energy transfers for a few representative conditions. In order to compare the results in a wider range of conditions, we have integrated the energy losses over time in the plasma.

Figure VIII.4 shows the relative contributions of the time-integrated electron energy losses of the six main energy loss processes as a function of E/N and for a gas temperature of 300 K and an ionization degree of 10^{-6}.

Other minor processes accounting for the remaining electron energy losses (attachment reactions, CO ionization, ...) are not shown here, for the sake of clarity. As there is no clear dependence to gas temperature in the electron energy pathways, the results of figure VIII.4 can be considered representative of the different gas temperatures.

At low E/N, CO_2 vibrational excitation is, by far, the main electron energy loss process. CO_2 vibrations receive up to 95 % of the electron energy. The rest of the electron energy is lost to CO vibrations. Electron impact CO_2 dissociation starts to become non-negligible from 40 Td and accounts for up to 21 % of the electron energy losses at high E/N (i.e., above 100 Td). CO_2 electronic excitation becomes more important around 60 Td and even becomes the main electron energy loss at high E/N, accounting for up to 39% of the electron energy losses at 200 Td.

The electron energy lost to CO varies between 4 % and 13 %. It is interesting to note that although the CO_2 conversion, and thus the CO density, decreases with increasing E/N (see figure VIII.1), the losses to CO are more important above 100

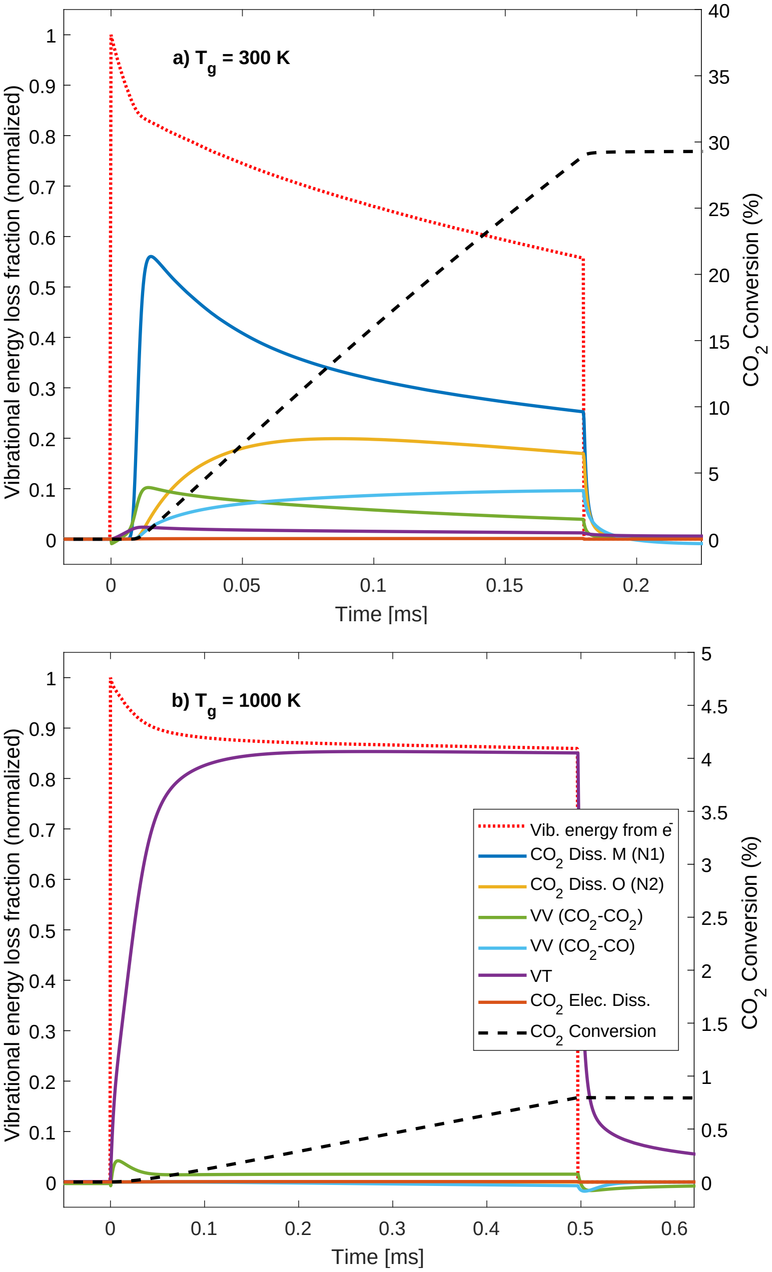

Figure VIII.3: Vibrational energy loss processes (left y-axis) and CO_2 conversion (right y-axis) as a function of time for a reduced electric field of 50 Td, an ionization degree of 10^{-6}, a pressure of 100 mbar and a gas temperature of 300 K (panel a, top) and 1000 K (panel b, bottom). The energy loss is normalized to the maximum of the total energy that the CO_2 vibrational levels received from the electrons.

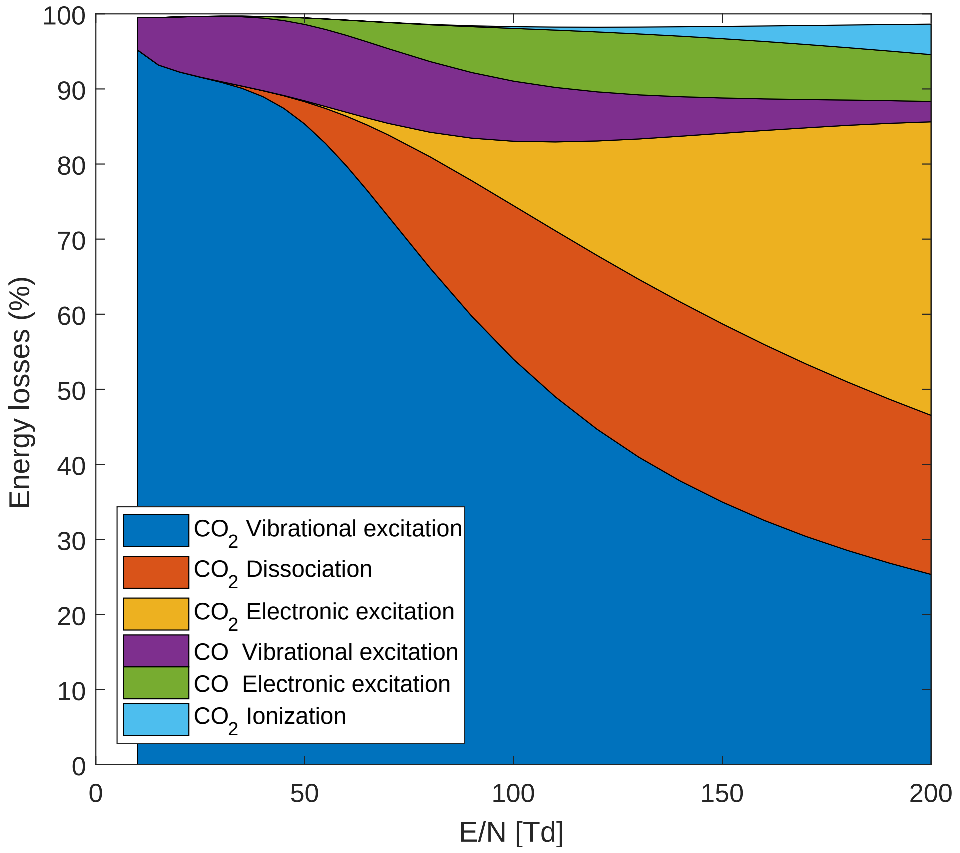

Figure VIII.4: Relative contribution of the main processes responsible for the electron energy loss as a function of the reduced electric field E/N, for a gas temperature of 300 K, an ionization degree of 10^{-6} and a pressure of 100 mbar. The electron energy losses are integrated over the plasma for each value of E/N.

Td than at 45 Td. This can be explained by the relatively low energy threshold of CO electronic excitation (from 6.22 eV to 10.01 eV, see table V.2), which makes CO electronic excitation an important electron energy loss at high E/N.

The electron energy loss pathways depend only on the value of the reduced electric field and the density of the various species colliding with the electrons. Therefore, the results of figure VIII.4 can be considered representative of all the conditions considered in this chapter. At different gas temperatures and different ionization degrees, only the losses to CO will vary to some extent, due to the change in CO density.

Figure VIII.5 illustrates the main processes responsible for the vibrational energy losses, for different conditions, integrated over time. The integrated energy losses are again normalized to the energy received by the CO_2 vibrational levels from the electrons.

As mentioned earlier, the value of E/N and the ionization degree only have an indirect effect on the vibrational energy pathways. However, some differences can still be found.

In the first, called 'standard' case, at $T_g = 300$ K, E/N = 50 Td and $\alpha_i = 10^{-6}$, as observed in figure VIII.3 a, the main vibrational energy loss process is reaction N1, i.e., dissociation of the vibrational levels upon collision with any molecule M (51 %), followed by reaction N2, i.e., dissociation upon collision with an O atom (25 %). CO_2-CO and CO_2-CO_2 VV reactions have a similar relative weight (each around 11 %). VT relaxation only accounts for 2.5%. With a higher E/N (e.g. 150 Td), the results are practically identical; see second case.

Upon higher ionization degree, the plasma residence time to reach the same total SEI of 2eV/molec (cf. section VIII.2.2) is much smaller (about a factor 100 for $\alpha_i = 10^{-4}$). Hence, there is less time for VT reactions to occur and the vibrational population becomes much larger.

Therefore, VT energy losses become negligible (in the entire range of E/N investigated), and dissociation upon impact with any molecule M is the main vibrational energy loss (76 % at $\alpha_i = 10^{-4}$, 300 K and E/N = 50 Td see third case). As a consequence, the CO_2 conversion is somewhat higher (see figure VIII.1).

Note that, at lower E/N, the energy deposition per time is smaller and thus the plasma residence time to reach 2eV/molec is longer. Therefore, at still lower E/N than 50 Td, VT relaxation as well as CO_2-CO VV relaxation still can become somewhat more important than in the cases shown here (i.e. 50 Td) and dissipate a larger proportion of the energy. In this case, the residence time is thus an important parameter in the dissipation of the vibrational energy, so if the residence time is 100-fold shorter at a 100 times higher ionization degree ($\alpha_i = 10^{-4}$ vs $\alpha_i = 10^{-6}$), VT and CO_2-CO VV relaxation again become negligible. This explains the higher conversion at very low E/N, observed in figure VIII.1 upon higher ionization degree, and it also explains why the difference is larger than at 50 Td.

At $T_g = 1000$ K and $\alpha_i = 10^{-6}$ (case 4), almost all the vibrational energy is lost to VT relaxation and thus, there is very little vibration-induced dissociation. The very limited CO_2 conversion that occurs at this temperature (ca. 0.7 %, see figure VIII.1) is almost entirely due to electron impact processes, mainly electron impact dissociation.

On the other hand, with $\alpha_i = 10^{-4}$, the power density is much higher and thus the plasma residence time to reach the same SEI of 2 eV/molec is lower. This favors vibration-induced dissociation above VT relaxation (see case 5 in figure VIII.5), although it needs to be mentioned that the O atoms do not recombine much with CO_2 molecules, as they do not have enough time, after creation, to collide with another CO_2

molecule within this short time. Nevertheless, because vibration-induced dissociation upon collision with any molecule M is again much more important at higher ionization degree, the CO_2 conversion is much higher (ca. 16%, see figure VIII.1).

Finally, at $T_g = 2000$ K, CO_2-CO_2 VV reverse reactions become more important than the forward reactions, meaning that the highly energetic vibrational levels tend to be 'pumped down' towards the ground state; see last case in figure VIII.5. VT transfers dissipate all the energy obtained by the vibrational levels, explaining why the CO_2 conversion is nearly negligible in figure VIII.1.

Figures VIII.4 and VIII.5 give clues to understand the trends observed in figure VIII.1, namely the increase of CO_2 conversion and energy efficiency with decreasing reduced electric field, increasing ionization degree and decreasing gas temperature (in the range 300K - 2000K).

To summarize, at lower E/N, the electrons transfer more of their energy to the vibrational modes of CO_2, while at higher E/N, electron impact dissociation and electronic excitation processes become prominent. These processes are costly, due to their high energy thresholds, and are thus detrimental to the energy efficiency. Because vibration-induced dissociation is the most efficient dissociation pathway, enhancing vibrational excitation leads to a better energy efficiency.

Furthermore, a higher gas temperature will lead to more VT energy losses, which renders vibration-induced dissociation very unlikely at temperatures of 2000K (and above). A higher ionization degree originates from a higher power density, which in turn decreases the plasma residence time, for a given SEI. Decreasing the plasma residence time diminishes the VT energy losses and thus favors vibration-induced dissociation.

Experimentally, MW and GA plasmas, as well as glow discharges, work at moderate E/N values (around 50 - 100Td). However, the ionization degree is typically rather low in these discharges (around 10^{-6}), notably due to the lower ionization rate coefficient at low E/N (i.e. lower electron temperature). Furthermore, the gas temperature can also be relatively high in these discharges, as observed in chapter VI, especially when they operate at relatively high pressure.

DBDs, on the other hand, operate at higher E/N (200 Td and above), which makes electron impact dissociation the main dissociative process. The vibrational population is thus not so important, and therefore, the fact that they exhibit relatively low gas temperatures and high ionization degrees does not lead to an improved conversion.

Hence, there is clearly room for optimization of the most common discharges used for CO_2 conversion, by using setups working simultaneously at low E/N, gas temperatures close to room temperature and high ionization degrees.

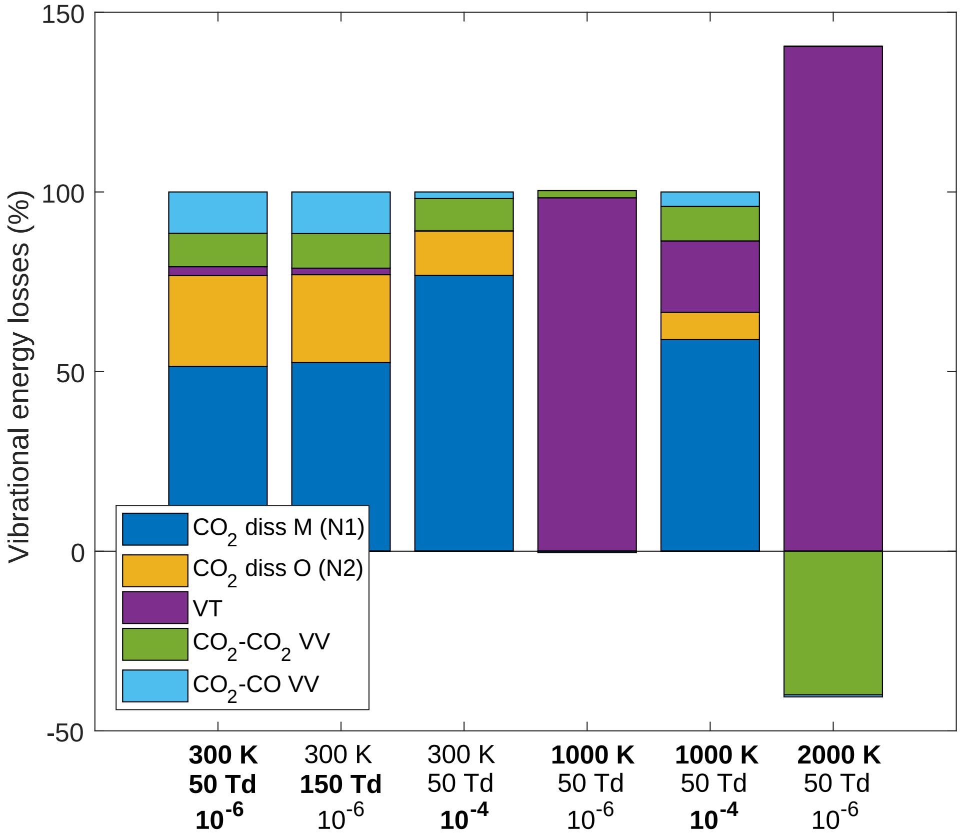

Figure VIII.5: Relative contribution of the main processes responsible for the vibrational energy losses integrated over time, for different conditions of gas temperature, reduced electric field and ionization degree, and at a pressure of 100 mbar. The parameters written in bold indicate the differences with the first case.

VIII.3.1.4 Vibrational distribution functions

The vibrational energy loss mechanisms are of course very dependent on the degree of vibrational excitation. Therefore, the shape of the VDF is an important parameter to understand the results of figure VIII.5. Figure VIII.6 presents the VDFs in the middle of the plasma (i.e. half of the plasma residence time) for the same conditions as figure VIII.5. The equilibrium Boltzmann distributions corresponding to the same gas temperatures are shown with dashed lines. The shape of the VDF is determined by the relative importance of the different processes studied above, mainly electron impact vibrational excitation, VV and VT transfers, and dissociation reactions. The first part of the VDF can usually be described by a Treanor distribution[123], while the tail of the distribution is strongly affected by VT and dissociative processes, which are not included in Treanor's theory (see our previous chapter VI for a more detailed comparison/discussion).

As also pointed out in chapter VI, a higher gas temperature brings the VDF closer to thermal equilibrium (i.e., higher vibrational levels less overpopulated), by enhancing VT reactions (cf. cases 4 and 6 in figure VIII.5 and VIII.6, compared to the 'standard' case 1). The energy of the electrons is thus ultimately dissipated to heat and there is almost no vibration-induced dissociation.

This also explains the trends observed in figure VIII.1. It is quite obvious that a large vibrational population is required in order to favor vibration-induced dissociation. Therefore, any condition favoring vibrational excitation will also favor vibration-induced dissociation, provided that VT energy losses are not too fast, thus provided that VT losses do not counter-balance the gain of a large vibrational excitation.

On the other hand, a higher ionization degree originates from a higher power density, which increases the electron impact vibrational excitation rate. This results in a VDF with a clear over-population of the higher vibrational levels compared to the Boltzmann case (see curves 3 and 5). This is even true at 1000K (curve 5): although VT relaxation increases with temperature, a strong-enough electron impact vibrational excitation is still able to overcome this VT relaxation.

Finally, it is interesting to note that the two VDFs at $T_g = 300$ K and $\alpha_i = 10^{-6}$ with E/N = 50 Td and 150 Td practically overlap (i.e., curves 1 and 2). Indeed, although at higher E/N a smaller part of the electron energy goes to vibrational energy, it also gives a higher power deposition density. These two effects compensate each other here and make the two VDFs look very much alike. However, the residence time decreases with increasing E/N (or equivalently power density), so the total energy going to the vibrational levels (integrated over the whole simulation time) is still lower with a higher E/N.

VIII.3.1.5 Dissociation mechanisms

We now combine the above results of the electron energy transfers and vibrational energy transfers to elucidate the main processes responsible for CO_2 conversion. Their relative contributions are plotted in figure VIII.7 for the same conditions as in figure VIII.5. In the 'standard' case, the conversion is mainly caused by neutral dissociative reactions. The dissociation upon collision with any molecule M (N1, see table A.10 in appendix A.2) is responsible for about 62%, while the dissociation upon collision by an O atom (N2, see table A.10 in appendix A.2) accounts for 34 %. Electron impact dissociation (X4, see table A.6 in appendix A.2) accounts for only 3 % of the conversion.

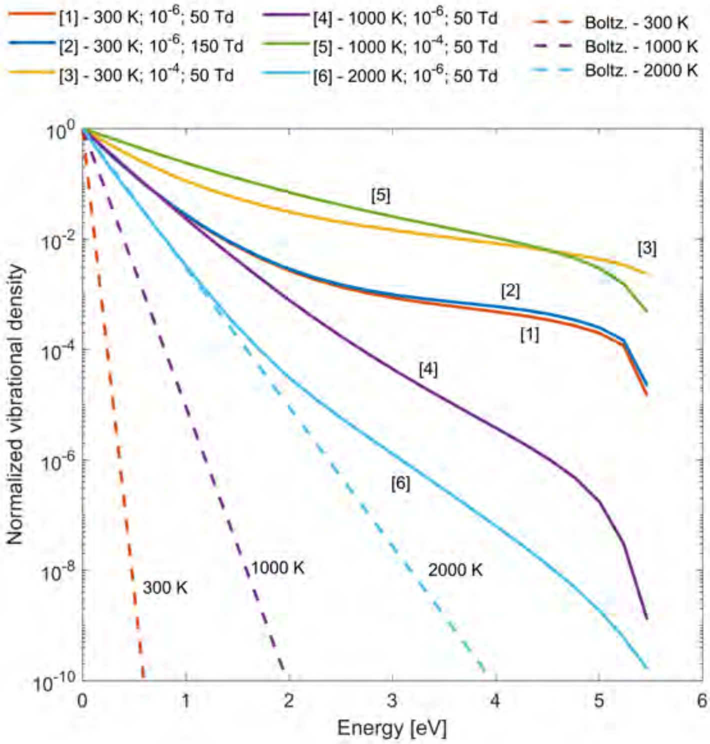

Figure VIII.6: Vibrational distribution functions (VDFs) of the asymmetric mode vibrational levels of CO_2 at half of the 'plasma residence time', for various conditions, as also presented in figure VIII.5. The legend of each curve indicates the gas temperature, the ionization degree and the reduced electric field, respectively, and the numbers of the curves correspond to the cases of figure VIII.5. The Boltzmann distributions corresponding to the gas temperatures considered here are shown with dashed lines.

Upon increase of the reduced electric field to 150 Td (case 2), the contribution of electron impact dissociation becomes much more important (44 %), as can also be deduced from figure VIII.2 b. On the other hand, with E/N = 50 Td and $\alpha_i = 10^{-4}$ (case 3), the contribution of reaction N1 becomes much larger (75 %). Indeed, the plasma residence time (to reach the same SEI of 2 eV/molec) is here much lower, so the O atoms created in reaction N1 do not have enough time to dissociate an extra CO_2 molecule.

At 1000 K, 50 Td and $\alpha_i = 10^{-6}$ (case 4), there is very little vibrational excitation (see figure VIII.6). Therefore, the main mechanism is electron impact dissociation. Note that, although its relative contribution is close to 100 % (figure VIII.7), its absolute contribution is small, due to the low rate of this process, explaining the low CO_2 conversion in this case (cf. figure VIII.1).

On the other hand, at 1000 K, 50 Td but $\alpha_i = 10^{-4}$ (case 5), the major processes resemble more the corresponding 300 K case (case 3), because there is now enough electron impact vibrational excitation due to the higher ionization degree. Still, the CO_2 conversion is lower than at 300 K (cf. figure VIII.1), because of more prominent vibrational loss due to VT relaxation (cf. figure VIII.5: case 5 vs case 3).

Finally, at 2000K and $\alpha_i = 10^{-6}$ (case 6), only electron impact dissociation is possible, due to the strong VT relaxation, yielding only a very low population of the vibrational levels (cf. figure VIII.6), just like in case 4. Again, although the relative contribution of electron impact dissociation is close to 100 %, its absolute contribution is low, explaining the very low CO_2 conversion (see figure VIII.1).

VIII.3.1.6 Vibrational energy consumption

When inspecting figure VIII.7 and figure VIII.5, a question raises itself. Why does dissociation reaction N2 (i.e., upon collision with O atoms) consume such a large proportion of the vibrational energy, despite its lower activation energy (E_a(N1) = 4.53 eV for N1 and E_a(N2) = 2.28 eV for N2) and lower reaction enthalpy than reaction N1 (ΔH°(N1) = 5.52 eV for N1 and ΔH°(N2) = 0.35 eV for N2)?

Therefore, we plot in figure VIII.8 the mean vibrational energy consumption per dissociation event, for the same conditions as in figure VIII.5 and figure VIII.7. The mean vibrational energy consumed by dissociation reaction l is calculated using:

$$E_{cons,l} = \frac{\sum_k R_{l,k} E_{vib,k}}{\sum_k R_{l,k}} \tag{VIII.1}$$

where the index k refers to each of the CO_2 vibrational levels, $E_{vib,k}$ is their energy, and $R_{l,k}$ is the reaction rate of the dissociation reaction l from this vibrational level k.

As explained in section III.2, in the absence of significant thermal excitation, only molecules with a vibrational energy $E_v \gtrsim E_a/\alpha$ can react in a reaction with activation energy E_a. E_a/α can thus be considered as an effective activation energy for vibration-induced dissociation reactions.

The vibrational energy of the reacting molecule is consumed in the reaction and the excess energy, i.e. $E_v - \Delta H^\circ$, is wasted to heat. The mean vibrational energy consumption of a dissociation reaction is thus equal to the mean energy of the vibrational levels contributing to that reaction. For the most energy efficient dissociation processes, the mean vibrational energy consumption should be equal to the enthalpy of the dissociation reaction. The more the mean vibrational energy consumption exceeds

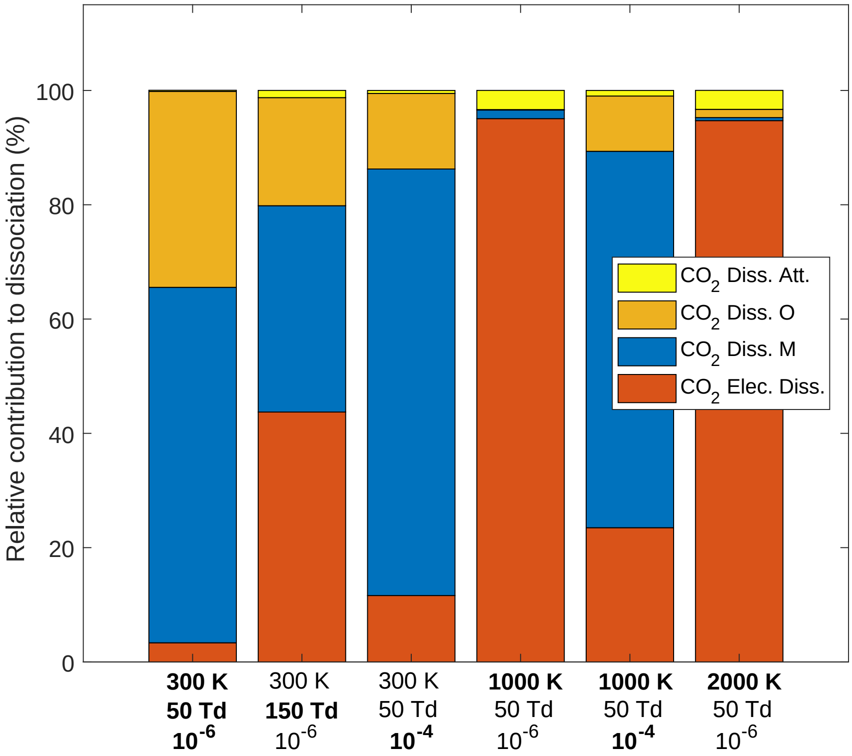

Figure VIII.7: Relative contribution of the main processes responsible for CO_2 dissociation for different conditions (as in figure VIII.5), integrated over time, and at a pressure of 100 mbar. The parameters written in bold indicate the differences with the first case. The dotted and dashed lines show the activation energy of reactions (N1) and (N2), i.e. dissociation upon impact by any molecule M and upon O atom impact, respectively.

above the enthalpy of that reaction, the more vibrational energy will be wasted (i.e., spent without strictly being needed for dissociation).

As the gas temperature increases, the molecules acquire translational energy, which they can also use to overcome the activation energy E_a of the reaction. Therefore, the mean vibrational energy can be less than the activation energy of the dissociation reaction. At high enough gas temperatures, molecules at the tail of the translation energy distribution can have enough translational energy to overcome the activation energy barrier without the help of vibrational excitation. The dissociation process is then more thermal than vibration-induced.

For all conditions shown in figure VIII.8 here, the vibrational energy consumption of dissociation upon reaction N1 (i.e., collision with any molecule M) is close to its activation energy. More precisely, for temperatures of 1000K and below, it is slightly higher, so it means that only the high vibrational levels can effectively dissociate through N1 and their vibrational energy is consumed in reaction N1.

However, CO_2 molecules reacting with O atoms (in N2) have on average (i.e., averaged over all vibrational levels) about twice the energy required to overcome the activation energy barrier, and thus also much more than the reaction enthalpy, so it means that this excess vibrational energy is wasted. The α_O parameter, chosen according to the Fridman-Macheret theory[22] ($\alpha_O = 0.5$), describes the efficiency of vibrational excitation to overcome the activation energy barrier. In pure vibration-induced dissociation, vibrational levels actually 'see' an activation energy of $E_a(\mathrm{N2})/\alpha_O$ for reaction N2, explaining why they need so much vibrational energy to react.

At 2000K (case 6), the energy required to overcome the activation energy of N1 slightly decreases, due to thermal energy. The temperature is thus still not high enough to overcome the high activation energy of this reaction (4.52 eV) without the help of vibrational energy. The drop in vibrational energy consumption of N2 is, however, much more substantial for two reasons: (*i*) as seen in figure VIII.6, there are less highly excited vibrational levels at $T_g = 2000$ K and (*ii*) the activation energy of N2 (2.28 eV) is lower than the activation energy of N1. The energy required to overcome the activation energy barrier of N2 can thus be given by the translational energy of the reacting molecules, instead of vibrational energy. Thus, the vibrational energy is not used in reaction N2 at 2000K, since this process is now thermally-induced, but thermal conversion is not efficient whatsoever.

Note that in this case, as seen in figure VIII.7, both N1 and N2 are minor dissociation processes since the population of highly excited vibrational levels is too low to induce significant vibration-induced dissociation.

CO_2 electron impact dissociation only consumes little vibrational energy in most cases, as it occurs mainly from the ground state. Indeed, although the rate coefficient of electron impact dissociation increases upon higher vibrational levels, the lower population of these levels typically compensates for the increase. It is interesting to note that in the cases with higher vibrational excitation, like cases 3 and 5, electron impact dissociation appears to occur preferably from vibrational levels around 1 eV. This is due to the large population of vibrationally excited states. No vibrational energy can be considered wasted here, since the electron energy consumed in electron impact dissociation decreases anyway when it occurs from a vibrationally excited state of CO_2.

As explained above and in section III.2, in pure vibration-induced conversion (i.e. no significant thermal energy), a CO_2 molecule needs a vibrational energy $E_v \gtrsim E_a/\alpha$ to react in endothermic dissociation reactions, such as N1 and N2. From the point of view of energy conservation, the minimum energy consumption of a reaction in standard

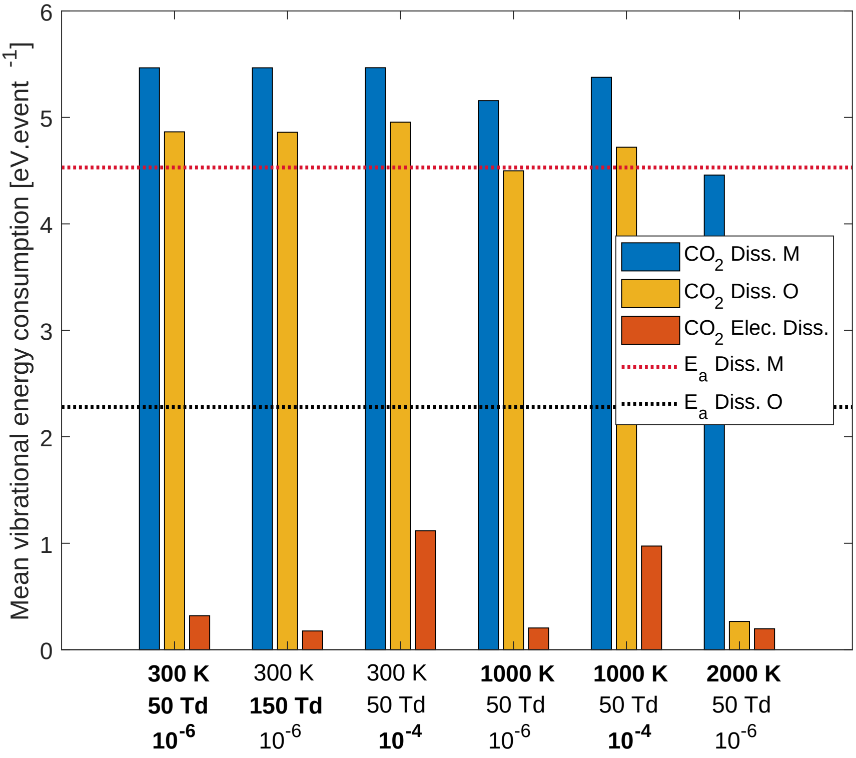

Figure VIII.8: Mean vibrational energy consumption per dissociation event for different conditions (as in figure VIII.5), integrated over time, and at a pressure of 100 mbar. The parameters written in bold indicate the differences with the first case. The dotted lines show the activation energy of reactions (N1) and (N2), i.e. dissociation upon impact by any molecule M and upon O atom impact, in red and in black, respectively.

conditions should be its enthalpy ΔH°. Thus, we have $E_a/\alpha \geq \Delta H^{\circ}$. However, in particular for reaction N2, the difference is quite large, since $E_a(\mathrm{N2})/\alpha_O = 4.5$ eV and $\Delta H^{\circ}(\mathrm{N2}) = 0.35$ eV. Therefore, as an example, if a CO_2 molecule with a vibrational energy $E_v \gtrsim E_a(\mathrm{N2})/\alpha_O$ reacts in N2, a total vibrational energy of $E_v - \Delta H^{\circ}(\mathrm{N2})$ can be considered wasted, since it is transformed into heat, while a vibrational energy of only $\Delta H^{\circ}(\mathrm{N2})$ is effectively used for dissociation.

The high mean vibrational energy consumption of dissociation upon collision with O atoms appears to be a strong limitation to the energy efficiency obtained in the model, as this excess energy (above the reaction enthalpy) is just wasted. Indeed, the maximum theoretical energy efficiency obtained in our current model, at the most ideal conditions for energy efficient CO_2 conversion, is only around 45 % (see figure VIII.1), while experiments have reported energy efficiencies up to 90 % at ideal conditions (i.e., strong vibrational excitation and thermal non-equilbrium, due to reduced pressure and supersonic flow in MW discharges[33]). Although these results have not yet been reproduced since then, more recent MW experiments also reveal energy efficiencies of about 50% at reduced pressure and supersonic flow, or at reverse vortex flow[34], at probably not-yet-ideal conditions (smaller reactor, lower power deposition). Moreover, even at non-ideal conditions (e.g., MW or GA at atmospheric pressure, where the VDF is too close to thermal, see chapter VI), the measured energy efficiency is already around 30 %[37;40]. Thus, we may wonder whether this waste of vibrational energy, as predicted by the model, might be overestimated, thus leading to an underestimation of the predicted energy efficiency.

It must be stressed that this result depends on our assumption for the value of the α_O parameter, which is adopted from Fridman[22], but it is subject to uncertainty. In the previous chapter, we investigated the effect of uncertainties on the rate coefficients of various reactions (chapter VII), but we did not study the effect of the α parameters. Therefore, we will consider in the following two sections the effect of the two α parameters of reactions N1 and N2 (section VIII.3.2.1) and of the activation energy of reaction N2 (section VIII.3.2.2), in particular with respect to the obtained CO_2 conversion and energy efficiency, in order to elucidate how the variation of these parameters can yield higher predicted values for the conversion and energy efficiency.

VIII.3.2 Influence of the dissociation rate coefficients on CO_2 conversion and energy efficiency.

VIII.3.2.1 Role of α in the CO_2 dissociation reactions N1 and N2

In this section, we vary the values of the α parameters of N1 and N2, the two main neutral dissociation reactions. There is of course no possibility to vary these parameters experimentally. However, knowing their effect on the plasma variables can help to design experiments used to determine these coefficients, as for now, they are estimated based on simplified theories[22] and their values also depend on the activation energies, which are also subject to uncertainties. We name these parameters α_M and α_O, for reaction N1 and N2, respectively.

Figure VIII.9 illustrates the behavior of the CO_2 conversion (left z-axis) and energy efficiency (right z-axis) as a function of α_M and α_O, at a gas temperature of 300 K, an ionization degree of 10^{-5} and a reduced electric field of 50 Td (figure VIII.9 a) and 150 Td (figure VIII.9 b). Note that the standard values of α_M and α_O, used up to now in the model, are 0.82 and 0.5, respectively (see cross symbols in figure VIII.9).

At E/N = 50 Td, there is a sharp increase in the predicted CO_2 conversion and energy efficiency for $\alpha_M > 0.8$, reaching up to a maximum of 43 % and 62 %, respectively, for $\alpha_M = \alpha_O = 1$. The effect of α_O is much smoother than the effect of α_M. At the other end of the parameter space, $\alpha_M = \alpha_O = 0.25$ gives 7 % conversion and 10 % energy efficiency.

Conversely, at E/N = 150 Td, the effect of α_M and α_O is less pronounced. The CO_2 conversion and energy efficiency rise from 9 % and 13 %, respectively, for $\alpha_M = \alpha_O = 0.25$, to 22 % and 32 %, respectively, for $\alpha_M = \alpha_O = 1$. Since the role of electron impact dissociation is more important at 150 Td (cf. figure VIII.7 above), it is indeed quite straightforward that the CO_2 conversion and energy efficiency would be less affected by the choice of the two α parameters.

In order to understand these variations of the CO_2 conversion and energy efficiency with the values of α_M and α_O, figure VIII.10 a shows the main processes responsible for CO_2 conversion and figure VIII.10 b depicts the mean vibrational energy consumption per dissociation event, for various values of the α parameters. The meaning of mean vibrational energy consumption per dissociation event was explained in detail in section VIII.3.1.6.

As illustrated in figure VIII.10 a, with low values of α_M and α_O, the conversion is almost entirely due to electron impact dissociation, both at 50 Td and 150 Td, explaining (*i*) why variations in the value of these α parameters do not largely affect the calculated conversion and energy efficiency, and (*ii*) why the resulting conversion and energy efficiency are rather limited, because electron impact dissociation is a less efficient process than neutral dissociation from the CO_2 vibrational levels (N1 and N2). With higher values of α_M and α_O, at 50 Td, the contributions of N1 and N2 are equally important, contributing for nearly 50 %, while electron impact dissociation is only a minor process. On the other hand, at E/N = 150 Td, and $\alpha_M = \alpha_O = 1$, the three dissociation reactions have similar contributions to the overall CO_2 conversion.

Figure VIII.10 b indicates that mean the vibrational energy consumption of N1 is close to the reaction enthalpy (5.52 eV) for $\alpha_M < 0.82$, both at 50 and 150 Td. This means that only the highest vibrational level of CO_2 reacts in reaction N1, i.e. the level with an energy almost equal to the enthalpy of reaction N1 (or, equivalently, to the dissociation energy of CO_2). On the other hand, with $\alpha_M = 1$, the mean vibrational energy consumption of reaction N1 becomes close to the activation energy (4.5 eV), again at both values of the reduced electric field. As $E_a(\mathrm{N1}) < \Delta H^{\circ}(\mathrm{N1})$, this indicates that CO_2 molecules with vibrational energies significantly lower than the CO_2 dissociation energy can dissociate, in the absence of thermal energy, which should in theory not be possible. The fact that the model would allow that would mean that the energy is not conserved and thus we advise against the use of a value of α_M above 0.82 using this rate coefficient.

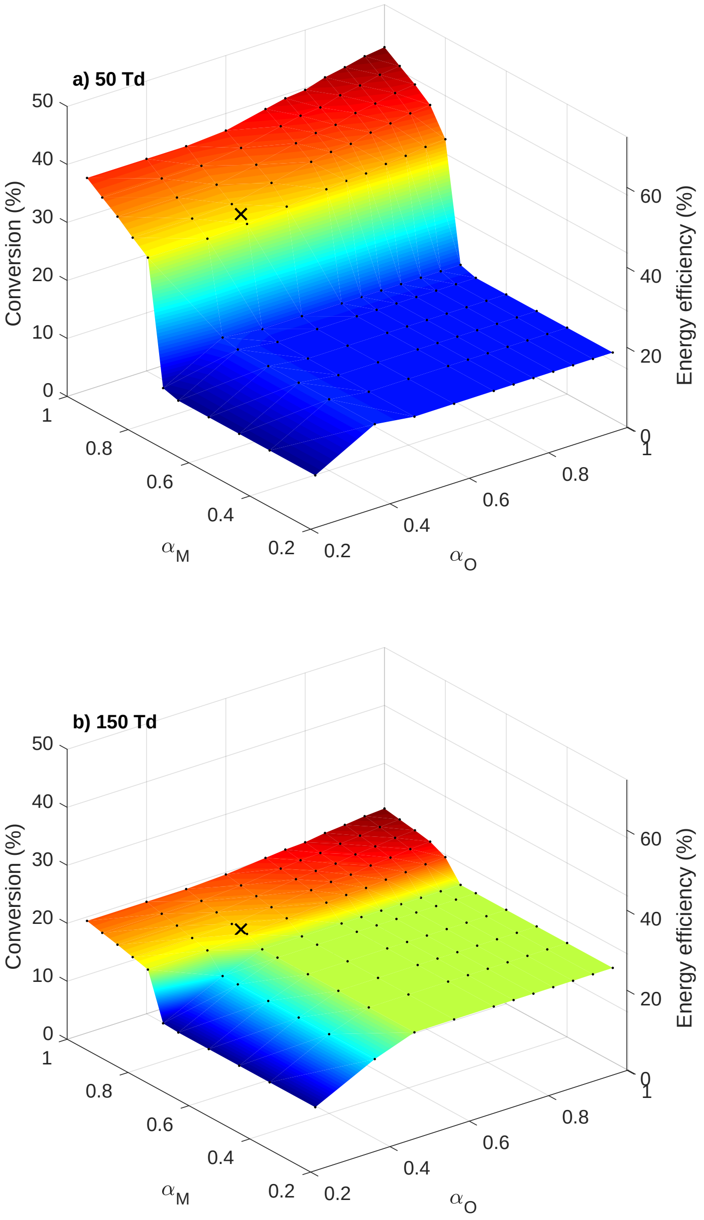

Figure VIII.9: CO_2 conversion and energy efficiency as a function of the α_M and α_O parameters, for a gas temperature of 300 K, an ionization degree of 10^{-5}, a pressure of 100 mbar, and a reduced electric field of 50 Td (panel a, top) and 150 Td (panel b, bottom). The cross symbols indicate the standard values of α_M and α_O, used up to now in the model, i.e., $\alpha_M = 0.82$ and $\alpha_O = 0.5$.

Baulch *et al.* pointed out in their review[174] that the activation energy of reaction N1 was significantly lower than the reaction enthalpy in the various experimentally derived values of the rate coefficient of reaction N1, but made no recommendation as to its value. They give two possible explanations for this anomaly: (*i*) the complexity of the reaction mechanisms of purely thermal CO_2 dissociation and (*ii*) the effect of impurities. More investigation will be needed to obtain a more accurate value of the rate coefficient, and in particular its activation energy, based on careful experiments in thermal conditions and on an improved analysis of the reaction scheme.

For reaction N2, on the other hand, the mean vibrational energy consumption decreases drastically with increasing values of α_O, both at 50 and 150 Td. With $\alpha_O = 1$, the mean vibrational energy consumption is close to the activation energy of the reaction (E_a(N2) = 2.28 eV), which means that the vibrational energy consumed by reaction N2 is only the energy necessary to overcome its activation energy. Reaction N2 then becomes much more likely to occur, which in turn increases the CO_2 conversion and the energy efficiency (cf figure VIII.9). However, if reaction N2 becomes faster, the concentration of O atoms may become the limiting factor. That is why the contribution of dissociation by O atoms cannot exceed 50 % of the total dissociation.

It may seem surprising that an increase of α_O does not lead to extra conversion for $\alpha_M < 0.7$. It can be explained as follows: reaction N1, for $\alpha_M \geq 0.8$, is efficient in dissociating the CO_2 molecules at the tail of the VDF and therefore depopulates it, resulting in the shape observed in figure VIII.6. However, N1 is very unlikely to occur significantly for $\alpha_M < 0.7$. Therefore, the tail of the VDF becomes more and more populated and the distribution resembles the Treanor distribution[123] mentioned above. The population of the highly excited states then becomes even larger than that of the states with energies comparable to the activation energy of N2 (E_a(N2) = 2.28 eV). Hence, even at increased values of α_O, N2 is still more likely to take place from highly excited states, since they are more populated. However, due to the limiting concentration of O atoms, N2 is not efficient at depopulating the tail of the VDF, since it is not as fast as vibrational pumping. This results in a high mean vibrational energy consumption of N2, much higher than its activation energy, despite an α_O close to 1, and is responsible for the relatively low conversion and energy efficiency at high α_O and low α_M.

It is also interesting to note that for $\alpha_M = \alpha_O = 0.25$ and E/N = 50 Td, because neutral dissociation reactions are practically not occurring, the vibrational energy is partially dissipated by electron impact dissociation, while at higher values of the α parameters or higher E/N, the vibrational energy consumed by electron impact dissociation is nearly negligible.

Finally, the comparison of the case with $\alpha_M = 0.8$ and $\alpha_O = 0.5$ at E/N = 50

Td with case 1 of figure VIII.7 (same conditions but with $\alpha_M = 0.82$) illustrates the competition between reactions N1 and N2. Indeed, shifting α_M only from 0.8 to 0.82 changes the ratio $\frac{R(\mathrm{N1})}{R(\mathrm{N2})}$ from 1.1 (figure VIII.10 b) to 1.77 (figure VIII.8). That is because the pre-exponential factor of reaction N1 is higher than that of reaction N2 (see table A.10 in appendix A.2), and because the concentration of O atoms can limit reaction N2. However, both reactions require highly excited vibrational levels of CO_2 to overcome their activation energy barrier. Thus, enhancing reaction N1 is detrimental for reaction N2, because it will consume the highly excited vibrational levels of CO_2 that would have reacted in N2 otherwise.

This value of $\alpha_M \approx 0.82$ can be considered as a sort of critical value α_{crit} for reaction N1, which can be understood from the discussion related to equations (III.4) and (III.5) (see section III.2). At low gas temperature (i.e. well below the activation energy), reaction N1 can only be significant if the vibrational energy of the CO_2 molecule (E_{vib}) follows $\alpha_M E_{vib} \gtrsim E_a(\mathrm{N1})$. In our state-to-state model, the highest vibrational level considered is CO_2[v21], with a vibrational energy $E_{v21} = 5.47eV$, i.e., close to the dissociation limit ($\Delta H^{\circ}(\mathrm{N1}) = 5.52$ eV). Therefore, for N1 to occur, it is required that $\alpha_M \gtrsim E_a/E_{v21} \simeq 0.83$, which explains the sharp rise in CO_2 conversion and energy efficiency for $\alpha_M > 0.8$, also noted in figure VIII.9 a. Note that with $\alpha_M = 0.82$, as standardly used in our model, this reaction can still occur for the highest vibrational levels, as thermal energy still has a small contribution.

The fact that this ratio $R(\mathrm{N1})/R(\mathrm{N2})$ is so sensitive to the change of α_M around 0.8 is due to the fact that $\alpha_M E_{v21} \approx 4.5$ eV$= E_a(\mathrm{N1})$ for $\alpha_M \approx 0.82$, where E_{v21} is the energy of the highest CO_2 vibrational level. Therefore, for $\alpha_M < 0.8$, even the highest vibrational level CO_2[v21] sees an activation energy, while it only sees a small activation energy (or even none) for $\alpha_M > 0.8$.

To sum up the findings of this section, we first recommend to use a value of $\alpha_M = 0.82$, following the explanations given above. Using a higher value of α_M may lead to loss of energy conservation and is thus not recommended. The model results are less sensitive to the value of α_O and we can consider at this stage that a value of 0.5 gives reasonable results, i.e. following equation (III.5) with the rate coefficient presented in table A.10 in appendix A.2. Although the energy losses due to reaction N2 have been identified as being the limiting factor for energy efficient CO_2 conversion, an increase of the value of α_O does not lead to a very significant improvement of the energy efficiency calculated by the model, especially when using the recommended value of $\alpha_M = 0.82$. Therefore, the difference between the values of energy efficiency determined by the experiments and predicted by the model cannot be solely explained by the choice of α_O. However, as mentioned above, the activation energy of N2 is also subject to uncertainties. The effect of the activation energy of N2, and its coupling with the

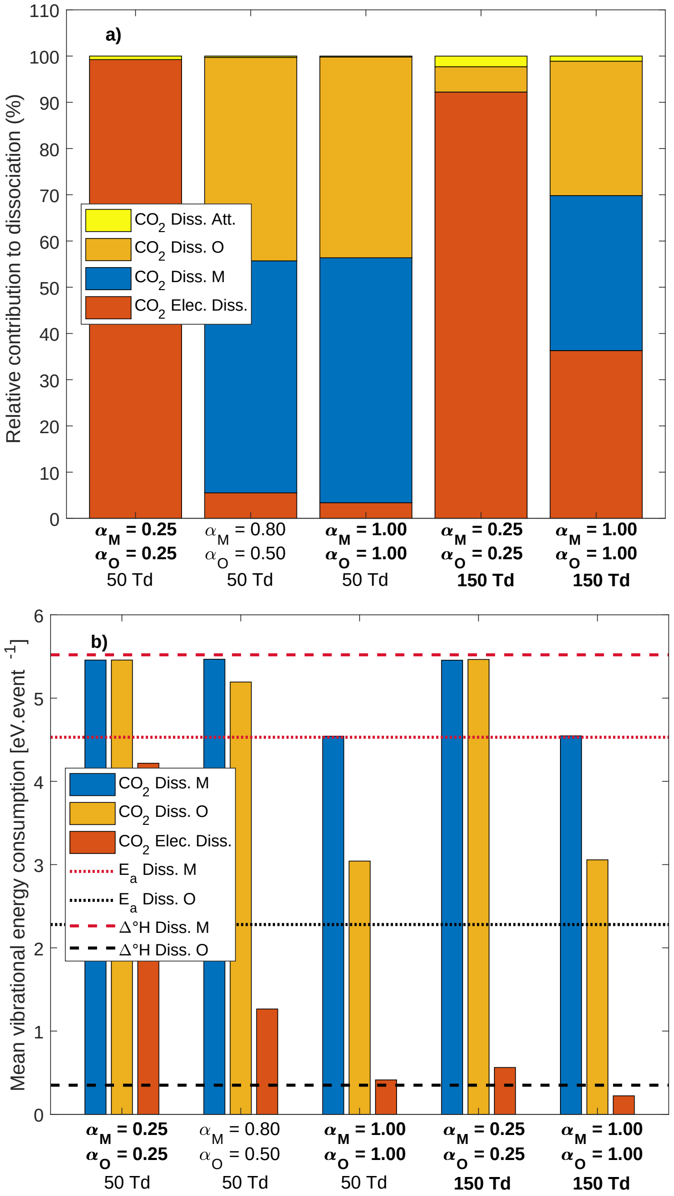

Figure VIII.10: Main processes responsible for CO_2 dissociation (a) and mean vibrational energy consumption per dissociation event (b) for different conditions, integrated over time, for a temperature of 300 K, an ionization degree of 10^{-5} and a pressure of 100 mbar. The parameters written in bold indicate the differences with the second case. The dotted and dashed lines in (b) show the activation energy and the standard reaction enthalpy, respectively, of reactions (N1) and (N2), i.e. dissociation upon impact by any molecule M and upon O atom impact, in red and in black, respectively.

value of α_O, may thus provide better insights on the limitations to the energy efficiency predicted by the model.

VIII.3.2.2 Role of the activation energy of dissociation reaction N2

In the previous chapter on the uncertainties in the rate coefficients (chapter VII), we assumed that the uncertainty was contained in the pre-exponential factor. This choice is valid in a given temperature range, where the rate coefficient has been derived experimentally and where the uncertainty in the pre-exponential factor also contains the uncertainty in the activation energy.

However, the uncertainty on the activation energy of the various reactions considered in this model can be particularly important when dealing with vibrationally excited molecules. Indeed, the previous assumption may not hold anymore, as the vibrationally excited levels will lower this activation energy, so the effect of uncertainty can become quite critical. The choice of the parameter α is closely related to the value of the activation energy considered. Given the variety of rate coefficients found for reaction N2[22;23;174] and the differences in their activation energies, it is likely that the rate coefficient considered in our model overestimates its activation energy. Indeed, values ranging between 1.4 eV and 2.9 eV are found in the NIST database[23], while Baulch *et al.*[174] recommend a value of 2.28 eV (considered in our model) and Fridman[22] considers a value of 1.43 eV. Baulch *et al.*[174], being a review of various sources, appeared to us as the most reliable source.

Following the work of Kozak and Bogaerts[57], we study in this section the effect of the activation energy of N2 and its coupling with α_O. Note that we have kept the pre-exponential factor of the rate coefficient constant. This means that the rate coefficient of N2 increases exponentially with decreasing activation energy. Since ΔH°(N2)=0.35 eV/molec is the theoretical minimum, we consider values of E_a(N2) from 0.35 eV to 2.5 eV. We consider here 2.5 eV as a maximum value of the activation efficiency, since 2.28 eV, the value adopted in our model, may already be an overestimation, given the fact that our predicted energy efficiency is limited compared to some experimental record values in literature.

We do not study here the effect of the value of the activation energy of reaction N1, since by our choice of $\alpha_M = 0.82$, we ensure that only CO_2 molecules with vibrational energies close to the dissociation limit can effectively dissociate through N1. Moreover, given that most experimentally derived value of E_a(N1) are even below the reaction enthalpy, as explained above, it seems unlikely that the activation energy of this reaction is significantly higher than the reaction enthalpy (5.52 eV)

Figure VIII.11 illustrates the CO_2 conversion (left z-axis) and energy efficiency (right z-axis) as a function of E_a(N2) and α_O, again at a gas temperature of 300 K, an ionization degree of 10^{-5} and a reduced electric field of 50 Td (figure VIII.11 a) and 150 Td (figure VIII.11 b). A value of 0.82 is considered for α_M, in accordance with the first section of this chapter (section VIII.3.1) and with the recommendations of section VIII.3.2.1.

At 50 Td (figure VIII.11 a), the conversion and energy efficiency vary from 30 % and 43 %, respectively, for E_a(N2) $= 2.5$ eV and $\alpha_O = 0$, to 50 % and 72 %, respectively, with E_a(N2) $= 0.35$ eV and $\alpha_O = 1$. The increase is quite smooth with both α_O and E_a(N2), in comparison with the increase in CO_2 conversion caused by α_M (figure VIII.9).

At 150 Td (figure VIII.11 b), the conversion and energy efficiency vary from 17 % and 25 %, respectively, for E_a(N2) $= 2.5$ eV and $\alpha_O = 0$, to 29 % and 42 %, respectively, with E_a(N2) $= 0.35$ eV and $\alpha_O = 1$. The evolution of the CO_2 conversion and energy efficiency with α_O and E_a(N2) resembles that of the 50 Td case, but with lower absolute values.

To understand these results, figure VIII.12 again presents the relative importance of the main processes responsible for CO_2 conversion (figure VIII.12 a) and the mean vibrational energy consumption per dissociation event (figure VIII.12b) for different choices of α_O, E_a(N2) and E/N. The results are integrated over time, for a temperature of 300 K, an ionization degree of 10^{-5} and a pressure of 100 mbar.

The reaction rate of N2 is subject to a very strong influence of both α_O and E_a(N2). In the most favorable case (i.e. E_a(N2) $= 0.35$ eV and $\alpha_O = 1$), reaction N2 accounts for half of the CO_2 conversion, both at 50 and 150 Td (see case 3 and 5 in figure VIII.12 a). This means that all the O atoms produced by the other CO_2 dissociation reactions (i.e., upon collision with any molecule M, or due to electron impact dissociation, which is important at 150 Td; cf figure VIII.12 a) dissociate an extra CO_2 molecule. The presence of O atoms is then the limiting factor for reaction N2 to occur. On the other hand, with a low value of α_O, the relative contribution of N2 to CO_2 conversion is practically negligible (cf. case 1 and 4 in figure VIII.12 a, for $\alpha_O = 0.25$). This means that the O atoms produced by CO_2 conversion will recombine together, forming O_2, and thus will not contribute to the conversion of CO_2.

In case 2, reaction N2 still accounts for almost half of the total dissociation, despite an activation energy of 2.25 eV. That is due to the competition between reactions N1 and N2 to dissociate the highly excited vibrational levels of CO_2, as explained above in section VIII.3.2.1. With $\alpha_O = 1$ and E_a(N2) $= 2.25$ eV, reaction N2 can easily occur for vibrational energies above 2.25 eV, hence the second half of the VDF. N2 can thus occur with vibrational levels that cannot react with N1, and the concentration of O atoms becomes then again the limiting factor of N2. Hence, the mean vibrational

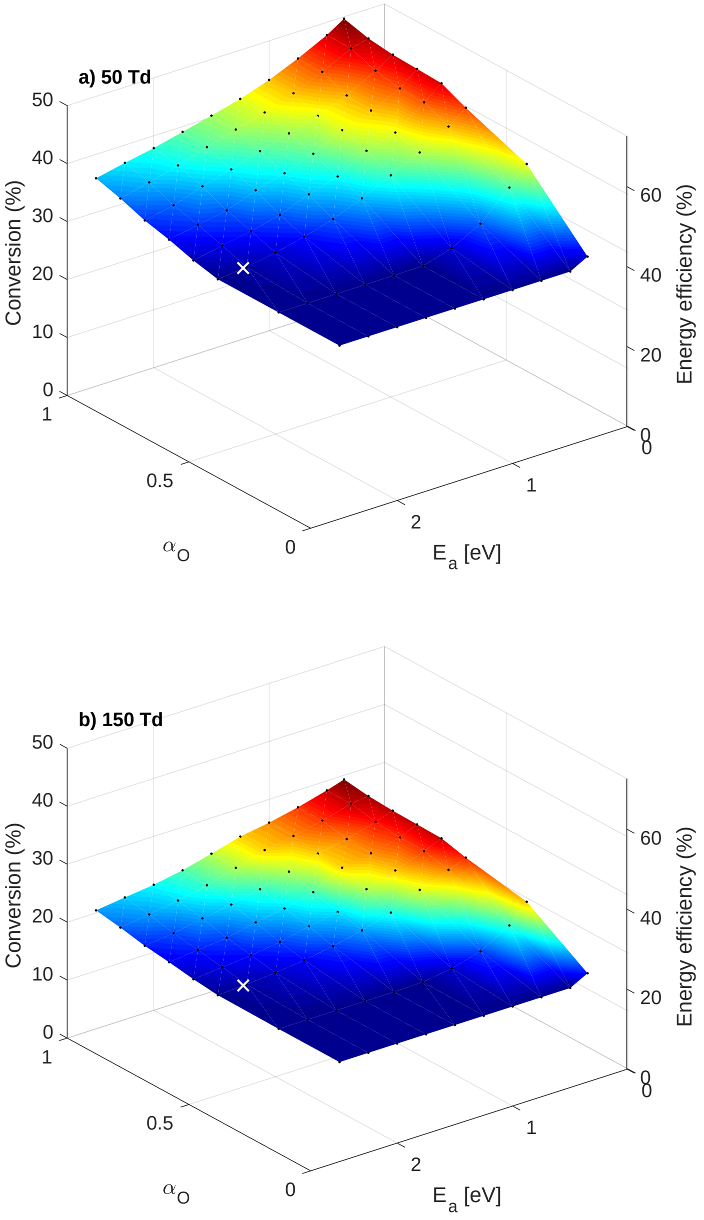

Figure VIII.11: CO_2 conversion and energy efficiency as a function of the α_O parameter and the activation energy of reaction N2, for a gas temperature of 300 K, an ionization degree of 10^{-5}, a pressure of 100 mbar, and a reduced electric field of 50 Td (panel a, top) and 150 Td (panel b, bottom). The cross symbols indicate the standard values of E_a(N2) and α_O, used up to now in the model, i.e., $E_a(\text{N2}) = 2.28$ eV and $\alpha_O = 0.5$.

energy consumption of N2 drops to about 3.2 eV, as can be observed in figure VIII.12 b.

As expected, the mean vibrational energy consumption of reaction N2 is strongly affected by both α_O and E_a(N2), as is clear from figure VIII.12 b. Increasing α_O and/or decreasing E_a(N2) allows the O atoms to react with lower vibrationally excited CO_2 molecules and still give rise to dissociation, thus reducing the mean vibrational energy consumption, and hence improving the conversion and energy efficiency predicted by the model (cf figure VIII.11).

VIII.3.3 Maximum theoretical energy efficiency

We have seen in the previous sections that the excess vibrational energy required to overcome the activation energy barrier of the two main dissociation reactions, i.e. N1 and N2, leads to a considerable energy loss for the conversion, especially concerning reaction N2. In this section, we derive a formula that gives the maximum energy efficiency that can be reached in the model. This formula is derived to give a mathematical framework to the observations of the previous sections. More specifically, it provides insight in the effect of the input parameters in the model (i.e., activation energies of reactions N1 and N2, and corresponding α parameters, being a measure for the efficiency of the vibrational levels to overcome these activation energies) for predicting the theoretical maximum energy efficiency. Furthermore, it is helpful in order to understand how the experimental energy efficiency can be improved. The actual values of the activation energy and α parameters are not used in this section on purpose, given the uncertainties present on their values.

In conditions of pure vibration-induced dissociation, the minimum vibrational energy required to dissociate a CO_2 molecule through either N1 or N2 is given by E_a/α. The products of the dissociation reactions (i.e. CO and/or O_2) are assumed to be formed in ground vibrational state. Thus an energy of at least $E_a/\alpha - \Delta H^\circ$ is dissipated into heating. For reaction N1, we have used $E_a(\mathrm{N1})/\alpha_M = 4.53\mathrm{eV}/0.82 = 5.52$ eV as standard values in our model. In the case of reaction N2, we have considered $E_a(\mathrm{N2})/\alpha_O = 2.28\mathrm{eV}/0.5 = 4.56$ eV. Thus, in our standard model, only the vibrational levels with energy $\gtrsim$ 5.52 eV and 4.56 eV can contribute to CO_2 dissociation through N1 and N2, respectively, in the absence of thermal (translational) energy, i.e., in the case of pure vibration-induced dissociation. For N1, this means that only the highest vibrational level (v_{21}) can contribute, in the absence of thermal (translational) energy.

In the case of electron impact dissociation, an electron energy $E_{e^-,diss}$ is consumed by each event, where $E_{e^-,diss}$ is the energy threshold of electronic dissociation. In this study, we have considered $E_{e^-,diss}$ =7eV , as advised by previous research[64;104].

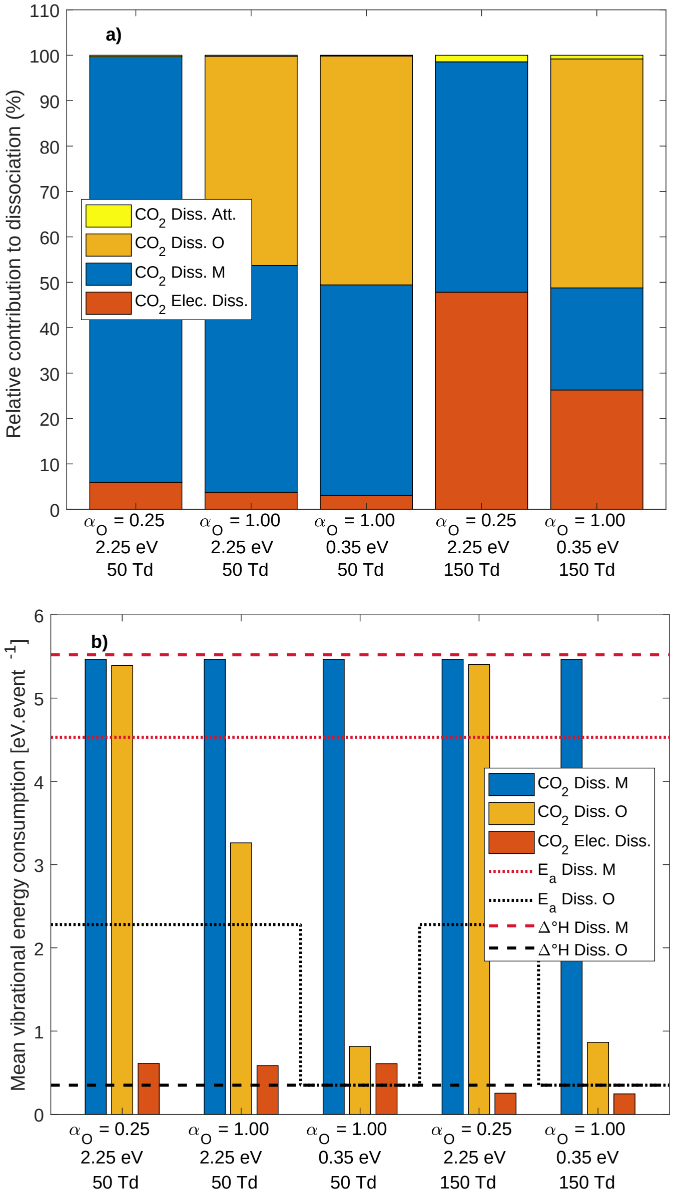

Figure VIII.12: Main processes responsible for CO_2 dissociation (a) and mean vibrational energy consumption per dissociation event (b) for different conditions, integrated over time, for a temperature of 300 K, an ionization degree of 10^{-5} and a pressure of 100 mbar. The dotted and dashed lines in (b) show the activation energy and the standard reaction enthalpy, respectively, of reactions (N1) and (N2), i.e. dissociation upon impact by any molecule M and upon O atom impact, in red and in black, respectively. Note that the activation energy of reaction N2 is not the same for the different cases, as indicated below the x-axis for each case.

The following inequality is thus verified:

$$E_a(\mathrm{N2})/\alpha_O < E_a(\mathrm{N1})/\alpha_M < E_{e^-,diss} \tag{VIII.2}$$

Note that since reaction N2 requires O atoms to be created by previous dissociation reactions in order to occur, we have $R_{\mathrm{N1}} + R_{e^-,diss} \geq R_{\mathrm{N2}}$, where R_{N1}, R_{N2}, $R_{e^-,diss}$ are the reaction rates of reaction N1, N2 and electron impact dissociation, respectively.

Given inequality (VIII.2), the best energy efficiency, or equivalently the lowest energy cost per CO_2 molecule converted, is reached for $R_{\mathrm{N1}} = R_{\mathrm{N2}}$ and $R_{e^-,diss} = 0$. In other words, this means that CO_2 molecules are first dissociated by reaction N1 and the O atom produced subsequently reacts again in reaction N2 to dissociate another CO_2 molecule.

Following all these considerations, we can derive a formula of the minimum energy cost per CO_2 molecule converted:

$$E_{cost} = \frac{1}{2}\{E_a(\mathrm{N1})/\alpha_M + E_a(\mathrm{N2})/\alpha_O\} \tag{VIII.3}$$

The $\frac{1}{2}$ factor originates from the fact that two CO_2 molecules are converted by reaction N1 followed by reaction N2. Note that this formula effectively gives the minimum energy cost, as it assumes that the total energy cost is only due to vibrational energy cost, i.e., considering pure vibration-induced dissociation, which is the most energy efficient dissociation process, as discussed above.

This yields a simple formula for the maximum energy efficiency, depending only on the activation energies of both neutral-induced dissociation reactions N1 and N2, and the corresponding α parameters (i.e., efficiency of the vibrational levels to overcome these activation energies):

$$\eta_{max} = \frac{2.93\mathrm{eV/molec}}{\frac{1}{2}\{E_a(\mathrm{N1})/\alpha_M + E_a(\mathrm{N2})/\alpha_O\}} \tag{VIII.4}$$

As mentioned above, 2.93eV/molec is the reaction enthalpy of $CO_2 \rightarrow CO + \frac{1}{2}\ O_2$. It is useful to know that this formula is based on the following assumptions:

1. The conversion mechanisms are purely vibration-induced and not thermal. This means that the mean translational energy of the molecules is much lower than the activation energy of the different reactions. Following the results of section VIII.3.1, this approximation is not valid anymore at gas temperatures of 2000K and above. However, thermal processes are typically less energy efficient than non-thermal processes[22]. The formula is thus likely to still be verified in the thermal case.

2. The excess vibrational energy needed by CO_2 molecules to overcome the activation energy barrier of a dissociative reaction is lost to heat. This implies that the CO molecules created are in ground state. In reality, CO might however acquire part of the surplus vibrational energy after dissociation, which could actually increase the energy efficiency of the conversion. Indeed, given the fast VV CO_2-CO transfers, this CO vibrational energy could transfer to CO_2 vibrational modes and used again for dissociation, and thus it might not all be wasted.

Figure VIII.13 presents the CO_2 conversion (left y-axis) and corresponding energy efficiency (right y-axis), predicted by our model, as a function of the reduced electric field E/N for a gas temperature of 300 K and an ionization degree α_i of 10^{-4}, i.e. the conditions showing the maximum conversion and energy efficiency in figure VIII.1, and for three different values of $E_a(\text{N2})/\alpha_O$ (0.35 eV, 1.64 eV and 4.50 eV). A value $E_a(\text{N1})/\alpha_M = \Delta H^{\circ}(\text{N1}) = 5.52$ eV is considered here, as in section VIII.3.1.

The last value corresponds to our standard model, with $E_a(\text{N2})/\alpha_O = 2.28$ eV and $\alpha_O = 0.5$; the first value corresponds to the minimum $E_a(\text{N2})$ of 0.35 eV (equal to the reaction enthalpy) and $\alpha_O = 1$ (see section VIII.3.2.2); and finally, the middle value is $E_a(\text{N2})/\alpha_O = 1.64$ eV, with $E_a(\text{N2}) = 1$ eV and $\alpha_O = 0.61$, as calculated with the Fridman-Macheret model (equation (III.5)).

The dashed lines of the corresponding colors indicate the maximum theoretical energy efficiencies calculated with equation (VIII.4), for these three different values of $E_a(\text{N2})/\alpha_O$, yielding 100 %, 82 % and 58 %, respectively. These results are shown to see how this maximum theoretical energy efficiency, which is determined based on the rate coefficient expressions of N1 and N2 (more specifically the activation energies and corresponding α parameters), influences the results of CO_2 conversion and energy efficiency. Note that a value of $E_a(\text{N2})/\alpha_O = 4.5$ eV corresponds to the case presented in figure VIII.1 (standard model).

The increase in CO_2 conversion and energy efficiency upon lower E/N, that was observed in figure VIII.1 (for $E_a(\text{N2})/\alpha_O = 4.5$ eV) for low E/N becomes even more pronounced with lower values of $E_a(\text{N2})/\alpha_O$, especially with 0.35 eV (i.e. $E_a(\text{N2})/\alpha_O = \Delta H^{\circ}(\text{N2})$). The maximum energy efficiency calculated at 10 Td is 46 %, 65 % and 86 % for $E_a(\text{N2})/\alpha_O = 4.5$ eV, 1.64 eV and 0.35 eV, respectively. In all three cases, the maximum energy efficiency calculated by the model (i.e. at 10 Td) is thus quite close to the theoretical maximum energy efficiency, derived following equation (VIII.4). This implies that the conditions plotted in figure VIII.13, i.e. $T_g = 300$ K, $E/N = 10$ Td and $\alpha_i = 10^{-4}$, are quite optimal. The fact that the maximum calculated energy efficiency is not entirely equal to the theoretical maximum is due to other losses, that are not accounted for in the formula of equation (VI.1), i.e., the fact that not all plasma power goes into electron energy, and especially that not all electron energy goes into vibrational excitation; see below.

At low pressure (1550 Pa), Andreev *et al.*[67] showed that their CO_2 glow discharge was self-sustained for reduced electric fields of 38.4 Td and above. In order to reach lower values of E/N, a second power source, enhancing ionization using a higher E/N had to be used. Therefore, these low values of E/N, especially 10 Td, in combination with an ionization degree of 10^{-4}, may be difficult to reach experimentally, unless a second power source is used. These values can however be considered as recommendations towards future experiments. Indeed, as also discussed in section VIII.3.1.3 above, there is clearly room for optimization of the most common discharges used for CO_2 conversion, by using setups working simultaneously at low E/N, gas temperatures close to room temperature and high ionization degrees.

Using particularly favorable conditions (10 Td, 300 K, $\alpha_i = 10^{-4}$), and $E_a(\mathrm{N1})/\alpha_M = \Delta H^{\circ}(\mathrm{N1})$ and $E_a(\mathrm{N2})/\alpha_O = \Delta H^{\circ}(\mathrm{N2})$, our model predicts a maximum energy efficiency of 86 %. This value seems to be a practical limit for the energy efficiency due to the kinetics of the CO_2 discharge, and in particular the fact that electrons always lose part of their energy to processes other than CO_2 vibrational excitation (see figure VIII.4). Indeed, the latter is not included in the formula for the maximum theoretical energy efficiency (equation (VIII.4)), yielding a value of 100 % in this case. Using a lower SEI may reduce the electron energy losses to CO vibration and electronic excitation, since it would also reduce the conversion and thus the CO density.

The fact that the energy efficiency presented in figure VIII.1 does not reach this maximum value of 86 % is thus entirely due to the choice of the rate coefficient expressions (i.e., the value of the activation energies and α parameters). Using the values presented in Kozak and Bogaerts[57] and in Fridman[22], i.e., $E_a(\mathrm{N1}) = 5.58$ eV, $E_a(\mathrm{N2}) = 1.43$ eV, $\alpha_M = 1$ and $\alpha_O = 0.5$, we obtain a maximum energy efficiency of 70%. However, in our previous study on the uncertainties in the rate coefficients (see chapter VII), we have not been able to verify the origin of these rate coefficients, and therefore we are reluctant to use them in our standard model. This greatly underlines the importance of the choice of rate coefficients and values of α.

To sum up, experimentally, energy efficiencies up to 90% have been reported[33] in non-thermal conditions. Assuming these are not the result of experimental errors, two explanations can be considered for the differences between the maximum model predictions and the maximum experimental CO_2 conversion and energy efficiency in conditions of pure vibration-induced dissociation.

(i) A first explanation could be due to uncertainties in the activation energy of the neutral dissociation reactions, as discussed in this chapter. Assuming that $E_a(\mathrm{N1})/\alpha_M = 5.52$ eV, i.e. the enthalpy of the reaction, equation (VIII.4) indicates that in order to

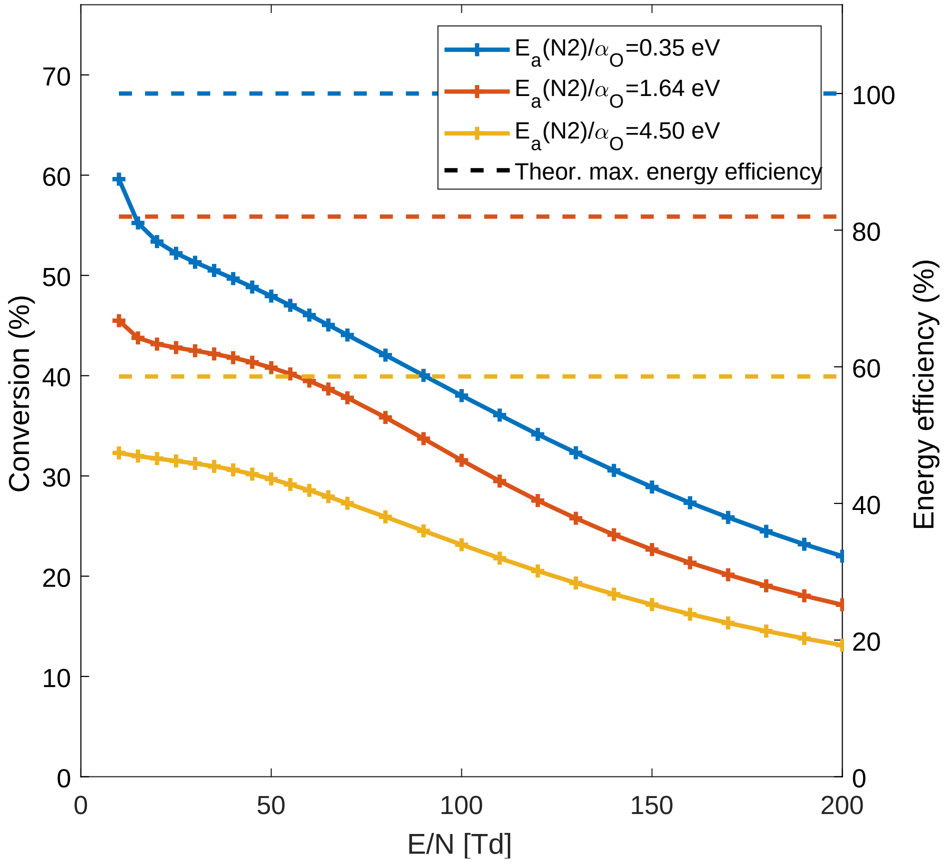

Figure VIII.13: CO_2 conversion (left y-axis) and corresponding energy efficiency (right y-axis) as a function of the reduced electric field E/N, for three values of $E_a(\mathrm{N2})/\alpha_O$ (0.35 eV, 1.64 eV, 4.50 eV), and for a gas temperature of 300 K, and an ionization degree of 10^{-4}. The dashed lines indicate the corresponding maximum theoretical energy efficiency using equation (VIII.4) in each case. The value of $E_a(\mathrm{N1})/\alpha_M$ is taken equal to 5.52 eV, as in our standard model.

have $\eta_{max} \gtrsim 90\%$, it is required to have $E_a(\mathrm{N2})/\alpha_O \lesssim 1$ eV . To our knowledge, there are no measurements of $E_a(\mathrm{N2})$ that would yield $E_a(\mathrm{N2})/\alpha_O \lesssim 1$ eV. Therefore, while it is possible that the conversion and energy efficiency are underestimated in our model due to the uncertainties in the rate coefficients, it is unlikely that an energy efficiency of 90% could be reached only by considering a more accurate value for $E_a(\mathrm{N2})/\alpha_O$.

(ii) Another explanation could be that the second assumption listed above is not fulfilled, i.e. the vibrational modes of the dissociation products, and in particular CO, receive part of the surplus vibrational energy in a dissociation event. This energy could then be redistributed to CO_2 vibrational modes and be used again for dissociation, thus increasing the energy efficiency of the conversion. To our knowledge, there is no study quantifying this phenomena, but it would be interesting to investigate this in future work.

The activation energy of the reaction of CO_2 dissociation upon collision with O atoms seems to be, in any case, a limiting factor to energy-efficient CO_2 conversion, as it is much higher than the reaction enthalpy. A way to enhance the energy efficiency could be the combination of plasma and catalysis. Indeed, a catalyst could enhance the dissociation rate of CO_2 upon collision with O atoms by lowering the activation energy barrier of this reaction, thus also reducing its vibrational energy consumption. Promising results have been obtained in the field of plasma-catalysis[94;175;176], although more research is needed to precisely understand the mechanisms of the plasma-catalyst interactions in plasma-catalytic CO_2 conversion.

VIII.4 Conclusion

We have elucidated the underlying (energy transfer) processes and the limiting reactions for energy efficient CO_2 conversion in a non-equilibrium plasma, in a range of different conditions, by means of a zero-dimensional chemical kinetics model.

In the first section, we show the electron energy losses and the vibrational energy losses, as well as the VDFs and the contributions of the various processes to CO_2 conversion, varying the reduced electric field, the ionization degree and the gas temperature, and we use these results to explain the calculated CO_2 conversion and energy efficiency in this range of conditions. In the second section, in order to understand the theoretical limitations to the energy efficiency, we vary the values of the α parameters for the neutral dissociation reactions and the activation energy of the dissociation of CO_2 upon impact with O atoms, and we investigate their effect on both the CO_2 conversion and the energy efficiency, as well as on the underlying dissociation mechanisms and their energy consumption.

The model reveals the important role of vibrational excitation, particularly at low gas temperatures. A lower E/N increases the contribution of the electron energy going to vibrational excitation of CO_2. Furthermore, at low gas temperatures, this leads to a large part of the energy used for dissociation, upon collision of the vibrational levels with neutral molecules (either molecules M or O atoms), which is thus beneficial for the energy efficiency. At higher gas temperatures, VT relaxation becomes more prominent, so the vibrational energy primarily dissipates to heat. The ionization degree also has an important effect, since a higher ionization degree leads to a shorter plasma residence time (to reach the same fixed specific energy input of 2 eV/molec, used in this study), and thus a larger vibrational population.

Using standard values for the α parameters for the neutral dissociation reactions and for the activation energy of dissociation of CO_2 upon impact with O atoms, our model predicts a CO_2 conversion and energy efficiency up to 32 % and 47 %, respectively, for a gas temperature of 300 K, an ionization degree of 10^{-4}, and a very low reduced electric field (10 Td). At 50 Td, the corresponding values are 30 % and 43 %, respectively. At ionization degrees typical of gliding arc and microwave discharges (i.e. around 10^{-6}), a maximum conversion and energy efficiency of 29 % and 42 %, are reached, respectively, for a reduced electric field of 45 Td and a gas temperature of 300 K. Plasma can still be sustained at this low E/N, as e.g. shown experimentally in a glow discharge by Andreev *et al.*[67].

Furthermore, we identified that the vibrational energy consumption of dissociation is a strong limitation to the energy efficiency. Indeed, the activation energy of the dissociation of CO_2 upon collision with an O atom is quite high (we considered a value of 2.25 eV in this study), while the enthalpy of the reaction is significantly lower (0.35 eV at standard conditions). Moreover, the vibrational energy only has a limited efficiency to overcome the activation energy barrier of this reaction. It thus requires an energy $E_a(\mathrm{N2})/\alpha_O$ to overcome the barrier. Therefore, the vibrational energy required to overcome the activation energy barrier is high and the excess energy is typically wasted to heat.

By varying the parameters α of the two main dissociation reactions (i.e., upon collision with any neutral molecule, or upon collision with O atoms), we can increase the conversion and energy efficiency up to 62 % (at E/N = 50 Td, 300 K and an ionization degree of 10^{-5}). Furthermore, by varying the parameter α as well as the activation energy of the dissociation upon collision with an O atom, the conversion and energy efficiency can be further increased up to 72 %. Using the most optimal values of activation energy and α, as well as plasma operating conditions (E/N = 10 Td, 300 K and an ionization degree of 10^{-4}), the model predicts an energy efficiency up to 86 %. The fact that this is not 100 % is attributed to other losses in the kinetics of CO_2 conversion, more specifically the fact that still not all electron energy will go to vibrational excitation of CO_2, but some fraction is also spent to the dissociation products (CO and O_2).

Finally, we derived an empirical expression for the theoretical maximum energy efficiency that can be reached by this model, given certain values for the activation energy and α parameters of the two neutral dissociation reactions. This formula can be used to identify the theoretical limitations to the energy efficiency, based on a given set of rate coefficients. Using the most optimal values of activation energy and α, a theoretical maximum energy efficiency of 100 % is predicted.

Using the activation energies (and thus rate coefficients) and the α values adopted from literature, a theoretical maximum energy efficiency of 58 % was reached. Comparing this value with the actual values predicted by the model, with a maximum of 47 %, shows that a very low E/N (10 Td), low gas temperature (300K) and a high ionization degree (10^{-4}) are nearly ideal for the most energy efficient CO_2 conversion. The most common discharges used for CO_2 conversion operate at clearly different conditions, i.e., somewhat higher E/N (50 - 100 Td), higher gas temperature (up to a few 1000 K) and lower ionization degree (10^{-6}) for MW and GA discharges, and significantly higher E/N (200 Td and above) for DBDs. This indicates that there is clearly room for optimization of the most common discharges used for CO_2 conversion, by modifying the setups, or developing new devices, working simultaneously at low E/N, gas temperatures close to room temperature and high ionization degrees.

CHAPTER IX

Conclusions and future prospects

In this thesis, I modeled the conversion of CO_2 in a microwave plasma. This process is gaining increasing interest, as it would allow chemical energy storage of intermittent renewable energy. Indeed, microwave plasmas can offer high energy efficiencies for CO_2 dissociation, which is particularly important in the framework of energy storage, and they can be turned on and off in a matter of seconds, which means they can easily adapt to the fast changes of electricity production by renewable energy sources.

It was reported in the 1980's that vibrational excitation is one of the keys to achieve good energy efficiencies, which can explain the high energy efficiency obtained with microwave plasmas. However, there is still a lack of detailed understanding of the processes occurring in a CO_2 discharge and the high energy efficiencies obtained in the 1980's are therefore not easily reproducible. This thesis focuses on modeling microwave plasmas and their kinetics, and in particular their vibrational kinetics.

Chapter I presents a short review of the various energy storage technologies and the different plasma sources used for CO_2 dissociation, as well as the state of the art in research on energy-efficient plasma-based CO_2 dissociation, to better understand the context in which this research took place. The theory forming the basis of the models developed during this doctoral work is detailed in chapter II, as well as the equations that are solved in the models. The CO_2 chemistry set and the different scaling laws required to model the complex vibrational kinetics are presented in chapter III.

In chapter IV, a 2D-axisymmetric microwave plasma model was developed for argon as a first step, containing and coupling the description of the electromagnetic waves, heat transfers, flow properties and plasma kinetics. This model gave meaningful insights in the shape and the properties of a microwave plasma, useful for the later 0D plasma chemistry models in CO_2.

The chemistry set of CO_2 is, however, too large to be modeled in 2D or 3D, given the numerical resources currently at our disposal. Therefore, chapter V presents a reduction of the chemistry set and a level-lumping method for the asymmetric mode vibrational levels of CO_2 in order to reduce the number of equations to be solved in the model and thus the computational load. This method was later successfully implemented in a similar 2D classical gliding arc model for CO_2 conversion1[171] and the plan is to implement this method in a 2D model for a CO_2 microwave plasma as well, in follow-up work by another PhD student in the group PLASMANT.

Subsequently, in chapter VI, we investigated more in detail the mechanisms leading to dissociation of CO_2 in a microwave discharge, by means of a 0D model developed for this purpose. The model shows that the vibrational non-equilibrium required for energy efficient CO_2 dissociation is typically not enough exploited in conventional laboratory scale microwave discharges, since the plasma thermalizes too fast. The pressure and gas temperature are found to be key parameters to control the speed of thermalization, i.e., a higher pressure and temperature lead to faster thermalization.

Following the work of Turner[163], in chapter VII, we verified the rate coefficients used in the CO_2 0D model and we estimated their uncertainties, based on a detailed literature search. We then implemented a Monte Carlo-like procedure to determine the corresponding uncertainty in the model outputs. It was found that the uncertainty can be quite high (in the order of 100 %) , mainly on the CO_2 conversion and the vibrational level populations. Moreover, statistical methods were used to determine the rate coefficients responsible for most of the uncertainty. While the error on the model results is found to be quite high, the trends obtained from the model appear to be reliable. A list of ‘good practices’ is provided, in accordance with the recommendations of Turner.

Finally, in chapter VIII, following the work on the dissociation mechanisms, we focused on analysing the energy transfers occurring in a plasma, in order to understand how to improve the energy efficiency of CO_2 dissociation in the discharge. The model reveals that a low gas temperature, high ionization degree and low reduced electric field give the most optimal conditions for energy efficient CO_2 dissociation. Moreover, the choice of rate coefficients and scaling parameters appeared crucial for the determination of the energy efficiency and a formula was derived to express the maximum energy efficiency that can be obtained in the model.

In general, our modeling would greatly benefit from additional experimental verification of the rate coefficients for which scaling laws considered. Moreover, developing models in higher dimensions for CO_2 would give meaningful insights in the processes occurring in more complex discharges, such as vortex flow configurations, that cannot be modeled in 0D. These configurations are likely to exhibit a higher degree of non-equilibrium and modeling could thus enable better designs that would lead to higher energy efficiencies. Indeed, combining modeling and experimental findings is likely to be the key to reach the understanding of CO_2 dissociation needed to build energy efficient industrial scale reactors.

Based on our current model, we can already give some suggestions to overcome the limitations to the energy efficiency identified in the model. In particular, using a Laval nozzle reactor with a supersonic flow could improve the non-equilibrium aspect of the discharge, as already demonstrated experimentally in literature[22;33], since it might create a cold low pressure zone located right after the nozzle. Similarly, pulsing the plasma could also enhance the non-equilibrium aspect of the discharge, when the plasma does not get enough time to reach high gas temperatures. These suggestions have also been considered experimentally already, and we hope that they can further inspire experimental researchers to continue exploring the possibilities of energy efficient CO_2 dissociation in a microwave plasma.

Summary

It is now widely accepted that the anthropogenic carbon emissions are responsible for the increase of the surface temperature on Earth. Hence, there is a growing interest into various methods to find alternative renewable energy sources. These energy sources typically have an important drawback: the intermittency of their power generation. Therefore, over the last few years, large research efforts have been directed towards finding solutions for energy storage. One of these methods, the conversion of CO_2 into value-added compounds, has recently received great interest. In particular, the conversion of CO_2 to CO (and oxygen) by non-equilibrium plasmas, followed by conversion into hydrocarbons through the Fischer-Tropsch process, would be an interesting way to store energy via a carbon-neutral process.

However, the control of non-equilibrium plasmas is far from trivial, as their kinetics is complex and cannot be directly controlled by adjusting external parameters. Therefore, the energy efficiency currently achieved in plasma-based CO_2 dissociation needs to be enhanced for potential industrial applications, and thus, there is a need for a more detailed understanding of the processes occurring in a CO_2 plasma.

Microwave plasmas are found to be one of the most energy efficient plasma sources for CO_2 dissociation, as they exhibit important vibrational non-equilibrium. Indeed, vibration-induced dissociation is considered the most energy efficient way to dissociate CO_2. Therefore, this thesis focuses on modeling of CO_2 microwave plasmas, looking into aspects important for the improvement of current models, as well as using these models to reveal the underlying CO_2 plasma kinetics.

First, the spatial properties of a microwave discharge were studied using a 2D-axisymmetric argon model, operating over a wide range of pressure. This model, albeit for argon as a first step into the development of a 2D model for CO_2, provides good insight into the wave propagation and the effect of pressure on the microwave plasma, to obtain information on how the microwave energy is distributed in space. This is of interest for the 0D model, subsequently developed to study more in detail the complex chemical kinetics of CO_2 dissociation in a microwave plasma.

The dissociation mechanisms were investigated and the model reveals that the discharge tends to thermalize faster at high gas temperature and high pressure, since vibration-translation relaxation occurs faster. The non-equilibrium of the discharge is thus typically not well exploited, as is also revealed by experimental evidence. Potential solutions to overcome this limitation for industrial applications are discussed, such as the use of supersonic flows, which create a cold low pressure zone, or pulsing of the plasma power, which may prevent thermalization. The energy transfers occurring in the discharge and leading to CO_2 dissociation are also investigated, to pinpoint what

are possible losses in the energy efficiency of the process. It is shown how a low reduced electric field enhances the energy transfers towards vibrational levels of CO_2 and how a lower gas temperature and a higher ionization degree enhance the non-equilibrium required for energy efficient CO_2 dissociation. Indeed, obtaining a large degree of non-equilibrium requires that the energy put into vibrations exceeds by far the energy lost by relaxation processes, which is only the case at specific conditions.

A reduction of the chemistry set and a level-lumping method designed to reduce the computational load associated with the description of the CO_2 kinetics are also presented. These modeling techniques enable to model the CO_2 microwave discharge in higher- dimensional models in future work. Moreover, the effect of uncertainties associated with the rate coefficients on the model results is studied and it is found that, while the error on the model results can be significant, the trends predicted by the model can be considered reliable. The reactions mostly responsible for these uncertainties are identified, in order to pinpoint which of them should be investigated in more detail, to obtain a better precision in the kinetic modeling. Similarly, the effect of the parameters chosen in the scaling laws applied to model the vibrational kinetics of CO_2 is investigated and the role of these parameters is found to be crucial for the determination of the energy efficiency. This allows to derive a formula to better understand the limitations to the energy efficiency obtained by the model, which is needed for further improvements.

In summary, this PhD thesis increases our knowledge on the kinetics of CO_2 discharges and gives useful directions. There is of course still a long way to go before plasma-based CO_2 conversion can be used in industrial scale devices, but we believe that this work paves the way for future modeling and experimental research. Moreover, CO_2 conversion appears to be one of the promising techniques for chemical energy storage applications, which will become increasingly essential with the energy transition.

Samenvatting

Het is nu algemeen aanvaard dat de antropogene koolstofemissies verantwoordelijk zijn voor de verhoging van de oppervlaktetemperatuur op de aarde. Vandaar is er een groeiende interesse naar alternatieve energiebronnen. Die energiebronnen hebben een groot nadeel, namelijk hun niet-continu karaketer. Dit heeft als gevolg dat er in de afgelopen jaren grote onderzoeksinspanningen zijn gericht op het vinden van oplossingen voor energieopslag. Een van deze methoden, de conversie van CO_2 in chemicalien met toegevoegde waarde, heeft recent veel belangstelling gekregen. In het bijzonder de conversie van CO_2 naar CO (en zuurstof) door niet-evenwichtsplasma's, gevolgd door de conversie van deze moleculen naar koolwaterstoffen met behulp van het Fischer-Tropsch-proces, zou een interesante manier zijn om energie op te slaan.

De controle van niet-evenwichtsplasma's is echter ver van triviaal, omwille van hun complexe kinetiek die niet direct kan worden gecontroleerd door het aanpassen van externe parameters. Bovendien moet de energie-efficiëntie die momenteel wordt bereikt in plasma-gebaseerde CO_2 dissociatie worden verbeterd voor potentiële industriële toepassingen. Daarom is er behoefte aan een meer gedetailleerd inzicht in de processen die plaatsvinden in een CO_2 plasma.

Microgolfplasma's blijken een van de meest energie-efficiënte plasmabronnen voor CO_2 dissociatie te zijn, omdat ze een belangrijk vibrationeel niet-evenwicht vertonen. Vibratie-geïnduceerde dissociatie wordt beschouwd als de meest energie-efficiënte manier om CO_2 te dissociëren. Daarom concentreert dit proefschrift zich op het modelleren van CO_2 microgolfplasma's, waarbij gekeken wordt naar aspecten die belangrijk zijn voor de verbetering van de huidige modellen, evenals het gebruik van deze modellen om de onderliggende CO_2 plasmakinetiek te onthullen.

Eerst werden de ruimtelijke eigenschappen van een microgolfontlading bestudeerd met behulp van een 2D-asymmetrisch argon model dat over een breed drukbereik werkt. Dit model, hoewel voor argon als een eerste stap in de ontwikkeling van een 2D-model voor CO_2, biedt goed inzicht in de golfvoortplanting en het effect van druk op het microgolfplasma, om informatie te verkrijgen over hoe de microgolfenergie wordt gedistribueerd in de ruimte. Dit is van belang voor het 0D-model, dat vervolgens is ontwikkeld om de complexe chemische kinetiek van CO_2 dissociatie in een microgolfplasma meer gedetailleerd te bestuderen.

De dissociatiemechanismen werden onderzocht en het model laat zien dat de ontlading sneller lijkt te thermaliseren bij hoge gastemperatuur en hoge druk, omdat vibrationele-translationele relaxatie sneller optreedt. Het niet-evenwichtskarakter van de ontlading wordt dus typisch niet goed geëxploiteerd, zoals ook blijkt uit experimentele metingen. Potentiële oplossingen om deze beperking voor industriële toepassingen te overwinnen worden besproken, zoals het gebruik van supersonische stromingen die een koude lagedrukzone creëren, en het pulsen van het plasmavermogen dat het thermaliseren kan voorkomen. De energieoverdrachten die plaatsvinden in de ontlading, en die leiden tot CO_2 dissociatie, worden ook onderzocht om vast te stellen wat mogelijke verliezen zijn in de energie-efficiëntie van het proces. Er wordt getoond hoe een laag gereduceerd elektrisch veld de energieoverdrachten naar vibrationele niveaus van CO_2 verbetert en hoe een lagere gastemperatuur en een hogere ionisatiegraad het niet-evenwicht versterken, dat vereist is voor energie-efficiënte CO_2 dissociatie. Het verkrijgen van een grote mate van niet-evenwicht vereist dat de energie die in vibraties wordt gestoken, de energie die verloren gaat door relaxatieprocessen ver overschrijdt, wat alleen het geval is bij specifieke omstandigheden.

Een reductie van de chemieset en een groepering van de energieniveaus, om de computationele belasting geassocieerd met de beschrijving van de CO_2 kinetiek te verminderen, wordt eveneens gepresenteerd. Deze modelleringstechnieken maken het mogelijk de CO_2 microgolfontlading in hogere dimensionale modellen te beschrijven in toekomstig werk. Voorts wordt het effect van onzekerheden in verband met de snelheidscoëfficiënten op de modelresultaten bestudeerd. Er werd vastgesteld dat hoewel de fout op de modelresultaten aanzienlijk kan zijn, de trends die door het model worden voorspeld als betrouwbaar kunnen worden beschouwd. De reacties die voor het grootste deel verantwoordelijk zijn voor deze onzekerheden worden geïdentificeerd, om vast te stellen welke van hen in meer detail moeten worden onderzocht om een betere precisie in de kinetische modellering te verkrijgen.

Vervolgens werd het effect van de parameters, die zijn gekozen in de schaalwetten en zijn toegepast om de trillingskinetiek van CO_2 te modelleren, onderzocht. De rol van deze parameters blijkt cruciaal te zijn voor het bepalen van de energie-efficiëntie. Dit maakt het mogelijk om een formule af te leiden om de beperkingen van de energie-efficiëntie van het model beter te begrijpen, wat nodig is voor verdere verbeteringen.

Samenvattend vergroot dit proefschrift onze kennis over de kinetiek van CO_2 ontladingen en geeft het nuttige aanwijzingen. Er is natuurlijk nog een lange weg te gaan voordat plasma-gebaseerde CO_2 conversie op industriële schaal kan worden gebruikt, maar wij zijn van mening dat dit werk de weg vrijmaakt voor toekomstige modellering en experimenteel onderzoek. Bovendien lijkt CO_2 conversie een van de veelbelovende technieken te zijn voor chemische energieopslagtoepassingen, die steeds essentiëler worden voor de energietransitie.

List of publications and conference contributions

List of publications

- A. Berthelot, S. Kolev, and A. Bogaerts. *Different pressure regimes of a surface-wave discharge in argon: a modeling investigation.* Proceedings of IX International Workshop on Microwave discharges: Fundamentals and Applications, September 7-11, 2015, Cordoba, Spain, 2015

- A. Berthelot and A. Bogaerts. Modeling of plasma-based CO_2 conversion: lumping of the vibrational levels. *Plasma Sources Science and Technology*, 25(4):045022, 2016. DOI: 10.1088/0963-0252/25/4/045022

- A. Berthelot and A. Bogaerts. Modeling of CO_2 Splitting in a Microwave Plasma: How to Improve the Conversion and Energy Efficiency. *The Journal of Physical Chemistry C*, 121(15):8236–8251, 2017. DOI: 10.1021/acs.jpcc.6b12840

- A. Berthelot and A. Bogaerts. Modeling of CO_2 plasma: effect of uncertainties in the plasma chemistry. *Plasma Sources Science and Technology*, 26(11):115002, 2017. DOI: 10.1088/1361-6595/aa8ffb

- A. Berthelot and A. Bogaerts. Pinpointing energy losses in plasma-based CO_2 conversion. *Journal of CO_2 Utilization*, 2018. In press

- V. Georgieva, A. Berthelot, T. Silva,S. Kolev, W. Graef, N. Britun, G. Chen, J. van der Mullen, T. Godfroid, D. Mihailova, J. van Dijk, R. Snyders, A. Bogaerts, and M. Delplancke-Ogletree. Understanding Microwave Surface-Wave Sustained Plasmas at Intermediate Pressure by 2D Modeling and Experiments. *Plasma Processes and Polymers*, 14 (4-5):1600185, 2017.

- A. Bogaerts, W. Wang, A. Berthelot, and V. Guerra. Modeling plasma-based CO_2 conversion: crucial role of the dissociation cross section. *Plasma Sources Science and Technology*, 25(5):055016, 2016. DOI: 10.1088/0963-0252/25/5/055016
- W. Wang, A. Berthelot, S. Kolev, X. Tu, and A. Bogaerts. CO_2 conversion in a gliding arc plasma: 1D cylindrical discharge model. *Plasma Sources Science and Technology*, 25(6):065012, 2016. DOI: 10.1088/0963-0252/25/6/065012

List of conference contributions

- A. Berthelot, S. Kolev and A. Bogaerts, CO_2 conversion in a microwave plasma: a modeling study, 1st RAPID Symposium, November 3-7, 2014, Manchester, United Kingdom: Oral presentation.
- A. Berthelot and A. Bogaerts, 2D self-consistent modeling of an argon microwave plasma over a wide range of pressure, 22nd International Symposium on Plasma Chemistry , July 5-10, 2015, Antwerp, Belgium: Oral presentation.
- A. Berthelot, S. Kolev and A. Bogaerts, Different pressure regimes of a surface-wave discharge in argon: a modeling investigation (poster), 9th International Workshop on Microwave Discharges, September 7-11, 2015, Cordoba, Spain: Oral presentation.
- A. Berthelot, S. Kolev and A. Bogaerts, Different pressure regimes of a surface-wave discharge in argon: a modeling investigation, 9th International Workshop on Microwave Discharges, September 7-11, 2015, Cordoba, Spain: Poster presentation.
- A. Berthelot, S. Kolev and A. Bogaerts, A COMSOL-based 2D self-consistent microwave plasma model, Comsol Conference, October 13-16, 2015, Grenoble, France: Poster presentation.
- A. Berthelot and A. Bogaerts, A self-consistent microwave discharge model, 3rd RAPID Symposium, October 26-29, 2015, Perpignan, France: Oral presentation.
- A. Berthelot and A. Bogaerts, Dissociation and recombination mechanisms of CO_2 in a microwave discharge, Fourth RAPID Symposium, October 4-7, 2016, Eindhoven, the Netherlands: Oral presentation.
- A. Berthelot and A. Bogaerts, Level-lumping method for the modeling of CO_2 vibrational kinetics, Gaseous Electronics Conference, October 10-14, 2016, Bochum, Germany: Oral presentation.

- A. Berthelot, W. Wang, S. Heijkers and A. Bogaerts, Kinetic modeling of vibrationally excited plasmas, RAPID Workshop - Emerging Concepts in Diagnostics and Modeling, April 11-13, 2017, Eindhoven, The Netherlands: Invited lecture.

- A. Berthelot and A. Bogaerts, CO_2 conversion in a microwave plasma: a modeling study, 9th International Workshop on Microplasmas, June 6-9, 2017, Garmisch-Partenkirchen, Germany.

- A. Berthelot and A. Bogaerts, Modeling of CO_2 conversion in a microwave plasma (3 min pitch-presentation), 23rd International Symposium on Plasma Chemistry, July 30 – August 4, 2017, Montreal, Canada: 3 min pitch-presentation and Poster presentation

APPENDIX A

Lists of chemical reactions

A.1 Chemistry set 1

The chemistry set presented in this section corresponds to the first CO_2 models and is considered in chapters V and VI.

Table A.1: Electron impact reactions calculated with cross sections data, using the calculated EEDF, as explained in section III.2

No.	Reaction	Ref	Note
(X1)	$e + CO_2 \rightarrow e + CO_2$	177	a
(X2)	$e + CO_2 \rightarrow 2e + CO_2^+$	177	a
(X3)	$e + CO_2 \rightarrow 2e + CO + O^+$	177	b
(X4)	$e + CO_2 \rightarrow 2e + CO^+ + O$	177	b
(X5)	$e + CO_2 \rightarrow 2e + O_2 + C^+$	177	b
(X6)	$e + CO_2 \rightarrow CO + O^-$	109	b
(X7)	$e + CO_2 \rightarrow e + CO + O$	109	b
(X8)	$e + CO_2 \rightarrow e + CO_2^*$	109	a
(X9)	$e + CO_2 \rightarrow e + CO_2v_x$	109	c
(X10)	$e + CO \rightarrow e + CO$	109	a
(X11)	$e + CO \rightarrow e + C + O$	178	
(X12)	$e + CO \rightarrow e + COv_x$	109	c
(X13)	$e + CO \rightarrow 2e + CO^+$	179	a
(X14)	$e + CO \rightarrow e + C^+ + O$	179	b
(X15)	$e + CO \rightarrow e + C + O^+$	179	b
(X16)	$e + CO \rightarrow e + C + O^-$	179	b
(X17)	$e + CO \rightarrow e + COe_{1,2}$	109	a
(X18)	$e + CO \rightarrow e + COe_{2,3}$	179	a
(X19)	$e + O_2 + M \rightarrow e + O_2^- + M$	109	
(X20)	$e + O_2 \rightarrow 2e + O + O^-$	109	
(X21)	$e + O_2 \rightarrow 2e + O_2^+$	180	
(X22)	$e + O_2 \rightarrow 2e + O^+ + O$	181	
(X23)	$e + O_2 \rightarrow e + O_2v_x$	180	
(X24)	$e + O_2 \rightarrow e + O + O$	180	
(X25)	$e + O_2 \rightarrow e + O_2e_{1,2}$	180	
(X26)	$e + O_3 \rightarrow e + O_2 + O$	75	
(X27)	$e + O_3 \rightarrow O + O_2^-$	182	
(X28)	$e + O_3 \rightarrow O_2 + O^-$	182	
(X29)	$e + O_3 \rightarrow 2e + O_2^+ + O$	75	
(X30)	$e + O_3 \rightarrow O^+ + O^- + O + e$	75	
(X31)	$e + C_2 \rightarrow e + 2C$	183	
(X35)	$e + C_2 \rightarrow 2e + C_2^+$	183	
(X36)	$e + O \rightarrow O+ + 2\ e$	184	
(X37)	$e + C \rightarrow C+ + 2\ e$	185	

a) Same cross section also used for CO_2v_i (i = the various vibrationally excited levels)

b) Cross section also used for CO_2v_i, modified by lowering the energy threshold by the energy of the excited state of CO_2v_i

c) Cross section for the various levels (i,j) adopted from $e+CO_2v_0 \rightarrow e+CO_2v_1$, but scaled and shifted using Fridman's approximation[22;56]

Table A.2: Electron impact reactions using analytical expressions for the rate coefficients, given in m^3/s and m^6/s, for two-body and threebody reactions, respectively. T_g and T_e are given in K and eV, respectively.

No.	Reaction	Rate coefficient	Reference
(E1)	$e + CO_2^+ \rightarrow CO + O$	$2.0 \times 10^{-11} T_e^{-0.5} T_g^{-1}$	26
(E2)	$e + CO_2^+ \rightarrow C + O_2$	$3.94 \times 10^{-13} T_e^{-0.4}$	186
(E3)	$e + C_2O_2 + \rightarrow 2\ CO$	$4.0 \times 10^{-13} Te^{-0.34}$	29
(E4)	$e + CO_4^+ \rightarrow CO_2 + O_2$	$1.61 \times 10^{-13} Te^{-0.5}$	186
(E5)	$e + CO^+ \rightarrow C + O$	$3.68 \times 10^{-14} Te^{-0.55}$	187
(E6)	$e + C_2O_3^+ \rightarrow CO_2 + CO$	$5.4 \times 10^{-14} Te^{-0.7}$	29
(E7)	$e + C_2O_4^+ \rightarrow 2\ CO_2$	$2.0 \times 10^{-11} Te^{-0.5} Tg^{-1}$	29
(E8)	$e + C_2^+ \rightarrow 2\ C$	$1.79 \times 10^{-14} Te^{-0.5}$	29
(E9)	$e + O_2^+ + M \rightarrow O_2 + M$	3.0×10^{-42}	28
(E10)	$e + O_2^+ \rightarrow 2\ O$	$6.0 \times 10^{-13} Te^{-0.5} Tg^{-0.5}$	26
(E11)	$e + O^+ + M \rightarrow O + M$	10^{-38}	75
(E12)	$e + O_4^+ \rightarrow 2\ O_2$	$2.25 \times 10\ -^{13}\ Te^{-0.5}$	188
(E13)	$e + O_3 + M \rightarrow O_3^- + M$	$5.0 \times 10^{-43} Te^{-0.5}$	29
(E14)	$e + O + M \rightarrow O^- + M$	10^{-43}	28

Table A.3: Heavy particle reactions involving ions. The rate coefficients are in [$m^3.s^{-1}$] or [$m^6.s^{-1}$] for the two-body and threebody reactions, respectively. M represents any neutral species taken into account in the model. The same rate coefficient is used for every species. T_g is given in K

No.	Reaction	Rate coefficient	Ref
(I1)	$CO_2 + O^+ \rightarrow O_2^+ + CO$	9.4×10^{-16}	186
(I2)	$CO_2 + O^+ \rightarrow CO_2^+ + O$	4.5×10^{-16}	186
(I3)	$CO_2 + C^+ \rightarrow CO^+ + CO$	1.1×10^{-15}	189
(I4)	$CO_2 + CO^+ \rightarrow CO_2^+ + CO$	1.0×10^{-15}	189
(I5)	$CO_2 + O^- + M \rightarrow CO_3^- + M$	9.0×10^{-41}	26
(I6)	$CO_2 + O_2^- + M \rightarrow CO_4^- + M$	1.0×10^{-41}	26
(I7)	$CO_2 + O_3^- \rightarrow O_2 + CO_3^-$	5.5×10^{-16}	28
(I8)	$CO_2 + O_4^- \rightarrow CO_4^- + O_2$	4.8×10^{-16}	29
(I9)	$CO_2 + CO_2^+ + M \rightarrow C_2O_4^+ + M$	3.0×10^{-40}	29
(I10)	$CO_2 + O_2^+ + M \rightarrow CO_4^+ + M$	2.3×10^{-41}	186
(I11)	$CO + O^+ \rightarrow CO^+ + O$	$4.9 \times 10^{-18}(T_g/300\mathrm{K})0.5\exp(-4580\mathrm{K}/T_g)$	189
(I12)	$CO + O^- \rightarrow CO_2 + e$	5.5×10^{-16}	186
(I13)	$CO + CO_3^- \rightarrow CO_2 + CO_2 + e$	5.0×10^{-19}	26
(I14)	$CO + C_2O_3^+ \rightarrow CO_2 + C_2O_2^+$	1.1×10^{-15}	29
(I15)	$CO + C_2O_4^+ \rightarrow C_2O_3^+ + CO_2$	9.0×10^{-16}	29
(I16)	$CO + C_2O_3^+ + M \rightarrow C_2O_2^+ + CO_2 + M$	2.6×10^{-38}	29
(I17)	$CO + C_2O_4^+ + M \rightarrow C_2O_3^+ + CO_2 + M$	4.2×10^{-38}	29
(I18)	$CO + C^+ \rightarrow CO^+ + C$	5.0×10^{-19}	186
(I19)	$O_2 + CO_2^+ \rightarrow O_2^+ + CO_2$	5.3×10^{-17}	189
(I20)	$O_2 + CO^+ \rightarrow O_2^+ + CO$	1.2×10^{-16}	189
(I21)	$O_2 + C_2O_2^+ \rightarrow CO + CO + O_2^+$	5.0×10^{-18}	29
(I22)	$O_2 + C^+ \rightarrow CO + O^+$	6.2×10^{-16}	189
(I23)	$O_2 + C^+ \rightarrow CO^+ + O$	3.8×10^{-16}	186
(I24)	$O_2 + O^+ \rightarrow O_2^+ + O$	$1.9 \times 10^{-17}(300\mathrm{K}/T_g)0.5$	186

Continued on next page

Table A.3 – continued from previous page

No.	Reaction	Rate coefficient	Ref
(I25)	$O_2 + O_2^+ + M \rightarrow O_4^+ + M$	2.4×10^{-42}	188
(I26)	$O_2 + O_2^- + M \rightarrow O_4^- + M$	3.5×10^{-43}	188
(I27)	$O_2 + O^- \rightarrow O_3 + e$	1.0×10^{-18}	29
(I28)	$O_2 + O^- + M \rightarrow O_3^- + M$	$3.0 \times 10^{-40}(300\mathrm{K}/T_g)$	29
(I29)	$O_2 + O_2^- \rightarrow O_2 + O_2 + e$	2.18×10^{-24}	75
(I30)	$O_2 + O_3^- \rightarrow O_2 + O_3 + e$	2.3×10^{-17}	75
(I31)	$CO^+ + C \rightarrow CO + C^+$	1.1×10^{-16}	189
(I32)	$O_2^+ + C \rightarrow CO^+ + O$	5.2×10^{-17}	189
(I33)	$O_2^+ + C \rightarrow C^+ + O_2$	5.2×10^{-17}	189
(I34)	$C_2^+ + C \rightarrow C_2 + C^+$	1.1×10^{-16}	189
(I35)	$O + CO_2^+ \rightarrow O_2^+ + CO$	1.64×10^{-16}	189
(I36)	$O + CO_2^+ \rightarrow O^+ + CO_2$	9.62×10^{-17}	189
(I37)	$O + CO^+ \rightarrow CO + O^+$	1.4×10^{-16}	189
(I38)	$O + CO_3^- \rightarrow CO_2 + O_2^-$	8.0×10^{-17}	26
(I39)	$O + CO_4^- \rightarrow CO_3^- + O_2$	1.1×10^{-16}	186
(I40)	$O + CO_4^- \rightarrow CO_2 + O_2 + O^-$	1.4×10^{-17}	186
(I41)	$O + CO_4^- \rightarrow CO_2 + O_3^-$	1.4×10^{-16}	186
(I42)	$O + O^+ + M \rightarrow O_2^+ + M$	1.0×10^{-41}	75
(I43)	$O + O^- \rightarrow O_2 + e$	2.3×10^{-16}	190
(I44)	$O + O_2^- \rightarrow O_2 + O^-$	3.3×10^{-16}	75
(I45)	$O + O_2^- \rightarrow O_3 + e$	3.3×10^{-16}	190
(I46)	$O + O_3^- \rightarrow O_2 + O_2 + e$	1.0×10^{-19}	29
(I47)	$O + O_3^- \rightarrow O_2^- + O_2$	2.5×10^{-16}	29
(I48)	$O + O_3^- \rightarrow O_3 + O^-$	1.0×10^{-19}	191
(I49)	$O + O_4^- \rightarrow O_3^- + O_2$	4.0×10^{-16}	188
(I50)	$O + O_4^- \rightarrow O^- + O_2 + O_2$	3.0×10^{-16}	188
(I51)	$O + O_4^+ \rightarrow O_2^+ + O_3$	3.0×10^{-16}	188
(I52)	$O_3 + CO_4^- \rightarrow CO_2 + O_3^- + O_2$	1.3×10^{-16}	29

Continued on next page

Table A.3 – continued from previous page

No.	Reaction	Rate coefficient	Ref
(I53)	$O_3 + O^- \rightarrow O_3^- + O$	8.0×10^{-16}	29
(I54)	$O_3 + O^- \rightarrow O_2 + O_2 + e$	3.0×10^{-16}	191
(I55)	$O_3 + O_2^- \rightarrow O_3^- + O_2$	4.0×10^{-16}	75
(I56)	$O_3 + O_3^- \rightarrow 3O_2 + e$	3.0×10^{-16}	29
(I57)	$O_3 + O^+ \rightarrow O_2^+ + O_2$	1.0×10^{-16}	188
(I58)	$O_2^- + M \rightarrow O_2 + M + e$	$2.7 \times 10^{-16}(T_g/300\mathrm{K})0.5\exp(-5590\mathrm{K}/T_g)$	186
(I59)	$O_3^- + M \rightarrow O_3 + M + e$	2.3×10^{-17}	186
(I60)	$O^- + M \rightarrow O + M + e$	4.0×10^{-18}	29
(I61)	$O_4^- + M \rightarrow O_2^- + O_2 + M$	4.0×10^{-18}	191
(I62)	$O_4^+ + M \rightarrow O_2^+ + O_2 + M$	1.73×10^{-19}	188
(I63)	$C_2O_2^+ + M \rightarrow CO^+ + CO + M$	1.0×10^{-18}	29
(I64)	$C_2O_4^+ + M \rightarrow CO_2^+ + CO_2 + M$	1.0×10^{-20}	29
(I65)	$CO_3^- + CO_2^+ \rightarrow CO_2 + CO_2 + O$	5.0×10^{-13}	26
(I66)	$CO_4^- + CO_2^+ \rightarrow CO_2 + CO_2 + O_2$	5.0×10^{-13}	26
(I67)	$O_2^- + CO_2^+ \rightarrow CO + O_2 + O$	6.0×10^{-13}	26
(I68)	$CO_3^- + C_2O_2^+ \rightarrow CO_2 + CO + CO + O$	5.0×10^{-13}	29
(I69)	$CO_4^- + C_2O_2^+ \rightarrow CO_2 + CO + CO + O_2$	5.0×10^{-13}	29
(I70)	$O_2^- + C_2O_2^+ \rightarrow CO + CO + O_2$	6.0×10^{-13}	29
(I71)	$CO_3^- + C_2O_3^+ \rightarrow CO_2 + CO_2 + CO + O$	5.0×10^{-13}	29
(I72)	$CO_4^- + C_2O_3^+ \rightarrow CO_2 + CO_2 + CO + O_2$	5.0×10^{-13}	29
(I73)	$O_2^- + C_2O_3^+ \rightarrow CO_2 + CO + O_2$	6.0×10^{-13}	29
(I74)	$CO_3^- + C_2O_4^+ \rightarrow 3CO_2 + O$	5.0×10^{-13}	29
(I75)	$CO_4^- + C_2O_4^+ \rightarrow 3CO_2 + O_2$	5.0×10^{-13}	29
(I76)	$O_2^- + C_2O_4^+ \rightarrow 2CO_2 + O_2$	6.0×10^{-13}	29
(I77)	$O_2^+ + CO_3^- \rightarrow CO_2 + O_2 + O$	3.0×10^{-13}	26
(I78)	$O_2^+ + CO_4^- \rightarrow CO_2 + O_2 + O_2$	3.0×10^{-13}	26
(I79)	$O^+ + O_2^- \rightarrow O + O_2$	2.7×10^{-13}	190
(I80)	$O_2^+ + O_2^- \rightarrow O_2 + O_2$	2.0×10^{-13}	190

Continued on next page

Table A.3 – continued from previous page

No.	Reaction	Rate coefficient	Ref
(I81)	$O_2^+ + O_2^- \rightarrow O_2 + O + O$	4.2×10^{-13}	26
(I82)	$O_2^+ + O_2^- + M \rightarrow O_2 + O_2 + M$	2.0×10^{-37}	75
(I83)	$O^+ + O_2^- + M \rightarrow O_3 + M$	2.0×10^{-37}	75
(I84)	$O_2^+ + O_3^- \rightarrow O_2 + O_3$	2.0×10^{-13}	75
(I85)	$O_2^+ + O_3^- \rightarrow O + O + O_3$	1.0×10^{-13}	75
(I86)	$O^+ + O_3^- \rightarrow O_3 + O$	1.0×10^{-13}	75
(I87)	$O^+ + O^- \rightarrow O + O$	4.0×10^{-14}	184
(I88)	$O^+ + O^- + M \rightarrow O_2 + M$	2.0×10^{-37}	75
(I89)	$O_2^+ + O^- \rightarrow O_2 + O$	1.0×10^{-13}	26
(I90)	$O_2^+ + O^- \rightarrow 3O$	2.6×10^{-14}	190
(I91)	$O_2^+ + O^- + M \rightarrow O_3 + M$	2.0×10^{-37}	75

Table A.4: Neutral reactions between vibrationally excited molecules, as well as the references where the data are adopted from and the uncertainty of the data (expressed relative to the mean value). The rate coefficients are given in m^3/s and m^6/s, for two-body and threebody reactions, respectively. T_g is given in K.

No.	Reaction	Rate coefficient	References
(V1)	$CO_2v_a + M \rightarrow CO_2 + M$	$7.14 \times 10^{-15}\, exp(-177\, T_g^{-1/3} + 451\, T_g^{-2/3})$	192
(V2a)	$CO_2v_1 + M \rightarrow CO_2v_a + M$	$4.25 \times 10^{-7}\, exp(-407\, T_g^{-1/3} + 824\, T_g^{-2/3})$	192
(V2b)	$CO_2v_1 + M \rightarrow CO_2v_b + M$	$8.57 \times 10^{-7}\, exp(-404\, T_g^{-1/3} + 1096\, T_g^{-2/3})$	192
(V2c)	$CO_2v_1 + M \rightarrow CO_2v_c + M$	$1.43 \times 10^{-7}\, exp(-252\, T_g^{-1/3} + 685\, T_g^{-2/3})$	192
(V3)	$COv_1 + M \rightarrow CO + M$	$1.0 \times 10^{-18}\, T_g\, exp(-150.7\, T_g^{-1/3})$	111
(V4)	$O_2v_1 + M \rightarrow O_2 + M$	$1.3 \times 10^{-14}\, exp(-158.7\, T_g^{-1/3})$	192
(V5)	$CO_2v_1 + CO_2 \rightarrow CO_2v_a + CO_2v_b$	$1.06 \times 10^{-11}\, exp(-242\, T_g^{-1/3} + 633\, T_g^{-2/3})$	192
(V6)	$CO_2v_1 + CO_2 \rightarrow CO_2 + CO_2v_1$	$1.32 \times 10^{-18}\, (\frac{T_g}{300})^{0.5} \frac{250}{T_g}$	193;194
(V7)	$COv_1 + CO \rightarrow CO + COv_1$	$1.5 \times 10^{-21} exp(1.97 T_g^{-1/3} + 82.3 T_g^{-2/3})$	111
(V8)	$CO_2v_1 + CO \rightarrow CO_2 + COv_1$	$4.8 \times 10^{-12}\, exp(-153\, T_g^{-1/3})$	192

Table A.5: Reactions of neutrals. Rate coefficients in $[m^3.s^{-1}]$ or in $[m^6.s^{-1}]$for the two-body and threebody reactions, respectively. T_g is in K. α is the parameter used to determine the rate constants of the same reactions with vibrationally excited CO_2 molecules. See[56] for more information

No.	Reaction	Rate coefficient	$\Delta H_r(eV)$	α	Ref
(N1)	$CO_2 + M \rightarrow CO + O + M$	$4.39 \times 10^{-13}\exp(-65000/T_g)$	5.52	1	22
(N2)	$CO_2 + O \rightarrow CO + O_2$	$7.77 \times 10^{-18}\exp(-16600/T_g)$	0.35	0.5	22
(N3)	$CO + O + M \rightarrow CO_2 + M$	$8.2 \times 10^{-46}\exp(-1510/T_g)$	-5.52	0	28
(N4)	$CO + O_2 \rightarrow CO_2 + O$	$1.23 \times 10^{-18}\exp(-12800/T_g)$	-0.35	0.5	22
(N5)	$CO_2 + C \rightarrow CO + CO$	1.0×10^{-21}	-5.64		29
(N6)	$CO + O_3 \rightarrow CO_2 + O_2$	4.0×10^{-31}	-4.41		186
(N7)	$CO + C + M \rightarrow C_2O + M$	6.5×10^{-44}			28
(N8)	$O_2 + C \rightarrow CO + O$	3.0×10^{-17}	-5.99		28
(N9)	$CO + M \rightarrow O + C + M$	$1.52 \times 10^{-10}(T_g/298)^{-3.1}\exp(-129000/T_g)$	11.16	1	195
(N10)	$O + C + M \rightarrow CO + M$	$2.14 \times 10^{-41}(T_g/300)^{-3.08}\exp(-2114/T_g)$	-11.16		186
(N11)	$O + C_2O \rightarrow CO + CO$	5.0×10^{-17}			29
(N12)	$O_2 + C_2O \rightarrow CO_2 + CO$	3.3×10^{-19}			28
(N13)	$O + O_3 \rightarrow O_2 + O_2$	$3.1 \times 10^{-20}T_g^{0.75}\exp(-1575/T_g)$	-4.06		28
(N14)	$O_3 + M \rightarrow O_2 + O + M$	$4.12 \times 10^{-16}\exp(-11430/T_g)$	1.10		186
(N15)	$O + O_2 + M \rightarrow O_3 + M$	$6.11 \times 10^{-46}(T_g/300)^{-2.6}$	-1.10		188
(N16)	$O + O + M \rightarrow O_2 + M$	$1.27 \times 10^{-44}(T_g/300)^{-1}\exp(-170/T_g)$	-5.17		196

A.2 Chemistry set 2

The chemistry set presented in this section was verified in chapter VII and is considered in chapters chapters VII and VIII.

Table A.6: Electron impact reactions calculated with cross sections data, using the calculated EEDF, as explained in section III.2, as well as the references where the data are adopted from and the uncertainty of the data (expressed relative to the mean value). When not explicitly shown in the original source, the errors have been taken according to the values given by M. Hayashi[197].

No.	Reaction	Ref	$\frac{\Delta A}{A}$	Note
(X1)	$e + CO_2 \to 2e + CO_2^+$	[109]	0.1	
(X2)	$e + CO_2 \to 2e + O + CO^+$	[109]	0.3	
(X3)	$e + CO_2 \to O^- + CO$	[109]	0.3	
(X4)	$e + CO_2 \to e + O + CO$	[109]	0.3	
(X5)	$e + CO_2 \to e + CO_2^*$	[109]	0.3	
(X6)	$e + CO_2 \to e + CO_2v_x$	[109]	0.3	x=a,b,c,d
(X7)	$e + CO_2v_i \to e + CO_2v_j$	[109]	0.3	
(X8)	$e + CO \to 2e + CO^+$	[198]	0.1	
(X9)	$e + CO \to C + O^-$	[199]	0.3	
(X9bis)	$e + CO \to e + C + O$	[179]	0.3	
(X10)	$e + CO \to e + CO(E_x)$	[179]	0.3	x=1,2,3,4
(X11)	$e + CO \to e + COv_i$	[179]	0.3	i=1,2,3
(X12)	$e + O_2 \to e + O + O$	[200]	0.25	
(X12M)	$e + O_2 + M \to e + O_2^- + M$	[200]	0.25	
(X13)	$e + O_2 \to O + O^-$	[200]	0.25	
(X14)	$e + O_2 \leftrightarrow e + O_2v_i$	[200]	0.25	i=1,2,3
(X17)	$e + O_2 \leftrightarrow e + O_2E_i$	[200]	0.25	i=1,2

a) Same cross section also used for CO_2v_i (i = the various vibrationally excited levels)
b) Cross section also used for CO_2v_i, modified by lowering the energy threshold by the energy of the excited state of CO_2v_i
c) Cross section for the various levels (i,j) adopted from $e+CO_2v_0 \to e+CO_2v_1$, but scaled and shifted using Fridman's approximation

Table A.7: Electron impact reactions using analytical expressions for the rate coefficients, given in m^3/s and m^6/s, for two-body and threebody reactions, respectively, as well as the references where the data are adopted from and the uncertainty of the data (expressed relative to the mean value). T_g and T_e are given in K and eV, respectively.

No.	Reaction	Rate coefficient	$\frac{\Delta A}{A}$	Reference
(E1a)	$e + CO_2^+ \rightarrow CO(v_1) + O$	$(1 - \beta_{E1}) \times 2.0 \times 10^{-11} T_e^{-0.5} T_g^{-1}$	0.08	201;202
(E1b)	$e + CO_2^+ \rightarrow C + O_2$	$\beta_{E1} \times k_{E1a} = \frac{k_{E1a}}{2}$		186
(E2)*	$e + CO_4^+ \rightarrow CO_2 + O_2$	$1.61 \times 10^{-13} T_e^{-0.5}$	0.3	186
(E3)	$e + CO^+ \rightarrow C + O$	$3.46 \times 10^{-14} T_e^{-0.48}$	0.25	168;203
(E4)*	$e + O + M \rightarrow O^- + M$	1×10^{-43}	0.5	202

* The primary source was not accessible and/or the uncertainty was not given

Table A.8: Ion-ion and ion-neutral reactions, as well as the references where the data are adopted from and the uncertainty of the data (expressed relative to the mean value). The rate coefficients are given in m^3/s and m^6/s, for two-body and threebody reactions, respectively. T_g is given in K.

No.	Reaction	Rate coefficient	$\frac{\Delta A}{A}$	Reference
(I1)	$CO_2 + CO^+ \rightarrow CO_2^+ + CO$	1.0×10^{-15}	0.2	204;205
(I2a)[a]	$CO_2 + O^- + CO_2 \rightarrow CO_3^- + CO_2$	1.5×10^{-40}	0.3	204;206
(I2b)[a]	$CO_2 + O^- + CO \rightarrow CO_3^- + CO$	1.5×10^{-40}	0.3	204;206
(I2c)	$CO_2 + O^- + O_2 \rightarrow CO_3^- + O_2$	3.1×10^{-40}	0.3	204;206
(I3)	$CO_2 + O_2^- + M \rightarrow CO_4^- + M$	4.7×10^{-41}	0.3	204;206
(I4)	$CO + O^- \rightarrow CO_2 + e$	5.5×10^{-16}	0.3	204;207
(I5)	$CO + CO_3^- \rightarrow 2CO_2 + e$	5×10^{-19}	0.2	208
(I6)*	$CO_3^- + CO_2^+ \rightarrow 2CO_2 v_b + O$	5×10^{-13}	0.5	202
(I7)*	$CO_4^- + CO_2^+ \rightarrow 2CO_2 v_b + O_2$	5×10^{-13}	0.5	202
(I8)*	$O_2^- + CO_2^+ \rightarrow CO_2 v_1 + O_2 + O$	6×10^{-13}	0.5	202
(I9)	$CO_3^- + O \rightarrow CO_2 + O_2^-$	8×10^{-17}	1	209
(I10a)*	$CO_4^- + O \rightarrow CO_3^- + O_2 + O$	1.12×10^{-16}	1	204
(I10b)*	$CO_4^- + O \rightarrow CO_2 + O_2 + O^-$	1.4×10^{-17}	1	204
(I11)	$O + O^- \rightarrow O_2 + e$	2.3×10^{-16}	0.2	210
(I12)*	$O + O_2^- \rightarrow O_2 + O^-$	1.5×10^{-16}	1	204
(I13)	$O_2^- + M \rightarrow O_2 + M + e$	$2.7 \times 10^{-16} (\frac{T_g}{300})^{0.5} exp(-5590/T_g)$	0.11	211;212
(I14)[b]	$O^- + M \rightarrow O + M + e$	$2.3 \times 10^{-15} exp(-26000/T_g)$	0.5	212–214

* The primary source was not accessible and/or the uncertainty was not given

[a] The rate coefficient of $CO_2 + O^- + He \rightarrow CO_3^- + He$ was used, due to the lack of further information.

[b] For usual values of gas temperature, i.e. $T_g \ll 26000$ K, the rate coefficient is very low, as pointed out by Gudmundsson[215].

Table A.9: Neutral reactions between vibrationally excited molecules, as well as the references where the data are adopted from and the uncertainty of the data (expressed relative to the mean value). The rate coefficients are given in m^3/s and m^6/s, for two-body and threebody reactions, respectively. T_g is given in K.

No.	Reaction	Rate coefficient	$\frac{\Delta A}{A}$	References*
(V1)	$CO_2v_a + M \rightarrow CO_2 + M$	$7.14 \times 10^{-15}\, exp(-177\, T_g^{-1/3} + 451\, T_g^{-2/3})$	0.3	[192;216;217]
(V2a)	$CO_2v_1 + M \rightarrow CO_2v_a + M$	$4.25 \times 10^{-7}\, exp(-407\, T_g^{-1/3} + 824\, T_g^{-2/3})$	0.1	[192;218;219]
(V2b)	$CO_2v_1 + M \rightarrow CO_2v_b + M$	$8.57 \times 10^{-7}\, exp(-404\, T_g^{-1/3} + 1096\, T_g^{-2/3})$	0.1	[192;218;219]
(V2c)	$CO_2v_1 + M \rightarrow CO_2v_c + M$	$1.43 \times 10^{-7}\, exp(-252\, T_g^{-1/3} + 685\, T_g^{-2/3})$	0.1	[192;218;219]
(V3)	$COv_1 + M \rightarrow CO + M$	$1.0 \times 10^{-18}\, T_g\, exp(-150.7\, T_g^{-1/3})$	0.15	[111]
(V4)	$O_2v_1 + M \rightarrow O_2 + M$	$1.3 \times 10^{-14}\, exp(-158.7\, T_g^{-1/3})$	0.1	[192;217]
(V5)	$CO_2v_1 + CO_2 \rightarrow CO_2v_a + CO_2v_b$	$1.06 \times 10^{-11}\, exp(-242\, T_g^{-1/3} + 633\, T_g^{-2/3})$	0.1	[192;218;219]
(V6)	$CO_2v_1 + CO_2 \rightarrow CO_2 + CO_2v_1$	$1.32 \times 10^{-18}\, (\frac{T_g}{300})^{0.5} \frac{250}{T_g}$	0.1	[193;194]
(V7)	$COv_1 + CO \rightarrow CO + COv_1$	$3.4 \times 10^{-16} (\frac{T_g}{300})^{0.5}\, (1.64 \times 10^{-6}\, T_g + \frac{1.61}{T_g})$	0.1	[220;221]
(V8)	$CO_2v_1 + CO \rightarrow CO_2 + COv_1$	$4.8 \times 10^{-12}\, exp(-153\, T_g^{-1/3})$	0.1	[192;222]

* Blauer and Gilmore[192] collected data from different sources and derived analytical expressions for the rate coefficients, without assessing the uncertainty. We estimated the value of $\frac{\Delta A}{A}$ based on the primary source of the data.

Table A.10: Neutral-neutral reactions, as well as the references where the data are adopted from and the uncertainty of the data (expressed relative to the mean value). The rate coefficients are given in m^3/s and m^6/s, for two-body and threebody reactions, respectively. T_g is given in K. The α parameter determines the effectiveness of lowering the activation energy for reaction involving vibrationally excited levels of the molecules (see details in[22;56]).

No.	Reaction	Rate coefficient	$\frac{\Delta A}{A}$	α	References*
(N1)	$CO_2 + M \rightarrow CO + O + M$	$6.06 \times 10^{-16} exp(-52525/T_g)$	0.15	0.8	[223]
(N2)[a]	$CO_2 + O \rightarrow CO + O_2$	$2.8 \times 10^{-17} exp(-26500/T_g)$	2	0.5	[174;224]
(N3)[b]	$CO_2 + C \rightarrow 2CO$	$< 10^{-21}$	-	n.a.	[225]
(N4)[c]	$CO + O + M \rightarrow CO_2 + M$	$8.3 \times 10^{-46} exp(-1510/T_g)$	1	0.0	[224;226]
(N5)[a]	$O_2 + CO \rightarrow CO_2 + O$	$4.2 \times 10^{-18} exp(-24000/T_g)$	1	0.5	[224]
(N6)	$O_2 + C \rightarrow CO + O$	$1.99 \times 10^{-16} exp(-2010/T_g)$	0.5	0.0	[227]
(N7)[d]	$O + C + M \rightarrow CO + M$	$2.14 \times 10^{-41} (\frac{T_g}{300})^{-3.08} exp(-2144/T_g)$	2	n.a.	[174;224]
(N8)[e]	$O + O + M \rightarrow O_2 + M$	$5.2 \times 10^{-47} exp(900/T_g)$	0.3	n.a.	[174;224]
(N9)[e]	$O_2 + M \rightarrow O + O + M$	$3.0 \times 10^{-12} \frac{1}{T_g} exp(-59380/T_g)$	0.3	0.0	[174;224]

* Baulch et al.[174] and Tsang et al.[224] are reviews assessing the reliability of different sources. Baulch et al.[174] derived rate coefficient expressions based on different sources and gave a value for the error. We consider it to be the primary source.

[a] Baulch et al.[174] suggests that $\frac{\Delta A}{A}$ is 1 at 1500 K and 0.5 at 3000 K. Tsang et al.[224] suggests $\frac{\Delta A}{A} = 2$.

[b] A rate coefficient is randomly chosen between 0 and 10^{-21} m^3/s, the maximum value.

[c] Multiply by 7, 3 or 12 for M= CO_2, CO or O_2 respectively; Baldwin et al.[226] suggests that $\frac{\Delta A}{A}$ is 0.2 at $T_g = 300$ K and 1 at $T_g = 800$ K.

[d] Baulch et al.[174] gives an uncertainty $\frac{\Delta A}{A} = 0.75$ at 7000 K. We have thus chosen a larger uncertainty, since the temperatures in this work are much lower.

[e] Baulch et al.[174] gives $\frac{\Delta A}{A} = 0.2$ at 190 K and 0.6 at 4000 K. Given the typical temperature values used, we chose a value of 0.3.

Bibliography

[1] J. Cook, D. Nuccitelli, S. A. Green, et al. Quantifying the consensus on anthropogenic global warming in the scientific literature. *Environmental Research Letters*, 8(2):024024, 2013. DOI: 10.1088/1748-9326/8/2/024024.

[2] IPCC 2013, Fifth Assesment Report: Climate Change 2013 Synthesis Report, www.ipcc.ch.

[3] NASA Global Climate Change: Vital Signs of the Planet,http://climate.nasa.gov, Data retrieved: 24/11/2017.

[4] Eurostat, Renewable Energy Statistics, http://ec.europa.eu/eurostat, Data retrieved: 29/11/2017.

[5] European Commision, Climate Action, http://ec.europa.eu/clima/, Data retrieved: 29/11/2017.

[6] Réseau de Transport d'Électricité (RTE), Open Data, https://opendata.rte-france.com, Data retrieved: 30/11/2017.

[7] M. A. Delucchi and M. Z. Jacobson. Providing all global energy with wind, water, and solar power, Part II: Reliability, system and transmission costs, and policies. *Energy Policy*, 39(3):1170–1190, 2011. DOI: 10.1016/j.enpol.2010.11.045.

[8] W. Katzenstein, E. Fertig, and J. Apt. The variability of interconnected wind plants. *Energy Policy*, 38(8):4400–4410, 2010. DOI: 10.1016/j.enpol.2010.03.069.

[9] H. Lund. Large-scale integration of optimal combinations of PV, wind and wave power into the electricity supply. *Renewable Energy*, 31(4):503–515, 2006. DOI: 10.1016/j.renene.2005.04.008.

[10] GE Energy, May 2010. Western and Solar Integration Study, National Renewable Energy Laboratory, Golden, Colorado. NREL/SR-550-47434.

[11] F. Díaz-González, A. Sumper, O. Gomis-Bellmunt, and R. Villafáfila-Robles. A review of energy storage technologies for wind power applications. *Renewable and Sustainable Energy Reviews*, 16(4):2154–2171, 2012. DOI: 10.1016/j.rser.2012.01.029.

[12] I. A. G. Wilson, P. G. McGregor, and P. J. Hall. Energy storage in the UK electrical network: Estimation of the scale and review of technology options. *Energy Policy*, 38(8):4099–4106, 2010. DOI: 10.1016/j.enpol.2010.03.036.

[13] S. Koohi-Kamali, V. Tyagi, N. Rahim, N. Panwar, and H. Mokhlis. Emergence of energy storage technologies as the solution for reliable operation of smart power systems: A review. *Renewable and Sustainable Energy Reviews*, 25:135–165, 2013. DOI: 10.1016/j.rser.2013.03.056.

[14] X. Luo, J. Wang, M. Dooner, and J. Clarke. Overview of current development in electrical energy storage technologies and the application potential in power system operation. *Applied Energy*, 137:511–536, 2015. DOI: 10.1016/j.apenergy.2014.09.081.

[15] S. Rehman, L. M. Al-Hadhrami, and M. M. Alam. Pumped hydro energy storage system: A technological review. *Renewable and Sustainable Energy Reviews*, 44(October 2017):586–598, 2015. DOI: 10.1016/j.rser.2014.12.040.

[16] Z. Yang, J. Zhang, M. C. W. Kintner-Meyer, et al. Electrochemical Energy Storage for Green Grid. *Chemical Reviews*, 111(5):3577–3613, 2011. DOI: 10.1021/cr100290v.

[17] B. Zalba, J. M. Marín, L. F. Cabeza, and H. Mehling. Review on thermal energy storage with phase change: materials, heat transfer analysis and applications. *Applied Thermal Engineering*, 23(3):251–283, 2003. DOI: 10.1016/S1359-4311(02)00192-8.

[18] J. A. Martens, A. Bogaerts, N. De Kimpe, et al. The Chemical Route to a Carbon Dioxide Neutral World. *ChemSusChem*, 10(6):1039–1055, 2017. DOI: 10.1002/cssc.201601051.

[19] R. C. Brady and R. Pettit. Mechanism of the Fischer-Tropsch reaction. The chain propagation step. *Journal of the American Chemical Society*, 103(5):1287–1289, 1981. DOI: 10.1021/ja00395a081.

[20] G. Centi and S. Perathoner. Opportunities and prospects in the chemical recycling of carbon dioxide to fuels. *Catalysis Today*, 148(3-4):191–205, 2009. DOI: 10.1016/j.cattod.2009.07.075.

[21] R. Snoeckx and A. Bogaerts. Plasma technology: a novel solution for CO_2 conversion? *Chem. Soc. Rev.*, 46(19):5805–5863, 2017. DOI: 10.1039/C6CS00066E.

[22] A. Fridman. *Plasma Chemistry.* Cambridge University Press, 2008. DOI: 10.1017/CBO9780511546075.

[23] NIST Chemistry WebBook, NIST Standard Reference Database Number 69 Constants of Diatomic Molecules, retrieved 5 June 2017. http://webbook.nist.gov.

[24] J. R. Roth. *Industrial Plasma Engineering: Principles Volume 1.* Taylor & Francis Ltd, London, United Kingdom, 1995. DOI: ISBN: 0750303174.

[25] C. K. N. Patel. Continuous-Wave Laser Action on Vibrational-Rotational Transitions of CO_2. *Physical Review*, 136(5A):A1187–A1193, 1964. DOI: 10.1103/PhysRev.136.A1187.

[26] H. Hokazono and H. Fujimoto. Theoretical analysis of the CO_2 molecule decomposition and contaminants yield in transversely excited atmospheric CO_2 laser discharge. *Journal of Applied Physics*, 62(5):1585–1594, 1987. DOI: 10.1063/1.339606.

[27] H. Hokazono, M. Obara, K. Midorikawa, and H. Tashiro. Theoretical operational life study of the closed-cycle transversely excited atmospheric CO_2 laser. *Journal of Applied Physics*, 69(10):6850–6868, 1991. DOI: 10.1063/1.347675.

[28] A. Cenian, A. Chernukho, V. Borodin, and G. Śliwiński. Modeling of Plasma-Chemical Reactions in Gas Mixture of CO_2 Lasers I. Gas Decomposition in Pure CO_2 Glow Discharge. *Contributions to Plasma Physics*, 34(1):25–37, 1994. DOI: 10.1002/ctpp.2150340105.

[29] A. Cenian, A. Chernukho, and V. Borodin. Modeling of Plasma-Chemical Reactions in Gas Mixture of CO_2 lasers. II. Theoretical Model and its Verification. *Contributions to Plasma Physics*, 35(3):273–296, 1995. DOI: 10.1002/ctpp.2150350309.

[30] R. S. Luce. An investigation of the reduction of carbon dioxide in a silent electric discharge. Technical report, Lockheed Missiles and Space Co.;, Sunnyvale, CA, United States, 1978. Document ID: 19780017824.

[31] A. Vesel, M. Mozetic, A. Drenik, and M. Balat-Pichelin. Dissociation of CO2 molecules in microwave plasma. *Chemical Physics*, 382(1-3):127–131, 2011. DOI: 10.1016/j.chemphys.2011.03.015.

[32] V. Guerra, T. Silva, P. Ogloblina, et al. The case for in situ resource utilisation for oxygen production on Mars by non-equilibrium plasmas. *Plasma Sources Science and Technology*, 26(11):11LT01, 2017. DOI: 10.1088/1361-6595/aa8dcc.

[33] R. I. Asisov, A. K. Vakar, V. K. Jivotov, et al. Non-equilibrium plasma-chemical process of CO_2 decomposition in a supersonic microwave discharge. *Proceedings of the USSR Academy of Sciences*, 271(1), 1983.

[34] W. Bongers, H. Bouwmeester, B. Wolf, et al. Plasma-driven dissociation of CO_2 for fuel synthesis. *Plasma Processes and Polymers*, 14(6):1600126, 2017. DOI: 10.1002/ppap.201600126.

[35] L. F. Spencer and A. D. Gallimore. CO_2 dissociation in an atmospheric pressure plasma/catalyst system: a study of efficiency. *Plasma Sources Science and Technology*, 22(1):015019, 2012. DOI: 10.1088/0963-0252/22/1/015019.

[36] T. Silva, N. Britun, T. Godfroid, and R. Snyders. Optical characterization of a microwave pulsed discharge used for dissociation of CO_2. *Plasma Sources Science and Technology*, 23(2):025009, 2014. DOI: 10.1088/0963-0252/23/2/025009.

[37] N. den Harder, D. C. M. van den Bekerom, R. S. Al, et al. Homogeneous CO_2 conversion by microwave plasma: Wave propagation and diagnostics. *Plasma Processes and Polymers*, 14(6):1600120, 2017. DOI: 10.1002/ppap.201600120.

[38] A. Indarto, D. R. Yang, J. W. Choi, H. Lee, and H. K. Song. Gliding arc plasma processing of CO_2 conversion. *Journal of Hazardous Materials*, 146(1-2):309–315, 2007. DOI: 10.1016/j.jhazmat.2006.12.023.

[39] T. Nunnally, K. Gutsol, A. Rabinovich, et al. Dissociation of CO_2 in a low current gliding arc plasmatron. *Journal of Physics D: Applied Physics*, 44(27):274009, 2011. DOI: 10.1088/0022-3727/44/27/274009.

[40] M. Ramakers, G. Trenchev, S. Heijkers, W. Wang, and A. Bogaerts. Gliding Arc Plasmatron: Providing an Alternative Method for Carbon Dioxide Conversion. *ChemSusChem*, 10(12):2642–2652, 2017. DOI: 10.1002/cssc.201700589.

[41] D. Mei, X. Zhu, Y.-L. He, J. D. Yan, and X. Tu. Plasma-assisted conversion of CO_2 in a dielectric barrier discharge reactor: understanding the effect of packing materials. *Plasma Sources Science and Technology*, 24(1):15011–15021, 2015. DOI: 10.1088/0963-0252/24/1/015011.

[42] S. Paulussen, B. Verheyde, X. Tu, et al. Conversion of carbon dioxide to value-added chemicals in atmospheric pressure dielectric barrier discharges. *Plasma Sources Science and Technology*, 19(3):034015, 2010. DOI: 10.1088/0963-0252/19/3/034015.

[43] I. Belov, S. Paulussen, and A. Bogaerts. Appearance of a conductive carbonaceous coating in a CO_2 dielectric barrier discharge and its influence on the electrical properties and the conversion efficiency. *Plasma Sources Science and Technology*, 25(1):015023, 2016. DOI: 10.1088/0963-0252/25/1/015023.

[44] I. Michielsen, Y. Uytdenhouwen, J. Pype, et al. CO_2 dissociation in a packed bed DBD reactor: First steps towards a better understanding of

plasma catalysis. *Chemical Engineering Journal*, 326:477–488, 2017. DOI: 10.1016/j.cej.2017.05.177.

[45] M. S. Moss, K. Yanallah, R. W. K. Allen, and F. Pontiga. An investigation of CO_2 splitting using nanosecond pulsed corona discharge: effect of argon addition on CO_2 conversion and energy efficiency. *Plasma Sources Science and Technology*, 26(3):035009, 2017. DOI: 10.1088/1361-6595/aa5b1d.

[46] M. Scapinello, L. M. Martini, G. Dilecce, and P. Tosi. Conversion of CH_4/CO_2 by a nanosecond repetitively pulsed discharge. *Journal of Physics D: Applied Physics*, 49(7):075602, 2016. DOI: 10.1088/0022-3727/49/7/075602.

[47] J.-y. Wang, G.-g. Xia, A. Huang, et al. CO_2 Decomposition Using Glow Discharge Plasmas. *Journal of Catalysis*, 185(1):152–159, 1999. DOI: http://linkinghub.elsevier.com/retrieve/pii/S0021951799924995.

[48] M. Ramakers, I. Michielsen, R. Aerts, V. Meynen, and A. Bogaerts. Effect of Argon or Helium on the CO 2 Conversion in a Dielectric Barrier Discharge. *Plasma Processes and Polymers*, 12(8):755–763, 2015. DOI: 10.1002/ppap.201400213.

[49] R. Aerts, T. Martens, and A. Bogaerts. Influence of Vibrational States on CO_2 Splitting by Dielectric Barrier Discharges. *The Journal of Physical Chemistry C*, 116(44):23257–23273, 2012. DOI: 10.1021/jp307525t.

[50] L. D. Pietanza, G. Colonna, G. D'Ammando, A. Laricchiuta, and M. Capitelli. Vibrational excitation and dissociation mechanisms of CO_2 under non-equilibrium discharge and post-discharge conditions. *Plasma Sources Science and Technology*, 24(4):042002, 2015. DOI: 10.1088/0963-0252/24/4/042002.

[51] L. D. Pietanza, G. Colonna, G. D'Ammando, A. Laricchiuta, and M. Capitelli. Electron energy distribution functions and fractional power transfer in "cold" and excited CO_2 discharge and post discharge conditions. *Physics of Plasmas*, 23(1), 2016. DOI: 10.1063/1.4940782.

[52] L. D. Pietanza, G. Colonna, G. D'Ammando, A. Laricchiuta, and M. Capitelli. Non equilibrium vibrational assisted dissociation and ionization mechanisms in cold CO_2 plasmas. *Chemical Physics*, 468:44–52, 2016. DOI: 10.1016/j.chemphys.2016.01.007.

[53] L. D. Pietanza, G. Colonna, V. Laporta, et al. Influence of Electron Molecule Resonant Vibrational Collisions over the Symmetric Mode and Direct Excitation-Dissociation Cross Sections of CO_2 on the Electron Energy Distribution Function and Dissociation Mechanisms in Cold Pure CO_2 Plasmas. *Journal of Physical Chemistry A*, 120(17):2614–2628, 2016. DOI: 10.1021/acs.jpca.6b01154.

[54] L. D. Pietanza, G. Colonna, G. D'Ammando, and M. Capitelli. Time-dependent coupling of electron energy distribution function, vibrational kinetics of the asymmetric mode of CO_2 and dissociation, ionization and electronic excitation kinetics under discharge and post-discharge conditions. *Plasma Physics and Controlled Fusion*, 59(1):014035, 2017. DOI: 10.1088/0741-3335/59/1/014035.

[55] M. Capitelli, G. Colonna, G. D'Ammando, et al. Coupling of Plasma Chemistry, Vibrational Kinetics, Collisional-Radiative Models and Electron Energy Distribution Function Under Non-Equilibrium Conditions. *Plasma Processes and Polymers*, 14(1-2):1600109, 2017. DOI: 10.1002/ppap.201600109.

[56] T. Kozák and A. Bogaerts. Splitting of CO_2 by vibrational excitation in non-equilibrium plasmas: a reaction kinetics model. *Plasma Sources Science and Technology*, 23(4):045004, 2014. DOI: 10.1088/0963-0252/23/4/045004.

[57] T. Kozák and A. Bogaerts. Evaluation of the energy efficiency of CO_2 conversion in microwave discharges using a reaction kinetics model. *Plasma Sources Science and Technology*, 24(1):015024, 2015. DOI: 10.1088/0963-0252/24/1/015024.

[58] S. Heijkers, R. Snoeckx, T. Kozák, et al. CO_2 Conversion in a Microwave Plasma Reactor in the Presence of N_2: Elucidating the Role of Vibrational Levels. *The Journal of Physical Chemistry C*, 119(23):12815–12828, 2015. DOI: 10.1021/acs.jpcc.5b01466.

[59] S. Heijkers and A. Bogaerts. CO_2 Conversion in a Gliding Arc Plasmatron: Elucidating the Chemistry through Kinetic Modeling. *The Journal of Physical Chemistry C*, 121(41):22644–22655, 2017. DOI: 10.1021/acs.jpcc.7b06524.

[60] P. Koelman, S. Heijkers, S. Tadayon Mousavi, et al. A Comprehensive Chemical Model for the Splitting of CO_2 in Non-Equilibrium Plasmas. *Plasma Processes and Polymers*, 14(4-5):1600155, 2017. DOI: 10.1002/ppap.201600155.

[61] S. Ponduri, M. M. Becker, S. Welzel, et al. Fluid modelling of CO_2 dissociation in a dielectric barrier discharge. *Journal of Applied Physics*, 119(9), 2016. DOI: 10.1063/1.4941530.

[62] A. Bogaerts, T. Kozák, K. van Laer, and R. Snoeckx. Plasma-based conversion of CO_2: current status and future challenges. *Faraday Discussions*, 183:217–232, 2015. DOI: 10.1039/C5FD00053J.

[63] A. Bogaerts, C. De Bie, R. Snoeckx, and T. Kozák. Plasma based CO_2 and CH_4 conversion: A modeling perspective. *Plasma Processes and Polymers*, 14(6):e201600070, 2017. DOI: 10.1002/ppap.201600070.

[64] A. Bogaerts, W. Wang, A. Berthelot, and V. Guerra. Modeling plasma-based CO_2 conversion: crucial role of the dissociation cross section. *Plasma Sources Science and Technology*, 25(5):055016, 2016. DOI: 10.1088/0963-0252/25/5/055016.

[65] G. J. M. Hagelaar and L. C. Pitchford. Solving the Boltzmann equation to obtain electron transport coefficients and rate coefficients for fluid models. *Plasma Sources Science and Technology*, 14(4):722–733, 2005. DOI: 10.1088/0963-0252/14/4/011.

[66] A. Janeco, N. R. Pinha, and V. Guerra. Electron Kinetics in He/CH_4/CO_2 Mixtures Used for Methane Conversion. *Journal of Physical Chemistry C*, 119:109–120, 2015. DOI: 10.1021/jp509843e.

[67] S. Andreev, V. Zakharov, V. Ochkin, and S. Savinov. Plasma-chemical CO_2 decomposition in a non-self-sustained discharge with a controlled electronic component of plasma. *Spectrochimica Acta Part A: Molecular and Biomolecular Spectroscopy*, 60(14):3361–3369, 2004. DOI: 10.1016/j.saa.2004.01.034.

[68] C. Tendero, C. Tixier, P. Tristant, J. Desmaison, and P. Leprince. Atmospheric pressure plasmas: A review. *Spectrochimica Acta Part B: Atomic Spectroscopy*, 61(1):2–30, 2006. DOI: 10.1016/j.sab.2005.10.003.

[69] A. Bogaerts, E. Neyts, R. Gijbels, and J. van der Mullen. Gas discharge plasmas and their applications. *Spectrochimica Acta Part B: Atomic Spectroscopy*, 57(4):609–658, 2002. DOI: 10.1016/S0584-8547(01)00406-2.

[70] A. V. Pipa, J. Koskulics, R. Brandenburg, and T. Hoder. The simplest equivalent circuit of a pulsed dielectric barrier discharge and the determination of the gas gap charge transfer. *Review of Scientific Instruments*, 83(11):115112, 2012. DOI: 10.1063/1.4767637.

[71] Y. P. Raizer. *Gas Discharge Physics*. Springer Berlin Heidelberg, Berlin, Heidelberg, 1991. DOI: 10.1007/978-3-642-61247-3.

[72] A. Fridman, A. Chirokov, and A. Gutsol. Non-thermal atmospheric pressure discharges. *Journal of Physics D: Applied Physics*, 38(2):R1–R24, 2005. DOI: 10.1088/0022-3727/38/2/R01.

[73] U. Kogelschatz, B. Eliasson, and W. Egli. From ozone generators to flat television screens: history and future potential of dielectric-barrier discharges. *Pure and Applied Chemistry*, 71(10):1819–1828, 1999. DOI: 10.1351/pac199971101819.

[74] U. Kogelschatz. Ozone and beyond: the marvelous development of dielectric barrier discharges. *Journal of Physics D: Applied Physics*, 50(5):051001, 2017. DOI: 10.1088/1361-6463/50/5/051001.

[75] B. Eliasson, M. Hirth, and U. Kogelschatz. Ozone synthesis from oxygen in dielectric barrier discharges. *Journal of Physics D: Applied Physics*, 20(11):1421–1437, 1987. DOI: 10.1088/0022-3727/20/11/010.

[76] R. Aerts, W. Somers, and A. Bogaerts. Carbon Dioxide Splitting in a Dielectric Barrier Discharge Plasma: A Combined Experimental and Computational Study. *ChemSusChem*, 8(4):702–716, 2015. DOI: 10.1002/cssc.201402818.

[77] A. Ozkan, A. Bogaerts, and F. Reniers. Routes to increase the conversion and the energy efficiency in the splitting of CO 2 by a dielectric barrier discharge. *Journal of Physics D: Applied Physics*, 50(8):084004, 2017. DOI: 10.1088/1361-6463/aa562c.

[78] S. Sun, H. Wang, D. Mei, X. Tu, and A. Bogaerts. CO_2 conversion in a gliding arc plasma: Performance improvement based on chemical reaction modeling. *Journal of CO_2 Utilization*, 17:220–234, 2017. DOI: 10.1016/j.jcou.2016.12.009.

[79] M. Ramakers, J. A. Medrano, G. Trenchev, F. Gallucci, and A. Bogaerts. Revealing the arc dynamics in a gliding arc plasmatron: a better insight to improve CO_2 conversion. *Plasma Sources Science and Technology*, 26(12):125002, 2017. DOI: 10.1088/1361-6595/aa9531.

[80] S. C. Kim, M. S. Lim, and Y. N. Chun. Reduction characteristics of carbon dioxide using a plasmatron. *Plasma Chemistry and Plasma Processing*, 34(1):125–143, 2014. 10.1007/s11090-013-9499-8.

[81] E. Cleiren, S. Heijkers, M. Ramakers, and A. Bogaerts. Dry Reforming of Methane in a Gliding Arc Plasmatron: Towards a Better Understanding of the Plasma Chemistry. *ChemSusChem*, 10(20):4025–4036, 2017. DOI: 10.1002/cssc.201701274.

[82] R. Sorrentino and G. Bianchi. *Microwave and RF Engineering.* John Wiley & Sons, Ltd, Chichester, UK, 2010. DOI: ISBN: 978-0-470-75862-5.

[83] M. Moisan and Z. Zakrzewski. Plasma sources based on the propagation of electromagnetic surface waves. *Journal of Physics D: Applied Physics*, 24(7):1025–1048, 1991. DOI: 10.1088/0022-3727/24/7/001.

[84] J. D. Cobine and D. A. Wilbur. The Electronic Torch and Related High Frequency Phenomena. *Journal of Applied Physics*, 22(6):835–841, 1951. DOI: 10.1063/1.1700055.

[85] M. Moisan, G. Sauve, Z. Zakrzewski, and J. Hubert. An atmospheric pressure waveguide-fed microwave plasma torch: the TIA design. *Plasma Sources Science and Technology*, 3(4):584–592, 1994. DOI: 10.1088/0963-0252/3/4/016.

[86] M. Jimenez-Diaz, J. van Dijk, and J. J. a. M. van der Mullen. Effect of remote field electromagnetic boundary conditions on microwave-induced plasma torches. *Journal of Physics D: Applied Physics*, 44(16):165203, 2011. DOI: 10.1088/0022-3727/44/16/165203.

[87] M. Moisan, C. Beaudry, and P. Leprince. A Small Microwave Plasma Source for Long Column Production without Magnetic Field. *IEEE Transactions on Plasma Science*, 3(2):55–59, 1975. DOI: 10.1109/TPS.1975.4316875.

[88] M. Moisan, Z. Zakrzewski, and R. Pantel. The theory and characteristics of an efficient surface wave launcher (surfatron) producing long plasma columns. *Journal of Physics D: Applied Physics*, 12(2):219–237, 1979. DOI: 10.1088/0022-3727/12/2/008.

[89] J. F. de la Fuente, S. H. Moreno, A. I. Stankiewicz, and G. D. Stefanidis. Reduction of CO_2 with hydrogen in a non-equilibrium microwave plasma reactor. *International Journal of Hydrogen Energy*, 41(46):21067–21077, 2016. DOI: 10.1016/j.ijhydene.2016.08.032.

[90] J. F. de la Fuente, S. H. Moreno, A. I. Stankiewicz, and G. D. Stefanidis. On the improvement of chemical conversion in a surface-wave microwave plasma reactor for CO_2 reduction with hydrogen (The Reverse Water-Gas Shift reaction). *International Journal of Hydrogen Energy*, 42(18):12943–12955, 2017. DOI: 10.1016/j.ijhydene.2017.04.040.

[91] G. Chen, T. Silva, V. Georgieva, et al. Simultaneous dissociation of CO_2 and H_2O to syngas in a surface-wave microwave discharge. *International Journal of Hydrogen Energy*, 40(9):3789–3796, 2015. DOI: 10.1016/j.ijhydene.2015.01.084.

[92] G. Chen, V. Georgieva, T. Godfroid, R. Snyders, and M.-P. Delplancke-Ogletree. Plasma assisted catalytic decomposition of CO_2. *Applied Catalysis B: Environmental*, 190:115–124, 2016. DOI: 10.1016/j.apcatb.2016.03.009.

[93] G. Chen, T. Godfroid, N. Britun, et al. Plasma-catalytic conversion of CO_2 and CO_2/H_2O in a surface-wave sustained microwave discharge. *Applied Catalysis B: Environmental*, 214:114–125, 2017. DOI: 10.1016/j.apcatb.2017.05.032.

[94] G. Chen, N. Britun, T. Godfroid, et al. An overview of CO_2 conversion in a microwave discharge: the role of plasma-catalysis. *Journal of Physics D: Applied Physics*, 50(8):084001, 2017. DOI: 10.1088/1361-6463/aa5616.

[95] V. Shapoval, E. Marotta, C. Ceretta, et al. Development and Testing of a Self-Triggered Spark Reactor for Plasma Driven Dry Reforming of Methane. *Plasma Processes and Polymers*, 11(8):787–797, 2014. DOI: 10.1002/ppap.201400007.

[96] J. A. Bittencourt. *Fundamentals of Plasma Physics.* Springer New York, New York, NY, 2004. DOI: 10.1007/978-1-4757-4030-1.

[97] T. Grasser, H. Kosina, M. Gritsch, and S. Selberherr. Using six moments of Boltzmann's transport equation for device simulation. *Journal of Applied Physics*, 90(5):2389–2396, 2001. DOI: 10.1063/1.1389757.

[98] M. A. Lieberman and A. J. Lichtenberg. *Principles of Plasma Discharges and Materials Processing.* John Wiley & Sons, Inc., Hoboken, NJ, USA, 2005. DOI: 10.1002/0471724254.

[99] Y. M. Aliev, H. Schlüter, and A. Shivarova. *Guided-Wave-Produced Plasmas.* Springer Berlin Heidelberg, Berlin, Heidelberg, 2000. DOI: 10.1007/978-3-642-57060-5.

[100] S. Pancheshnyi, B. Eismann, G.J.M. Hagelaar, L.C. Pitchford, Computer code ZDPlasKin, http://www.zdplaskin.laplace.univ-tlse.fr (University of Toulouse, LAPLACE, CNRS-UPS-INP, Toulouse, France, 2008).

[101] V. Guerra, E. Tatarova, F. M. Dias, and C. M. Ferreira. On the self-consistent modeling of a traveling wave sustained nitrogen discharge. *Journal of Applied Physics*, 91(5):2648–2661, 2002. DOI: 10.1063/1.1446229.

[102] O. Schenk, K. Gärtner, W. Fichtner, and A. Stricker. PARDISO: a high-performance serial and parallel sparse linear solver in semiconductor device simulation. *Future Generation Computer Systems*, 18(1):69–78, 2001. DOI: 10.1016/S0167-739X(00)00076-5.

[103] C. G. Petra, O. Schenk, M. Lubin, and K. Gärtner. An augmented incomplete factorization approach for computing the schur complement in stochastic optimization. *SIAM Journal on Scientific Computing*, 36(2):C139–C162, 2014. DOI: 10.1137/130908737.

[104] M. Grofulović, L. L. Alves, and V. Guerra. Electron-neutral scattering cross sections for CO_2: a complete and consistent set and an assessment of dissociation. *J. Phys. D: Appl. Phys.*, 49:395207, 2016. DOI: 10.1088/0022-3727/49/39/395207.

[105] G. H. K. P. Huber. *Molecular Spectra and Molecular Structure IV. Constant of diatomic molecules.* Van Nostrand Rienhold Company, 1979. DOI: 10.1007/978-1-4757-0961-2.

[106] I. Suzuki. General anharmonic force constants of carbon dioxide. *Journal of Molecular Spectroscopy*, 25(4):479–500, 1968. DOI: 10.1016/S0022-2852(68)80018-9.

[107] G. Herzberg. *Molecular Spectra and Molecular Structure: Spectra of Diatomic Molecules*, volume 1. Princeton, NJ: Van Nostrand, 1950.

[108] H. G. Huber K. NIST Chemistry WebBook, NIST Standard Reference Database Number 69 Constants of Diatomic Molecules, retrieved 4 December 2013. http://webbook.nist.gov.

[109] A. V. Phelps. Phelps database retrieved from www.lxcat.net on september 4, 2014. DOI: http://jilawww.colorado.edu/.

[110] R. N. Schwartz, Z. I. Slawsky, and K. F. Herzfeld. Calculation of Vibrational Relaxation Times in Gases. *The Journal of Chemical Physics*, 20(May 2013):1591, 1952. DOI: 10.1063/1.1700221.

[111] M. Capitelli, C. M. Ferreira, B. F. Gordiets, and A. I. Osipov. *Plasma kinetics in atmospheric gases.* Springer Berlin Heidelberg, springer s edition, 2000. DOI: 10.1007/978-3-662-04158-1.

[112] R. D. Levine and R. B. Bernstein. *Thermodynamic Approach to Collision Processes*, pages 323–364. Springer US, Boston, MA, 1976. DOI: 10.1007/978-1-4757-0644-4_7.

[113] R. D. Hake and A. V. Phelps. Momentum-Transfer and Inelastic-Collision Cross Sections for Electrons in O_2, CO, and CO_2. *Physical Review*, 158(1):70–84, 1967. DOI: 10.1103/PhysRev.158.70.

[114] G. D. Billing. *Vibration-Vibration and Vibration-Translation Energy Transfer, Including Multiquantum Transitions in Atom-Diatom and Diatom-Diatom Collisions*, pages 85–112. Springer Berlin Heidelberg, Berlin, Heidelberg, 1986. DOI: 10.1007/978-3-642-48615-9_4.

[115] D. Rapp and P. Englander-Golden. Resonant and Near-Resonant Vibrational—Vibrational Energy Transfer between Molecules in Collisions. *The Journal of Chemical Physics*, 40(2):573–575, 1964. DOI: 10.1063/1.1725158.

[116] R. D. Sharma and C. A. Brau. Energy Transfer in Near-Resonant Molecular Collisions due to Long-Range Forces with Application to Transfer of Vibrational Energy from ν_3 Mode of CO_2 to N_2. *The Journal of Chemical Physics*, 50(2):924–930, 1969. DOI: 10.1063/1.1671145.

[117] A. E. DePristo, S. D. Augustin, R. Ramaswamy, and H. Rabitz. Quantum number and energy scaling for nonreactive collisions. *The Journal of Chemical Physics*, 71(2):850–865, 1979. DOI: 10.1063/1.438376.

[118] I. V. Adamovich, S. O. MacHeret, J. W. Rich, and C. E. Treanor. Vibrational Energy Transfer Rates Using a Forced Harmonic Oscillator Model. *Journal of Thermophysics and Heat Transfer*, 12(1):57–65, 1998. DOI: 10.2514/2.6302.

[119] I. V. Adamovich and J. W. Rich. Three-dimensional nonperturbative analytic model of vibrational energy transfer in atom–molecule collisions. *The Journal of Chemical Physics*, 109(18):7711–7724, 1998. DOI: 10.1063/1.477417.

[120] G. Billing Sørensen. Semiclassical three-dimensional model for vibrational energy transfer in diatomic molecules. *Chemical Physics*, 5(2):244–254, 1974. DOI: 10.1016/0301-0104(74)80022-4.

[121] G. D. Billing and E. Fisher. VV and VT rate coefficients in N_2 by a quantum-classical model. *Chemical Physics*, 43(3):395–401, 1979. DOI: 10.1016/0301-0104(79)85207-6.

[122] E. Kustova and E. Nagnibeda. On a correct description of a multi-temperature dissociating CO2 flow. *Chemical Physics*, 321(3):293–310, 2006. DOI: 10.1016/j.chemphys.2005.08.026.

[123] C. E. Treanor, J. W. Rich, and R. G. Rehm. Vibrational Relaxation of Anharmonic Oscillators with Exchange-Dominated Collisions. *The Journal of Chemical Physics*, 48(4):1798–1807, 1968. DOI: 10.1063/1.1668914.

[124] A. Berthelot, S. Kolev, and A. Bogaerts. *Different pressure regimes of a surface-wave discharge in argon: a modeling investigation.* Proceedings of IX International Workshop on Microwave discharges: Fundamentals and Applications, September 7-11, 2015, Cordoba, Spain, 2015.

[125] H. Schluter and A. Shivarova. Travelling-wave-sustained discharges. *Physics Reports*, 443(4-6):121–255, 2007. DOI: 10.1016/j.physrep.2006.12.006.

[126] C. M. Ferreira and M. Moisan. The similarity laws for the maintenance field and the absorbed power per electron in low-pressure surface wave produced plasmas and their extension to HF plasmas in general. *Physica Scripta*, 38(3):382–399, 1988. DOI: 10.1088/0031-8949/38/3/008.

[127] E. Castaños Martinez, Y. Kabouzi, K. Makasheva, and M. Moisan. Modeling of microwave-sustained plasmas at atmospheric pressure with application to discharge contraction. *Physical Review E*, 70(6):066405, 2004. DOI: 10.1103/PhysRevE.70.066405.

[128] Y. Kabouzi, D. B. Graves, E. Castaños-Martínez, and M. Moisan. Modeling of atmospheric-pressure plasma columns sustained by surface waves. *Physical Review E*, 75(1):016402, 2007. DOI: 10.1103/PhysRevE.75.016402.

[129] M. Baeva, A. Bösel, J. Ehlbeck, and D. Loffhagen. Modeling of microwave-induced plasma in argon at atmospheric pressure. *Physical Review E*, 85(5):056404, 2012. DOI: 10.1103/PhysRevE.85.056404.

[130] M. Baeva, M. Andrasch, J. Ehlbeck, D. Loffhagen, and K.-D. Weltmann. Temporally and spatially resolved characterization of microwave induced argon plasmas: Experiment and modeling. *Journal of Applied Physics*, 115(14):143301, 2014. DOI: 10.1063/1.4870858.

[131] J. van Dijk, K. Peerenboom, M. Jimenez, D. Mihailova, and J. van der Mullen. The plasma modelling toolkit Plasimo. *Journal of Physics D: Applied Physics*, 42(19):194012, 2009. DOI: 10.1088/0022-3727/42/19/194012.

[132] M. Jimenez-Diaz, E. a. D. Carbone, J. van Dijk, and J. J. a. M. van der Mullen. A two-dimensional Plasimo multiphysics model for the plasma–electromagnetic interaction in surface wave discharges: the surfatron source. *Journal of Physics D: Applied Physics*, 45(33):335204, 2012. DOI: 10.1088/0022-3727/45/33/335204.

[133] S. Rahimi, M. Jimenez-Diaz, S. Hübner, et al. A two-dimensional modelling study of a coaxial plasma waveguide. *Journal of Physics D: Applied Physics*, 47(12):125204, 2014. DOI: 10.1088/0022-3727/47/12/125204.

[134] V. Georgieva, A. Berthelot, T. Silva, et al. Understanding Microwave Surface-Wave Sustained Plasmas at Intermediate Pressure by 2D Modeling and Experiments. *Plasma Processes and Polymers*, 14(4-5):1600185, 2017. DOI: 10.1002/ppap.201600185.

[135] S. Kolev and A. Bogaerts. A 2D model for a gliding arc discharge. *Plasma Sources Science and Technology*, 24(1):015025, 2014. DOI: 10.1088/0963-0252/24/1/015025.

[136] E. W. McDaniel and E. A. Mason. *The mobility and diffusion of ions in gases [by] Earl W. McDaniel [and] Edward A. Mason.* Wiley New York, 1973.

[137] C. M. Ferreira, J. Loureiro, and A. Ricard. Populations in the metastable and the resonance levels of argon and stepwise ionization effects in a low-pressure argon positive column. *Journal of Applied Physics*, 57(1):82–90, 1985. DOI: 10.1063/1.335400.

[138] BIAGI-v7.1, 2004. database and collected from LxCat; transcribed from S F Biagi's Fortran code MAGBOLTZ, version 7.1.

[139] H. A. Hyman. Electron-impact ionization cross sections for excited states of the rare gases (Ne, Ar, Kr, Xe), cadmium, and mercury. *Physical Review A*, 20(3):855–859, 1979. DOI: 10.1103/PhysRevA.20.855.

[140] K. Bartschat and V. Zeman. Electron-impact excitation from the (3p$ˆ5$4s) metastable states of argon. *Physical Review A*, 59(4):R2552–R2554, 1999. DOI: 10.1103/PhysRevA.59.R2552.

[141] N. a. Dyatko, Y. Z. Ionikh, I. V. Kochetov, et al. Experimental and theoretical study of the transition between diffuse and contracted forms of the glow discharge in argon. *Journal of Physics D: Applied Physics*, 41(5):055204, 2008. DOI: 10.1088/0022-3727/41/5/055204.

[142] J. Jonkers, M. V. D. Sande, A. Sola, et al. The role of molecular rare gas ions in plasmas operated at atmospheric pressure. *Plasma Sources Science and Technology*, 12(3):464–474, 2003. DOI: 10.1088/0963-0252/12/3/323.

[143] A. J. Cunningham, T. F. O'Malley, and R. M. Hobson. On the role of vibrational excitation in dissociative recombination. *Journal of Physics B: Atomic and Molecular Physics*, 14(4):773–782, 1981. DOI: 10.1088/0022-3700/14/4/024.

[144] A. Bultel, B. van Ootegem, A. Bourdon, and P. Vervisch. Influence of Ar_2^+ in an argon collisional-radiative model. *Physical Review E*, 65(4):046406, 2002. DOI: 10.1103/PhysRevE.65.046406.

[145] D. P. Lymberopoulos and D. J. Economou. Fluid simulations of glow discharges: Effect of metastable atoms in argon. *Journal of Applied Physics*, 73(8):3668–3679, 1993. DOI: 10.1063/1.352926.

[146] S. K. Lam, C.-e. Zheng, D. Lo, A. Dem'yanov, and A. P. Napartovich. Kinetics of Ar_2^* in high-pressure pure argon. *Journal of Physics D: Applied Physics*, 33(3):242–251, 2000. DOI: 10.1088/0022-3727/33/3/310.

[147] J. Gregório, P. Leprince, C. Boisse-Laporte, and L. L. Alves. Self-consistent modelling of atmospheric micro-plasmas produced by a microwave source. *Plasma Sources Science and Technology*, 21(1):015013, 2012. DOI: 10.1088/0963-0252/21/1/015013.

[148] A. Bogaerts, R. Gijbels, and J. Vlcek. Collisional-radiative model for an argon glow discharge. *Journal of Applied Physics*, 84(1):121–136, 1998. DOI: 10.1063/1.368009.

[149] A. Sola, J. Cotrino, A. Gamero, and V. Colomer. Study of surface-wave-produced plasma column lengths. *Journal of Physics D: Applied Physics*, 20(10):1250–1258, 1987. DOI: 10.1088/0022-3727/20/10/007.

[150] A. Sola, A. Gamero, J. Cotrino, and V. Colomer. Empirical similarity laws for argon plasmas produced by a surface wave at 2.45 GHz. *Journal of Physics D: Applied Physics*, 21(7):1112–1116, 1988. DOI: 10.1088/0022-3727/21/7/009.

[151] M. D. Calzada, M. Moisan, a. Gamero, and a. Sola. Experimental investigation and characterization of the departure from local thermodynamic equilibrium along a surface-wave-sustained discharge at atmospheric pressure. *Journal of Applied Physics*, 80(1):46, 1996. DOI: 10.1063/1.362748.

[152] C. Boisse-Laporte, A. Granier, E. Dervisevic, P. Leprince, and J. Marec. Microwave discharges produced by surface waves in argon gas. *Journal of Physics D: Applied Physics*, 20(2):197–203, 1987. DOI: 10.1088/0022-3727/20/2/008.

[153] A. Berthelot and A. Bogaerts. Modeling of plasma-based CO_2 conversion: lumping of the vibrational levels. *Plasma Sources Science and Technology*, 25(4):045022, 2016. DOI: 10.1088/0963-0252/25/4/045022.

[154] K. Peerenboom, A. Parente, T. Kozák, A. Bogaerts, and G. Degrez. Dimension reduction of non-equilibrium plasma kinetic models using principal component analysis. *Plasma Sources Science and Technology*, 24(2):025004, 2015. DOI: 10.1088/0963-0252/24/2/025004.

[155] H. P. Le, A. R. Karagozian, and J.-L. Cambier. Complexity reduction of collisional-radiative kinetics for atomic plasma. *Physics of Plasmas*, 20(12):123304, 2013. DOI: 10.1063/1.4849417.

[156] A. Guy, A. Bourdon, and M.-Y. Perrin. Consistent multi-internal-temperatures models for nonequilibrium nozzle flows. *Chemical Physics*, 420:15–24, 2013. DOI: 10.1016/j.chemphys.2013.04.018.

[157] A. Guy, A. Bourdon, and M.-Y. Perrin. Consistent multi-internal-temperature models for vibrational and electronic nonequilibrium in hypersonic nitrogen plasma flows. *Physics of Plasmas*, 22(4):043507, 2015. DOI: 10.1063/1.4917338.

[158] A. Berthelot and A. Bogaerts. Modeling of CO_2 Splitting in a Microwave Plasma: How to Improve the Conversion and Energy Efficiency. *The Journal of Physical Chemistry C*, 121(15):8236–8251, 2017. DOI: 10.1021/acs.jpcc.6b12840.

[159] W. Wang, A. Berthelot, S. Kolev, X. Tu, and A. Bogaerts. CO_2 conversion in a gliding arc plasma: 1D cylindrical discharge model. *Plasma Sources Science and Technology*, 25(6):065012, 2016. DOI: 10.1088/0963-0252/25/6/065012.

[160] A. Berthelot and A. Bogaerts. Modeling of CO_2 plasma: effect of uncertainties in the plasma chemistry. *Plasma Sources Science and Technology*, 26(11):115002, 2017. DOI: 10.1088/1361-6595/aa8ffb.

[161] M. M. Turner. Uncertainty and error in complex plasma chemistry models. *Plasma Sources Science and Technology*, 24(3):035027, 2015. DOI: 10.1088/0963-0252/24/3/035027.

[162] M. M. Turner. Uncertainty and sensitivity analysis in complex plasma chemistry models. *Plasma Sources Science and Technology*, 25(1):015003, 2016. DOI: 10.1088/0963-0252/25/1/015003.

[163] M. M. Turner. Computer Simulation in Low-Temperature Plasma Physics: Future Challenges. *Plasma Processes and Polymers*, page 201600121, 2016. DOI: 10.1002/ppap.201600121.

[164] N. Pinhão, A. Moura, J. Branco, and J. Neves. Influence of gas expansion on process parameters in non-thermal plasma plug-flow reactors: A study applied to dry reforming of methane. *International Journal of Hydrogen Energy*, 41(22):9245–9255, 2016. DOI: 10.1016/j.ijhydene.2016.04.148.

[165] E. L. Crow and K. Shimizu. *Lognormal Distributions: Theory and Applications (Statistics: A Series of Textbooks and Monographs)*. CRC Press, 1987.

[166] M. Alvo and P. L. Yu. *Statistical Methods for Ranking Data*. Number 1976. Springer New York, New York, NY, 2014. DOI: 10.1007/978-1-4939-1471-5.

[167] I. V. Novobrantsev and A. N. Starostin. Decay instability of vibrational relaxation in molecular gases. *Journal of Applied Mechanics and Technical Physics*, 15(2):283–285, 1974. DOI: 10.1007/BF00850675.

[168] D. Mcelroy, C. Walsh, A. J. Markwick, et al. The UMIST database for astrochemistry 2012. *Astronomy & Astrophysics*, 550(A36), 2013. DOI: 10.1051/0004-6361/201220465.

[169] L. C. Pitchford, L. L. Alves, K. Bartschat, et al. LXCat : an Open-Access , Web-Based Platform for Data Needed for Modeling Low Temperature Plasmas. *Plasma Processes and Polymers*, 14(1-2), 2017. DOI: 10.1002/ppap.201600098.

[170] A. Berthelot and A. Bogaerts. Pinpointing energy losses in plasma-based CO_2 conversion. *Journal of CO_2 Utilization*, 2018. In press.

[171] W. Wang, D. Mei, X. Tu, and A. Bogaerts. Gliding arc plasma for CO_2 conversion: Better insights by a combined experimental and modelling approach. *Chemical Engineering Journal*, 330(July):11–25, 2017. DOI: 10.1016/j.cej.2017.07.133.

[172] W. Wang and A. Bogaerts. Effective ionisation coefficients and critical breakdown electric field of CO_2 at elevated temperature: effect of excited states and ion kinetics. *Plasma Sources Science and Technology*, 25(5):055025, 2016.

[173] L. D. Pietanza, G. Colonna, and M. Capitelli. Non-equilibrium plasma kinetics of reacting CO: an improved state to state approach. *Plasma Sources Science and Technology*, page Accepted manuscript, 2017. DOI: 10.1088/1361-6595/aa93bd.

[174] D. L. Baulch, D. D. Drysdale, J. Duxbury, and S. Grant. *Evaluated Kinetic Data for High Temperature Reactions, Volume 3: Homogeneous Gas Phase Reactions of the O_2-O_3 System, the CO-O_2-H_2 System, and of the Sulphur-containing Species*. Butterworth, London, 1976.

[175] J. C. Whitehead. Plasma-catalysis: the known knowns, the known unknowns and the unknown unknowns. *Journal of Physics D: Applied Physics*, 49(24):243001, 2016. DOI: 10.1088/0022-3727/49/24/243001.

[176] E. C. Neyts, K. K. Ostrikov, M. K. Sunkara, and A. Bogaerts. Plasma Catalysis: Synergistic Effects at the Nanoscale. *Chemical Reviews*, 115(24):13408–13446, 2015. DOI: 10.1021/acs.chemrev.5b00362.

[177] Y. Itikawa. Cross Sections for Electron Collisions With Carbon Dioxide. *Journal of Physical and Chemical Reference Data*, 31(3):749, 2002. DOI: 10.1063/1.1481879.

[178] Morgan database, extracted from LxCat, retrieved on december 4, 2015.

[179] J. E. Land. Electron scattering cross sections for momentum transfer and inelastic excitation in carbon monoxide. *Journal of Applied Physics*, 49(12):5716–5721, 1978. DOI: 10.1063/1.324589.

[180] A. V. Phelps. Tabulations of collision cross sections and calculated transport and reaction coefficients for electron collisions with o_2, 1985. DOI: JILA Pub. 3215.

[181] E. Krishnakumar and S. Srivastava. Cross-sections for electron impact ionization of O2. *International Journal of Mass Spectrometry and Ion Processes*, 113(1):1–12, 1992. DOI: 10.1016/0168-1176(92)87037-F.

[182] S. Matejcik, A. Kiendler, P. Cicman, et al. Electron attachment to molecules and clusters of atmospheric relevance: oxygen and ozone. *Plasma Sources Science and Technology*, 6(2):140–146, 1997. DOI: 10.1088/0963-0252/6/2/007.

[183] R. Janev, J. Wang, I. Murakami, and T. Kato. NIFS_DATA vol 68. Technical report, 2001.

[184] R. R. Laher and F. R. Gilmore. Updated Excitation and Ionization Cross Sections for Electron Impact on Atomic Oxygen. *Journal of Physical and Chemical Reference Data*, 19(1):277–305, 1990. DOI: 10.1063/1.555872.

[185] R. K. Janev and D. Reiter. Collision Processes of Hydrocarbon Species in Hydrogen Plasmas. Part 1. The Methane Family. *ChemInform*, 34(25), 2003. DOI: 10.1002/chin.200325274.

[186] T. G. Beuthe and J.-S. Chang. Chemical Kinetic Modelling of Non-Equilibrium Ar-CO_2 Thermal Plasmas. *Japanese Journal of Applied Physics*, 36(Part 1, No. 7B):4997–5002, 1997. DOI: 10.1143/JJAP.36.4997.

[187] W. Liu and G. A. Victor. Electron energy deposition in carbon monoxide gas. *The Astrophysical Journal*, 435:909, 1994. DOI: 10.1086/174872.

[188] I. A. Kossyi, A. Y. Kostinsky, A. A. Matveyev, and V. P. Silakov. Kinetic scheme of the non-equilibrium discharge in nitrogen-oxygen mixtures. *Plasma Sources Science and Technology*, 1(3):207–220, 1992. DOI: 10.1088/0963-0252/1/3/011.

[189] J. Woodall, M. Agúndez, A. J. Markwick-Kemper, and T. J. Millar. The UMIST database for astrochemistry 2006. *Astronomy & Astrophysics*, 466(3):1197–1204, 2007. DOI: 10.1051/0004-6361:20064981.

[190] J. T. Gudmundsson and E. G. Thorsteinsson. Oxygen discharges diluted with argon: dissociation processes. *Plasma Sources Science and Technology*, 16(2):399–412, 2007. DOI: 10.1088/0963-0252/16/2/025.

[191] A. A. Ionin, I. V. Kochetov, A. P. Napartovich, and N. N. Yuryshev. Physics and engineering of singlet delta oxygen production in low-temperature plasma. *Journal of Physics D: Applied Physics*, 40(2):R25–R61, 2007. DOI: 10.1088/0022-3727/40/2/R01.

[192] J. A. Blauer and G. R. Gilmore. A survey of vibrational relaxation rate data for processes important to CO_2-N_2-H_2O infrared plume radiation. *Ultrasystems, Inc. Technical Report*, pages afrpl–tr–7, 1973.

[193] R. D. Sharma. Near Resonant Vibrational Energy Transfer among Isotopes of CO_2. *Physical Review*, 177(5):102–107, 1969.

[194] T. G. Kreutz, J. A. O'Neill, and G. W. Flynn. Diode Laser Absorption Probe of Vibration-Vibration Energy Transfer in CO_2. *The Journal of Physical Chemistry*, 91(22):5540–5543, 1987.

[195] H.-j. Mick, M. Burmeister, and P. Roth. Atomic Resonance Absorption Spectroscopy Measurements on High-Temperature CO Dissociation Kinetics. *AIAA Journal*, 31(4):671–676, 1993. DOI: 10.2514/3.11602.

[196] S. Hadj-Ziane, B. Held, P. Pignolet, R. Peyrous, and C. Coste. Ozone generation in an oxygen-fed wire-to-cylinder ozonizer at atmospheric pressure. *Journal of Physics D: Applied Physics*, 25(4):677, 1992. DOI: 10.1088/0022-3727/25/4/014.

[197] M. Hayashi. *Swarm Studies and Inelastic Electron-Molecule Collisions*. Springer-Verlag, New-York, 1987. DOI: ISBN: 978-1-4612-4662-6.

[198] C. Tian and C. R. Vidal. Cross sections of the electron impact dissociative ionization of CO, CH_4 and C_2H_2. *Journal of Physics B: Atomic, Molecular and Optical Physics*, 31(4):895–909, 1998. DOI: 10.1088/0953-4075/31/4/031.

[199] D. Rapp and D. D. Briglia. Total Cross Sections for Ionization and Attachment in Gases by Electron Impact. II. Negative Ion Formation. *The Journal of Chemical Physics*, 43(5):1480–1489, 1965. DOI: 10.1063/1.1696958.

[200] S. A. Lawton and A. V. Phelps. Excitation of the $b^1\Sigma_g^+$ state of O_2 by low energy electrons. *The Journal of Chemical Physics*, 69(3):1055, 1978. DOI: 10.1063/1.436700.

[201] C. S. Weller and M. A. Biondi. Measurements of Dissociative Recombination of CO_2^+ Ions with Electrons. *Physical Review Letters*, 19(2):59–61, 1967. DOI: 10.1103/PhysRevLett.19.59.

[202] J. Thoenes and S. C. Kurzius. Plasma Chemistry Processes in the Closed Cycle EDL - Technical Report DRCPM-HEL-CR-79-11-VOL-1. Technical report, Lockheed Missiles and Space Co Inc, Huntsville AL, 1979.

[203] J. B. A. Mitchell and H. Hus. The dissociative recombination and excitation of CO^+. *Journal of Physics B: Atomic and Molecular Physics*, 18(3):547–555, 1985. DOI: 10.1088/0022-3700/18/3/029.

[204] D. Albritton. Ion-neutral reaction-rate constants measured in flow reactors through 1977. *Atomic Data and Nuclear Data Tables*, 22(1):1–101, 1978. DOI: 10.1016/0092-640X(78)90027-X.

[205] N. Adams, D. Smith, and D. Grief. Reactions of H_nCO^+ ions with molecules at 300 K. *International Journal of Mass Spectrometry and Ion Physics*, 26(4):405–415, 1978. DOI: 10.1016/0020-7381(78)80059-X.

[206] F. C. Fehsenfeld and E. E. Ferguson. Laboratory studies of negative ion reactions with atmospheric trace constituents. *The Journal of Chemical Physics*, 61(8):3181–3193, 1974. DOI: 10.1063/1.1682474.

[207] M. Mcfarland, D. L. Albritton, F. C. Fehsenfeld, E. E. Ferguson, and A. L. Schmeltekopf. Flow-drift technique for ion mobility and ion-molecule reaction rate constant measurements. III. Negative ion reactions of O^- with CO, NO, H_2, and D_2. *Journal of Chemical Physics*, 59(12):6629–6635, 1973. DOI: 10.1063/1.1680043.

[208] D. Price and J. Moruzzi. Negative ion molecule reactions in CO_2 at high pressures and temperatures. *Vacuum*, 24(11-12):591–593, 1974. DOI: 10.1016/0042-207X(74)90038-4.

[209] F. C. Fehsenfeld, A. L. Schmeltekopf, H. I. Schiff, and E. E. Ferguson. Laboratory measurements of negative ion reactions of atmospheric interest. *Planetary and Space Science*, 15(2):373–379, 1967. DOI: 10.1016/0032-0633(67)90201-2.

[210] S. G. Belostotsky, D. J. Economou, D. V. Lopaev, and T. V. Rakhimova. Negative ion destruction by $O(^3P)$ atoms and $O_2(a^1\Delta_g)$ molecules in an oxygen plasma. *Plasma Sources Science and Technology*, 14(3):532–542, 2005. DOI: 10.1088/0963-0252/14/3/016.

[211] J. L. Pack and A. V. Phelps. Electron Attachment and Detachment. II. Mixtures of O_2 and CO_2 and of O_2 and H_2O. *The Journal of Chemical Physics*, 45(11):4316–4329, 1966. DOI: 10.1063/1.1727491.

[212] M. H. Bortner, T. Bourer, and C. A. Blank. Reaction Rate Handbook, Second Edition AD 763699. Technical report, Defense Nuclear Agency, 1972.

[213] J. B. Hasted and R. A. Smith. The Detachment of Electrons from Negative Ions. *Proceedings of the Royal Society A: Mathematical, Physical and Engineering Sciences*, 235(1202):349–353, 1956. DOI: 10.1098/rspa.1956.0087.

[214] L. Frommhold. Über verzögerte Elektronen in Elektronenlawinen, insbesondere in Sauerstoff und Luft, durch Bildung und Zerfall negativer Ionen (O^-). *Fortschritte der Physik*, 12(11):597–642, 1964. DOI: 10.1002/prop.19640121102.

[215] J. T. Gudmundsson. A critical review of the reaction set for a low pressure oxygen processing discharge. Technical report, University of Iceland, 2004. DOI: RH-17-2004.

[216] C. J. S. M. Simpson, T. R. D. Chandler, and A. C. Strawson. Vibrational Relaxation in CO_2 and CO_2–Ar Mixtures Studied Using a Shock Tube and a Laser–Schlieren Technique. *The Journal of Chemical Physics*, 51(5):2214–2219, 1969. DOI: 10.1063/1.1672319.

[217] R. Taylor and S. Bitterman. Survey of Vibrational Relaxation Data for Processes Important in the CO_2-N_2 Laser System. *Reviews of Modern Physics*, 41(1):26–47, 1969. DOI: 10.1103/RevModPhys.41.26.

[218] W. A. Rosser, A. D. Wood, and E. T. Gerry. Deactivation of Vibrationally Excited Carbon Dioxide (ν_3) by Collisions with Carbon Dioxide or with Nitrogen. *The Journal of Chemical Physics*, 50(11):4996–5008, 1969. DOI: 10.1063/1.1670996.

[219] K. F. Herzfeld. Deactivation of Vibrations by Collision in the Presence of Fermi Resonance. *The Journal of Chemical Physics*, 47(2):743–752, 1967. DOI: 10.1063/1.1711947.

[220] R. L. DeLeon and J. Rich. Vibrational energy exchange rates in carbon monoxide. *Chemical Physics*, 107(2-3):283–292, 1986. DOI: 10.1016/0301-0104(86)85008-X.

[221] C. Flament, T. George, K. A. Meister, et al. Nonequilibrium vibrational kinetics of carbon monoxide at high translational mode temperatures. *Chemical Physics*, 163(2):241–262, 1992. DOI: 10.1016/0301-0104(92)87106-J.

[222] W. A. Rosser, R. D. Sharma, and E. T. Gerry. Deactivation of Vibrationally Excited Carbon Dioxide (001) by Collisions with Carbon Monoxide. *The Journal of Chemical Physics*, 54(3):1196–1205, 1971. DOI: 10.1063/1.1674955.

[223] M. Burmeister and P. Roth. ARAS measurements on the thermal decomposition of CO_2 behind shock waves. *AIAA Journal*, 28(3):402–405, 1990. DOI: 10.2514/3.10406.

[224] W. Tsang and R. F. Hampson. Chemical Kinetic Data Base for Combustion Chemistry. Part I. Methane and Related Compounds. *Journal of Physical and Chemical Reference Data*, 15(3):1087–1279, 1986. DOI: 10.1063/1.555759.

[225] D. Husain and A. N. Young. Kinetic investigation of ground state carbon atoms, $C(2^3P_J)$. *Journal of the Chemical Society, Faraday Transactions 2*, 71(February):525, 1975. DOI: 10.1039/f29757100525.

[226] R. R. Baldwin, D. Jackson, A. Melvin, and B. N. Rossiter. The second limit of hydrogen + carbon monoxide + oxygen mixtures. *International Journal of Chemical Kinetics*, 4(3):277–292, 1972. DOI: 10.1002/kin.550040305.

[227] A. J. Dean, D. F. Davidson, and R. K. Hanson. A shock tube study of reactions of carbon atoms with hydrogen and oxygen using excimer photolysis of C_3O_2 and carbon atom atomic resonance absorption spectroscopy. *The Journal of Physical Chemistry*, 95(1):183–191, 1991. DOI: 10.1021/j100154a037.